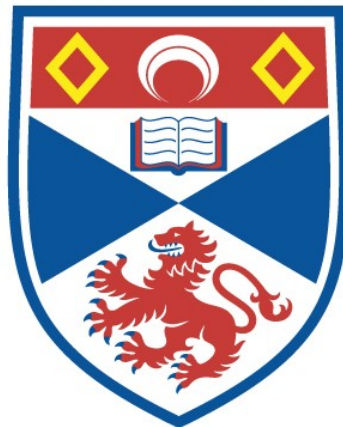


NEGATIVELY CHARGED IONS IN THE DEEP EARTH:
QUANTIFYING THE CHEMICAL SPECIATION OF F AND N IN
SILICATE MELTS AND PHASES

Filippo Formoso

A Thesis Submitted for the Degree of PhD
at the
University of St Andrews



2022

Full metadata for this thesis is available in
St Andrews Research Repository

at:

<http://research-repository.st-andrews.ac.uk/>

Identifiers to use to cite or link to this thesis:

DOI: <https://doi.org/10.17630/sta/260>

<http://hdl.handle.net/10023/26905>

This item is protected by original copyright

This item is licensed under a
Creative Commons License

<https://creativecommons.org/licenses/by-nd/4.0>

Negatively charged ions in the deep Earth:
quantifying the chemical speciation of F and N in
silicate melts and phases

Filippo Formoso



University of
St Andrews

This thesis is submitted in partial fulfilment for the degree of

Doctor of Philosophy (PhD)

at the University of St Andrews

July 2022

Candidate's declaration

I, Filippo Formoso, do hereby certify that this thesis, submitted for the degree of PhD, which is approximately 60,000 words in length, has been written by me, and that it is the record of work carried out by me, or principally by myself in collaboration with others as acknowledged, and that it has not been submitted in any previous application for any degree. I confirm that any appendices included in my thesis contain only material permitted by the 'Assessment of Postgraduate Research Students' policy.

I was admitted as a research student at the University of St Andrews in September 2018.

I received funding from an organisation or institution and have acknowledged the funder(s) in the full text of my thesis.

Date 04/11/22

Signature of candidate

|

Supervisor's declaration

I hereby certify that the candidate has fulfilled the conditions of the Resolution and Regulations appropriate for the degree of PhD in the University of St Andrews and that the candidate is qualified to submit this thesis in application for that degree. I confirm that any appendices included in the thesis contain only material permitted by the 'Assessment of Postgraduate Research Students' policy.

Date 04/11/22

Signature of supervisor

Permission for publication

In submitting this thesis to the University of St Andrews we understand that we are giving permission for it to be made available for use in accordance with the regulations of the University Library for the time being in force, subject to any copyright vested in the work not being affected thereby. We also understand, unless exempt by an award of an embargo as requested below, that the title and the abstract will be published, and that a copy of the work may be made and supplied to any bona fide library or research worker, that this thesis will be electronically accessible for personal or research use and that the library has the right to migrate this thesis into new electronic forms as required to ensure continued access to the thesis.

I, Filippo Formoso, confirm that my thesis does not contain any third-party material that requires copyright clearance.

The following is an agreed request by candidate and supervisor regarding the publication of this thesis:

Printed copy

No embargo on print copy.

Electronic copy

No embargo on electronic copy.

Date 04/11/22

Signature of candidate

Date 04/11/22

Signature of supervisor

Underpinning Research Data or Digital Outputs

Candidate's declaration

I, Filippo Formoso, understand that by declaring that I have original research data or digital outputs, I should make every effort in meeting the University's and research funders' requirements on the deposit and sharing of research data or research digital outputs.

Date 04/11/22

Signature of candidate

Permission for publication of underpinning research data or digital outputs

We understand that for any original research data or digital outputs which are deposited, we are giving permission for them to be made available for use in accordance with the requirements of the University and research funders, for the time being in force.

We also understand that the title and the description will be published, and that the underpinning research data or digital outputs will be electronically accessible for use in accordance with the license specified at the point of deposit, unless exempt by award of an embargo as requested below.

The following is an agreed request by candidate and supervisor regarding the publication of underpinning research data or digital outputs:

No embargo on underpinning research data or digital outputs.

Date 04/11/22

Signature of candidate

Date 04/11/22

Signature of supervisor

~ ABSTRACT ~

Nitrogen and fluorine are essential volatile elements to study in the bulk silicate Earth (BSE) due to their respective influence over the onset of habitability on Earth or over physical and chemical properties of the phases which contain them. Nitrogen is abnormally depleted in the BSE relative to CI chondrite, while fluorine is abnormally enriched, hence questions arise about their chemical speciation and storage mechanisms within planetary reservoirs.

The speciation of nitrogen in high pressure silicate melts was studied using solid-state nuclear magnetic resonance (NMR) and Raman spectroscopy and was found to be heavily influenced by oxygen fugacity. The former technique provided superior results in quantifying the abundance of individual species and higher sensitivity, however it requires ^{15}N enrichment, low-Fe samples and performs only bulk analysis, while the latter was found to be an efficient *in situ* technique regardless of sample composition, but it struggled at detecting low-abundance N species.

The speciation of fluorine in silicate melts was studied via NMR spectroscopy at BSE-like concentrations, thanks to this techniques high F sensitivity. F was found to be binding solely with Mg at atmospheric pressure, and this speciation remains predominant until c.a. 8 GPa, where relevant quantities of F start binding with Ca. This is likely due to the changing coordination number of the major components of the melt, but a change in the coordination of fluorine itself might also be occurring.

The ordering of fluoride and hydroxide in the framework of humite group minerals was studied via NMR spectroscopy and computational modelling. The incorporation of one F and one OH anion in neighbouring sites was found to be favoured relative to the incorporation of two identical ions, thanks to the formation of a hydrogen bond. This likely explains the extended stability field of clinohumite when it is F rich.

~ ACKNOWLEDGEMENTS ~

The first people that I would like to thank are my supervisors, Dr. Sami Mikhail, Prof. Sharon Ashbrook, Dr. Eleanor Mare, and Dr. Daniel Dawson. Their creative and positive attitude and extensive knowledge of the respective fields of science were indispensable for the unorthodox interdisciplinary research project that culminated with this thesis. Without their constant support, it would not have been possible for me to indulge in the science I so much loved during the latter 3 and a half years. I would also like to acknowledge the contribution given by Dr. Eva Stueeken during my yearly review meetings, and by Dr. Paul Savage, who also participated to said meetings and provided invaluable support as my pastoral supervisor.

I would then like to thank Dr. Suzi Pugh, Dr. Robert Moran, Dr. Nasima Kanwal, Cameron Rice, Bonifax Legrady and Zachary Davis for their patience in helping me learn how to properly operate a solid-state NMR spectrometer, and to all my colleagues in the SEMA research team in the School of Chemistry for accepting this strange geologist turned half chemist in their group and showing him a different way of being a scientist.

I also must thank Toby Boocock, Michele Rinaldi and all the undergraduate and postgraduate taught students that I interacted with in the Mikhail team, who all contributed diverse and precious insights in my research.

I also have to thank Dr. Paul Webb and Dr. David Miller for their help during the acquisition of Raman and FT-IR data and of Raman and SEM data respectively, and for teaching me how to critically approach these fascinating

instruments. I also acknowledge the contribution of Dr. Sebastian Fischer and Stuart Allison to the preparation of some of my samples, and Dr. David McKay for his contributions to the calculations and modelling performed on humite-type minerals.

I would also like to acknowledge all the people who contributed to my research from outside of the University of St Andrews. In more detail, I want to thank Dr. Geoff Bromiley (University of Edinburgh, UK), Dr. Bastian Joachim-Mrosko and Dr. Jürgen Konzett (Universität Innsbruck, AT), Caterina Melai and Prof. Daniel Frost (Bayerisches Geoinstitut, DE), Dr. Patrizia Fumagalli and Dr. Giulio Borghini (Università degli Studi di Milano, IT), and Prof. Andrew Berry (Australian National University, AU), for their assistance and supervision in the synthesis and analysis of the materials that were object of this thesis. Their contribution was particularly crucial given the sudden onset of the global pandemic, which made every collaboration exponentially more difficult to manage.

Outside of the purely academic sphere, I would like to thank my parents and all my friends in the UK, in Italy or wherever else in the world they are.

Finally, to every person or group of people not explicitly mentioned in these pages that still feels to have given a contribution to this work, please accept my apologies and rest assured that your input was as meaningful as the one from named contributors.

This work was funded and supported by the University of St Andrews (School of Earth and Environmental Sciences, School of Chemistry and St Leonards Postgraduate College).

~ CONTENTS ~

1. <u>Introduction.....</u>	1
1.1. General introduction.....	1
1.1.1. Volatility: a murky concept.....	3
1.1.2. The Earth's volatiles budget.....	4
1.2. Scope of this thesis.....	7
1.3. Introduction – Nitrogen.....	8
1.3.1. Introducing the problem with calculating the nitrogen budget of Earth.....	11
1.3.2. Nitrogen in different reservoirs.....	13
1.3.2.1. Nitrogen in the atmosphere.....	14
1.3.2.2. Nitrogen in the hydrosphere and biosphere.....	16
1.3.2.3. Nitrogen in the continental crust.....	17
1.3.2.4. Nitrogen in the oceanic crust.....	19
1.3.2.5. Nitrogen in the Bulk Silicate Earth.....	20
1.3.2.6. Nitrogen in the core.....	22
1.3.2.7. Nitrogen concentration in chondrites.....	24
1.3.2.8. Nitrogen concentration in achondrites.....	24
1.3.3. Nitrogen's global cycle: from the atmosphere to the deep Earth..	25
1.3.3.1. Nitrogen's surficial cycle.....	26
1.3.3.2. Nitrogen's deep cycle.....	27

1.4. Introduction – Fluorine.....	29
1.4.1. The F budget of chondrites.....	31
1.4.1.1. F and Cl in carbonaceous chondrites.....	34
1.4.1.2. F and Cl in enstatite chondrites.....	35
1.4.1.3. F and Cl in ordinary chondrites.....	37
1.4.2. The Earth’s fluorine reservoirs.....	38
1.4.2.1. F in surficial reservoirs.....	39
1.4.2.2. F in the continental and oceanic crust.....	40
1.4.2.3. F in the Bulk Silicate Earth and core.....	40
1.4.3. Fluorine storage in common BSE phases.....	41
1.4.4. F solubility in silicate systems and its speciation.....	43
2. <u>Methods</u>.....	46
2.1. Sample synthesis.....	46
2.1.1. Low pressure sample synthesis.....	47
2.1.1.1. Muffle furnace – Theory.....	47
2.1.1.2. Muffle furnace – Application.....	48
2.1.2. High pressure sample synthesis.....	51
2.1.2.1. End loaded piston cylinder press – Theory.....	52
2.1.2.2. End loaded piston cylinder press – Starting material preparation.....	55
2.1.2.3. End loaded piston cylinder press – Sample synthesis.....	57
2.1.2.4. Multi anvil press – Theory.....	59
2.1.2.5. Multi anvil press – Application.....	62
2.2. Analytical methodologies.....	64

2.2.1. MAS NMR Spectroscopy.....	64
2.2.1.1. N speciation analysis via ¹⁵ N MAS NMR.....	70
2.2.1.2. F speciation analysis via ¹⁹ F MAS NMR.....	71
2.2.1.3. F abundance quantification via ¹⁹ F MAS NMR.....	72
2.2.1.4. F speciation and F/OH quantification in humite group minerals via ¹⁹ F MAS NMR.....	75
2.2.2. Raman Spectroscopy.....	77
2.2.2.1. Raman spectroscopy of N-enriched silicate glasses.....	81
2.2.2.2. Raman spectroscopy of high pressure F-enriched silicate glasses.....	81
2.2.2.3. Phase identification and quantification in humite group minerals.....	82
2.2.3. Electron Microprobe Micro Analysis (EPMA).....	72
2.2.3.1. EPMA of N-enriched silicate glasses.....	86
2.2.3.2. EPMA of low P F-enriched silicate glasses.....	87
2.2.3.3. EPMA of high P F-enriched silicate glasses.....	87
2.2.4. Sensitive High-Resolution Ion Micro Probe (SHRIMP).....	90
2.2.5. Data Processing.....	92
2.2.6. Density Function Theory (DFT).....	92
3. <u>Investigation of Nitrogen Speciation in CMAS Silicate Melts using ¹⁵N</u> <u>MAS NMR.....</u>	95
3.1. Introduction.....	95
3.1.1. Nitrogen speciation in silicate melts and phases.....	95
3.1.1.1. Molecular nitrogen (N ₂).....	98

3.1.1.2. Ammoniacal nitrogen (N—H).....	99
3.1.2. Analytical challenges in measuring N speciation.....	100
3.1.3. Scope of this study.....	103
3.2. Methods summary.....	105
3.3. Results.....	106
3.3.1. Structural and compositional information.....	106
3.3.1.1. Glass homogeneity.....	106
3.3.1.2. EPMA results.....	108
3.3.1.3. SHRIMP results.....	109
3.3.2. Speciation analysis.....	112
3.3.2.1. DFT calculations outcome.....	112
3.3.2.2. Raman results.....	113
3.3.2.3. ¹⁵ N MAS NMR results.....	115
3.4. Discussion.....	119
3.4.1. Attainment of equilibrium.....	119
3.4.2. Peak assignment.....	120
3.4.2.1. ¹⁵ N MAS NMR spectra interpretation.....	120
3.4.2.2. Raman spectra interpretation.....	122
3.4.3. Advantages and disadvantages of spectroscopic techniques used.....	127
3.4.3.1. The case for ¹⁵ N MAS NMR spectroscopy.....	127
3.4.3.2. The case for Raman spectroscopy.....	128
3.4.4. Nitrogen speciation in silicate melts.....	130
3.5. Conclusions.....	132

4. <u>Evidence for F—Mg Local Bonding Environment in Low Pressure</u>	
<u>CMAS Silicate Melts: Implications for the Volatile Budget of</u>	
<u>Chondrites.....</u>	135
4.1. Introduction.....	135
4.1.1. The relationship between F and Mg during chondritic evolution.....	136
4.1.2. Scope of this study.....	141
4.2. Methods summary.....	142
4.3. Results and discussion.....	143
4.3.1. Chemical composition.....	143
4.3.1.1. Glass appearance and major elements composition.....	143
4.3.1.2. F concentration quantification.....	144
4.3.2. Fluorine speciation via ¹⁹ F MAS NMR spectroscopy.....	147
4.3.2.1. Peak assignment in reference materials.....	150
4.3.2.2. F speciation in silicate glasses.....	151
4.3.3. Attainment of equilibrium.....	153
4.3.4. Implication for F storage during chondritic evolution.....	154
4.4. Conclusions.....	156
5. <u>Investigating the effects of pressure on F speciation in CMAS silicate</u>	
<u>melts using ¹⁹F MAS NMR spectroscopy.....</u>	158
5.1. Introduction.....	158
5.1.1. Fluorine in the BSE.....	159
5.1.2. Fluorine in silicate melts.....	163
5.1.3. Scope of this study.....	165

5.2. Methods summary.....	166
5.3. Results.....	169
5.3.1. Chemical and phase composition.....	169
5.3.1.1. Glass appearance and major element composition.....	169
5.3.1.2. F concentration quantification using ^{19}F MAS NMR.....	170
5.3.1.3. Phase characterization using Raman spectroscopy.....	173
5.3.2. Identifying fluorine speciation using ^{19}F MAS NMR.....	174
5.3.2.1. F speciation up to 5 GPa.....	176
5.3.2.2. F speciation from 8 to 20 GPa.....	176
5.4. Discussion.....	177
5.4.1. Peak assignment and F speciation in high pressure CMAS7G silicate melts.....	177
5.4.1.1. Peak assignment in ^{19}F MAS NMR spectra.....	177
5.4.1.2. Attainment of equilibrium.....	181
5.4.1.3. Peak assignment in Raman spectra.....	182
5.4.2. The behaviour and speciation of fluorine in high pressure silicate melts.....	183
5.4.2.1. Fluorine loss in high T conditions.....	183
5.4.2.2. The effect of increasing pressure on F speciation.....	185
5.4.2.3. The impact of F speciation on the structure of the melt...	189
5.5. Conclusions.....	191
6. <u>Fluorine and hydroxide ordering in humite group minerals: a ^{19}F MAS NMR study.....</u>	193
6.1. Introduction.....	193

6.1.1. Humite group minerals and their stability.....	194
6.1.1.1. The Ti \leftrightarrow Mg substitution.....	197
6.1.1.2. The F \leftrightarrow OH exchange and solid solution.....	198
6.1.2. F and OH arrangement in humite group minerals frameworks..	201
6.1.2.1. The stabilizing effect of hydrogen bonds.....	203
6.1.3. Scope of this study.....	207
6.2. Methods summary.....	208
6.2.1. Numerical modelling.....	210
6.3. Results.....	218
6.3.1. Phase identification using Raman spectroscopy.....	218
6.3.2. ^{19}F MAS NMR spectroscopy.....	220
6.3.2.1. Quantification of the F/OH fraction.....	220
6.3.2.2. F speciation analysis.....	223
6.3.3. Numerical modelling.....	225
6.3.3.1. Model testing and optimization.....	225
6.3.3.2. F speciation prediction results.....	228
6.4. Discussion.....	230
6.4.1. F and OH ordering in humite group minerals.....	230
6.4.1.1. Modelled vs. experimentally determined F speciation....	230
6.4.1.2. Implications for humite group minerals stability.....	235
6.5. Conclusions.....	237
7. <u>Conclusions and further research</u>.....	240
7.1. Conclusions.....	240
7.2. Studying deep Earth fluids via NMR spectroscopy.....	243

7.3. Fluorine storage during melt crystallization.....	247
7.4. Quantification of fluorine loss during high temperature sample synthesis.....	248
7.5. The destabilization of Al—F species with increasing pressure.....	249
7.6. The driving force behind fluorine speciation in humite group minerals.....	250
8. <u>References</u>.....	253
9. <u>List of figures, tables and equations</u>.....	276

~1 — INTRODUCTION~

1.1 – GENERAL INTRODUCTION

The determination of the general and detailed composition of planet Earth has always been one of the main targets of the geosciences. For most of humanity's history the deep Earth's composition and structure has been virtually unknown. Thanks to the development of the natural sciences, it has been possible, during the last 350 or so years, to assess the chemistry of natural materials more quantitatively. This, alongside the understanding of concepts such as thermal and pressure stability of different phases, crystalline structures and, later, the velocity of seismic waves, allowed a rapid determination of the nature of the major mineral components of the Earth's crust (Plagioclase, K-feldspars, Micas, Quartz, Pyroxenes and Amphiboles), upper mantle (Quartz, Olivine, Pyroxene, Garnets, Spinels), lower mantle (Perovskites, Bridgmanite, Ca and Mg oxides) and core (molten and solid Taenite, i.e., (Fe, Ni) alloy); Klein & Hurlbut (1993).

By exploring the chemical composition of the minerals denoted above, and by investigating the structure of the deep Earth through seismic analysis, it was possible to infer the abundance of the main chemical constituents of our planet, which are remarkably few elements (Table 1.1, Allègre et al., 1995).

Element	Abundance (wt%)
O	44.79
Mg	22.78
Si	21.52
Fe	5.82
Ca	2.31
Al	2.16
Others	0.62

Table 1.1: Major constituents of planet Earth as a whole (Allègre et al., 1995), showing that more than 99% of the planet comprises just six elements.

Once the major chemical components of the Earth were adequately determined, attention then turned towards understanding the trace elements and minor isotopes, both stable and unstable (reported as “Others” in Table 1.1) that are present at different depths. This, however, proved a very different type of challenge, as the composition of common rock forming minerals could not be used as a guide. While the hunt for the heavier isotopes (e.g., rare earth elements, platinum group elements, other transition metals, etc.) can now be considered largely concluded, based on measurements performed on early solar system meteorites (Lodders & Fegley, 1998, and refs. therein) and their extension to the whole planet through different models (e.g., McDonough & Sun, 1995; Lodders, 2003), the abundances of the lighter elements are often still object of debate. Light stable isotopes (e.g., H, O, C, N and P) are key constituents of organic compounds, and therefore essential building blocks of life on Earth. Therefore, [1] their presence on the surface of an Earth-like planet is critical for the development of habitable conditions and [2] a constant availability of such

elements is crucial for the long-term persistence of these conditions, thus leading to the potential origin of organic-based life forms.

While understanding the origin of life is far beyond the scope of this thesis, it is important to underline how a study that is focused on something as potentially obscure as the behaviour of volatile elements in the depths of our planet potentially ties into a much broader and more general field of research. Perhaps more importantly, it must be stressed how the results and implications presented in this thesis are not strictly specific to Earth, but instead can be extended to any Earth-like planet.

1.1.1 - Volatility: a murky concept

Most of the times light elements such as oxygen, nitrogen, fluorine, or phosphorus are referred to as “volatiles”. Volatile elements are usually defined as those which either always, or mostly, behave as strong incompatibles during melting processes, thus often tending to be concentrated in fluid or gaseous phases in equilibrium with a coexisting silicate melt (Goldschmidt, 1937). This classification of elements however results in one key issue: the behaviour of an element, especially those that are light and strongly electronegative such as the “volatiles”, is heavily influenced by the way in which they are bonded to other atoms around them (Mueller, 2021; and refs. therein). An obvious example is carbon: C can be described as a volatile when bonded to atoms such as H (e.g., in CH₄, methane) or O (e.g., in CO₂, carbon dioxide), however when bonded to other C atoms (e.g., in diamond) it forms a solid, stable, and unreactive phase. It’s worth noting that

coordination number does not play a direct role in this difference, as while it is 6 in diamond, a solid, and 2 in CO₂, a gas, and 3 in graphite and fullerene, which are solids too. Therefore, the same element can behave in profoundly different ways solely based on its surrounding atomic environment. This is also true for the reactions in which an element can be involved: as an example, CH₄ can react with oxygen and undergo a combustion, unlike CO₂, which is instead the product of the same reaction, yet both phases are gaseous at equivalent conditions.

All of this leads to the conclusion that describing elements as complex in behaviour as the so-called volatiles as purely incompatible (or compatible) can be misleading.

1.1.2 – The Earth's volatiles budget

The different enrichment levels of volatiles in the Bulk Silicate Earth (BSE), when compared to reference reservoirs such as CI (Carbonaceous Iruna-type) chondrite (see Figure 1.1), the most primitive bodies of the solar system (Wasson & Kallemeyn, 1988), has long been object of debate. More specifically, the different abundance of an element in the BSE when compared to CI chondrite implies a change in chemical behaviour of this element between chondrite formation and planetary accretion. Investigations of such phenomena have so far been only partially conclusive (Johnson & Goldblatt, 2015; Harlov & Aranovich, 2018).

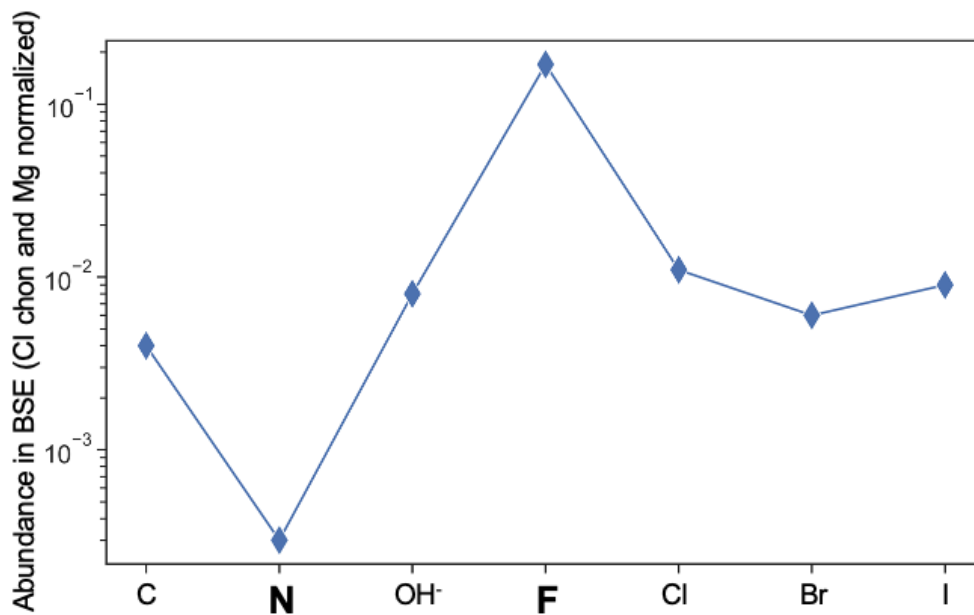


Figure 1.1: Abundance of some volatiles in the BSE relative to CI chondrite and Mg. The relative enrichment and depletion of F and N respectively is evident (data from McDonough & Sun, 1995, Lodders & Fegley, 1998, and Goldblatt et al., 2009), and shows a different behaviour during planetary accretion compared to CI chondrite formation.

One element whose depletion in the BSE is particularly evident is nitrogen (see Figure 1.1). Historically, the behaviour of N in the BSE has been closely associated with carbon, due to their various similarities. For example, C and N have similar atomic radii (70 vs 65 pm respectively; Shannon, 1976) and charge (+4 for C and usually ± 3 for N), and this results in C and N sometimes sharing a similar behaviour in the deep Earth (e.g., N being the most abundant impurity in diamonds; Mikhail & Howell, 2016). In other instances, however, the behaviour of C and N are remarkably different, for example their form at near surface conditions being graphite and N₂ respectively, the first being a solid highly susceptible to oxidation while the latter being an inert gas akin to a noble gas (Marty, 2012). As a result, nitrogen is the major component of the Earth's

atmosphere, with carbon being only a minor component of this, in its oxidized form (i.e., CO₂).

The different enrichment of N and C can be explained in two ways: [1] some of the differences between these two atomic species led to a different fractionation process during planetary accretion (Johnson & Goldblatt, 2015), or [2] that a yet undiscovered N reservoir exists in the deep Earth, which could account for the apparent N depletion (Zerkle & Mikhail, 2017). It is worth noting that the two eventualities are not mutually exclusive, as different chemical behaviour during fractionation processes might lead to the sequestration of one species but not the other in a possible unknown reservoir.

Another element whose behaviour is remarkably different from its closest relatives is fluorine (see Figure 1.1). Fluorine is the smallest of the halogens, with an ionic radius akin to oxygen (133 vs 140 pm for F⁻ and O²⁻ respectively; Shannon, 1976), a fact that sets it apart from the other halogens, which are instead all noticeably larger, and thus are expected to be more incompatible (Goldschmidt, 1937). The greatest similarity, however, is perhaps seen with the hydroxide ion (OH⁻), which also has an ionic radius of 133 pm (Jenkins & Thakur, 1979) and shares with F⁻ a charge of -1. This, alongside the common occurrence of solid solutions featuring the two anions (e.g., in clinohumite, (Mg, Fe)₉(SiO₄)₄(F,OH)₂), has been interpreted in the past as a sign of possible similar geochemical behaviour. Nevertheless, relevant differences between the two anions exist, such as the non-polarity of F⁻ compared with the polarity of OH⁻, alongside the fact that one is a monoatomic ion while the other consists of two atomic species. All of this could have resulted in differing pathways being followed

during planetary accretion, thus leading to a higher degree of F enrichment in the BSE (Harlov & Aranovich, 2018).

The elements brought forward as an example above were not chosen at random. N and F indeed played an undoubtedly crucial role in the onset of habitability on Earth, as [1] N is a key component of DNA and RNA molecules (Chargaff, 1950), while [2] the co-existence of F with hydroxide in various mineral phases is likely to have a great influence in water's mineral reservoirs, thus impacting the storage of water in the deep Earth and its eventual presence on the surface (Mi & Pan, 2018). Therefore, investigating their behaviour during both the early and current phases of Earth's history is paramount to understand the origin of life on this and similar planets.

1.2 – SCOPE OF THIS THESIS

This thesis was conceived to answer important questions about the location and evolution of volatile elements during Earth's history. This topic is of critical importance, as such elements often have either direct (Nitrogen) or indirect (Fluorine) effects on the habitability of a planet's surficial environments (see section 1.1.2). As this field of research is too wide for a single PhD thesis to encompass, specific topics were selected:

- 1) The chemical speciation of nitrogen and fluorine in low and high pressure silicate melts, as during the Earth's formation and accretion multiple planet-scale partial melting events occurred (Nakajima & Stevenson, 2015), and the local bonding environment of these elements could

influence whether they are retained by the melt phase until degassing or incorporated into minerals during crystallization.

- 2) The interaction between fluorine and neighbouring elements in crystalline phases. Humite group minerals were chosen for this study due to their importance as a water-carrying phase during subduction (Liu et al., 2019), and the incorporation of F in their framework has been shown to greatly expand their P-T field of stability (Grützner et al., 2017).

In studying the topics at points (1) and (2), this thesis aims to address some of the open questions about the fate of volatiles during the formation and evolution of the Earth and other akin planetary bodies, and thus to shed light on some of the geological processes necessary for the onset of habitable conditions.

The following subchapters will present the concepts regarding the geochemistry of nitrogen and fluorine necessary for the understanding of this thesis.

1.3 - INTRODUCTION – NITROGEN

Nitrogen is the lightest element in Group 15 (Period 2) of the periodic table. Its atomic number is 7, and average atomic mass is 14.007. ^{14}N is the major stable isotope (99.632(7)% of all stable N atoms), and the only other known stable isotope is ^{15}N , which makes up the remaining 0.368(7)% (see Table 1.2; Mueller,

2019). The main difference between the two, other than the atomic mass, is in the nuclear spin quantum number, I , which is 1 for ^{14}N and $\frac{1}{2}$ for ^{15}N (Meija et al., 2013). A number of unstable radioactive isotopes exist, with half-lives usually in the order of magnitude of seconds or minutes (see Table 1.2; Mills et al., 1988).

Isotope	Abundance	Nature	Half life
^{14}N	99.632(7)%	Stable	//
^{15}N	0.368(7)%	Stable	//
^{13}N	//	Radioactive	9.965 min
^{16}N	//	Radioactive	7.130 s
^{17}N	//	Radioactive	4.173 s

Table 1.2: Relative abundance, stability and half-lives of the isotopes of nitrogen (Mills et al., 1988; Mueller, 2019).

It is widely known that nitrogen in its molecular form (N_2 , $\text{N}\equiv\text{N}$) is the main constituent (78.084%) of Earth's atmosphere. This molecule consists of two N atoms bonded by a triple non-polar covalent bond, which takes a notable amount of energy to be broken (Mueller, 2019). This translates to the atmosphere of Earth consisting mostly of an inert gas, which in turn is a favourable condition for life to thrive on the surface of the planet. Despite its stability as N_2 , nitrogen on Earth's surface can be found in a wide variety of oxidation states (Zerkle, 2018), from strongly oxidised nitrate compounds (NO_x^{y-}) fixed, for example, by microorganisms on the ocean floor (Dalsgaard et al., 2005) to heavily reduced ammoniacal groups ($\text{NH}_x^{y+/-}$) formed in anaerobic environments (Goldblatt et al., 2009).

It is hard to overstate the essentiality of nitrogen for the existence and evolution of life on Earth, as it is a crucial component of both nucleic acids, DNA

and RNA (Chargaff, 1950). Therefore, understanding the pathways followed by nitrogen during Earth's history has always been paramount to the study of the onset of life on Earth-like planets (Zerkle & Mikhail, 2017). Despite this, the identity of the N stored in deep-Earth reservoirs (Li & Keppler, 2014), as well as variations in the N content of the atmosphere (Zhang & Zindler, 1993), have long been an object of discussion and, as of now, a consensus on the total N budget of the Earth, as well as its cycling between different reservoirs, has yet to be reached (Johnson & Goldblatt, 2015).

Attempting to resolve the whole controversy regarding the N budget and partitioning would have been outside the scope of this thesis. It was thus decided to narrow the focus of this study to the role played by the chemical speciation of nitrogen in mafic silicate melts, and its impact on the potential sequestration or outgassing of N during subduction of N-rich phases. To explain the significance of this very specific process, a general overview of nitrogen distribution throughout Earth's main N reservoirs is required. The following is not an exhaustive discussion of surficial and deep N cycles, but rather a brief overview of the concepts necessary to understand the research presented in this thesis.

1.3.1 – Introducing the problem with calculating the nitrogen budget of Earth.

The nitrogen budget of the Earth has always been enormously challenging to calculate. This has been primarily due to the difficulty in understanding and modelling its geochemical behaviour in different planetary reservoirs. While it has long been known that certain minerals (e.g., micas; Mayne, 1957) can potentially store thousands of ppm of nitrogen (Sokol et al., 2018), until relatively recently the main N reservoir on Earth was believed to be the atmosphere. Despite this being the reservoir with the highest N abundance (around 78 mol%), the sheer volume of the geosphere implies that, despite the comparatively low concentrations (often $\mu\text{g/g}$), the majority of Earth's N is likely stored in the BSE (Johnson & Goldblatt, 2015). More specifically, recent estimates (see Table 1.3) place the N content of the BSE at between 10^{18} to 10^{19} kg, compared to the 3.9×10^{18} kg of N present in the atmosphere (Jacobson et al., 2000).

N in BSE	Reference
9.07×10^{18} kg	Kerrich (2006)
$10.08 (\pm 5.1) \times 10^{18}$ kg	Goldblatt et al. (2009)
$24.2 (\pm 16) \times 10^{18}$ kg	Johnson & Goldblatt (2015)

Table 1.3: Most recent estimates for the amount of N contained in the BSE. Uncertainties for the measurement by Kerrich (2006) were not declared.

As evidenced by the uncertainties shown in Table 1.3, many questions about the behaviour of N in the deep Earth are yet unanswered. One such issue is the so called “missing nitrogen conundrum” (Zerkle & Mikhail, 2017). As evidenced in Figure 1.2, the only volatiles to be depleted in the BSE (relative to CI chondrite) with respect to the Late Veneer, a meteorite shower that occurred after the bulk of the core-mantle separation event took place (Kleine, 2016), are Nitrogen and Xenon (Marty, 2012). This is a peculiar occurrence, as these two elements have close to nothing in common outside of their gaseous nature at room temperature, with N being a light (atomic mass = 14) highly reactive element (with a Pauling electronegativity of 3.04, the third highest in the periodic table), and Xe being instead a heavy (atomic mass = 131) and inert noble gas. This has in the past been interpreted as a consequence of N being found on Earth as molecular nitrogen (N_2), which thanks to the triple covalent bond existing between the two N atoms is an extremely stable noble gas sized molecule (Halliday, 2013). Nevertheless, the storage of N as ammoniacal nitrogen by mineral phases (e.g., phyllosilicates), based on N—H bonds (e.g., NH_4^+), has been shown to occur in a wide variety of deep Earth settings (Halama et al., 2014, and refs. therein). This, therefore, suggests that any estimate that excludes such species (e.g., the N_2/Ar method; Marty, 2012) might be an underestimate, and thus that the Earth’s N budget might be closer to its C budget (see Figure 1.2; Zerkle & Mikhail, 2017).

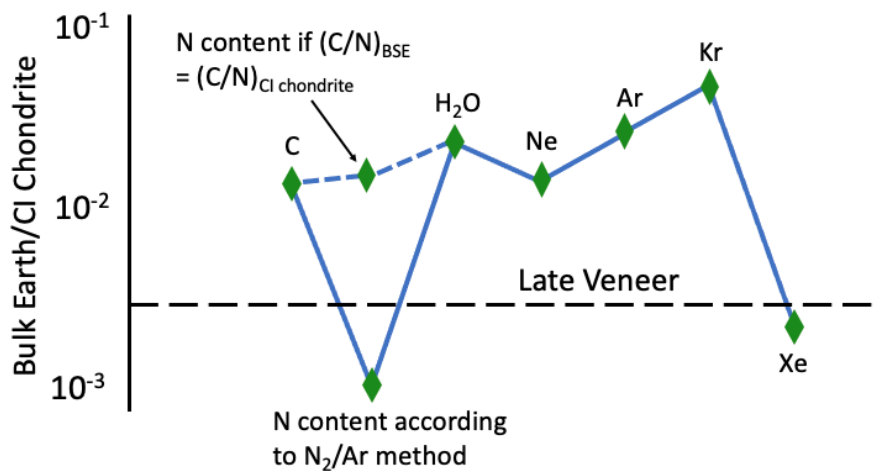


Figure 1.2: Abundance of some atmophile elements in the BSE relative to CI chondrite.

Noteworthy is how the use of different methods used to calculate the BSE's N budget results in vastly diverging estimates. Adapted from Zerkle & Mikhail (2017). The dotted line shows if the concentration is enriched or depleted compared with their concentration in the materials delivered during the late veneer event, with values plotting above it being enriched and below being depleted.

It is thus apparent how the behaviour of N in each of the Earth's reservoirs cannot prescind from the oxidation state in which it is found; thus, understanding its chemical speciation and the parameters controlling it is essential for an accurate evaluation of the Earth's N budget.

1.3.2 – Nitrogen in different reservoirs.

Owing to the many challenges involved with the study of the Earth's various N reservoirs, many questions still remain unanswered, particularly regarding deeper environments such as the core or the lower mantle (Yoshioka et al., 2018; Grewal et al., 2019). Subsequently, what follows should not be considered as a

comprehensive review of N abundance in deep Earth environments, but rather as an overview of the information necessary for the understanding of this thesis.

1.3.2.1 – Nitrogen in the atmosphere.

N₂ is currently the dominant component of Earth's atmosphere ($\sim 4.0 \times 10^{18}$ kg of N, c.a. 78% of the whole atmosphere). While this is certainly a relevant fraction of the Earth's N, recent estimates determined that this amounts to only 25-30% of the planet's N budget (Bebout et al., 2013). Furthermore, it is currently debated (Zerkle & Mikhail, 2017; Bebout et al., 2013) if this budget was constant throughout Earth's history (Zhang & Zindler, 1993; Tolstikhin & Marty, 1998) or if N concentrations were different in the early atmosphere (Goldblatt et al., 2009). Some authors (Zerkle & Mikhail, 2017) argue that a high enough N₂ content could have played a key role in maintaining Earth's surface temperature above the freezing point of water in presence of the faint young Sun (Goldblatt et al., 2009). This would be true only if all N in the atmosphere was speciated as N₂, thus sufficiently oxidising conditions to destabilise ammoniacal (N—H based, e.g., ammonia, NH₃) species must have been in place (Zerkle & Mikhail, 2017). The oxidation of primordial ammoniacal nitrogen could also have been a relevant source for liquid water itself in surficial environments (Li & Keppler, 2014).

The atmospheric partial pressure of N₂ (pN₂) throughout Earth's history has so far proven challenging to evaluate (Zerkle & Mikhail, 2017). Based on the method and/or model used for the estimate, three scenarios are plausible. [1] In the first scenario, a steady increase (Marty et al., 2013; Fischer et al., 2002) or decrease (Busigny et al., 2011) occurs in atmospheric pN₂ from the Archean to

the present day, primarily driven by tectonically controlled outgassing or sequestration respectively. [2] The second scenario features instead an initial net N influx towards the Earth's interior, followed by an inversion and thus a switch to net N outflux (Zerkle & Mikhail, 2017), possibly related to the Great Oxidation Event (GOE), the onset of subduction and/or a change in the influx of oxidants at subduction zones (Mikhail & Sverjensky, 2014), which are critical environments for N intake in the deep Earth (Halama et al., 2012). [3] The final scenario sees an oscillating balance between the influx and outflux of N in favour of one or the other component over time (Zerkle & Mikhail, 2017), resulting in an ever-changing pN_2 . This last scenario is likely the product of a complex system, with multiple components acting in favour of either N outgassing (e.g., intense volcanic activity) or sequestration (e.g., organic matter burial in anoxic environments) in varying relative intensity over time. This is not necessarily in contrast with scenarios [1] and [2], as it is possible to have an overall increase or decrease in pN_2 alongside more localised oscillations.

Based on what has been presented so far, the processes controlling pN_2 throughout Earth's history can be divided into [1] strictly surficial, thus related to the interactions between the biosphere, hydrosphere and surficial geological reservoirs (Zerkle, 2018), and [2] tectonically-driven, thus controlled predominantly by N sequestration at subduction zones (Halama et al., 2012) and N storage in deep Earth reservoirs (Li et al., 2013; Bebout et al., 2016; Sokol et al., 2018; Johnson & Goldblatt, 2015).

1.3.2.2 – Nitrogen in the hydrosphere and biosphere.

The role played by nitrogen in the biosphere is widely understood to serve multiple purposes in all life forms. Alongside carbon and phosphorus, nitrogen is also a key component of the so-called 'Redfield ratio', C:N:P = 106:16:1, (Redfield et al., 1963), often used to describe the stoichiometry of modern marine phytoplankton (Zerkle, 2018). Furthermore, because of the near ubiquity of C in oceanic environments, the limiting factors of primary production growth are often either N or P (Falkowski et al., 1998).

The vast majority of N in the biosphere-hydrosphere system arises from the dissolution of atmospheric nitrogen in the ocean, which is then fixed by N-fixing bacteria, that either release N in ammoniacal form as a waste or are consumed by other organisms (Johnson & Goldblatt, 2015). In both cases, this nitrogen is oxidized into NO_3^- through the nitrification process and can then be returned to the atmosphere by a plethora of different processes (e.g., denitrification, anammox reactions, etc. Thamdrup, 2012).

The processes described above are a very simplified description of the modern biological nitrogen cycle, which from the Cambrian onwards is likely the dominant component of the fast surficial cycling of nitrogen (Zerkle, 2018). It is worth pointing out that, before the Cambrian period (i.e., when life was less prevalent), abiotic processes likely played a crucial role in delivering nitrogen to the primitive biosphere (Dalsgaard et al., 2005). Reactions akin to these events are likely still occurring in environments such as hydrothermal vents near mid-ocean ridges (Lilley et al., 1993), which stresses the potential role played by plate tectonics in the origin of life on Earth.

In geological times, a small fraction of the nitrogen fixed by bacteria in the water column was buried in anaerobic conditions and therefore mostly sequestered by diagenetic fluids to compacted sediments. This N is then potentially carried over, during metamorphism, to minerals such as micaceous phases (Halama et al., 2012). This phenomenon represents the connection between the fast surficial biological N cycle and the much slower geological deep N cycle (Johnson & Goldblatt, 2015).

The total contribution of the biosphere and hydrosphere to the nitrogen budget of the Earth is negligible, when compared to the atmosphere and the geosphere (Zerkle & Mikhail, 2017). Nevertheless, despite their overall minor contribution to the planetary N budget, the ocean and the microorganisms which inhabit the water column are a key link between the atmosphere and the deep Earth, and thus their role in the global N cycle cannot be overstated.

1.3.2.3 – Nitrogen in the continental crust.

The N content of the continental crust, despite being an object of dispute as are most issues regarding the nitrogen budget of the Earth (Zerkle & Mikhail, 2017), has seen comparatively less disagreement compared to deeper reservoirs (Johnson and Goldblatt, 2015). This is likely due to the capacity to directly sample most of the reservoir, rather than having to rely on indirect estimates and measurements. The proposed value for the N amount in the continental crust is between 1.1×10^{18} kg (Rudnick & Gao, 2014) and 2.4×10^{18} kg (Goldblatt et al., 2009). These values are all in line with an average crustal concentration of 10-20 $\mu\text{g/g}$. However, this concentration is not homogeneous, with sedimentary rocks

and metasediments having an average N abundance of $> 400 \mu\text{g/g}$ (Busigny et al., 2013) and $200 \pm 36 \mu\text{g/g}$ (Johnson & Goldblatt, 2015) respectively, while granulites of the lower crust containing only around $17 \pm 6 \mu\text{g/g}$ (Plessen et al., 2010). The most recent estimate for the N stored in the continental crust is $1.7 (\pm 0.1) \times 10^{18} \text{ kg}$ (Johnson & Goldblatt, 2015), which, despite being of the same order of magnitude as the atmosphere, corresponds to an average concentration of $12 \pm 9 \mu\text{g/g}$.

The way in which N is stored in crustal rocks is largely dependent on the lithology. Surficial sedimentary rocks contain N typically in ammoniacal form, hosted by phases such as K^+ -rich clay minerals (Itihara et al., 1986). In addition, nitrate, and nitrite salts, alongside N-rich buried organic matter, also play a role (Johnson & Goldblatt, 2015). At greater depths, the main N-bearing mineral species are micas (e.g., biotite, phlogopite, muscovite, phengite), in which NH_4^+ ions substitute for similarly sized K^+ ions (Honma & Itihara, 1981), in both magmatic and metamorphic rocks. This same process also occurs in other alkali-bearing phases such as amphiboles (Busigny & Bebout, 2013). An interesting reservoir, albeit less quantitatively relevant, is cordierite, where N is stored in the form of N_2 in the channels typical of the cyclosilicate structure (Bebout et al., 2016).

While the nitrogen stored in the cratonic continental crust is relatively isolated from the deep nitrogen cycle (Johnson & Goldblatt, 2015), due to the relative stability of cratonic regions, hydrothermal alteration and/or partial melting processes, especially near subduction zones, can cause the oxidation of N—H species to N_2 , thus promoting its degassing from melts or its sequestration by fluid phases (Hall, 1999).

1.3.2.4 – Nitrogen in the oceanic crust.

The oceanic crust is a comparatively minor N reservoir when compared to the continental crust (Johnson & Goldblatt, 2015, and refs. therein). Freshly formed oceanic crust at mid ocean ridges inherits the N concentration of the source mantle (usually around 1-2 $\mu\text{g/g}$; Halama et al., 2012). In contrast, N abundance in the sediments which are deposited on top of the crust is usually on the order of $10^2 \mu\text{g/g}$, or $10^3 \mu\text{g/g}$ for biogenic sediments (Quan et al., 2008). Diagenetic and metamorphic processes can carry part of the N from the enriched sediments to the underlying mafic rocks, which promotes its enrichment to around 7 $\mu\text{g/g}$ in these lithologies (Halama et al., 2012).

At subduction zones, the nitrogen stored in the oceanic crust is carried towards the deep Earth predominantly in micaceous phases and amphiboles formed during the metamorphism of sedimentary rocks in the accretion prism. In both minerals nitrogen is stored mostly as ammoniacal species (Busigny et al., 2003). With increasing P and T conditions, these phases will inevitably break down, and this typically causes partial melting events of relevant magnitude. Such melts can, as a result, be enriched in nitrogen, and the chemical species in which nitrogen occurs will influence the pathway taken by N itself (Halama et al., 2017): [1] if N speciates predominantly as N_2 it will then behave as an incompatible, and will likely remain dissolved in the melt until degassing occurs (Li & Keppler, 2014), whereas [2] if N mostly speciates as N—H it can be sequestered by micas, feldspars or amphiboles during fractional crystallization, and therefore remain in the mantle wedge or potentially continue its descent towards the deep Earth (Bebout et al., 2013). It is, thus, evident that despite the oceanic crust being a

relatively small N reservoir it plays a pivotal role with regards to N influx at subduction zones.

1.3.2.5 – Nitrogen in the Bulk Silicate Earth.

Estimates for the nitrogen budget of the BSE are heavily dependent on the method used to calculate these (Zerkle & Mikhail, 2017). Models based on the N_2/Ar ratio (e.g., Marty, 1995) place an upper limit of $\sim 1 \mu\text{g/g}$ on the abundance of N in the mantle, whereas different methodologies (e.g., the layered accretion model; Javoy, 1997) suggest a much higher concentration of $\sim 36 \mu\text{g/g}$. Nitrogen measurements of diamonds give a plausible range of concentrations of 2 to $40 \mu\text{g/g}$ (Cartigny et al., 2001), as the interpretation of these measurements is heavily dependent on the pathways potentially followed by N during its cycling in the deep Earth (Mikhail & Howell, 2016). The most recent estimate for N abundance in the mantle is $24(\pm 16) \mu\text{g/g}$ (Johnson & Goldblatt, 2015).

The variability of the measurements of N abundance in the BSE are due to the assumptions made for N speciation in the various deep Earth potential reservoirs (Zerkle & Mikhail, 2017). As an example, the N_2/Ar method (Marty et al., 1995) assumes all nitrogen to be speciated as N_2 , which is stored predominantly in Schottky defects and as interstitial impurities (Li et al., 2013). This, in turn, would make N in the BSE highly incompatible (Li & Keppler, 2014). However, it has also been suggested (Mikhail & Sverjensky, 2014) that a relevant fraction of N in the BSE could be speciated as ammoniacal nitrogen (e.g., NH_4^+), meaning it would be stored instead as a lattice-bound ion and thus behave more compatibly (Li et al., 2013). Another relevant upper mantle N reservoir could be

the (Fe, Ni)-based alloys that have been demonstrated to be stable at depths below ~250 km (Rohrbach et al., 2011) which, given the potentially siderophile behaviour of nitrogen at oxygen fugacity below the Fe-Wustite (IW) buffer (Speelmanns et al., 2019), could contain several wt% of N (Roskosz et al., 2013). This would explain the much lower average N content of sublithospheric diamonds (i.e., formed below 200 km) relative to their lithospheric counterparts (56 vs 235 $\mu\text{g/g}$ respectively; Smith & Kopylova, 2014).

One particularly poorly constrained reservoir is the lower mantle: this arises from the possibility that up to 1 wt% of it consists of Fe-based alloys (Frost et al., 2004), which at lower mantle P-T conditions could dissolve up to 8 wt% of N (Roskosz et al., 2013). It can, however, be argued that, with such high solubilities, full N saturation might not be reached in this environment.

Transition zone and lower mantle major mineral phases (e.g., bridgmanite, perovskite) have shown N solubilities from ~10 up to almost 200 $\mu\text{g/g}$ (Yoshioka et al., 2018).

All the uncertainties in N speciation and storage mechanisms in the deep Earth, translate (owing to the size of the BSE) into a potential N budget of the BSE between two and ten times the mass of N in the atmosphere (i.e., between $6.2 \pm 13 \times 10^{18}$ kg to $24 \pm 16 \times 10^{18}$ kg; Johnson & Goldblatt, 2015), a relevant part of which might be sequestered from the global N cycle, and therefore a virtually “hidden” reservoir, which could thus be the key to explaining the missing nitrogen conundrum (Zerkle & Mikhail, 2017).

1.3.2.6 – Nitrogen in the core.

The N budget of the Earth's core is even more obscure than reservoirs such as the transition zone and lower mantle (Speelmanns et al., 2019). Nitrogen solubility in metallic melts at core conditions has been found to be as high as 25 wt%, which is at least one order of magnitude higher than anything measured for silicate melts at equivalent conditions (Speelmanns et al., 2019, and refs. therein). Critically, however, any N stored in the outer and inner core would be completely segregated from the global N cycle since the core-mantle separation occurred early during Earth's accretion, due to chemical exchange across the core-mantle boundary likely being a sporadic phenomenon with no measurable impact on the lower mantle's geochemistry (Mundl-Petermeier, 2021).

Core formation is currently thought to have been a multi-step process, characterised by various stages of large-scale partial melting triggered by the impact of small planetesimals on the accreting Earth (Speelmanns et al., 2018), which caused the formation of multiple magma oceans at depths of 500 to 1000 km (Wood et al., 2006). Each of these events had the potential to sequester volatile elements in core (and potentially lower mantle) alloys. The potential siderophile behaviour of N at core-like P-T conditions (Mosenfelder et al., 2019) could explain both the missing nitrogen conundrum and the density deficit of the core (Speelmanns et al., 2019).

Despite the convenience of the explanation above for the fate of N during Earth's accretion, it is worth pointing out that while recent models place N solubility in the core as high as >3 wt% (e.g., Litasov et al., 2017), this does not

imply that the core is saturated in nitrogen. Other models (e.g., McDonough, 2014) estimate the N budget of the core to be at most a few tens of $\mu\text{g/g}$.

One key piece of evidence towards the abundance of N in the core, however, comes from carbon solubility in Fe-based alloys at equivalent P-T conditions, which is thought to be even higher (Dalou et al., 2017; Speelmanns et al., 2018), making it even more siderophile than N at core conditions. Unlike N, however, the Earth's C budget does not show any sign of depletion when compared to other similar volatiles (Zerkle & Mikhail, 2017), thus suggesting that the Earth's core is unlikely to be hosting a large N reservoir (Dalou et al., 2017; Speelmanns et al., 2019).

The delivery method of N during planetary accretion possibly also played a role in the N budget of the core (Grewal et al., 2021). If the bulk of Earth's nitrogen was carried by planetary embryos which differentiated at $f\text{O}_2$ below the IW buffer, it follows that most nitrogen would have already been segregated in the core of these bodies, due to the siderophile nature of nitrogen at such $f\text{O}_2$ (Grewal et al., 2021b). Therefore, the decoupled behaviour of C and N during planetary accretion could be due to the latter being carried from a different source from the former (Grewal et al., 2019). Nevertheless, it is worth noting that this explanation relies heavily on the hypothesis that the majority of the planet's N budget was delivered during the early stages of accretion. If this is not the case (e.g., with N being delivered mostly by a Late Veneer; Kleine, 2016), then the core would be less relevant as a N reservoir (Grewal et al., 2019b). Furthermore, low $f\text{O}_2$ levels (i.e., below the IW buffer), alongside a sufficient H abundance, are known to promote the stability of ammoniacal nitrogen species (Grewal et al.,

2021b), therefore promoting a lithophile behaviour rather than a siderophile one (Speelmanns et al., 2019).

1.3.2.7 – Nitrogen concentration in chondrites.

The concentration of nitrogen in different chondrite classes is, unsurprisingly, difficult to precisely quantify. This is because chondrites, which originated as early as the proto planetary nebula, are extremely prone to alteration. Therefore, an element potentially as mobile as nitrogen can easily be influenced by post-impact metamorphic and/or surficial processes.

Marty (2012) proposed a concentration of around 300 and 500 $\mu\text{g/g}$ of N in carbonaceous chondrites (CC) and enstatite chondrites (EC) respectively, based on one single meteorite per class, the only ones judged to have experienced a sufficiently low grade of metamorphism (Marty, 2012). Other authors instead (e.g., Johnson & Goldblatt, 2015, and refs. therein) preferred to accept a broader range of uncertainty, especially for CC, to include a higher number of meteorites in their dataset and proposed, therefore, an abundance of 1235 ± 440 and 605 ± 6 $\mu\text{g/g}$ of N in CC and EC respectively (Johnson & Goldblatt, 2015). The second approach suggests that some level of N loss might have occurred during chondritic evolution (CC are commonly interpreted as more primitive bodies than EC; Lodders & Fegley, 1998).

1.3.2.8 – Nitrogen concentration in achondrites.

Due to the more varied nature and differentiation of achondritic meteorites, it is perhaps not surprising to find a wider range of N abundances in this subgroup.

The highest levels of enrichment are by far those observed in Iron meteorites (Grady & Wright, 2002). Average values range between 18 $\mu\text{g/g}$ (Gibson et al., 1971) up to 200 $\mu\text{g/g}$ (Zipfel et al., 1997), however certain (Fe,Ni) alloys (e.g., taenite) may contain upwards of 0.3-0.4 wt% of N, and nitride phases (e.g., roaldite, $(\text{Fe,Ni})_4\text{N}$) can exist (Sugiura, 1998).

Outside of iron meteorites, N concentration in achondrites is relatively low, with ureillites and more primitive meteorites (e.g., acapulcoites, londranites and winonanites) contain at most 20-30 $\mu\text{g/g}$ of N (Grady et al., 1985; Kim & Marty, 1993). Meteorites belonging to the SNC and HED groups are very N poor, containing between 3 and 7 $\mu\text{g/g}$ (Fallick et al., 1983) and at most 2 $\mu\text{g/g}$ of N (Miura & Sugiura, 1993), respectively.

In conclusion, it is easily inferred how the composition as well as the differentiation history of a meteorite can play a major role in the retention or degassing of N by influencing to which elements it is bonded in the system (e.g., the siderophile nature of N strongly promotes its retention by iron meteorites; Grewal et al., 2021).

1.3.3 – Nitrogen's global cycle: from the atmosphere to the deep Earth.

Nitrogen is constantly cycling between different deep and surficial planetary reservoirs (Marty & Dauphas, 2003). The balance between inbound and outbound fluxes ultimately controls atmospheric N_2 levels; however, the

exchanges between each specific reservoir has so far eluded precise quantification, due to the complex and incompletely understood relationships between them (Zerkle & Mikhail, 2017).

The global nitrogen cycle can be divided into two main sub-cycles; a fast biologically driven surficial cycle, which concerns mostly the biosphere and hydrosphere (Zerkle, 2018, and refs. therein), and a comparatively slower deep cycling in the geosphere (Halama et al., 2012). Interactions between the two cycles occur, throughout geological time, on the seafloor and in subduction zones (Halama et al., 2017).

1.3.3.1 – Nitrogen's surficial cycle.

Nitrogen from the atmosphere is dissolved in the hydrosphere through osmosis, and from seawater it is then incorporated in the biosphere, mainly through the process of N_2 fixation (Zerkle & Mikhail, 2017). Once primary producers (or anything that feeds on those) die in the water column, the organic matter of which they consisted of starts to precipitate towards the seafloor, and while, or immediately after, this occurs decomposition returns most of the nitrogen to the ocean (Zerkle, 2018). However, if such aerobic processes are absent or only partial, a portion of the nitrogen in the organic matter can be buried and subjected to diagenetic processes, which in turn can lead to the partial segregation of nitrogen as ammoniacal species (e.g., NH_3 , NH_4^+) in geological reservoirs (e.g., phyllosilicates, Halama et al., 2017), and thus entering the deep geological cycle (Zerkle & Mikhail, 2017).

1.3.3.2 – Nitrogen's deep cycle.

The cycling of nitrogen in the deep Earth is critically tied to the chemical species in which it is stored. In the case of N_2 , it has historically been considered a mostly unreactive highly volatile molecule, akin to heavier noble gases such as Ar and Xe (Halliday, 2013; Marty, 2012). This has been motivated by [a] the strength of the $N\equiv N$ bond promoting its stability outside of heavily reducing conditions (i.e., around or below IW; Grewal et al., 2021b, and refs. therein) and [b] the similar degree of depletion of N and Xe in the BSE relative to CI Chondrite (see Figure 1; Marty, 2012). The primary storage mechanism for N_2 molecules is believed to be in amphiboles and microporous phases such as beryl and cordierite (Bebout et al., 2016). If released from such environments (e.g., in case of mineral breakdown or partial melting), N_2 indeed behaves as a highly incompatible chemical species (Li & Keppler, 2014).

For the case of N found in ammoniacal species cycling can be far more convoluted. More specifically, the ammonium ion (NH_4^+) is tetrahedral with an overall size comparable to large positively charged ions such as K^+ and Rb^+ (Mueller, 2019; Jenkins & Thakur, 1979). This allows it to behave as a moderately compatible element (in comparison with molecular nitrogen; Busigny & Bebout, 2013), being carried to greater depths in the subducting slab through storage in phases such as phengite (Abdel-Hak et al., 2020) and feldspars (Busigny et al., 2003; Sokol et al., 2018). Upon release from the ammonium-bearing phase and transfer to a melt phase, if the oxygen fugacity is sufficiently low the ammoniacal species can remain stable (Li et al., 2015) and thus enter phases such as clinopyroxenes or olivine (Watenphul et al., 2010; Li et al., 2013) in the upper

mantle, common lower mantle phases such as ringwoodite or wadsleyite (Yoshioka et al., 2018), and (Fe, Ni) alloys (Speelmanns et al., 2019). It is worth noting, however, that it is currently not well understood how much the deeper reservoirs (i.e., below the transition zone) effectively interact with the global cycling of nitrogen (Dalou et al., 2017).

As for what regards N outgassing, estimates for global volcanic N emissions seem to suggest a net outflux to the atmosphere (Fischer et al., 2002). However, if this was also true earlier in Earth's history is yet another matter of debate (Zerkle & Mikhail, 2017).

Critical environments for the fate of nitrogen in the deep Earth are subduction zones: this is because during subduction ample partial melting processes can occur, and in these contexts N-rich phases (e.g., muscovite, biotite; Harlov et al., 2000) often break down, thus releasing nitrogen to the melt phase. While the fO_2 is unlikely to be sufficiently low to promote the stability of ammoniacal species in such surficial environments, coexisting fluid phases are likely to contain stable ammoniacal species (Mikhail & Sverjensky, 2014). The nitrogen carried by such phases can then be sequestered by minerals during fluid-rock interaction processes (Mikhail et al., 2017). The importance of partial melting processes for the fate of N during subduction is underlined by the higher degree of N retention by the slab in cold subduction settings (Halama et al., 2012), which are characterized by lower degrees of partial melting.

In conclusion, the behaviour of nitrogen in silicate melts is a critical factor in determining its movement in the deep Earth, and this behaviour is primarily controlled by its chemical speciation (Roskosz et al., 2006).

1.4 - INTRODUCTION – FLUORINE

Fluorine is the smallest and lightest element in Group 17, which consists of Fluorine, Chlorine, Bromine, Iodine, Astatine and Tennessine (F, Cl, Br, I, At and Ts), commonly referred to as “halogens”. ^{19}F is the only stable isotope, although 6 additional unstable isotopes exist, all with half-lives of geologically insignificant length (see Table 1.4; Mueller, 2019).

Isotope	Abundance	Nature	Half life
^{17}F	//	Radioactive	64.5 s
^{18}F	//	Radioactive	1.83 h
^{19}F	100%	Stable	//
^{20}F	//	Radioactive	11.0 s
^{21}F	//	Radioactive	4.16 s
^{22}F	//	Radioactive	4.23 s
^{23}F	//	Radioactive	2.2 s

Table 1.4: Relative abundance, nature, and half-lives of all known isotopes of fluorine (Mueller, 2019).

Fluorine is the most electronegative element in the periodic table, and this results in it being highly reactive. Consequently, F is virtually absent from the atmosphere, and due to the low solubility of fluoride salts in water it is also much less abundant in the hydrosphere compared, for example, to Cl (19,000 vs 1.3 $\mu\text{g/g}$ for Cl and F respectively; Budisa et al., 2014). In addition, F is also very rare in the biosphere, with biogenic fluorine compounds having been only occasionally observed (O’Hagan et al., 2002). As for the geosphere, F is perhaps the most enriched volatile in the BSE, with an enrichment of 0.17 relative to Cl chondrite

and Mg, despite its chondritic abundance of 60 $\mu\text{g/g}$ being two orders of magnitude lower when compared with chlorine (McDonough & Sun, 1995), hinting that perhaps different pathways were followed during planetary evolution (Hanley & Koga, 2018) for the two elements. Indeed, important differences exist between F and Cl, chief among these the covalent radius of Cl being 25% larger than F's (99 vs 71 pm respectively) and the much higher atomic mass of Cl relative to F (35.45 vs 18.99 amu, respectively). These differences in basic atomic properties are likely to result in diverging geochemical behaviours during partial melting processes, according to Goldschmidt's rules (Goldschmidt, 1937).

The anion most similar to F^- is the hydroxyl ion (OH^-), due to the identical ionic radius (133 pm) and -1 charge (Meija et al., 2015). This has resulted in the F/OH ionic exchange being one of the most common solid solutions in the mineral world, as virtually any hydrous (i.e., OH-bearing) phase can also potentially host F^- (Mi & Pan, 2018).

Despite the similarity of OH^- and F^- , differences exist between the two anions. Perhaps the most relevant distinction is the monoatomic and non-polar nature of F^- , which is opposed to the diatomicity and polarity of OH^- . This has relevant effects on the structure of the host phase of the solid solution. Examples include [1] the preferential partitioning of F^- and OH^- in trioctahedral and dioctahedral sites respectively in mica frameworks (Robert et al., 1993), and [2] the H-bond formation and subsequently lower degree of disorder of F-rich clinohumite when compared to their F-poor counterparts (Griffin et al., 2010), which in turn leads to a wider field of stability in high P-T conditions (Grützner et al., 2017). It is, thus, perhaps not surprising that F^- and OH^- followed different

pathways during early planetary evolution, resulting therefore in a higher level of F^- enrichment in the BSE (relative to CI chondrite) when compared to OH^- (McDonough & Sun, 1995; Marty, 2012). The specific nature of these differences is however still elusive, likely due to the lack of precise constraints on the behaviour of F during chondritic differentiation and the intense partial melting processes characteristic of early planetary evolution, during which differences in compatibility between elements could have resulted in vastly different geochemical behaviours (Rubin & Choi, 2009).

What follows is a general overview of the concepts necessary for the understanding of the fluorine-related materials in this thesis, therefore it is not meant to be an exhaustive discussion of the geochemistry of fluorine, of which vastly more detailed discussion already exist (e.g., Harlov & Aranovich, 2018).

1.4.1 – The F budget of chondrites.

As a preliminary clarification, chlorine is used in this section in comparison to F to show the notable differences that distinguish F from the other halogens.

Chondrite meteorites are some of the most primitive bodies currently existing in the solar system (Wasson & Kallemeyn, 1988). Halogens, unlike many other volatiles (see Figure 1.3), show no sign of fractionation between the solar photosphere and CI chondrites (Lodders, 2003), implying that they can be powerful tracers of processes that occurred during the early stages of planetary accretion. Therefore, their chondritic abundance, alongside the parameters that drive this, is critical for the understanding of the halogen content of Earth and other planets (Brearly & Jones, 2018).

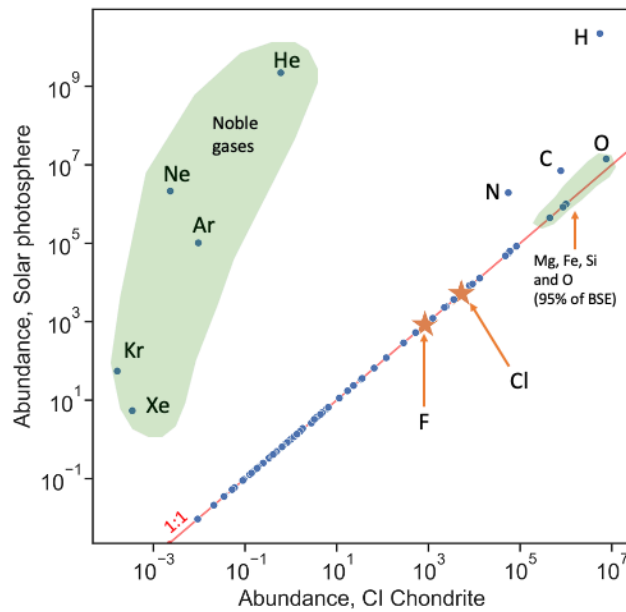


Figure 1.3: Abundance of major and trace elements in the solar photosphere vs abundance in CI chondrite (Lodders & Fegley, 1998; Lodders, 2003). Major BSE forming elements and volatiles are highlighted, clearly showing the different behaviour of halogens when compared to other volatiles.

CI carbonaceous chondrites are thought to be the most primitive meteorites known, with a composition close to the elemental abundances measured for the solar photosphere (Wasson & Kallemeyn, 1988). All other chondrite groups are the result of varying degrees of fractionation from CI chondrites, which resulted in the progressive depletion of the more volatile elements relative to the more refractory ones (Brearly & Jones, 2018). While halogens are generally thought to be highly volatile elements during chondritic evolution, F is a partial exception, as it is the sole halogen with a 50% condensation temperature above 640 K, thus qualifying it as a moderately volatile element (Lodders, 2003). This results in its behaviour being distinct from chlorine during differentiation, which manifests via the F/Cl ratio becoming progressively enriched relative to that in CI chondrite (see Table 1.5 and Figure 1.4a). Notably,

this variation is driven primarily by a depletion in Cl rather than an enrichment of F, which is present but comparatively minor (see Figure 1.4b).

Chondrite group	Fluorine (µg/g)	Chlorine (µg/g)	F/Cl ratio
CI (Carbonaceous Iruna)	60	700	1.00
CM (Carbonaceous Mighei)	38	430	1.03
CV (Carbonaceous Vigarano)	24	250	1.12
CO (Carbonaceous Omans)	30	280	1.25
CK (Carbonaceous Karoonda)	20	260	0.90
EH (Enstatite High Fe)	155	570	3.17
EL (Enstatite Low Fe)	140	230	7.10
L (Low Fe ordinary chondrites)	70	200	4.08
LL (Low Fe Low metal ordinary chondrites)	100	270	4.32
H (High Fe ordinary chondrites)	125	140	10.42

Table 1.5: F and chlorine concentration in all measured chondrite groups (data from Lodders & Fegley, 1998). Groups starting with the letter C are Carbonaceous chondrites, with letter E are Enstatite chondrites and the others are ordinary chondrites. Full meaning of each acronym is in parentheses in the first column. Carbonaceous chondrite groups take their name from their more representative meteorite shower, while Enstatite and Ordinary chondrite groups are classified based on their Fe and other metals abundance. F/Cl ratios are normalised to the F/Cl ratio of CI chondrite.

It needs to be pointed out that most of the halogens in chondrites are stored in secondary phases, which are product of alteration or thermal metamorphism, and that the primary halogen storage mechanisms are currently not well understood (Brearly & Jones, 2018). This is likely due to the lack of understanding of the chemical behaviour of halogens in environments (i.e., high T and low P ca. mafic silicate compositions) similar to those in which chondrites formed (Shimizu et al., 2021).

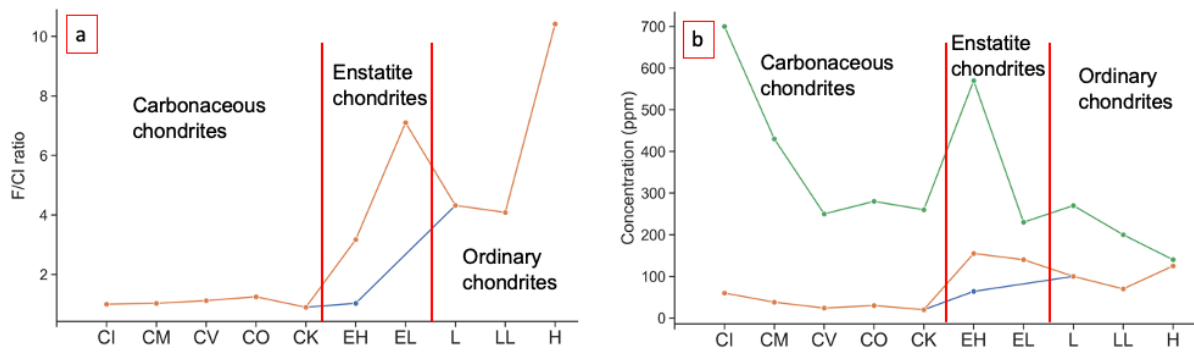


Figure 1.4: (a) The line in orange shows the F/Cl ratio in chondrite groups, normalised to F/Cl in CI chondrites (data from Lodders & Fegley, 1998). (b) F and Cl (orange and green, respectively) abundance ($\mu\text{g/g}$) in chondrite groups (data from Lodders & Fegley, 1998). In both figures, the partial blue line represents the F/Cl ratio and F abundance when not considering data from Reed (1964) and Greenland and Lovering (1965) for EH and EL chondrites, as recommended by Dreibus (1979).

1.4.1.1 - F and Cl in carbonaceous chondrites.

Carbonaceous chondrites are classified into different groups based on their presumed parent body, with the second letter in the groups' name indicating the most representative member (e.g., in CI chondrite, the letter I stands for the Ivuna meteorite shower). Carbonaceous chondrites, as the name suggests, can have extremely high organic C content, which is found as amino acids (Ehrenfreund et al., 2001) and as hydrocarbons (Wing & Bada, 1992). A more detailed discussion of this classification is beyond the scope of this thesis, particularly when considering that in certain groups (e.g., CR, CH) F abundances were never measured (Lodders & Fegley, 1998).

Most carbonaceous chondrites have experienced moderate to heavy degrees of aqueous alteration and thermal metamorphism (Alexander et al., 2013; and refs. therein). As a result, assessing the primary halogen content of these meteorites has proven challenging (Brearly & Jones, 2018). The values

reported in Table 1.5 suggest that F is around an order of magnitude depleted relative to Cl in all carbonaceous chondrites. However, recent studies have shown how the vast majority of halogens, especially Cl, are likely to have been added to the chondrite body as a result of late-stage alteration processes, and that the primary F budget is probably an order of magnitude enriched when compared to Cl (i.e., F: 0.1–0.2 $\mu\text{g/g}$ and Cl: 0.01–0.03 $\mu\text{g/g}$; Shimizu et al., 2021).

Despite CI chondrites having the highest halogen budget of all carbonaceous chondrites, no phase which contains halogens at major concentrations is present in these meteorites (Brearly & Jones, 2018). Instead, all halogens in such meteorites are either stored at trace concentrations in olivine, pyroxenes and in the glassy mesostases (Shimizu et al., 2021). CV, CO and CK chondrites contain major halogen-bearing phases, specifically sodalite ($\text{Na}_4\text{Al}_3\text{Si}_3\text{O}_{12}(\text{F},\text{Cl})$) and Wadalite ($\text{Ca}_6\text{Al}_5\text{Si}_2\text{O}_{16}(\text{F},\text{Cl})_3$), while CM chondrites have also been reported to contain halides (Barber, 1981) such as halite (NaCl) and sylvite (KCl), and rare occurrences of apatite ($\text{Ca}_5(\text{PO}_4)_3(\text{F},\text{Cl},\text{OH})$) have been also documented in CV chondrites (Dyl et al., 2014).

1.4.1.2 - F and Cl in enstatite chondrites.

Enstatite chondrites (or E-type chondrites) are heavily reduced ($f\text{O}_2$ is the lowest of any chondrite group) and anhydrous meteorites. They are subdivided into two subgroups: EH and EL, where H and L stand for “high Fe” (i.e., ~30% total Fe) and “low Fe” (i.e., ~25% total Fe) respectively (Cloutis et al., 2018).

It should be noted that the F budget of E-type chondrites has, in the past, been a matter of debate in the literature. The highest F concentrations in the E-

type group are associated with EL chondrites (Lodders & Fegley, 1998; Wasson & Kallemeyn, 1988), however all F measurements for this class of meteorites were performed on EL6 and EL7 meteorites. Such meteorites are classified as highly recrystallized materials, with few to no chondrules remaining, and thus the alteration state of these bodies has often been questioned (Brearly & Jones, 2018). Dreibus (1979) argues that any value measured in previous studies (i.e., Greenland & Lovering, 1965; Reed, 1964) is an inaccurate overestimate, and suggests that the sole accurate measurement has been performed on the Abee (type EH4) meteorite. This value corresponds to an F concentration of 64 $\mu\text{g/g}$, one order of magnitude lower relative to previously published data (100 to 280 $\mu\text{g/g}$, Greenland & Lovering, 1965; Reed, 1964). To further add to the controversy, more recent publications (Lodders & Fegley, 1998; Wasson & Kallemeyn, 1988) consider instead the data from earlier studies as accurate, thus disagreeing with Dreibus (1979). The latest published literature seems to regard all measurements as valid (Brearly & Jones, 2018), thus this thesis will assume the F abundance in E-type chondrites to be between 64 and 280 $\mu\text{g/g}$.

As evidenced from the data in Table 1.5 and Figure 1.4b, E-type chondrites are the most F enriched. These meteorites are the closest to Earth in chemical and isotopic composition (Savage & Moynier, 2013). F in these chondrites is primarily hosted in fluorophlogopite ($\text{K}(\text{Mg,Fe})_3\text{AlSi}_3\text{O}_{10}\text{F}_2$) and K-richterite ($\text{K}(\text{NaCa})\text{Mg}_5\text{Si}_8\text{O}_{22}(\text{F,OH})_2$), and in both cases it forms a complete solid solution with the OH^- ion (Rubin & Choi, 2009), a phenomenon which does not occur with chlorine, likely due to its larger ionic radius. This element is instead primarily stored in the glassy portions of the chondrules (Grossman et al., 1985;

Lin et al., 1998). Rare occurrences of Lawrencite (FeCl_2) have also been reported (Keil, 1968). It is worth pointing out how all these minerals are secondary phases, therefore the primary halogen carriers in these meteorites are yet unclear.

1.3.1.3 - F and Cl in ordinary chondrites.

As the name “ordinary” might suggest, most chondrites belong to this class (87% of finds), and almost half of these are thought to have originated from the fragmentation of a single parent body (Gaffey & Gilbert, 1998). Three main groups of ordinary chondrites have so far been defined, namely H (for “high Fe”), L (for “low Fe”) and LL (for “low Fe and low metal”), based on the general Fe and metal content of the meteorite (Lodders & Fegley, 1998).

Halogen abundances in ordinary chondrites, despite this class consisting of the vast majority of all known chondrites, have been only rarely measured (Brearly & Jones, 2018). All halogens outside of F appear to be heavily depleted relative to Cl chondrite (see Table 1.3; Lodders & Fegley, 1998), which leads to the hypothesis that the main driving force behind halogen enrichment in ordinary and E-type chondrites is their electronegativity (Rubin & Choi, 2009). Primary halogen enrichment in these chondrites could have thus occurred in one common phase (Brearly & Jones, 2018). Nevertheless, recent studies have shown that F can show high enrichments relative to other halogens in carbonaceous chondrites too, in addition to F being depleted relative to Cl in ordinary chondrites instead (Shimizu et al., 2021). This implies then that halogen enrichment throughout different chondrite classes might not be as predictable as previously thought.

The determination of primary halogen carriers in ordinary chondrites has also been matter of debate, as the majority of halogen-rich phases are secondary (e.g., sodalite, wadalite, apatite), although recent studies suggest that most halogens are stored in the chondrules mesostases (Brearly & Jones, 2018; Shimizu et al., 2021). This hints that halogens were primarily hosted by chondrule-forming phases (e.g., olivine, pyroxene), thus suggesting an enrichment process possibly analogous to E-type chondrites (Rubin & Choi, 2009; Shimizu et al., 2021).

1.4.2 – The Earth's fluorine reservoirs.

The abundance of F throughout the planet's more relevant reservoirs is presented in Table 1.6. Its distribution throughout the various planetary environments is unique when compared with the other halogens: while Cl, Br and I are mainly concentrated at or near the Earth's surface (e.g., hydrosphere and sedimentary rocks), F is more enriched in the BSE (e.g., continental crust, upper mantle), due to its relatively more compatible geochemical behaviour (Clay, 2021). The following subsections will provide a brief review of the current knowledge of the main F reservoirs throughout the planet's interior, with a focus on the topics more relevant to the scope of this thesis.

Reservoir	F concentration (µg/g)
Hydrosphere	~1
UCC	~610
LCC	~430
AOC	~400
Primitive MORB	~130
BSE	18-25

Table 1.6: F concentration in main planetary reservoirs (data from Koga & Rose-Koga, 2018, and refs. therein). UCC = Upper Continental Crust, LCC = Lower Continental Crust, AOC = Altered Oceanic Crust, MORB = Mid Ocean Ridge Basalt, BSE = Bulk Silicate Earth.

1.4.2.1 – F in surficial reservoirs.

The abundance of Fluorine in the hydrosphere is the lowest of all halogens, due to its comparatively lower solubility in water (Worden, 2018). The commonly accepted F concentration in seawater is around 1 µg/g (Li, 1991), while in meteoric and ground water it is generally not measured (Koga & Rose-Koga, 2018). This low solubility in water affects its concentration in evaporites: while all other halogens see orders of magnitude of enrichment relative to their crustal abundance, fluorine is two orders of magnitude depleted (Price, 1996).

For clastic sedimentary rocks, the F abundance is similar to the average concentration of the continental crust of ca. 550 µg/g (Krauskopf, 1979). Its concentration is mainly dependent on the hydrothermal alteration and weathering the rocks undergo, due to the very high mobility of F in sedimentary environments (Koga & Rose-Koga, 2018).

1.4.2.2 – F in the continental and oceanic crust.

The concentration of F in the continental crust is the highest of all halogens, and it is between ~430 $\mu\text{g/g}$ in the lower crust and ~610 $\mu\text{g/g}$ in the upper crust (Gao et al., 1998). Generally, F abundance is higher in volcanic rocks than in their intrusive counterparts, presumably due to F behaving as a moderately volatile element during degassing; however, the concentration remains in the same order of magnitude (i.e., 100s $\mu\text{g/g}$) in both cases (Koga & Rose-Koga, 2018).

Volcanic rocks of the oceanic crust have highly variable F contents: while Ocean Island Basalts (OIBs) rarely contain more than a few 10s of $\mu\text{g/g}$ of F, Mid Ocean Ridge Basalts (MORBs) can easily reach upwards of 600 $\mu\text{g/g}$ of F, even in cases of consecutive partial melting episodes of the same source material (Koga & Rose-Koga, 2018, and refs. therein). Nevertheless, the average F concentration in primitive MORBs is thought to be around 130 $\mu\text{g/g}$ (Saal et al., 2002). During alteration processes of the oceanic crust (e.g., serpentinization), F behaves as a moderately compatible element, resulting thus in a higher average F concentration (i.e., ca. 400 $\mu\text{g/g}$) relative to unaltered rocks (Kendrick et al., 2013).

1.4.2.3 – F in the Bulk Silicate Earth and core.

F is unique compared to the other halogens in its planetary distribution, as most of it is believed to be stored in the BSE and not in surficial reservoirs (Clay, 2021). The F content of the BSE is currently thought to be between 18 and 25 $\mu\text{g/g}$, the vast majority of which is stored in the mantle (Hanley & Koga, 2018). Notably, this value is not too distant from estimates for the depleted mantle (DM) of ca. 11 $\mu\text{g/g}$

(Salters & Stracke, 2004), suggesting how partial melting processes might not cause significant F depletion. All current estimates rely on indirect methods (e.g., F/P or F/Nd ratio; Salters & Stracke, 2004). This is because of [1] the overall scarcity of direct F measurements in mantle xenoliths and [2] of the significant variability present in the available xenolith data, which range from a few $\mu\text{g/g}$ (Jagoutz, 1979) to hundreds of $\mu\text{g/g}$ (Arzamastsev & Glaznev, 2008), resulting in the impossibility of a robust direct assessment of the F abundance in the mantle (Hanley & Koga, 2018).

Little is known about F in the Earth's core: the few available experimental results suggest poor F solubility in typical core forming materials (e.g., metal alloys, sulfides) relative to other halogens (Koga & Rose-Koga, 2018). This, alongside the lack of any F detection in iron meteorites (Lodders & Fegley, 1998; Brearly & Jones, 2018), suggests that the core is unlikely to be a relevant F reservoir.

1.4.3 – Fluorine storage in common BSE phases.

As fluorine, unlike all other halogens, is predominantly stored in the BSE, its storage mechanisms in common mantle forming minerals (e.g., olivine, pyroxene) are worth discussing. A range of different mechanisms have been proposed in literature for F incorporation in upper mantle mafic phases (Joachim et al., 2015), of which the most well understood are: [1] intergrowth of clinohumite lamellae $((\text{Mg, Fe})_9(\text{SiO}_4)_4(\text{F, OH})_2)$ within olivine crystals (Griffin et al., 2010b; Stalder & Ulmer, 2001), [2] the $[\text{MgO}_2]^{2-} = [\otimes\text{F}_2]^{2-}$ substitution (\otimes = vacancy) in Mg-rich phases (Bernini et al., 2013), [3] clustered F^- and OH^- defects ($[\text{SiO}_4]^{4-} =$

[halide]⁴⁻) forming around Si vacancies (Crepisson et al., 2014), [4] the coupled substitution $\text{Al}^{3+} + 4[\text{halide}]^{-} = \text{Si}^{4+} + \text{O}^{2-}$ in clinopyroxene (Dalou et al., 2012), and [5] $\text{Al}^{3+} + [\text{halide}]^{-} = [\text{Mg}_2\text{O}]^{2+}$ in orthopyroxene (Mosenfelder & Rossman, 2013). It must be noted that the formation of clinohumite lamellae has recently been questioned, at least under upper mantle conditions, due to lack of TEM evidence (Joachim et al., 2015). The presence of F in humite group mineral frameworks has been linked to a much greater field of stability in high P-T, possibly up to transition zone-like environments (Grützner et al., 2017). This is corroborated by the lack of evidence for OH-rich clinohumite stability at transition zone level conditions (Stalder & Ulmer, 2001), and could be possibly due to the lower degree of disorder in the humite framework caused by H-bond formation between F and OH pairs (Griffin et al., 2010b). This has direct consequences on water transport in the deep Earth, as an increased field of stability of humite group minerals would facilitate OH intake. If, however, F enrichment is a necessary requirement for increased stability, it also follows that this would negatively impact the total amount of OH that could be carried towards greater depths. Therefore, understanding the precise dynamics surrounding this substitution is critical for the assessment of this specific mechanism of water transport in the deep Earth.

With such a wide variety of possible incorporation mechanisms, it is easy to picture that multiple processes could occur, although not necessarily at the same P-T conditions. In addition, while assessing the active mechanisms is already a challenging endeavour, understanding the conditions which promote the onset of one over the other is another complex task. One of the critical factors, however, is likely to be the context in which the minerals form (Mi & Pan, 2018),

therefore understanding the behaviour of F in silicate melts and its impact on the crystallizing phases is essential to investigate its partitioning patterns (Joachim et al., 2017).

1.4.4 – F solubility in silicate systems and its speciation.

F solubility in silicate melts depends largely on the melt composition (Dalou et al., 2015) and possibly on pressure (Webster et al., 2018). The bulk of current knowledge concerns felsic environments (e.g., Mysen et al., 2004; Dolejš & Baker, 2005; Webster et al., 2009; Baasner et al., 2014; Liu & Tossell., 2003; Stebbins et al., 2000; Liu & Nekvasil, 2002; Dolejš & Zajacz, 2018), and under such conditions, F solubility in silicate melts can be as high as 5 wt% (Dolejš & Baker, 2004). Studies regarding mafic and intermediate systems are scarcer (e.g., Beyer et al., 2012; Kiczanski et al., 2004; Li et al., 2014; Dalou et al., 2012; Webster et al., 2018), possibly due to the relatively higher temperatures required (i.e., at least above 1100 °C), which translate to more challenging experimental set ups. Nevertheless, studies have shown how intermediate melts can dissolve up to 1 wt% of F, while solubilities in basaltic systems are at most 0.5 wt% (Webster et al., 2018). These values have a similar order of magnitude to water solubility by the same systems (Dalou et al., 2012; Stolper, 1982), a fact that has been interpreted as indication of equivalent incorporation mechanisms for F⁻ and OH⁻ (Dolejš & Zajacz, 2018).

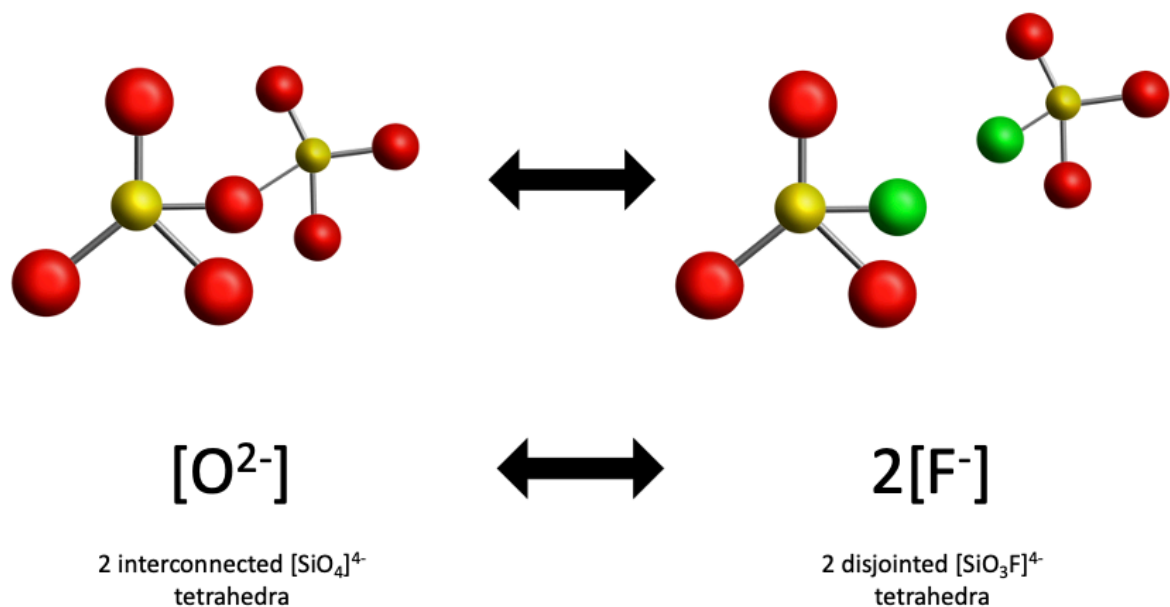


Figure 1.5: Schematic representation of the depolymerising role played by F when substituting for O in a melt's silicate tetrahedra network. The difference in charge between the two ions causes the disconnection of two tetrahedra in the melt's structure (Webb & Dingwell, 1990).

F is dissolved in silicate melts through interactions with both network forming (e.g., Si and Al) and network modifying (e.g., alkali, alkali earths) cations (Webster et al., 2018; Dolejš & Zajacz, 2018). Fluorine is generally regarded as a depolymerising agent in the melt structure (Webb & Dingwell, 1990), due to its tendency to interrupt the chains of silicate tetrahedra (see Figure 1.5) when substituting for O^{2-} in the melt structure (Dolejš & Zajacz, 2018). Examples of the former include $Al-F-Na(n)$ and $Si-F-Na(n)$, in which F coordinates to a network-forming element (Al or Si) and to a variable number of network modifying cations, effectively substituting for a non-bridging oxygen. Examples of the latter include $Al-F-Al$ and $Si-F-Al$, where F replaces a bridging oxygen (Zeng & Stebbins, 2000; Stamboulis et al., 2004; Mysen et al., 2004; Baasner et al., 2014). In less polymerised mafic melts, $Mg-F$ and $Al/Si-F$ bonds have been identified

(Kiczinski et al., 2004), although the dissolution of fluorine in such systems is less well understood (Webster et al., 2018). On top of this, while the effect of pressure on the coordination state of major components of silicate melts is well understood (Solomatova & Caracas, 2019; and refs. therein), the impact of coordination state changes with pressure on F speciation is poorly constrained (Webster et al., 2018). This translates to notable gaps in the understanding of arguably the most enriched volatile in the BSE relative to CI chondrite (McDonough & Sun, 1995). Therefore, it is paramount to investigate and accurately determine its speciation in both silicate melts and in the phases in which it is hosted alongside water in OH⁻ form. This would, in turn, lead to a better assessment of F's importance on melts rheological properties, as well as on water transport towards the deep Earth.

~2 — METHODS~

This chapter will firstly present on the general theory behind each experimental and analytical technique used in this thesis, and then detail their specific applications in the context of the research presented in the following chapters. Due to the covid-19 pandemic, the author of this thesis was sometimes unable to access the necessary facilities in person to carry out the syntheses and analyses described in this chapter. Whenever these were performed by collaborators, it is specified in the subsection where the specific experiments are described. All people actively involved in the making of this thesis are also mentioned in the Acknowledgements at the start of this thesis.

2.1 – SAMPLE SYNTHESIS

As this thesis revolved around the study of high-temperature silicate melts and phases, extensive use of high temperature and pressure (often abbreviated as high P-T) instrumentation was involved in the synthesis of all samples. The choice of the instrumentation used to produce each sample was based on the pressure required: [1] low P materials (i.e., 1 atm) were synthesized in a muffle furnace, [2] high P samples (i.e., up to 3 GPa) were produced with end loaded piston cylinder apparatuses, while for [3] very high P samples (i.e., from 5 to 20 GPa) a multi anvil press was used.

2.1.1 – Low pressure sample synthesis.

2.1.1.1 – Muffle furnace – Theory.

Synthesis of all low P silicate melts was performed using an electric front-loaded muffle furnace. The choice was motivated by the simplicity of this instrumentation, which consists of a heating element (i.e., an electrical resistance), a refractory casing for the hot chamber and a surrounding metal container (see Figure 2.1).

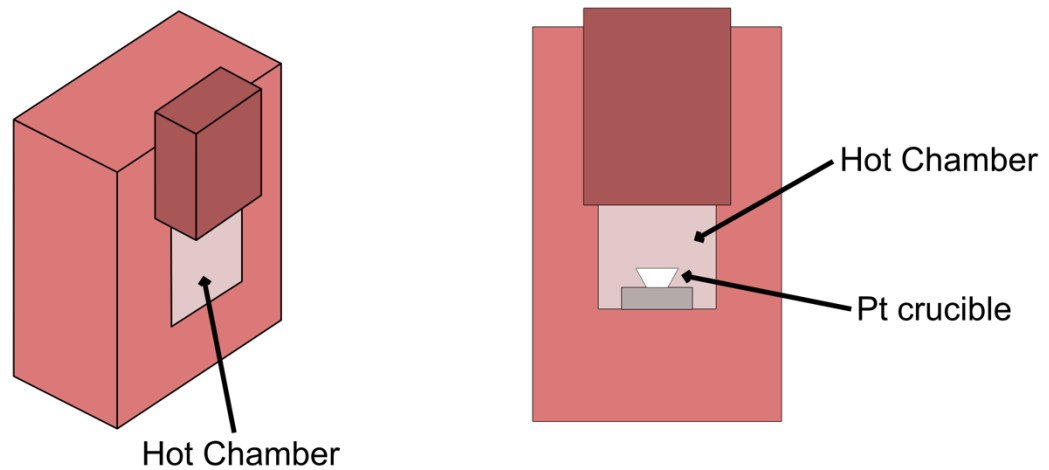


Figure 2.1: Schematic representation of a muffle furnace (modelled after Nag, 2011). Total volume of the furnace is usually around 1 m³, depending on the size of the external casing.

A muffle furnace is ideal for synthesis of high T materials at atmospheric pressures. However, no control is possible on the atmospheric composition inside the hot chamber, thus it is not feasible to use for applications in which this parameter is a concern (e.g., in presence of graphite, which easily oxidizes at high T).

The starting materials typically consist of powdered chemicals homogeneously mixed together, then poured into a crucible made of high T resistant material (e.g., native Pt). The crucible is inserted into the furnace, heated at the desired temperature, and kept in these conditions for the desired time. Subsequently, the hot melt is quenched to a glass, scraped off the crucible and stored for analysis.

The only limitations on the amount of glass that can be produced via a muffle furnace are the size of the crucible and the size of the furnace itself. Even a relatively small crucible (i.e., around 15 mm in diameter and 20 mm in height) could be used to produce 10s of g of glass, which is orders of magnitude more than what can be synthesized with the high pressure instrumentation described in section 2.1.2.

2.1.1.2 – Muffle furnace – Application.

A muffle furnace was used for the synthesis of all silicate glasses studied for chapter 4 (i.e., samples EdiF_2h, EdiF_4h, EdiF_7.5h, EdiF_18h, EdiF_MAS1 and EdiF_CMSe), and for the synthesis of the starting glass used for multi anvil high pressure annealing experiments used to produce the samples studied in chapter 5 (see subsection 2.1.2.5 for details). The compositions of glasses of chapter 4 were either CMAS7G, MAS1 or CMSe, while glasses of chapter 5 were always CMAS7G (see Table 2.1 for compositions). Samples were all synthesized by the author of this thesis and Dr. Geoff Bromiley at the School of Geosciences of the University of Edinburgh.

Starting materials always consisted of ACS reagent grade chemicals (i.e., 98.0% guaranteed purity for MgO, and 99.0% for any other material used), which were weighed on a scale with a precision of ± 0.1 mg. All composition of the melts produced were either of the CMAS (i.e., CaO + MgO + Al₂O₃ + SiO₂), MAS (i.e., MgO + Al₂O₃ + SiO₂), or CMS (i.e., CaO + MgO + SiO₂) systems. Mg, Al and Si were added to the mixtures as oxides (i.e., MgO + Al₂O₃ + SiO₂), while Ca was added as a carbonate (CaCO₃), as CaO is highly hygroscopic and the glasses needed to be as OH-free as possible, to avoid any unwanted competition for the same sites between F and OH. MgO is also hygroscopic but was still used due to it being a minor component of the CMAS7G mixture compared to CaO (see Table 2.1). In the case of the MAS1 and CMSe mixtures MgO is instead a major component, however it was used due to the unavailability of MgCO₃ at the time of the synthesis of the samples of these compositions.

F was added as CaF₂ to CMAS and CMS mixtures, and as MgF₂ to the MAS mixture, due to the need for the latter system to be nominally Ca-free. All starting mixtures were mixed (homogenized) using an agate pestle and mortar, and then poured into a Pt crucible of ca. 15 mm in diameter and 20 mm in height. A two-step firing procedure was performed: firstly, the mixtures were fired at 850(± 10) °C for 1 h to decarbonate CaCO₃. This step was followed by the addition of the fluorides and a final stage of heating at 500(± 10) °C to dehydrate the final mixes. See Table 2.1 for the starting compositions of the glasses produced via muffle furnace for the research of chapters 4 and 5. The crucible was then inserted into the furnace and heated at the desired temperature for the target duration (see Table 2.2). Subsequently, the hot melt was quenched to a glass by

removal from the furnace and immersion into distilled water, scraped off the crucible and stored in a sealed glass vial.

	CaO (wt%)	MgO (wt%)	Al₂O₃ (wt%)	SiO₂ (wt%)	CaF₂ (wt%)	MgF₂ (wt%)
CMAS7G	25.00	2.37	12.50	59.26	0.87	0.00
MAS1	0.00	20.07	17.09	62.19	0.00	0.66
CMSe	18.50	23.83	0.00	56.87	0.79	0.00

Table 2.1: Nominal compositions of the starting mixtures used for glasses of chapters 4 and 5.

Sample	Temperature / °C	Duration / h	Composition
EdiF_2h	1250	2	CMAS7G
EdiF_4h	1250	4	CMAS7G
EdiF_7.5h	1250	7.5	CMAS7G
EdiF_18h	1250	18	CMAS7G
EdiF_MAS1	1450	8	MAS1
EdiF_CMSe	1450	8	CMSe
Starting glass	1250	0.5	CMAS7G

Table 2.2: Compositions and synthetic conditions used for the preparations of glasses of chapter 4 and for the starting glass for multi anvil experiments of chapter 5 (labelled as “Starting glass”).

Due to the considerable cost of platinum, the same crucible was reused for all experiments. The cleaning procedure consisted of filling this with boron carbonate ($C_3B_2O_9$) and heating at 500 °C for ca. 15 mins, before quenching in distilled water. This allows the carbonate to adsorb any impurity, thus avoiding cross-contamination between different syntheses.

Error margin temperature was estimated as ca. $\pm 20^\circ\text{C}$, based on the calibration of the instrument, and thus was deemed negligible in the context of this study.

2.1.2 – High pressure sample synthesis.

The synthesis of samples under high P conditions (i.e., >1 GPa) requires the use of a hydraulic press. Such instruments make use of various compression geometries, based on the P required. As P is inversely correlated to the area over which the force is applied, minimizing the area is far more efficient than increasing the applied force. However, this has the adverse effect of the amount of sample produced being miniscule (i.e., tens of mg with piston cylinder and a few mg with multi anvil devices), which presents a range of challenges in the subsequent analyses. As a result, less efficient geometries (e.g., a piston cylinder press) are still widely used for lower pressures, as they allow the production of samples with higher volumes (see subsections 2.1.2.1 and 2.1.2.3 for examples relevant to this thesis).

Another notable challenge during sample synthesis is the application of isotropic pressure: outside of tectonically active contexts, pressure in the deep

Earth is almost solely hydrostatic (i.e., exerted equally from all directions). However, a standard hydraulic press exerts pressure along a single axis, therefore more complex geometries need to be implemented, as shown schematically in Figure 2.2.

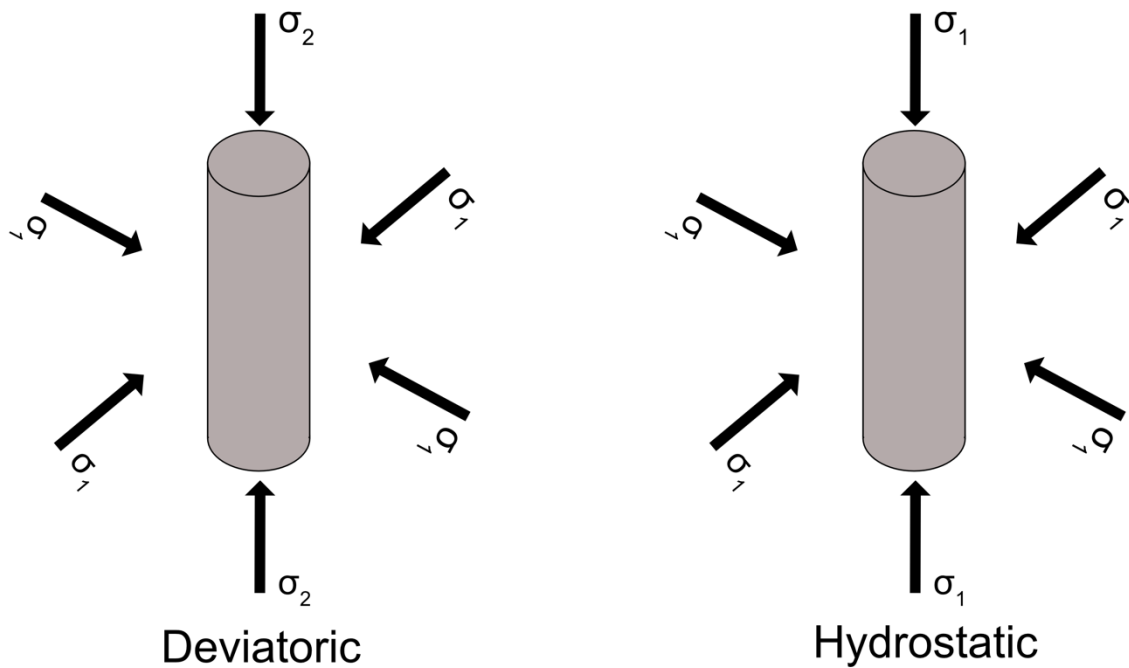


Figure 2.2: Schematic showing the difference between deviatoric stress (exerted preferentially along one axis) and hydrostatic pressure (exerted equally along all axes). The arrows (σ) represent the stress vectors.

The following subsections present the instrumentation used for the synthesis of high P samples and their specific applications in this thesis.

2.1.2.1 – End loaded piston cylinder press – Theory.

This sub-type of piston cylinder press (first described by Boyd & England, 1960) relies on the use of two hydraulic rams of different diameters to exert pressure on

the sample, and on the surrounding pressure medium, respectively, to transform a deviatoric stress into a hydrostatic pressure (see Figure 2.3). This architecture can safely reach pressures of ca. 3-4 GPa; however, experiments at higher pressures (i.e., upwards of ~5 GPa) can also be attempted, depending largely on the expendability of the apparatus.

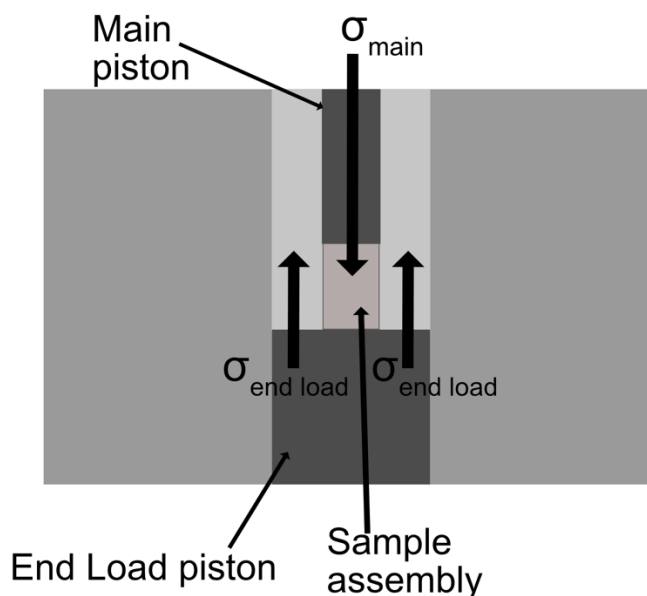


Figure 2.3: Schematic showing a cut out of an end loaded piston cylinder press. The lower ram (end load piston) exerts pressure on a confining medium around the assembly, therefore translating into a confining pressure on the sample. The main piston then applies a deviatoric pressure on the sample. The arrows (σ) represent the stress vectors

The powdered starting mixture is inserted into a Pt cylindrical capsule of ca. 5-10 mm in length and with an inner diameter of ca. 3.0-3.5 mm, which is then welded shut with an argon-shielded point welder. Longer capsules allow for larger samples to be prepared but can also be subject to comparatively higher temperature gradients which are difficult to predict (as the hot point of the heating mechanism is in the centre of the capsule, while the point at which T is measured

is at the top). The Pt capsules are inserted in assemblies which, from the outside, consist of a talc cylinder, a pyrex glass cylinder, a cylindrical graphite furnace sealed at the bottom end and a MgO sleeve. The capsule stands on a MgO spacer, and an Al_2O_3 disc is positioned on top of the capsule. This is used to avoid direct contact between the capsule and the thermocouple used for temperature monitoring, which is kept in place by a MgO sleeve, and a steel base plug surrounded by a talc cylinder (see Figure 2.4).

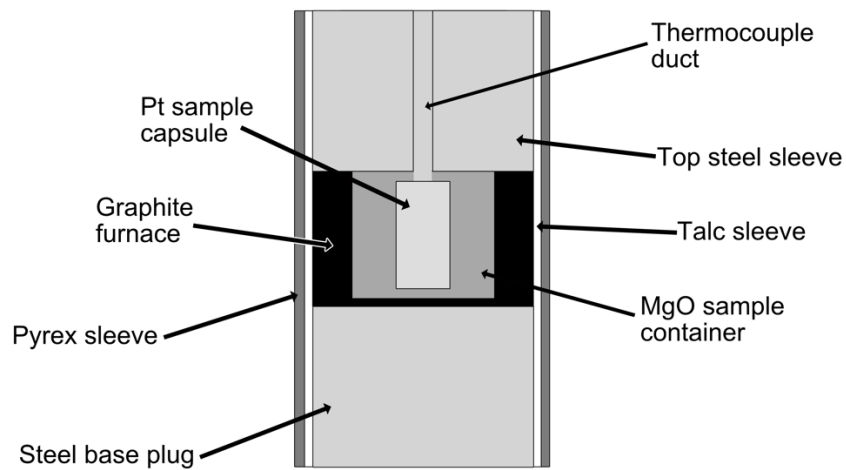


Figure 2.4: Schematic representation of the assembly used in an end loaded piston cylinder type press (horizontal proportions are exaggerated for clarity). Minor differences can exist between individual instruments.

Once the sample assembly is inserted in the press, an end load of 200-300 MPa is applied, followed by heating by running a current through the graphite furnace and pressurisation through applying pressure on the main cylinder. Once the experiment is finished, the assembly is quenched by cutting the current to the furnace, and after T reaches ambient levels, the main pressure is gradually removed. The end load is subsequently lifted, and the assembly is removed from

the press and opened to remove the Pt capsule, which is subsequently opened to recover the sample.

2.1.2.2 – End loaded piston cylinder press – Starting material preparation.

End loaded piston cylinder apparatuses were used for the synthesis of all N-enriched silicate glasses of chapter 3 (i.e., samples Edi01, Edi02, Edi03 and Edi04), F-enriched silicate glasses EdiF_01 and EdiF_02 of chapter 5 and all synthetic humite group minerals of chapter 6 (i.e., samples D1658, C4346, C4602, C3095 and CH001. See Table 6.2 in chapter 6 for phase composition). The composition of all glasses was CMAS7G (see Table 2.3). ¹⁵N enrichment for samples Edi01 to Edi04 was achieved via adding a ¹⁵N-bearing compound to the starting mixture (see Table 2.5), while F enrichment for samples EdiF_01 and EdiF_02 was performed via adding CaF₂ following the proportions given in Table 2.1.

CMAS7G	Abundance (wt%)	Abundance (mol%)
CaO	25.22	27.63
MgO	2.39	3.64
Al₂O₃	12.61	7.60
SiO₂	59.78	61.13

Table 2.3: percentage in oxides of the CMAS7G composition (O'Neill & Eggins, 2002).

Sample CH001 was synthesized within the context of this thesis (see Table 2.4 for composition of starting mixture) at the School of Geosciences of the University of Edinburgh, while all other humite group minerals were synthesized before the conception of this thesis at Imperial College (London, UK). All starting mixtures were in the same system of sample CH001, however the relative proportions between individual components were not preserved.

	MgO (wt%)	SiO₂ (wt%)	MgF₂ (wt%)	Mg(OH)₂ (wt%)
CH001	52.70	38.53	0.07	0.03

Table 2.4: Composition of the starting mixture used for sample CH001 of chapter 6.

Starting mixtures for F-enriched silicate glasses were prepared following the same procedure described in subsection 2.1.1.2 until after the two-step firing procedure. N-bearing starting mixtures were instead prepared by mixing ACS reagent grade CaO, MgO, Al₂O₃ and SiO₂ in the desired relative proportions (see Table 2.3) in an agate pestle and mortar, then N-enriching compounds, H₂O and Si metal were added (see Table 2.5).

	Edi01	Edi02	Edi03	Edi04
CMAS7G	46.7 mg	55.3 mg	39.7 mg	43.0 mg
¹⁵N-bearing compound	2.9 mg NH ₄ NO ₃	1.7 mg NH ₄ NO ₃	4.8 mg NH ₄ Cl	4.4 mg NH ₄ Cl
H₂O	2.5 µL	2.0 µL	4 µL	4 µL
Si metal	-	0.2 mg	-	0.1 mg

Table 2.5: Final starting mixtures for the synthesis of the N-enriched silicate glasses of chapter 3. In both ¹⁵N-bearing compounds 98% of total N was ¹⁵N.

The starting mixture for the synthesis of sample CH001 is given in Table 2.4 and was obtained by mixing together ACS reagent grade chemicals. Starting mixtures for all other humite samples consisted of the same chemicals of sample CH001 in different relative proportions, however the samples were synthesized in 2009 (i.e., 9 years before the start of the PhD project of this thesis) and precise compositions of each starting mixture were not preserved.

2.1.2.3 – End loaded piston cylinder press – Sample synthesis.

Empty Pt capsules were annealed with a blow torch to improve malleability, then filled with the starting mixtures and welded shut with an Ar-shielded TIG welder, before being inserted in a talc-pyrex-graphite assembly (see Figure 2.4) as described in subsection 2.1.2.1. Assemblies were then wrapped in lead foil and lubricated with Molykote paste to reduce friction. A type R thermocouple (Pt-Pt/Rh) was used to monitor the temperature within the assembly during the synthesis of all samples.

N-bearing glasses were all synthesized under the same conditions ($P = 2.0$ GPa and $T = 1450$ °C) for 1 h, after which assemblies were quenched at room T by cutting power to the apparatus while maintaining a constant P. Once the temperature had stabilised, the pressure was lowered to atmospheric level, the end load was lifted, assemblies were removed from the press and opened to recover the assemblies. All samples were synthesized at the School of Geosciences of the University of Edinburgh by Dr. Eleanor Mare and Dr. Geoff Bromiley.

F-bearing glasses were both synthesized at a T of 1450 °C and at a pressure of 2 and 1 GPa for samples EdiF_01 and EdiF_02 respectively. After 2 h at high T, samples were quenched to 800 °C by reducing the power of the transformer, pressurized again to balance the contraction caused by the quenching and kept at these conditions for further 2 h, before being quenched to room temperature by cutting power to the furnace. This procedure was used to better preserve the high-pressure coordination environment of Al (Gaudio et al., 2015). After this, samples were quenched to room T, the main load was lifted followed by the end load, and assemblies were recovered from the press. All samples were synthesized at the School of Geosciences of the University of Edinburgh by the author of this thesis and Dr. Geoff Bromiley.

Assemblies were pried open to recover the capsules, which were then opened and ~50 mg of glass was recovered from each. Small chips (~5-10 mg of weight) were retained for chemical analysis, while the remaining glass was ground under ethanol in a pestle and mortar for NMR analysis and stored in labelled vials.

Humite group minerals were synthesized by pressurizing at 2 GPa and heating at 1000 °C. Duration of the experiment was 48 h for samples C4602 and C3095 and 24 h for all other samples. After this, quenching at room temperature was performed and the main load was gradually lifted, followed by the end load. The assemblies were removed from the press and pried open to recover the Pt capsules. Once these were opened, a small chip of sample C3095 was preserved for chemical analysis and the rest of it was ground. All other samples were fully ground under ethanol in a pestle and mortar for NMR analysis and stored in labelled vials. Sample CH001 was synthesized by Dr. Geoff Bromiley at the University of Edinburgh, all other samples by Prof. Andrew Berry at Imperial College (London, UK).

Error margin on pressure and temperature were estimated as ca. $\pm 5\%$ and $\pm 25^\circ\text{C}$ respectively, based on the calibration of the instrument, and thus were deemed negligible in the context of this study.

2.1.2.4 – Multi anvil press – Theory.

Pressures above 5 GPa are impossible to reach for a piston cylinder press, due to intrinsic limitations of the experimental architecture. The multi anvil apparatus is based on a completely different approach, which involves a set of eight cubic anvils made of high hardness alloys (e.g., WC), each with one flattened corner (see Figure 2.5). This design results in the formation of an octahedral cavity in between the anvils, and when these are compressed the assembly inside the cavity is naturally subjected to hydrostatic pressure (see Figure 2.6). Compression is achieved by using two identical hydraulic rams acting in opposing

directions, each compressing four of the eight anvils. The face of each ram has a cavity which accommodates the cubic anvils which enclose the assembly (see Figure 2.7 for details of the interior of the assembly).

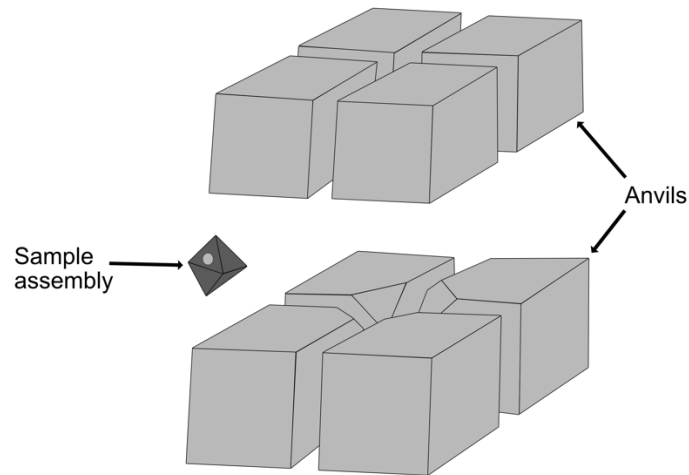


Figure 2.5: Schematic representing of the cubic anvils used in a Kawai-Endo type multi anvil press. The flattening of one corner of each anvil allows for the accommodation of an octahedral sample assembly.

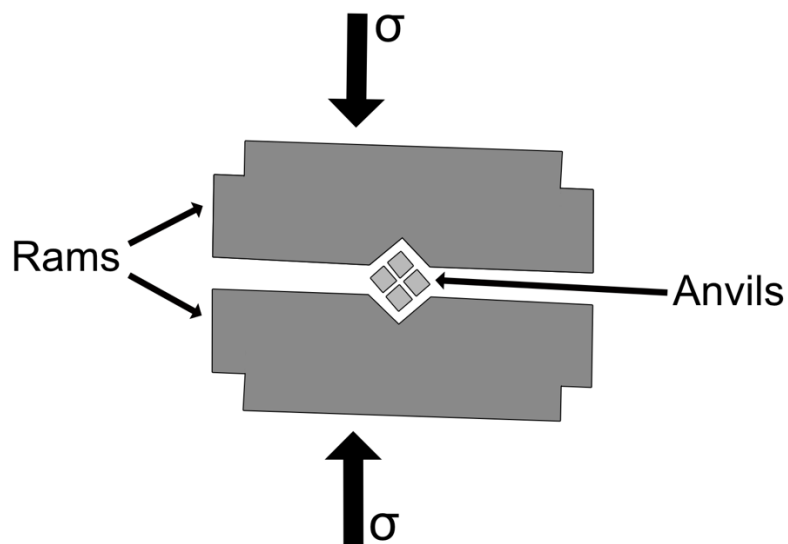


Figure 2.6: Schematic showing the compression architecture in a Kawai-Endo type multi anvil press. The cavity in each ram allows the isostatic compression of the anvils. The arrows (σ) represent the stress vectors.

The architecture in Figures 2.5 and 2.6 was first developed by Kawai & Endo (1970) and more modern assemblies can easily reach pressures in the tens of GPa (Walker et al., 1990). However, one crucial disadvantage when compared to piston cylinder presses is the production of considerably smaller samples. The production of larger samples requires much larger anvils, which in turn translates to wider rams, and therefore more voluminous presses. As of the writing of this thesis, only two multi anvil presses capable of producing samples up to 10-15 mg are known to exist: one is found at the Bayerisches Geoinstitut (in Germany) and the other at Ehime University (in Japan).

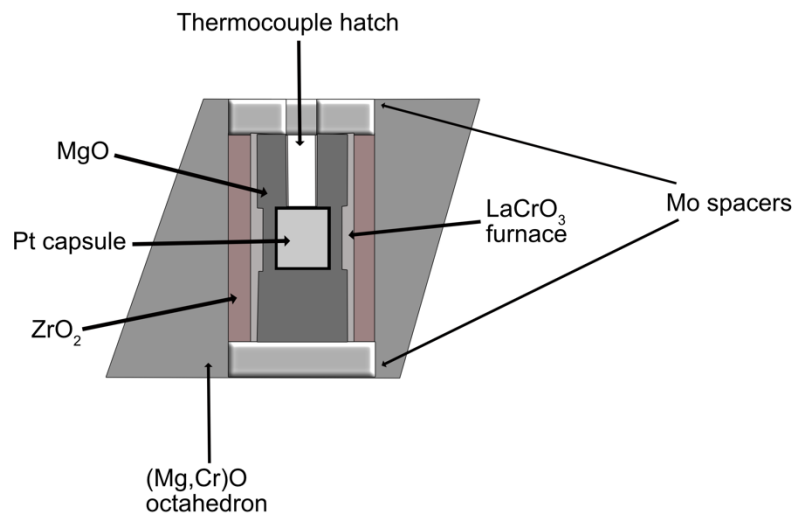


Figure 2.7: Schematic representing of the assembly used in a Kawai-Endo type multi anvil press. Minor differences can exist between different instruments.

Once the sample assembly is placed in between the anvils, pyrophyllite spacers are placed in the gaps between each anvil to act as a lubricant and avoid direct contact between the anvils, and the complete assembly is then placed on top of the lower ram. A load is then applied to the ram to pressurise the assembly

and heating is achieved by running a current through the LaCrO₃ furnace. The quenching and unloading procedure are analogous to that for the piston cylinder press: the current to the furnace is cut, and after T reaches ambient levels, the load is lifted from the ram. The assembly is then removed from the press and opened to remove the Pt capsule, which is subsequently opened to recover the sample.

2.1.2.5 – Multi anvil press – Application.

The multi anvil press in the context of this thesis was used for the high P annealing of F-enriched CMAS7G silicate glasses previously synthesized at 1 atm via muffle furnace (see subsection 2.1.1.2). A total of four samples were produced (BayF_01, BayF_02, BayF_03 and BayF_04), with the only difference between them being the pressure at which they were annealed (see Table 2.6). All samples were synthesized at the Bayerisches Geoinstitut of the University of Bayreuth (Bayreuth, DE) by Caterina Melai.

Sample	Annealing T / °C	Annealing time / h	Pressure / GPa
BayF_01	800	8	20
BayF_02	800	8	10
BayF_03	800	8	5
BayF_04	800	8	8

Table 2.6: Synthetic conditions for the high P samples annealed via multi anvil press.

The powdered starting glass was inserted into a Pt cylindrical capsule of ca. 2-3 mm in length and with an inner diameter of ca. 1.2-1.5 mm, which was then welded shut with an Ar-shielded TIG point welder. The capsule was then inserted into an octahedral assembly (see Figure 2.7) consisting of (from the outside): a (Mg,Cr)O octahedron, a zirconia cylinder, two molybdenum disks (one on each side of the assembly), a LaCrO₃ cylindrical furnace, a MgO cylinder with the Pt capsule inside and an opening on one side to accommodate the thermocouple, which is held in place by an Al₂O₃ sleeve. The assembly was then inserted into the press and heated at 100 °C, then pressurised (see Table 2.6 for details for each sample), and then heated at 800 °C for a run time of 8 h. After this, quenching was performed by cutting power to the furnace. The load was removed, and the assembly removed from the press. The recovered assembly was broken open using pliers to recover the Pt capsule. The capsule containing sample BayF_01 was then polished until a portion of the glass was exposed to perform chemical analyses, while all other capsules were unpolished post-recovery to minimise sample loss. All capsules were stored in labelled plastic vials and posted to the University of St Andrews for NMR analysis. The capsules were then pried open using pliers and razor blades, with the recovered glass ground under ethanol in an agate pestle and mortar and stored in labelled glass vials.

Error margin on pressure and temperature were estimated as ca. $\pm 8\%$ and $\pm 30^\circ\text{C}$ respectively, based on the calibration of the instrument, and thus were deemed negligible in the context of this study.

2.2 – ANALYTICAL METHODOLOGIES

As many chapters of this thesis involve the study of similar materials (i.e., N or F enriched silicate glasses and minerals), most analytical techniques were used for more than one study. These techniques were solid-state Magic Angle Spinning Nuclear Magnetic Resonance (MAS NMR) spectroscopy, Raman spectroscopy and Electron Probe Micro Analysis (EPMA). In addition, Reverse-Geometry Sensitive High-Resolution Ion Micro Probe (SHRIMP-RG) was utilised for the analysis of N concentration in silicate glasses of chapter 3. Density Functional Theory calculations were also performed, to aid the peak assignment in NMR spectra collected from glasses of chapter 3, and for determining the theoretical most stable distribution of F⁻ and OH⁻ ions in the framework of the humite group minerals of chapter 6. The following sections will provide a basic overview of each, followed by the settings utilised for each specific analysis. The tools used for data processing are also introduced.

2.2.1 – MAS NMR spectroscopy.

Since the first reports of the NMR phenomenon in the bulk phase in 1946 (Bloch, 1946; Purcell et al., 1946) steadily increasing interest has been shown in what has become a vital spectroscopic technique in the chemical sciences. Although early effort focused on high-resolution NMR spectroscopy of spin $I = 1/2$ nuclei in the liquid phase, the availability of higher magnetic fields and other technological advances has led to increases in the use of NMR spectroscopy for the study of

solid materials. The basic NMR phenomenon exploits the inherent angular momentum (or spin) of a nucleus, the magnitude of which is described by a spin quantum number, I , which can take integer or half integer values. In both solution and in the solid state, study of $I = 1/2$ nuclei is significantly less technically demanding than experiments involving nuclei with higher spin ($I > 1/2$) and the work in this thesis has focussed on $I = 1/2$ nuclei exclusively. NMR arises from the difference in energy of the $2I + 1$ different nuclear spin states when placed in an external magnetic field (B_0). Radiofrequency radiation can be applied to alter these spin states (noting the very small energy differences between the states) with transitions typically referred to in terms of their Larmor frequency (e.g., for ^1H at 9.4 T this would be 400 MHz). Modern NMR experiments are usually carried out using radiofrequency pulses that are able to excite all nuclear spins of one isotope simultaneously (as opposed to bringing each into resonance by varying the frequency of the radiation), enabling a spectrum (denoting the resonance frequency of each type of spin) to be acquired easily (see later).

The exact resonance frequency observed for a particular nucleus is affected by interactions between the spins, or between the spins and their environment (i.e., local magnetic fields or electric field gradients) and, as such, NMR is uniquely sensitive to the local chemical environment. Perhaps the most important of these interactions is the chemical shielding, which arises from the small magnetic fields created by the electrons that surround a nucleus, giving rise to detailed information on the number and type of surrounding atoms and the types of interactions or distances between these. A signal is, therefore, defined

by its chemical shift, usually quoted relative to a well-established reference compound in ppm, that uniquely defines its local environment.

The interactions that affect the nuclear spins are anisotropic in nature (Keeler, 2002), leading to significant line broadening in the spectrum. In the more established solution-state NMR spectroscopy (i.e., where the analyte is dissolved in a solvent), this issue is solved by the rapid tumbling of molecules, which averages the anisotropy but retains the isotropic components of the interactions, thereby providing sharp spectral lines (and high resolution) and separation of signals from chemically different spins. However, in the solid state such tumbling is not present, and anisotropies are retained leading to a significant broadening of the spectral signals (Ashbrook et al., 2014) for powdered samples, limiting both resolution and sensitivity. One approach to resolve this problem is Magic Angle Spinning (MAS). Here a powdered solid sample is packed in a rotor, which is then rotated rapidly (i.e., at frequencies in the kHz or 10s of kHz order of magnitude) around an axis inclined at an angle of 54.736° to B_0 (see Figure 2.8). This mimics the orientational averaging that occurs in solution and, as the anisotropic components of many of the aforementioned contributions to the NMR signal all have a similar orientational dependence proportional to $(3\cos^2\theta - 1) / 2$, which is zero if $\theta = 54.736^\circ$ (Ashbrook et al., 2014), this is able to remove these contributions provided spinning is sufficiently rapid.

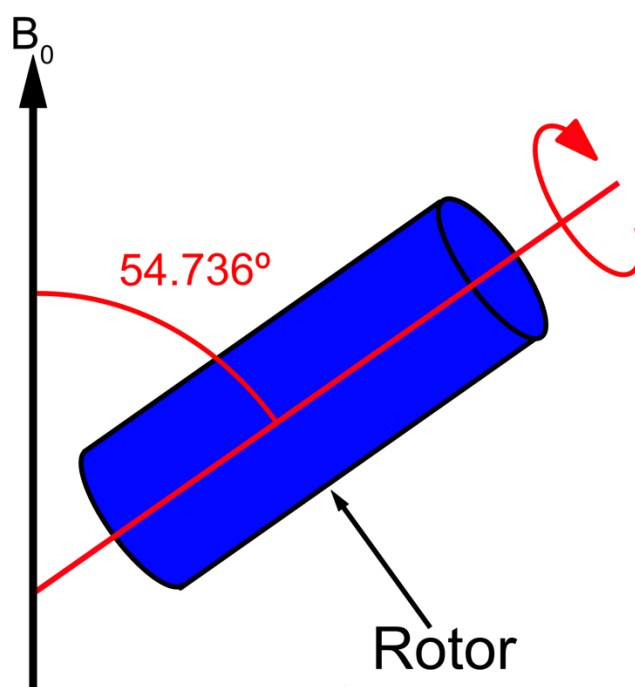


Figure 2.8: Schematic representing the tilting of the rotor relative to the magnetic field B_0 . The crystallites contained in the rotor are all in random orientations, therefore the fast rotation partially emulates the rapid tumbling of the molecules in a solution.

Typical rotation rates are between 5 and 60 kHz (although rates up to 130 kHz are possible on the most sophisticated equipment). Higher spin rates can be achieved with rotors of smaller diameter (e.g., 1.3 or 1.9 mm), however such rotors are unable to carry as much sample as their larger counterparts (e.g., 4 or 7 mm in diameter), which can be an issue when the analyte is of low NMR sensitivity. If the spinning rate is too slow (i.e., lower than the magnitude of the interaction in Hz), additional signals, termed spinning sidebands are observed spaced at multiples of the spinning frequency.

The simplest type of NMR experiment consists of the application of a single radiofrequency pulse (optimised to ensure maximum signal), after which

the precession of the nuclear spins is detected in the form of a Free Induction Decay (FID), as shown in Figure 2.9. In most cases, this experiment is repeated N times (after waiting for enough time for the spins to return to equilibrium – termed the recycle interval) and the set of FIDs are co-added to improve the signal-to-noise of the final spectrum. This is especially important when the signal is low and the noise is high, as is the case for nuclei with low Larmor frequency, or very dilute nuclei (through low natural abundance or chemical concentration). As the signal to noise ratio increases as $N^{1/2}$, in such cases a very large number of FIDs may need to be collected. This spectrum can then be obtained from a Fourier transform of the FID, as shown in Figure 2.10. More elaborate pulse sequences (consisting of multiple pulses and/or evolution periods) can provide more detailed information on the interactions between the spins but are mostly outside the scope of this thesis. One experiment that was employed in this work to improve the baseline and remove any background signal was the spin echo experiment (involving 90° and 180° pulses separated by an interval t).

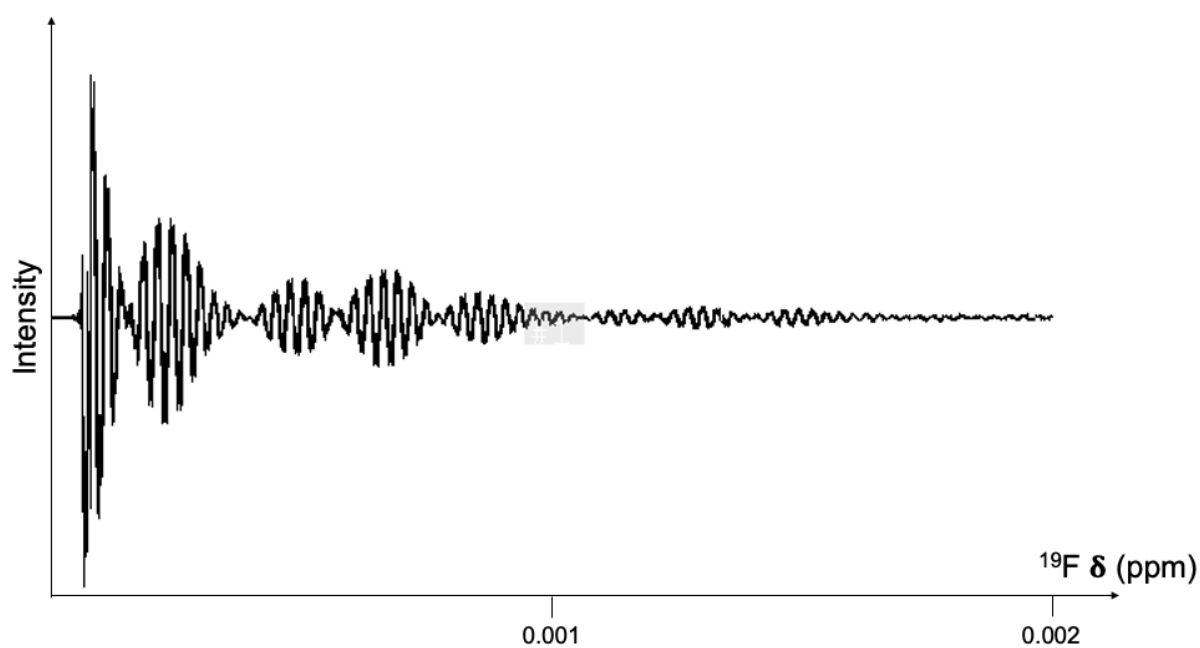


Figure 2.9: The sum of 8 ^{19}F FIDs collected during a single-pulse experiment performed on a humite group mineral analysed for this thesis. It is clear how the FID significantly decays as a result of relaxation.

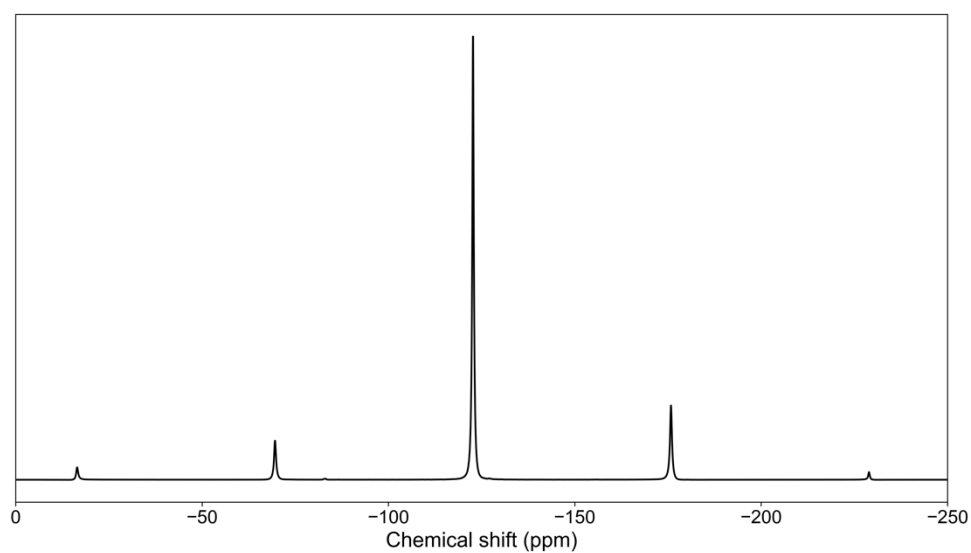


Figure 2.10: ^{19}F (9.4 T, 30 kHz MAS rate) NMR spectrum of polytetrafluoroethylene (PTFE, $(\text{C}_2\text{F}_4)_n$), used as a reference compound for all ^{19}F experiments. The position of the isotropic peak at -122.7 ppm confirms the presence of F-C bonds in the structure, while the other smaller peaks are spinning sidebands.

In this thesis work has focused on ^{19}F and ^{15}N MAS NMR spectra of glasses and humite group minerals. Chemical shifts are reported in ppm relative to CFCl_3 and CH_3NO_3 for ^{19}F and ^{15}N , respectively, using poly(tetrafluoroethylene) and ^{15}N -enriched glycine respectively as secondary solid references. The specific methodologies utilised for the NMR analyses performed for this thesis are described in the following subsections.

2.2.1.1 – N speciation analysis via ^{15}N MAS NMR.

^{15}N MAS NMR spectra were collected at 400 MHz on a Bruker AVANCE III spectrometer equipped with a 9.4 T wide-bore magnet at the University of St Andrews by the author of this thesis, under supervision from Dr. Daniel Dawson and Prof. Sharon Ashbrook. The ^{15}N background (from the BN stator block) in single pulse experiments was sufficiently high to make quantification impossible. To overcome this problem, a two pulse spin echo sequence was used. $(\text{NH}_4)_2\text{HPO}_4$ diammonium phosphate was used as a secondary reference in all experiments, with $d_{\text{iso}} = -356$ ppm relative to nitromethane (CH_3NO_2), which was used as the primary reference. All samples were rotated (sequentially) in the same 4 mm ZrO_2 rotor at a frequency of 10 kHz, which was sufficient to remove all spinning sidebands from the region of the central peaks. Due to the small amount of sample available (c.a. 30 mg), relative to the size of a 4 mm rotor, a N-free PTFE insert was used to restrict the sample volume to that in the centre of the coil. Pulse durations of 4 and 8 ms for 90° and 180° pulses, respectively. The fast relaxation times for all the studied bonding environments allowed the use of a recycle interval of 1 s. The acquisition time was 61.44 ms, and the total

number of scans summed was 157216, equivalent to a run time of 43.7 h for each spectrum.

A cross polarisation experiment was performed on sample Edi03 to better understand the nature of different N—H bonding environments. For this experiment, a 4 mm ZrO₂ rotor was spun at 5 kHz, a total of 150480 scans (equivalent to a 41.8 h experimental runtime) was performed and a recycle delay of 1 s was used. The acquisition time was 81.92 ms, and the contact pulse (ramped for ¹H) was 3 ms. Continuous wave ¹H decoupling ($n_1 = 90$ kHz) was employed during acquisition. Relative peak intensities in all spectra were measured by Pseudovoigt fits made with the Imfit Python library.

2.2.1.2 – F speciation analysis via ¹⁹F MAS NMR.

¹⁹F NMR spectra from silicate glasses of chapter 4 were acquired using a Bruker AVANCE III spectrometer equipped with a 9.4 T wide-bore magnet, while an analogous instrument equipped with a 14.1 T wide-bore magnet was utilised to collect ¹⁹F NMR spectra from silicate glasses of chapter 5. Both spectrometers are located at the University of St Andrews. The analytical procedure utilised on both instruments was the same. All analyses were performed by the author of this thesis.

Samples were packed into a standard ZrO₂ 1.9 mm rotor and rotated around an axis inclined at the magic angle to the external magnetic field at a rate of 30 kHz. A background spectrum was collected using ACS grade γ -Al₂O₃ and this was subtracted from each spectrum. As ¹⁹F abundance in all samples was expected to be low a single-pulse experiment was performed to maximise the

signal acquired from the analyte. Spectra for the glass samples were acquired with signal averaging of 157216 transients with a recycle interval of 1 s (equivalent to a total run time of 43.7 h), using a ^{19}F radiofrequency nutation rate of $n_1 \approx 83$ kHz. Peak fitting and integration were performed using the DMFit program (Massiot et al., 2002). Chemical shifts are reported in ppm relative to CFCl_3 using poly(tetrafluoroethylene) (PTFE, $d_{\text{F}} = -122.7$ ppm) as a secondary solid reference.

The mineral phases used as reference samples contained a notable amount of Fe, in the order of magnitude of 10^{-1} wt% (Hamilton et al., 1998). As F was present at stoichiometric abundances in both materials, a spin echo sequence was employed to reduce the F probe background, with 90° and 180° pulse durations of 4 and 8 ms, respectively. Spectra are the result of averaging 72000 transients with a recycle interval of 1 s (equivalent to a total run time of ca. 20 h).

2.2.1.3 – F abundance quantification via ^{19}F MAS NMR.

The quantification of an analyte via NMR spectroscopy is performed via collecting an NMR spectrum from a sample with unknown analyte concentration, and then by comparing it to a spectrum collected from a reference sample with known analyte concentration, collected via the same analytical procedure under identical ambient conditions. Ideally, the two spectra are collected back-to-back on the same instrument. The difference in the summed areas (scaled via equation 2.2 in order to remove its dependency from the difference in weight between the sample and the reference material) under all peaks present in each spectra is

proportional to the difference in analyte concentration. As this quantity is known for the reference sample, it can therefore be calculated for the unknown sample via equation 2.3.

Quantification of F abundances in the silicate glasses of chapters 4 and 5 was performed by using a richterite, which was known to contain 0.023 wt% (230 µg/g) of F (Pearson et al., 2003), as a reference sample. Due to the expected low concentration of F in the glasses, a single-pulse experiment was used (with a ¹⁹F radiofrequency nutation rate of $\nu_1 \approx 91$ kHz). All analyses were performed by the author of this thesis on a Bruker AVANCE III spectrometer equipped with a 14.1 T wide-bore magnet, with all parameters being as described in subsection 2.2.1.2, with the exception that signal averaging was performed for 72000 transients (equivalent to ca. 20 h for each acquisition). The shorter duration of each experiment was due to the necessity of keeping the total analytical run time as low as possible while still detecting a signal, as all analyses needed to be performed in one single sequence to guarantee consistency in the background signal.

After collection, all spectra were fitted using gaussian line shapes and a second order polynomial function was fitted as a baseline with the lmfit Python open-source library. The integrated peak area was calculated with equation 2.1.

$$Area_{peak} = \frac{a * \sigma}{0.3989}$$

Equation 2.1: Formula used to calculate the integrated intensity of a gaussian (normal) function; a = amplitude, σ = standard deviation.

The signal collected from each sample was scaled according to its mass relative to the mass of the reference material using equation 2.2.

$$Scaled\ Area_{sample} = \frac{Weight_{reference}}{Weight_{sample}} * Calculated\ Area_{sample}$$

Equation 2.2: Formula used to scale the calculated peak area (see Eqn. 2.1) in the MAS NMR spectra of the glass samples based on its mass relative to that of the reference material.

The F concentration was then calculated using equation 2.3. The fitting process was repeated 9 times for each spectrum, the mean values for amplitude and standard deviation were computed and used to calculate the integrated peak intensity. The extremes of the intervals were used to calculate the error margin on peak area, which was then propagated as an uncertainty in the F concentration of the samples.

$$F_{reference} : F_{sample} = Area_{reference} : Area_{sample}$$



$$F_{sample} = \frac{F_{reference} (\mu g/g) * Scaled\ Area_{sample}}{Area_{reference}} (\mu g/g)$$

Equation 2.3: Proportion and formula used to calculate the F abundance in glasses (F_{sample}) from this study based on integrated peak intensities. $F_{reference}$ = F abundance in the reference material.

2.2.1.4 – F speciation and F/OH quantification in humite

group minerals via ^{19}F MAS NMR.

^{19}F MAS NMR were collected on a Bruker AVANCE III spectrometer equipped with a 14.1 T wide-bore magnet at the University of St Andrews, with the exception of sample C3095, which was previously studied (using the same spectrometer) by Griffin et al. (2010). Spectra for F speciation analyses were collected by the author of this thesis, spectra for F/OH quantification by Dr. Daniel Dawson, and the spectrum for sample C3095 was collected by Prof. Sharon Ashbrook.

Samples were packed into a standard ZrO_2 1.9 mm rotor and rotated at the magic angle at a rate of 30 kHz. Due to the presence of F in stoichiometric abundance in all analysed samples, a single pulse experiment was used without any need for background suppression. Spectra were acquired by averaging 16 transients with a recycle interval of 30 s (total experiment time of 8 min), using a ^{19}F radiofrequency nutation rate of $n_1 \approx 83$ kHz. Chemical shifts are reported in ppm relative to CFCl_3 using poly(tetrafluoroethylene) (PTFE, $d_{\text{F}} = -122.7$ ppm) as a secondary solid reference. Peak fitting and integration were performed using the DMfit software (Massiot et al., 2002).

F/OH fraction quantification was performed via collecting a ^{19}F MAS NMR spectrum from each sample and then comparing the signal intensity in each spectrum to the signal acquired from a sample with known F/OH fraction. This procedure relies on the assumption that all F/OH sites in the samples were filled by either F or OH. Considering that no other elements that could have entered

these sites were present in the system during synthesis, this assumption was considered valid.

Reference material chosen for F quantification was a natural Ti-clinohumite, which had a F/OH fraction of 0.48 (Griffin et al., 2010). After spectral acquisition and integration, the combined intensity of the four signals in each spectrum was calculated and scaled according to the weight of the sample studied relative to the reference material using equation 2.4.

$$Scaled\ Area_{sample} = \frac{Weight_{reference}}{Weight_{sample}} \times Unscaled\ Area_{sample}$$

Equation 2.4: Formula used to scale the peak area calculated in the spectrum based on the sample weight relative to the weight of the reference material. Unscaled Area is provided by the software dmfit (Massiot et al., 2002).

The F/OH fraction was then calculated using Equation 2.5.

$$F/OH_{reference} : F_{sample} = Area_{reference} : Area_{sample}$$



$$F/OH_{sample} = \frac{F/OH_{reference} \times Scaled\ Area_{sample}}{Area_{reference}}$$

Equation 2.5: Equation used to calculate the F/OH fraction in samples D1658, C4346, C4602 and CH001.

F/OH_{reference} = F/OH fraction in the reference.

A further scaling of the calculated F/OH fraction based on the phases present in each sample was applied, as the same F absolute content in different humite group minerals corresponds to a different F/OH fraction. This is because each humite group mineral has a different ratio of brucite layers to forsterite layers,

which in turn influences the absolute number of F/OH sites present in the framework per unit mass. For example, 1 mol of chondrodite and 1 mol of norbergite contain 1.828 and 3.120 times as many F/OH sites respectively as 1 mol of clinohumite. The scaling factor to compensate for this effect is thus 1.828 for sample C4602 (a pure chondrodite) and 1.983 for sample CH001 (a mixture of 88% chondrodite and 12% norbergite).

2.2.2 – Raman spectroscopy.

Raman spectroscopy exploits the Raman scattering effect (Raman, 1928), which consists of the inelastic scattering of photons when interacting with matter. When photons impact a target, a small fraction of the incident radiation is scattered: most of these scattered photons undergo elastic, or Rayleigh, scattering, in which the scattered photon has the same energy as the incident photons. A very minor fraction instead undergoes inelastic, or Raman, scattering, where the scattered photons have different energies when compared to the incident radiation (Hollas, 2002). During inelastic scattering, the incident photons trigger the temporary transition of the molecules to a virtual higher energy state, which immediately decays back to a lower-energy state, which in turn, due to the inelasticity of the scattering, will be different from the initial state (see Figure 2.11). This is because the system's total energy must be conserved, and thus the energy difference between the scattered and incident photons must be balanced by an energy difference in the state of the molecule. Changes in rotational and vibrational energies can be observed (with the latter used in this thesis) and are possible only when the rotation/vibration induces a change in the polarizability (Hollas,

2002). More specifically, if the energy difference between the scattered and incident photons is negative ($\Delta E = E_{\text{scattered}} - E_{\text{incident}} < 0$) then the phenomenon is referred to as Stokes scattering, while in the opposite case (i.e., $\Delta E = E_{\text{scattered}} - E_{\text{incident}} > 0$) as anti-Stokes scattering. For vibrational energy changes the Stokes lines usually have much greater intensity owing to the low population of the higher vibrational states.

Changes in the vibrational state of a bond are particularly evident in non-polar and mostly covalent bonds (e.g., N—N), as the polarizability change that ultimately results in the Raman effect is not substantially obscured by the bond's polarity. The opposite is instead true for highly polar and mostly ionic bonds (e.g., C—O), where the change in polarization has hardly any detectable impact on the bond's pre-existing polarization (McCreery, 2000).

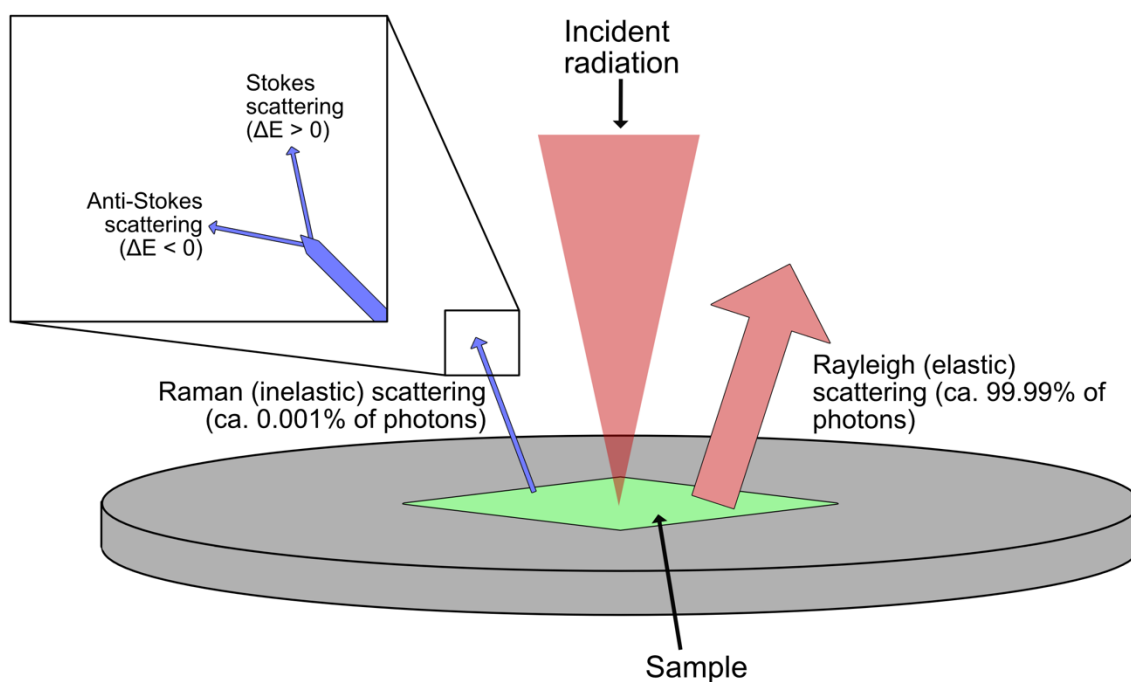


Figure 2.11: Simplified representation of the principle behind Raman spectroscopy. The incident radiation is scattered by the target through both elastic and inelastic scattering, with the latter radiation being the object of the Raman effect.

A typical Raman spectrometer targets a sample with radiation, usually from a visible light laser, although lower (e.g., IR) or higher (e.g., UV) frequencies are occasionally used. The scattered radiation is then detected, and the resulting Raman spectrum (see Figure 2.12 for an example) plots scattering intensity as a function of energy (in units of cm^{-1} in Figure 2.12), with the signal positions termed the “Raman shift”. The Raman shift indicates the types of bond present in the sample. As a whole, the Raman spectrum can be considered as a “chemical fingerprint” and therefore used for phase identification. Furthermore, investigation of specific peaks in the Raman spectrum can produce more detailed information

about certain characteristics (e.g., types of bonding or interatomic distance) of the associated atoms (McCreery, 2000).

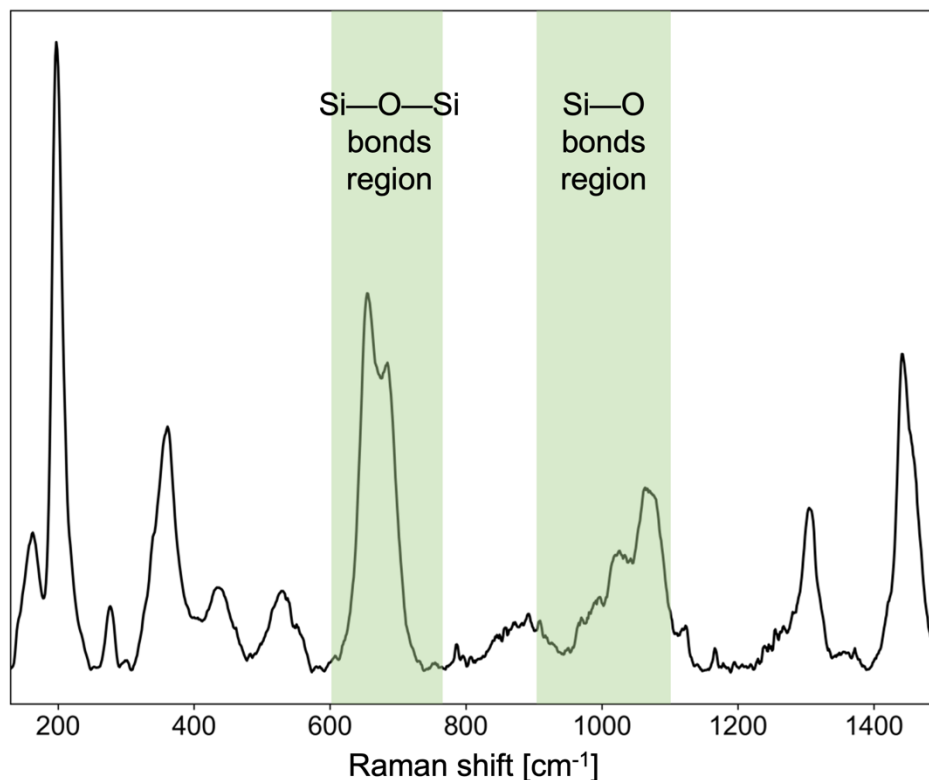


Figure 2.12: Raman spectrum collected from a natural phlogopite ($\text{KMg}_3\text{AlSi}_3\text{O}_{10}(\text{F},\text{OH})_2$), which was used as a standard material for NMR analysis. Each peak can be attributed to a specific type of bonding interaction in the mineral's framework (e.g., Si—O and Si—O—Si, evidenced in spectrum by peaks in the 1100-900 cm^{-1} and 750-600 cm^{-1} regions respectively).

Raman spectroscopy in this thesis was used for three purposes: [1] investigation of nitrogen speciation in the silicate glasses of chapter 3, [2] identification of changes in the coordination state of the major elements of silicate glasses with low NMR sensitivity (e.g., Mg, Al) in the high pressure silicate glasses of chapter 5, and [3] phase identification and quantification of humite

group mineral sample CH001 of chapter 6. The following subsections describe the specific set-ups used for each type of analysis.

2.2.2.1 – Raman spectroscopy of N-enriched silicate

glasses.

All Raman spectra were collected on a LabRAM HR800 Raman microscope using ultra-violet (325 nm) and visible (514 nm) light lasers at the Drochaid facility of the University of St Andrews, by the author of this thesis under supervision of Dr. Paul Webb. The laser beams were focused on the powdered glass samples through a 50× (for visible) or 15× (for UV) microscope objective lens. A large fluorescence background was present, hence the signals, collected in air, in the 2100-2500 cm^{-1} and 2800-4000 cm^{-1} regions of each spectrum were collected separately. This was to target the peaks related to the N—N and N—H bonds, respectively, in isolation. The baseline fitting was performed with a spline function following the procedure described in Dalou et al. (2019), via the rampy Python open-source library.

2.2.2.2 – Raman spectroscopy of high pressure F-enriched

silicate glasses.

Raman analyses were performed on one of the high pressure glasses produced via multi anvil annealing (sample BayF_04) and on the starting glass for the annealing experiments (see subsection 2.1.2.5), to determine if any micro- to nano-crystalline phases are present. Spectra were collected using a Renishaw

inVia Raman microscope with a visible (514 nm) light laser at the School of Chemistry, University of St Andrews, by Dr. David Miller. The laser beams were focused on the powdered glass samples through a 50× objective lens. Signal was collected in air, and only over the 100 to 1800 cm^{-1} region of the spectrum, as this was deemed sufficient to determine the presence of any major crystalline phases (i.e., silicates, carbonates, and fluorides). Spectra were processed using the rampy Python library with no baseline fitting.

2.2.2.3 – Phase identification and quantification in humite group minerals.

Analyses were performed using a Renishaw inVia Raman microscope using a visible (514 nm) light laser at the School of Chemistry of the University of St Andrews, by the author of this thesis under the supervision of Dr. David Miller. The laser beams were focused on the powdered samples through a ×30 objective lens. Signal was collected in the 100 to 3200 cm^{-1} region of the spectrum. The spectrum was plotted via the rampy Python library, a fifth-order polynomial baseline fitting was performed.

Phase quantification procedure, developed specifically for this thesis, was based on a comparison of the Raman spectrum of the unknown sample with Raman spectra from known reference samples (Frost et al., 2007), collected via an analogous analytical setting. A custom algorithm was built based on the lmfit python library and was used to fit the peak feature(s) in the 700 to 900 cm^{-1} region of the spectra. This region was chosen as it is influenced solely by the bending of Si—O bonds in the silicate tetrahedra of the forsterite layers, and the peaks

present are diagnostic of each humite group mineral (see Figure 2.13; Frost et al., 2007). This guarantees that the F/OH fraction of both the reference material and the unknown sample has no impact on the phase quantification procedure, as F does not take part in the Si—O bonds in the forsterite layers of humite group minerals.

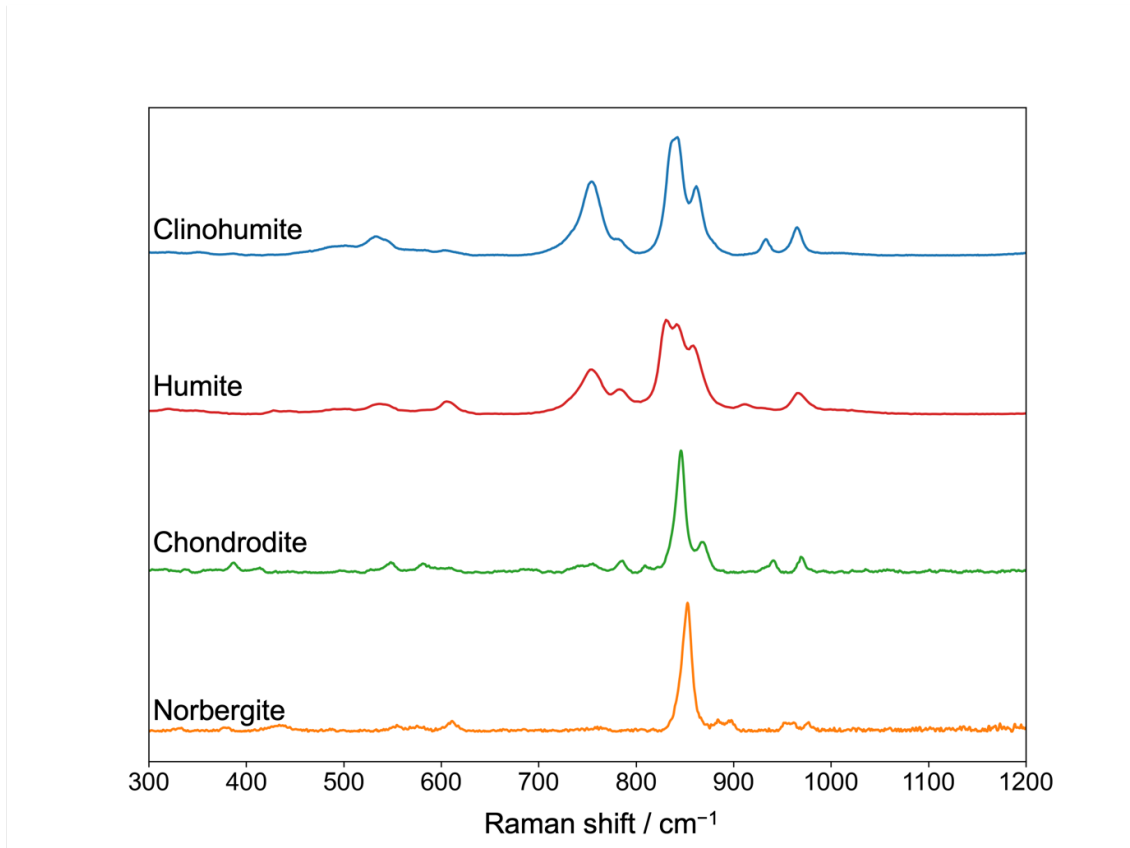


Figure 2.13: Raman spectra of humite group minerals (samples from the University of Arizona Mineral Museum; data from Frost et al., 2007, replotted for this figure).

2.2.3 – Electron Probe Micro Analysis (EPMA).

EPMA is a type of electron microscopy. The concept of utilising a focused electron (e^-) beam as a means for investigating solid matter has been well established since the early 1920's (Rudenberg & Rudenberg, 2010). The impact of e^- with the sample causes the emission of various forms of radiation, including X-rays, visible light, and further e^- , alongside transmission or scattering of the incident e^- themselves (see Figure 2.14). These phenomena can then be studied for different purposes (e.g., chemical analysis, imaging). Typically, different apparatuses are used to investigate different features, although usually some overlap between the capabilities of different systems exists.

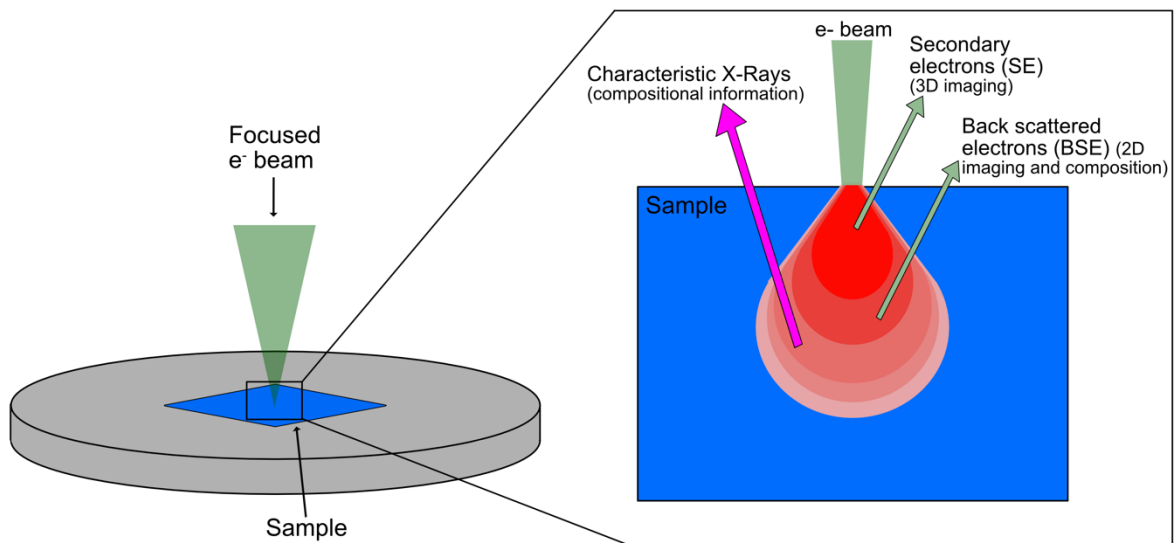


Figure 2.14: Schematic of a simplified representation of a focused electron beam impacting a conductive material. The electrons cause different effects in the sample depending on the depth at which the interaction takes place, resulting in a geometry sometimes referred to as an “electron pear” (in shades of red). For the sake of simplicity, only the effects mentioned in this thesis are reported.

The electron beam is generated using an electron gun (e.g., a W filament through which a current is passed), and then focused via the use of magnetic lenses. The electrons penetrate the sample until they impact with the atoms. This will occur at different depths, and results in different particles or radiation being emitted from the sample (Goldstein et al., 2018). Due to the peculiar shape of the depth profile traced by the e^- within the sample, this phenomenon is sometimes referred to as an “electron pear”. Different components of the electron pear, when detected, provide information on the various features of the sample (e.g., surface morphology, structural characteristics, chemical composition). Different analytical instruments are optimized in design to study different types of radiation and/or particles emitted by the sample.

For EPMA analysis, the sample needs to be able to conduct electrons: due to the naturally low electrical conductivity of the glasses and minerals investigated for this thesis, coating with a conductive layer (e.g., graphite, Au) was necessary.

EPMA instruments are equipped with a Wavelength Dispersion System (WDS) detector. This device allows for a high precision and low signal-to-noise ratio of characteristic X-rays and, when the detected signal is calibrated against a known reference, it can be used for quantification purposes. Detection limits depend largely on the experimental setup and the element analysed: it typically is on the order of hundreds of $\mu\text{g/g}$, although in optimal conditions this can be as low as $\sim 10 \mu\text{g/g}$.

EPMA instruments are designed primarily for chemical analysis, therefore they are not optimized for sample imaging. In practice, this translates to the impossibility of collecting 3D images, alongside lower quality 2D imaging

capabilities when compared to other electron microscopy techniques (e.g., Scanning Electron Microscopy, SEM). However, due to the morphological simplicity of the silicate glasses studied for this thesis, EPMA pictures were deemed of sufficient quality. As a result, the EPMA was used for both chemical analysis and imaging for all glass samples of chapter 3, 4 and 5.

Due to the limitations to travel and laboratory use in place while carrying out the analyses for this thesis, caused by the covid-19 pandemic, each set of glasses was studied on different machines, each managed by different operators, resulting in widely varying set-ups. Each set of analyses is thus described in its own subsection in the following pages.

2.2.3.1 – EPMA of N-enriched silicate glasses.

Major elemental analysis for all samples was performed by Dr. Eleanor Mare with a Cameca SX100 device at the University of Cambridge, operating at 15 kV with a 6 nA beam current and 10 μm beam diameter. All elements were analysed at their $K\alpha$ lines, with an LTAP crystal used for Mg, PET used for Ca, LPET for Cl, and TAP for Si and Al as reference. Calibration standards were diopside for Ca and Si, halite for Cl, corundum for Al and St. John's olivine for Mg, with oxygen added by difference. Sample glass chips were mounted in cylindrical epoxy resin mounts, polished at the μm scale and coated in Au to allow for e^- conduction across the sample.

The N abundance for all samples was analysed by Dr. Eleanor Mare at the Australian National University, Centre for Advanced Microscopy, using a JEOL 8530F Plus Electron Probe Micro Analyser, equipped with a Field Emission Gun

(FEG) electron source. The N analyses were conducted at 10 kV and 100 nA with a 40 μm beam diameter, at the $K\alpha$ line of N using a LDE1H crystal. GaN was used as a primary standard. Signal was collected for 120 s at the N peak position, and 60 s at each of four background positions. Four measurements were used to correct for the curved background around the region of the N peak. A Lorentzian lineshape was used to fit these four points, based on a wavelength scan obtained from sample Edi04. An 'area-peak factor' (APF) correction (Bastin and Heijligers, 1991) was applied based on the differences in the peak shape between GaN and a hydrous rhyolitic glass synthesised by Mallik et al. (2018). The N peak was also analysed at a slight offset from the GaN peak position, based on previous experience of the operator performing the analysis (145.250 vs 145.839 for GaN).

Background and APF corrections were applied to the raw data to generate a corrected k-ratio. The raw signal was then processed with the CalcZAF software, assuming major elements (excluding H) as fixed based on their analysis at 15 kV. N concentration was calculated by assuming full N_2 speciation, with H added by difference (as H_2O). This assumption was motivated by the fact that even if N was partially speciated as $(\text{NH}_4)_2\text{O}$ or similar species, the impact on the result would be negligible. N concentrations were then added to the major element compositions measured at the University of Cambridge.

2.2.3.2 – EPMA of low P F-enriched silicate glasses.

The major element geochemistry of the glasses was quantified using a JEOL 8100 Superprobe EPMA located at the Institute of Mineralogy and Petrology of the University of Innsbruck, by Dr. Bastian Joachim-Mrosko and Dr. Jürgen

Konzett. The acceleration voltage and beam current were 15 kV and 10 nA, respectively, with the electron beam operated in raster mode (raster size of $\sim 12 \times 7 \mu\text{m}$). Sample glass chips were mounted in cylindrical epoxy resin mounts, polished at the μm scale and coated in graphite. The following standards were used: synthetic oxides (Si, Al, Mg), and diopside (Ca). Raw X-ray counts were converted to element concentrations using the PRZ correction procedure. Fluorine was measured using a second step with the LDE1 crystal, where the averaged glass compositions was employed for matrix corrections. For fluorine, acceleration voltage and beam current were 15 kV and 100 nA, respectively, with the electron beam operated in raster mode (raster size of $\sim 12 \times 7 \mu\text{m}$). The measurement times coincided with peaks and backgrounds for the F K_{α} -line at 200 and 100 s, respectively. Background positions were selected based on the analysis of a synthetic glass in the system $\text{CaO-MgO-Al}_2\text{O}_3\text{-SiO}_2$ containing $\sim 3000 \mu\text{g/g}$ F. Natural F-bearing topaz was used as a standard material. This set of analytical conditions results in a detection limit of around $134 \mu\text{g/g}$. Backscattered electrons imaging of the glasses before and after the F-analyses did not yield any evidence for significant beam damage to the sample surface. For samples EdiF_MAS1 and EdiF_2h a total of 5 analyses per sample were performed to demonstrate sample homogeneity, while for all other samples 4 analyses each were deemed sufficient to guarantee the desired precision.

2.2.3.3 – EPMA of high P F-enriched silicate glasses.

Major element geochemistry of the analysed glass was quantified using a JEOL JXA-8200 EPMA located at the Bayerisches Geoinstitut of the University of

Bayreuth by Caterina Melai. The glass was mounted in a cylindrical epoxy resin mount, polished at the μm scale and coated in graphite. The acceleration voltage and beam current were 15 kV and 15 nA, respectively. The following standards were used: diopside (Ca, Si), enstatite (Mg) and spinel (Al), synthetic Fe_2O_3 (O) and LiF (F). Raw X-ray counts were converted to element concentrations using the ZAF correction procedure. This set of analytical conditions results in a detection limit of $\sim 200 \mu\text{g/g}$ for fluorine. Backscattered electron imaging of the glass before and after the analyses (see Figure 2.15) did not yield any evidence for significant beam damage to the sample surface. A total of 108 data points were analysed on the surface of the sample distributed along two parallel lines (see Figure 2.15), and the abundance of each element was determined from the average at each point. This set up enabled a precise quantification of all the major constituents of the glass (i.e., Ca, Mg, Al, Si, O), while F was found to always be below the detection limit of $200 \mu\text{g/g}$.

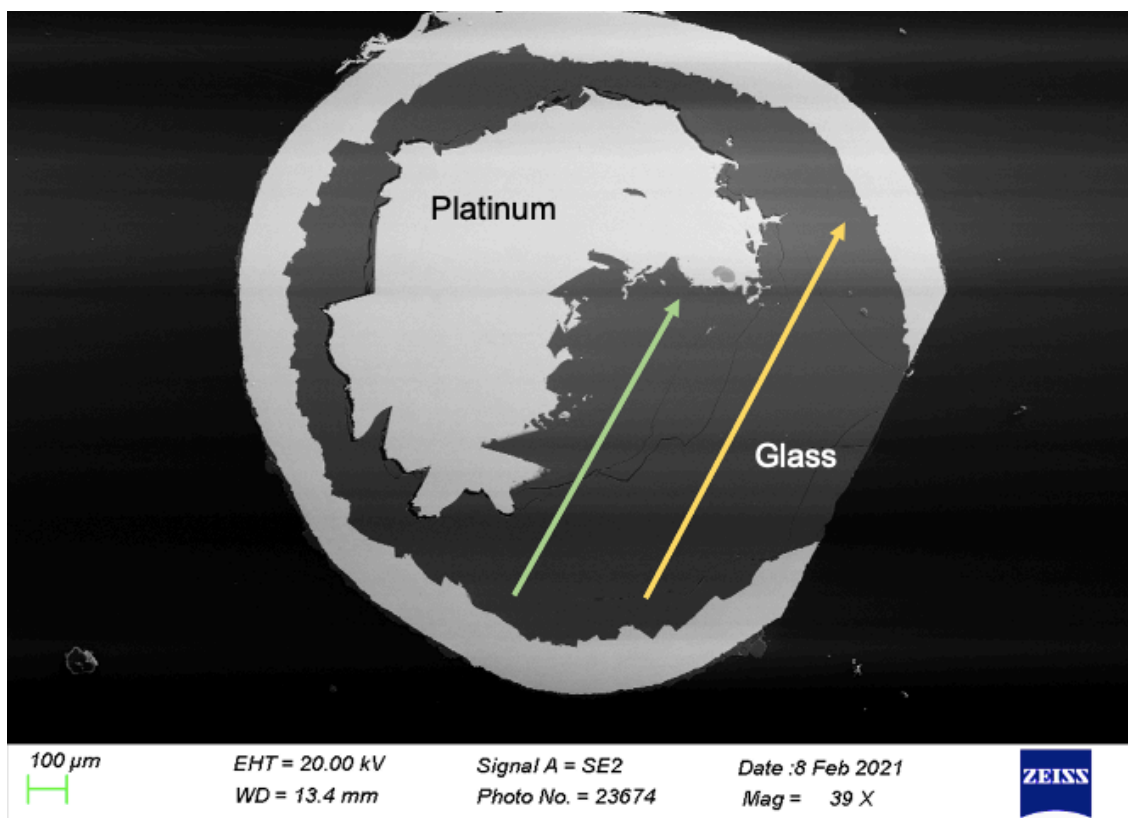


Figure 2.15: BSE image of sample BayF_01. The lines along which chemical analysis were performed are represented by the green and yellow arrows.

2.2.4 – Sensitive High-Resolution Ion Micro Probe (SHRIMP).

SHRIMP is a mass spectrometry technique. Mass spectrometry is a set of analytical techniques which are used to measure the mass of the individual particles present in a chemical system. This can allow the accurate determination of the chemical abundance of the minor and trace elements present in a compound. In crystalline solids, this can be achieved by physically separating each atomic species (e.g., via high T combustion), then directing them towards a detector on different trajectories based on their atomic mass (e.g., via a magnetic

field). The detector then allows to determine how many particles of each mass were present in the system. These techniques can easily measure elements at concentrations <1 ppm and have the additional advantage over spectroscopic techniques of being able to measure the concentration of individual isotopes, as they rely on atomic mass and not on the electron cloud to determine the nature of an atom. Due to the limited use made of mass spectrometry in this thesis, a more in depth description of its functioning was deemed unnecessary.

SHRIMP utilises a beam of accelerated ions focused on a sample's surface to remove a small portion of its atomic constituents in a process named sputtering. In order for this process to be effective, the sample needs to be electrically conductive. SHRIMP was utilised in this study to measure ^{15}N abundance in samples Edi01, Edi02 and Edi04 of chapter 3 (other elements were also measured for scopes outside of this thesis). All analyses were performed by Dr. Eleanor Mare at Australian National University (ANU). Glass chips from the samples were coated with a 50 nm Au layer. An O^{2+} primary beam was used (22 μm diameter, 3 nA) to sputter secondary ions, resulting in ~ 1 μm of material removed from the surface. Each analysis consisted of a 2.5 min raster followed by four cycles through five masses: $^{12}\text{C}^+$ for 5 s, $^{14}\text{Si}^{2+}$ for 5 s, $^{14}\text{N}^+$ for 30 s, $^{15}\text{N}^+$ for 30 s, $^{16}\text{O}^+$ for 1 s and $^{28}\text{Si}^+$ for 1 s. Data reduction involved averaging the four cycles for each analysis and rejecting any analyses where recorded beam currents were above 3.5 nA or below 2.5 nA.

2.2.5 – Data processing.

The analytical instruments used for the work presented in this thesis produced data in two formats: raster (i.e., a pixel matrix) EPMA, or as a spectrum (i.e., a 2D data table), for Raman, EPMA, SHRIMP and NMR spectroscopy measurements.

Data processing and background correction were performed either via the open-source programming language Python or via dedicated software: EPMA and Raman data were processed with the SciPy and Rumpy Python libraries respectively, while NMR data were processed with the TopSpin 4 software. Plotting of data was always performed via the matplotlib Python library. Peak fitting for Raman and ^{15}N NMR spectra was performed with the lmfit Python library, while the DMfit software (Massiot et al., 2002) was used for ^{19}F NMR spectra.

Graphic design and the production of figures was predominantly performed with the Affinity Designer software, although occasionally Microsoft PowerPoint was used for basic tasks. With the same rationale, basic operations on data tables were performed via Microsoft Excel.

2.2.6 – Density Functional Theory (DFT).

DFT is a theory utilised to calculate the electronic structure and properties of multi-atomic systems such as molecules or crystalline solids (Kurth et al., 2005). This is done via applying the Hohenberg-Kohn and Kohn-Sham theorems to solve the Schrodinger equation and thus to determine the true electron density of the ground state of a structure (Rindt & Gaastra-Nedea, 2015), thus allowing to

calculate all its properties dependent on it (e.g., potential energy). Due to the limited use made of DFT for this thesis, an extensive dissertation on the theory on which DFT is based on was deemed unnecessary. The following paragraphs present the specific applications of DFT within the context of this thesis.

DFT is often used to calculate the chemical shift associated to chemical species in an NMR spectrum, as this is primarily influenced by the electron distribution around the analysed nucleus. This aids in the assigning each peak to a specific bonding environment, and in understanding how changes to the local bonding environment of an atom in a structure might be represented by the NMR spectrum. For this thesis, this was done to identify the chemical shift of ^{15}N species in the spectra collected from the N-enriched silicate glasses of chapter 3. All computations were performed at the B3LYP/6-311+G(2d,p) theory level using the GAUSSIAN 09 revision D.01 program (GAUSSIAN 09 D.01, 2013), which is based on the NBO algorithm (Carpenter, 1987). Calculations were performed by Dr. Daniel Dawson on an individual 32-core Intel Broadwell node of the University of St Andrews computing cluster. Computed magnetic shieldings (s_{iso}) were converted to computed chemical shifts (d_{iso}) using $d_{\text{iso}} = s_{\text{ref}} - s_{\text{iso}}$, with $s_{\text{ref}} = 233.2354$ ppm, determined by setting d_{iso} of NH_4^+ to 0.0 ppm.

Another common use of DFT is to determine the changes in potential energy caused by atomic substitutions in a structure. This was used in this thesis to determine the theoretical most stable configuration of F and OH in the humite group minerals of chapter 6. More specifically, DFT+D calculations (CASTEP 19.11, PBE with a TS dispersion correction) were carried out to calculate the mixing enthalpies relative to the two end members (fully hydroxylated and fully

fluorinated) of a clinohumite structure. Two F atoms were substituted into a fully hydroxylated $2 \times 1 \times 1$ supercell of clinohumite (with 50% of H placed on site H1 and 50% on site H2 to give fully ordered H-bonded pairs), and the resulting mixing enthalpies were calculated. The same calculation was also performed in reverse, i.e., by introducing two OH groups into a fully fluorinated $2 \times 1 \times 1$ supercell of clinohumite. All calculations were performed by Prof. Sharon Ashbrook on an individual 32-core Intel Broadwell node of the University of St Andrews computing cluster.

~3 — INVESTIGATION OF NITROGEN

SPECIATION IN CMAS SILICATE MELTS

USING ¹⁵N MAS NMR~

3.1 – INTRODUCTION

3.1.1 – Nitrogen speciation in silicate melts and phases.

Silicate melts appear to feature two main local bonding environments: molecular nitrogen, N₂, and ammoniac nitrogen species, N—H. The latter is a family of species based on 1 N atom bonding with 1 to 4 H atoms, mostly consisting of NH₃ and NH₄⁺ (Busigny & Bebout, 2013). This duality of species perfectly conveys the importance of oxygen fugacity for N speciation (see Table 3.1). As the third most electronegative element in the periodic table, nitrogen exhibits a strong affinity for H, hence the existence of N—H species. However, a critical obstacle in the path towards these the formation of these species is O, which is the second most electronegative element on the periodic table. As one of the most abundant elements on Earth, O is thus the preferential bonding partner for H, leading to the formation of H₂O and OH⁻ dissolved in the structure of the melt, with N subsequently speciating as N₂ (Mysen, 2018). It follows that the only

conditions under which N—H species are formed would be at oxygen fugacity low enough to saturate all free O^{2-} ions with H^+ while still leaving some of the latter free to bind with N atoms. Such an eventuality would occur only below the IW fO_2 buffer (Armstrong et al., 2015), at strongly reducing conditions, which might have been far more common in the mantle during the planet's early history compared to the modern relatively more oxidised mantle (Trail et al., 2011; Grewal et al., 2021).

The existence of other species has been postulated, as potential N—O species have also been potentially observed (Roskosz et al., 2006). The conditions leading to the stability of these species in the Earth's interior are presently unknown; however, it is worth pointing out that NO_x ions are a common occurrence in the atmosphere, biosphere, and hydrosphere, and in surficial geological deposits nitrite (NO_2^- -based) and nitrate (NO_3^- -based) salts are a relatively common occurrence (Thamdrup, 2012). It is thus not unreasonable to expect that exceedingly oxidizing conditions might also cause the stabilisation of N—O species in silicate melts, however once again experimental evidence is currently lacking. In addition, no region of the Earth's mantle is at a high enough oxygen fugacity to stabilise NO_x ions (Kasting et al., 1993; Birner et al., 2018).

One final species of interest is the nitride ion (N^{3-}): while this has never been directly observed in a melt phase, it is the N species featured in metal alloys (Yoshioka et al., 2018) and diamonds (Mikhail & Howell, 2016). The stable dissolution of single nitrogen atoms in the melt structure would intuitively require almost perfectly anhydrous conditions, as any hydrogen ion would bind with N to form ammoniacal species. It is perhaps worth pointing out that analogous

conditions occur also at relatively high fO_2 , where all H is sequestered by O^{2-} ions, yet this results in the formation of N_2 molecules, not N^{3-} ions (Dalou et al., 2019). Hence, it can be inferred that extremely reducing conditions would be required to stabilise this specie (i.e., $fO_2 < IW - 3$; Grewal et al., 2019). Such oxygen fugacity is unlikely to have existed in the Earth's upper mantle after the Hadean eon (Smart et al., 2016; Grewal et al., 2021). This, in turn, might suggest that the stable N speciation in the melt phase at equilibrium conditions might not correspond with the N speciation observed in crystallized phases. If this is true, understanding which conditions promote the transformation of one species into another becomes even more important, as it could unveil significant insight into volatile incorporation during magma cooling.

N species	Melt fO_2	Main mineral reservoirs
NO_x	$fO_2 \gg FMQ$	Nitrate and nitrite salts
N_2	$IW < fO_2 < FMQ$, $fO_2 > FMQ$	Cordierite, tourmaline, beryl
NH_x	$fO_2 < IW$	Feldspar, mica, pyroxene
N^{3-}	$fO_2 \ll IW$	Diamond, metal alloys

Table 3.1: Oxygen fugacity (fO_2) fields of stability and main mineral containers of the currently known N species in anhydrous silicate melts (Bebout et al., 2016; Mikhail & Howell, 2016; Grewal et al., 2020; Mosenfelder et al., 2019). FMQ = Fayalite-Magnetite-Quartz redox buffer, IW = Iron-Wustite redox buffer.

The following subsections contain a more detailed description of the behaviour of molecular and ammoniacal nitrogen in the deep Earth. It must be stressed that the speciation of nitrogen in C-O-H-N and similar fluids, both when equilibrated with silicate melts and/or phases, is also a relevant field of research (e.g., Halama et al., 2017; Li et al., 2015; Mikhail & Sverjensky, 2014; Mysen,

2018; Sokol et al., 2017). However, as the production of fluid phases in equilibrium with silicate melts was not the scope of this study, this will not be discussed further.

3.1.1.1 – Molecular nitrogen (N₂).

N₂ is a non-polar molecule consisting of two nitrogen atoms joined by a triple covalent bond. This results in an extremely stable and inert molecule that in all surficial and most near-surface environments can effectively be considered akin to a monoatomic species. More specifically, the length of the covalent bond is close to the diameter of the electron cloud of mid-sized noble gases (i.e., Kr and Ar).

As with the noble gases it closely resembles, N₂ is a highly incompatible species, with no common mineral phase being able to stably incorporate it (Bebout et al., 2013). One important exception is represented by microporous silicates (e.g., clathrates; Momma et al., 2011), whose crystal structure consists of silicate ions arranged in ring-like or cage-like structures, thus resulting in an environment able to host notable amounts of N₂ and other neutral species (Armbruster, 1985).

The only microporous silicate sufficiently abundant in the crust to be a relevant N₂ container is cordierite, which is a significant component of metapelitic rocks in the shallow to mid-depth continental crust. N abundance in this mineral can reach upwards of 300-400 µg/g in HP metamorphic environments, while in pegmatitic and igneous settings cordierite generally contains less than 100 µg/g (Bebout et al., 2016; Lazzeri, 2012). Other phases such as beryl and tourmaline

can also contain similar amounts of N_2 , however their minor crustal abundance limits their importance as N crustal reservoirs (Bebout et al., 2016).

3.1.1.2 – Ammoniacal nitrogen (N—H).

Ammoniacal nitrogen species are the dominant N-bearing complexes in anhydrous silicate melts at fO_2 lower than IW (Dalou et al., 2019; Armstrong et al., 2015). Two main species are known, NH_3 and NH_4^+ , the former being of interest mostly for melt and fluid phases (Mikhail et al., 2017), while the latter is also suitable for incorporation in mineral phases (Li et al., 2013). NH_4^+ is a tetrahedral cation with an ionic radius of 175 pm, which alongside its charge of +1 makes it similar to the larger alkali elements/metals such as Rb^+ and Cs^+ (ionic radii of 152 and 167 pm respectively). Due to the inherent difference in structure between monoatomic cations and a tetrahedral cation with a strong negative charge in the centre, the ionic radius of NH_4^+ is likely to decrease more rapidly with increasing pressure (i.e., in deeper geological environments) than the alkali metals, thus impacting its partitioning coefficient as a function of P (Li et al., 2013).

The ammonium ion is typically found substituting for K^+ in mineral phases such as biotite ($K(Mg,Fe)_3(AlSi_3O_{10})(F,OH)_2$) and K-feldspar ($KAlSi_3O_8$) in the 1000s of $\mu g/g$ (Hall, 1999). However, it can also be incorporated into major upper mantle minerals such as clinopyroxene (Watenphul et al., 2010) and olivine (Li et al., 2013), and in lower mantle phases such as bridgmanite (Yoshioka et al., 2018).

One crucial caveat to the solubility limits discussed thus far is that while experimental studies have shown that N solubility in major upper mantle phases

can reach upwards of 100s of $\mu\text{g/g}$ (e.g., Li et al., 2013; Watenphul et al, 2010), this does not imply that conditions during the formation of these minerals effectively allowed for such concentrations to be reached. In other words, if oxygen fugacity was not low enough to guarantee N—H stability in the coexisting melt, certain potential N reservoirs in the deep Earth might not be N saturated.

3.1.2 – Analytical challenges in measuring N speciation.

The detection of different N species, particularly when coexisting, is a challenging endeavour. The most commonly used techniques to study an element's speciation are usually IR and Raman spectroscopy; however, each approach individually is not sufficient for nitrogen speciation analysis. This is because the two main N species (i.e., N_2 and N—H) are profoundly different, as the N—N non-polar covalent bond is Raman active but IR inactive, while the opposite is true for the strongly polar N—H bond (McCreery, 2000). A possible solution is the use of both techniques in tandem (e.g., Grewal et al., 2020) - however this introduces uncertainties in contexts where dual speciation is observed, as the two species would be detected by two different analyses, thus introducing uncertainty in absolute measurements. Furthermore, silicate glasses tend to produce strong fluorescence effects, especially when targeted by relatively high frequency radiation (e.g., the visible lasers used for Raman spectroscopy), and this considerably decreases the signal to noise ratio (e.g., Dalou et al., 2019; this study).

Another possible approach is the use of solid-state NMR spectroscopy. This technique can, in principle, easily detect ammoniacal and molecular nitrogen at the same time and has the further potential advantage of discriminating between different ammoniacal species (i.e., NH_3 , NH_4^+ , NH_2^- , NH^{2-}), a feat that is not easy to perform with IR or Raman spectroscopy. In addition, as NMR is element specific this allows the reduction of ambiguity during spectral interpretation. Nevertheless, the use of NMR spectroscopy introduces different challenges altogether. Firstly, ^{14}N , the overwhelmingly more naturally abundant N isotope (i.e., 99.632(7)% of all N; Meija, 2015), has a nuclear spin quantum number I of 1, and so spectra can be subject to significant spectral quadrupolar broadening hindering experimental acquisition in many cases (Mills, 1988). The solution is to measure the signal produced by ^{15}N instead (0.368(7)% of all N), which has a nuclear spin quantum number $I = 1/2$, and thus is easier to study experimentally. This is, however, counterbalanced by its abundance often being too low for detection at natural abundance levels, as N occurs as a trace element in silicate melts (Johnson & Goldblatt, 2015). This makes solid-state NMR unsuitable for the study of most natural materials, and effective only for the study of synthetic ^{15}N -enriched samples. One further obstacle is represented by oxygen fugacity buffering during sample synthesis: the IW redox buffer consists of the redox equilibrium reaction between Fe and FeO in an outer capsule surrounding the sample-bearing capsule. This, however, negatively impacts sample weight, which is already very low for high P samples (i.e., not more than 50 mg for a piston cylinder synthesized sample). Furthermore, contamination by strongly magnetic elements such as Fe can cause significant peak broadening in the NMR

spectrum, which adds to the already significant broadening effect of the amorphous structure of silicate melts and hinders the extraction of quantitative information. Consequently, care must be taken in sample preparation, as any Fe contamination of the inner capsule risks spoiling the experimental spectrum.

As just mentioned, the small sample size produced by high P apparatuses poses a logistical challenge, however this is even more problematic when the abundance of N and fO_2 measurement are considered. Both these analyses are usually performed by cutting the sample-containing capsule in half, mounting this half in epoxy resin, and subsequently analysing the sample using EPMA for both N abundance and oxygen saturation of the redox buffer. In addition, this allows the presence of a single-phase glass, with no crystalline phases, to be verified. This has the adverse effect, however, of halving the sample size, thus further reducing the already small sample weight available for NMR analyses, as a powdered sample is required for this approach. A possible solution to this is to open the capsule after the experiment instead of cutting into two, which enables the recovery of the glass in chips, some of which can then be mounted in resin for chemical analysis while the remainder can be powdered for NMR analysis, thus minimizing the sample loss. This approach, however, is only applicable for non-redox buffered experiments, as the content of the buffer-bearing outer capsule would mix with the glass-bearing inner capsule during the opening process. Also, this would impede any chemical analysis of the buffer on its own, which is imperative to verify if the redox reaction took place as expected.

In conclusion, both NMR and Raman/IR spectroscopy present their own sets of challenges, which must be accounted for when choosing the technique(s)

to use. This in turn suggests that an integrated approach (e.g., Roskosz et al., 2006) could also be a solution, with only some samples being ^{15}N enriched for NMR analytical purposes, while the rest being studied solely via Raman/IR spectroscopy.

3.1.3 – Scope of this study.

The initial aim of this study was to investigate N speciation in silicate melts as a function of $f\text{O}_2$, with the main target being to constrain the $f\text{O}_2$ at which ammoniacal and molecular nitrogen coexist in a silicate melt. This was in order to understand if such conditions are still met in the deep Earth, especially near the subduction zones where partial melting is critical in determining if N is either degassed by arc volcanism or retained in the mantle wedge. After the first samples were synthesized, however, the analytical hurdles discussed in section 3.1.2 became clear. Hence, the study was refocused on analytical procedure development, as a widely accepted strategy for ^{15}N analysis in silicate melts via MAS NMR does not exist at present.

Two sets of two silicate melts each were synthesized: the starting composition was kept the same for all except for the nitrogen source ($^{15}\text{NH}_4$, $^{15}\text{NO}_3$ and $^{15}\text{NH}_4\text{Cl}$ for each set) and for the addition of Si metal (reducing agent) to one sample for each set. More specifically, Si metal might be expected to lower the $f\text{O}_2$ of the system by forming SiO_4^- ions (i.e., binding to oxygen atoms) during its dissolution in the melt phase. When the nitrogen source is $^{15}\text{NH}_4^{15}\text{NO}_3$ this adds 3 moles of oxygen to the melt per each mole of $^{15}\text{NH}_4^{15}\text{NO}_3$. In contrast, $^{15}\text{NH}_4\text{Cl}$ is oxygen free, therefore it is reducing when compared to the nitrate. Both

strategies were in order to prompt a speciation change. The composition of all glasses was chosen as CMAS7G (O'Neill & Eggins, 2002), as this is an intermediate relatively Mg-poor and Fe-free composition (see Table 3.2). This latter feature is essential, due to the necessity to avoid paramagnetic elements in NMR analysis (see also section 2.2.1). Moreover, CMAS7G also has a relatively low melting point of 1129 °C at 1 atm (O'Neill & Eggins, 2002), and hence relatively lower temperatures were required for sample synthesis.

CMAS7G	Abundance (wt%)	Abundance (mol%)
CaO	25.22	27.63
MgO	2.39	3.64
Al₂O₃	12.61	7.60
SiO₂	59.78	61.13

Table 3.2: Composition in oxides of the CMAS7G starting material (O'Neill & Eggins, 2002).

The speciation was first studied by ¹⁵N MAS NMR spectroscopy, and later Raman analyses were also performed to enable a comparison of results from the different techniques. Major elements and N abundances were firstly investigated by EPMA. However, once again issues arose due to the relatively low N sensitivity of this technique, and thus the more precise (Ireland et al., 2008) Sensitive High Resolution Ion Micro Probe (SHRIMP) was also used.

3.2 – METHODS SUMMARY

Two sets of two silicate melts each were synthesized, following the procedure described in subsections 2.1.2.2 and 2.1.2.3. The starting composition was kept the same for all except for the nitrogen source and for the addition of Si metal (reducing agent) to one sample for each set (see Table 2.5).

Glasses were then analysed via EPMA to determine their major elements composition, to attain equilibrium and to determine N concentration (see subsection 2.2.3.1). Due to the low N concentrations measured, these were later measured via SHRIMP (see section 2.2.4). N speciation in all glasses was analysed via ^{15}N MAS NMR (see subsection 2.2.1.1) and Raman spectroscopy (see subsection 2.2.2.1). DFT calculations were also performed to aid in the assignment of peaks in the NMR spectra to the respective species (see section 2.2.6).

Results of all analyses are presented in the subchapter 3.3, while all discussion and interpretation are in subchapter 3.4.

3.3 – RESULTS

3.3.1 – Structural and compositional information.

3.3.1.1 – Glass homogeneity.

All samples when removed from the capsules appeared as a clear transparent glass. Glass chips from all samples were also studied via back-scattered electron (BSE) imaging to confirm this. Samples Edi01, Edi02 and Edi04 all consisted of a single-phase homogeneous glass with no evidence of crystallinity (see Figure 3.1), while sample Edi03 instead also contained a range of evenly dispersed μ -sized quench bubbles (see Figure 3.2). Moreover, some lighter coloured areas are also present in this sample, suggesting some level of heterogeneity, possibly also due to the quench process.

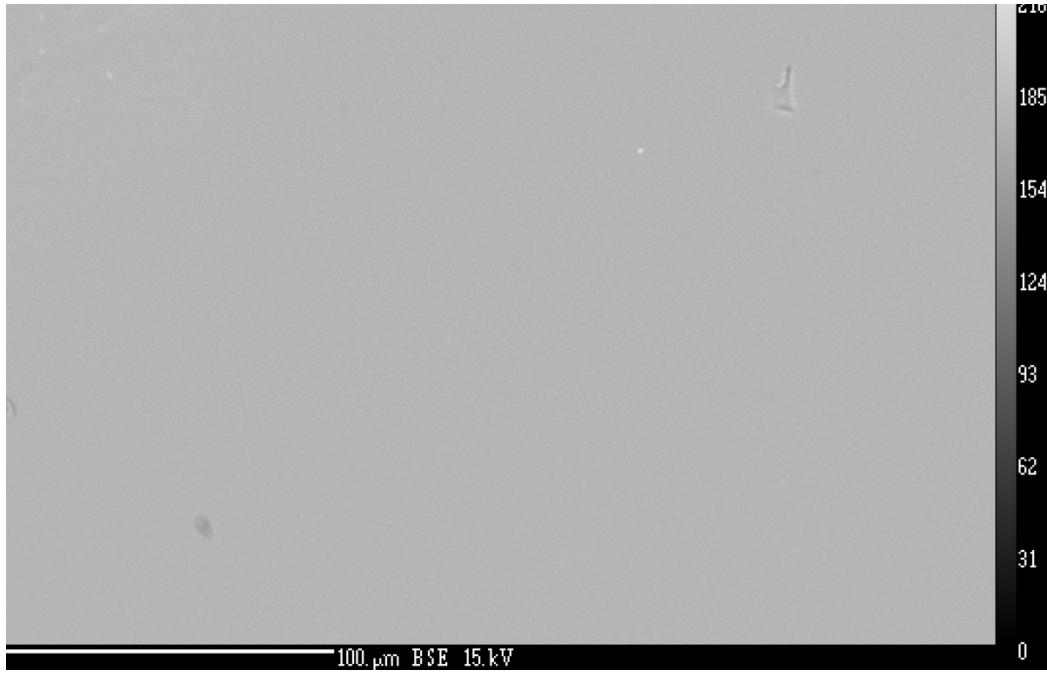


Figure 3.1: BSE picture of sample Edi04. The homogeneity of the glass is evident, with minute scratches caused by the polishing process. Samples Edi01 and Edi02 looked identical.

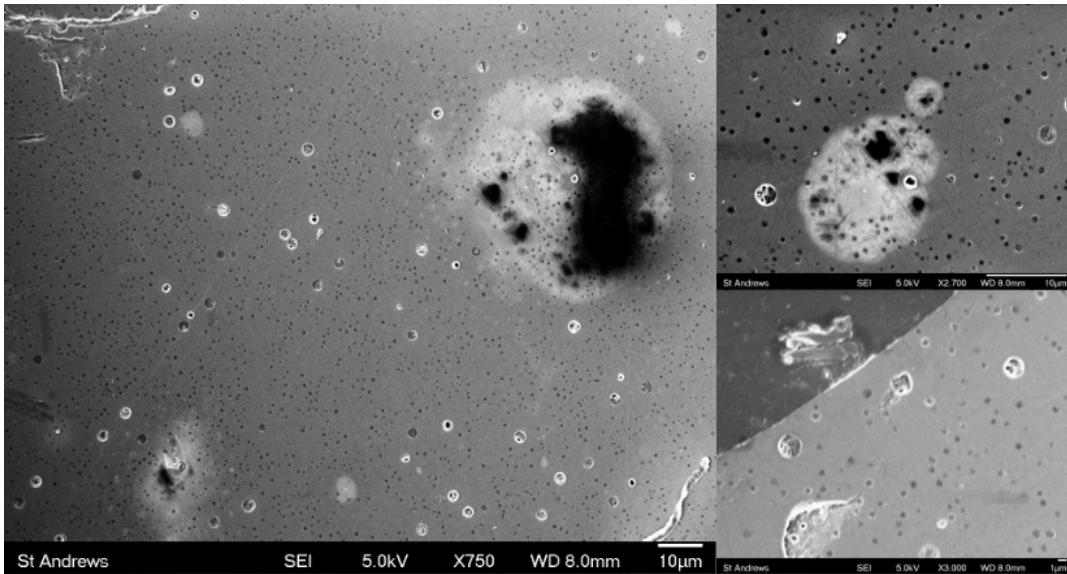


Figure 3.2: BSE pictures at different scales of sample Edi03. The abundant μm -sized bubbles give the glass a “degassing soda”-like texture, suggesting the quench-related origin of this feature.

3.3.1.2 – EPMA results.

The major and minor elemental composition of all samples is presented in Table 3.3.

	Edi01	2σ	Edi02	2σ	Edi03	2σ	Edi04	2σ
SiO₂	58.92	0.89	56.70	0.66	50.06	1.25	56.27	0.39
Al₂O₃	9.90	0.23	12.37	0.29	10.69	0.28	11.77	0.09
CaO	18.24	0.20	24.47	0.19	20.85	0.39	21.51	0.08
MgO	1.83	0.04	2.38	0.05	2.04	0.07	2.19	0.03
Na₂O	1.07	0.05	0.05	0.02	0.04	0.01	0.04	0.02
Cl	b.d.l.		b.d.l.		7.11	0.51	2.53	0.04
N	0.18	0.03	b.d.l.		0.63	0.02	0.38	0.02
H₂O*	9.86	0.03	4.04	0.02	4.36	0.01	5.32	0.02
N (mol%)	0.22	0.04	b.d.l.		0.87	0.02	0.51	0.02
n	15/4		15/5		9/5		9/5	

Table 3.3: Composition of samples from this study as measured by EPMA, given in wt% unless otherwise specified. n = number of analyses, where X/Y indicates X analyses at 15 kV (for major elements) and Y analyses at 10 kV (for nitrogen). b.d.l. = below detection limit. *H₂O is calculated using the 'volatiles by difference' method.

The detection limit for N was around 0.03 wt%, therefore N quantification was successful in all samples except for Edi02. In this sample, however, the calculated N abundance for five analyses is consistently negative (ranging from –0.003 to –0.04 wt%), likely pointing towards a background overestimate. If considered, this would result in an N content (in wt%) as high as 0.04 wt% in sample Edi02 (not reported in Table 3.3).

No Cl was measured in samples Edi01 and Edi02, while abundances compatible with the use of the $^{15}\text{NH}_4\text{Cl}$ ^{15}N -doping agent were measured in both samples Edi03 and Edi04.

3.3.1.3 – SHRIMP results.

Results of the SHRIMP analyses performed on samples Edi01, Edi02 and Edi04 are given in Table 3.4.

	Edi01	2σ	Edi02	2σ	Edi04	2σ
n	4		5		5	
^{12}C	95	7	46	2	1.6	0.4
$^{28}\text{Si}^{2+}$	923	107	652	68	27	2
^{14}N	2.3	0.2	0.4	0.1	0.1	0.0
^{15}N	58	7	13	2	2.2	0.2
^{16}O	1.3×10^5	1×10^4	1.1×10^5	1×10^4	3.4×10^3	2×10^2
^{28}Si	2.1×10^7	2×10^6	1.6×10^7	2×10^6	5.2×10^5	1×10^5
$^{14}\text{N}/^{28}\text{Si}$	1.1×10^{-7}	6×10^{-9}	2.7×10^{-8}	5×10^{-9}	1.3×10^{-7}	2×10^{-8}
$^{15}\text{N}/^{28}\text{Si}$	2.8×10^{-6}	1×10^{-7}	8.2×10^{-7}	7×10^{-8}	4.4×10^{-6}	4×10^{-7}

Table 3.4: Averaged counts per second for masses as analysed by SHRIMP. n = number of analyses. The final two rows are isotope ratios used to verify the extent of the isotopic enrichment process.

Sample Edi04 returned ^{28}Si and ^{16}O counts two orders of magnitude lower than the other samples. In the case of Si, this resulted in an anomalous $^{28}\text{Si}/\text{SiO}_2$ ratio. Thus, the $^{15}\text{N}/^{28}\text{Si}$ ratio was used to correct for this offset between the three samples. Through the plotting of this ratio against the N content as measured by EPMA in samples Edi01 and Edi04 (see Figure 3.5), it was possible to extrapolate N concentration in sample Edi02. Specifically, a linear calibration was used, and

the N abundance in sample Edi02 was then evaluated as $\sim 600 \pm 100 \mu\text{g/g}$ (light orange circles in Figure 3.3). The uncertainty quoted here is propagated through the calibration using the standard deviation of the $^{15}\text{N}/^{28}\text{Si}$ ratio over five analyses, and the 95% confidence interval on the slope of the calibration line, which was fitted using orthogonal distance regression (accounting for uncertainties in both dependent and independent variables), are reported in Table 3.4.

Strong matrix effects have been observed in the past when analysing N by ion probe spectrometry (e.g., increasing H_2O content promotes the useful ion yield of $^{14}\text{N}^+$ in rhyolitic glasses but decreases the ion yield in basaltic glasses; Regier et al., 2016). This hampered the accuracy of the analysis, due to the lack of matrix-matched standards for N dissolved in silicate glasses available at the time of the analysis. A straight line was fitted through the origin to the two calibration samples (Edi01 and Edi04), which fell within the 95% confidence interval of the results from sample Edi02. This suggests that SHRIMP analysis produced a reasonable value for the N concentration of sample Edi02.

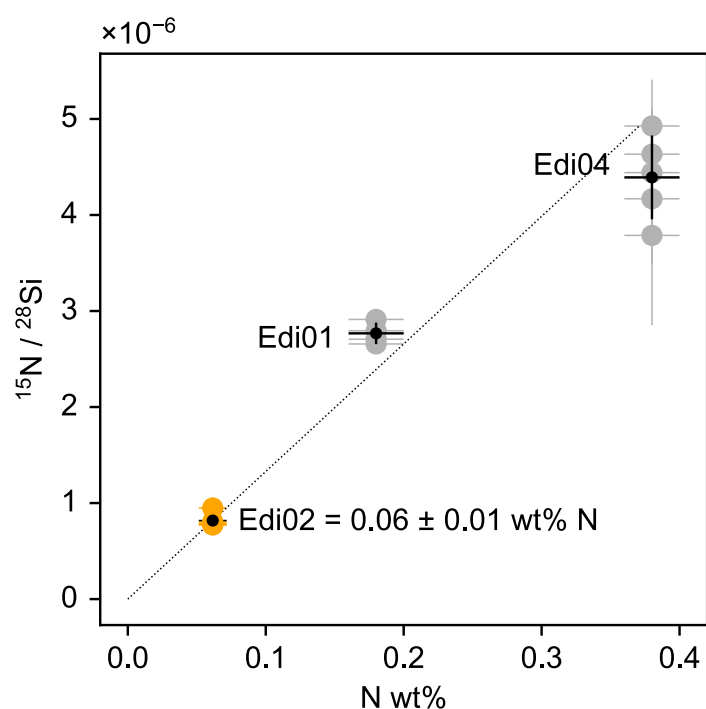


Figure 3.3: The ratio of $^{15}\text{N}/^{28}\text{Si}$, measured by SHRIMP, against N concentration as measured by EPMA for samples Edi01 and Edi04. Grey circles indicate individual analyses, and the black marker shows the average and standard deviation of all analyses for each sample. The dashed line is a calibration determined using orthogonal distance regression of Edi01, Edi04 and the origin. Using this calibration, the N content of Edi02 can then be calculated. The individual $^{15}\text{N}/^{28}\text{Si}$ ratios for each analysis are plotted at the calculated N abundance to demonstrate the small spread in the data over five analyses. The calibration line has a slope of $1.0(5) \times 10^{-5}$. Figure by Dr. Eleanor Mare.

SHRIMP analyses also provided data on the isotopic composition of N in all samples. As expected, ~97% of all N was ^{15}N , and this fraction is consistent with the level of ^{15}N -enrichment in the starting materials (i.e., ~98%, both in $^{15}\text{NH}_4^{15}\text{NO}_3$ and $^{15}\text{NH}_4\text{Cl}$). This is reflected in the $^{15}\text{N}/^{28}\text{Si}$ ratio, which is at least an order of magnitude larger than the $^{14}\text{N}/^{28}\text{Si}$ ratio in all samples. In contrast, natural abundance samples analyzed during the same session typically displayed a ratio of $^{15}\text{N}/^{28}\text{Si}$ two orders of magnitude smaller than the ratio of $^{14}\text{N}/^{28}\text{Si}$, which

is consistent with the natural isotopic composition of N (i.e., ^{14}N is 99.63% of all N; Meija, 2015).

3.3.2 – Speciation analysis.

3.3.2.1 – DFT calculations outcome.

Density Functional Theory (DFT) calculations were performed to predict the NMR chemical shift of the expected N species in the samples of this study. The results of these calculations are shown in Figure 3.4.

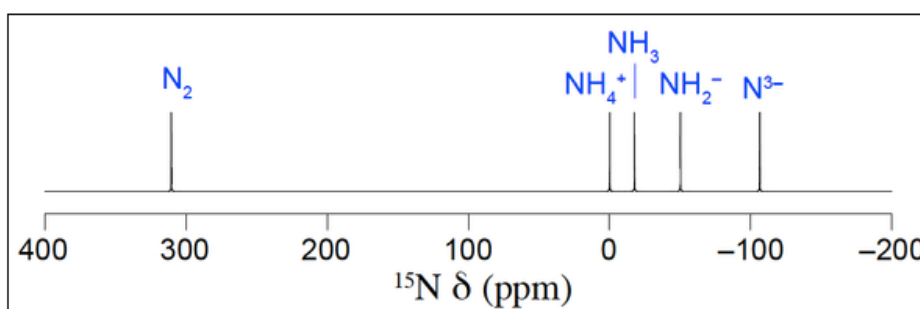


Figure 3.4: ^{15}N NMR chemical shift of molecular, ammoniac, and atomic nitrogen species as calculated by the GAUSSIAN 09 D.01 revision program. The chemical shift of $^{15}\text{NH}_4^+$ was arbitrarily set at 0.0 ppm.

Figure by Dr. Daniel Dawson.

The outcome of the DFT calculations shows that the chemical shift of $^{15}\text{N}_2$ is markedly distinct from other ^{15}N -based species and was estimated to fall at around +320 ppm relative to $^{15}\text{NH}_4^+$. As for the ^{15}N —H species, their predicted chemical shifts are in the order $^{15}\text{NH}_4^+ > ^{15}\text{NH}_3 > ^{15}\text{NH}_2^-$ order, while $^{15}\text{N}^{3-}$ is notably further shifted towards lower values. Expected chemical shifts from the computations are summarised in Table 3.5.

Specie	Chemical shift (ppm)
$^{15}\text{N}_2$	+320
$^{15}\text{NH}_4^+$	0.0
$^{15}\text{NH}_3$	-25
$^{15}\text{NH}_2^-$	-48
$^{15}\text{N}^{3-}$	-105

Table 3.5: Summary of calculated ^{15}N NMR chemical shift of nitrogen species expected in the samples analysed for this study.

The chemical shift assigned to $^{15}\text{N}^{3-}$ corresponds to a free N^{3-} ion dissolved in a gaseous phase, nitride ions in solids tend to have a chemical shift comprised between +60 and +90 ppm relative to $^{15}\text{NH}_4^+$ (MacKenzie & Smith, 2002), due to the covalent nature of the bond formed in solid phases. There is no direct measurement for the chemical shift of $^{15}\text{N}^{3-}$ dissolved in a liquid, especially in non-aqueous solutions such as silicate melts, hence the chemical shift calculated via DFT can't at present be verified with experimental results. Nevertheless, the experimental settings used for the samples studied here are highly unlikely to generate conditions compatible with $^{15}\text{N}^{3-}$ stability, hence further calculations were deemed unnecessary for the scope of this study.

3.3.2.2 – Raman results.

Raman spectra were collected in the 2150–2400 cm^{-1} and 2800–4000 cm^{-1} regions (see Figure. 3.5). These spectral regions typically contain peaks related to molecular nitrogen and ammoniac nitrogen, respectively (Roskosz et al., 2006; Mysen et al., 2008; Kadik et al., 2015). The background-corrected spectra

normalised to the maximum intensity is in Figure 3.5. Normalisation to the silicate peak heights or areas was not possible due to the signal being not strong enough to record a full spectrum.

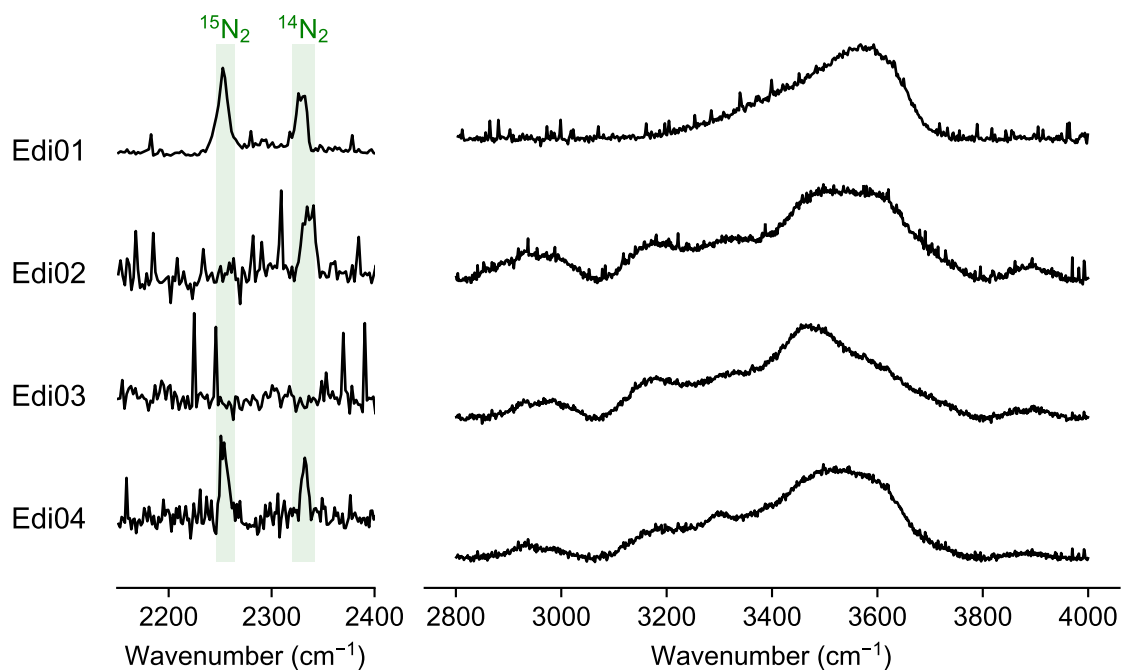


Figure 3.5: Raman spectra collected from all samples of this study over the 2150–2400 cm^{-1} and 2800–4000 cm^{-1} regions. Peak regions of the ^{14}N - ^{14}N and ^{15}N - ^{15}N bonds (Mysen, 2018; Roskosz et al., 2006) are shown in light green. Figure by Dr. Eleanor Mare.

In the 2150–2400 cm^{-1} region, a sharp peak is observed at about 2330 cm^{-1} in all samples except Edi03. The spectrum of sample Edi03 in this region suffered from large fluorescence, which obscured all signals. In samples Edi01 and Edi04, a second sharp peak is observed at about 2555 cm^{-1} .

In the 2800–4000 cm^{-1} region, a broad feature at around 3600 cm^{-1} is observed in all samples. In sample Edi01, this feature appears to be a single, broad, asymmetric peak. In all other samples, additional minor and broad features are observable in this region, mostly superimposed on the lower-wavenumber tail

of this peak, and one of varying intensity at higher wavenumber. Further details about the position of such features are provided in subsection 3.4.2.2, as the low intensity of such peaks makes their positioning itself an object of discussion, rather than straightforward reporting.

High levels of fluorescence were recorded in all spectra due to the glassy nature of the samples, resulting in higher-than-expected background noise.

3.3.2.3 – ^{15}N MAS NMR results.

MAS NMR spectra for all samples are presented in Figure 3.6. The spectrum for glass Edi01 consists of a single peak centered at -69 ± 0.8 ppm. The signal-to-noise ratio in sample Edi02 is relatively low with respect to the other spectra, nonetheless a peak at -69 ± 2 ppm can be clearly identified. The spectrum for sample Edi04 contains two peaks centered at -67 ± 0.7 ppm and -355 ± 1.3 ppm respectively, while the spectrum for sample Edi03 contains two major peaks at -74 ± 0.7 ppm and at -357 ± 1.6 ppm, and a minor but still identifiable peak at -348 ± 0.7 ppm. Peaks in the -60 to -80 ppm region were labelled as species A, and peaks in the -340 – -380 ppm (relative to nitromethane) region as species B.

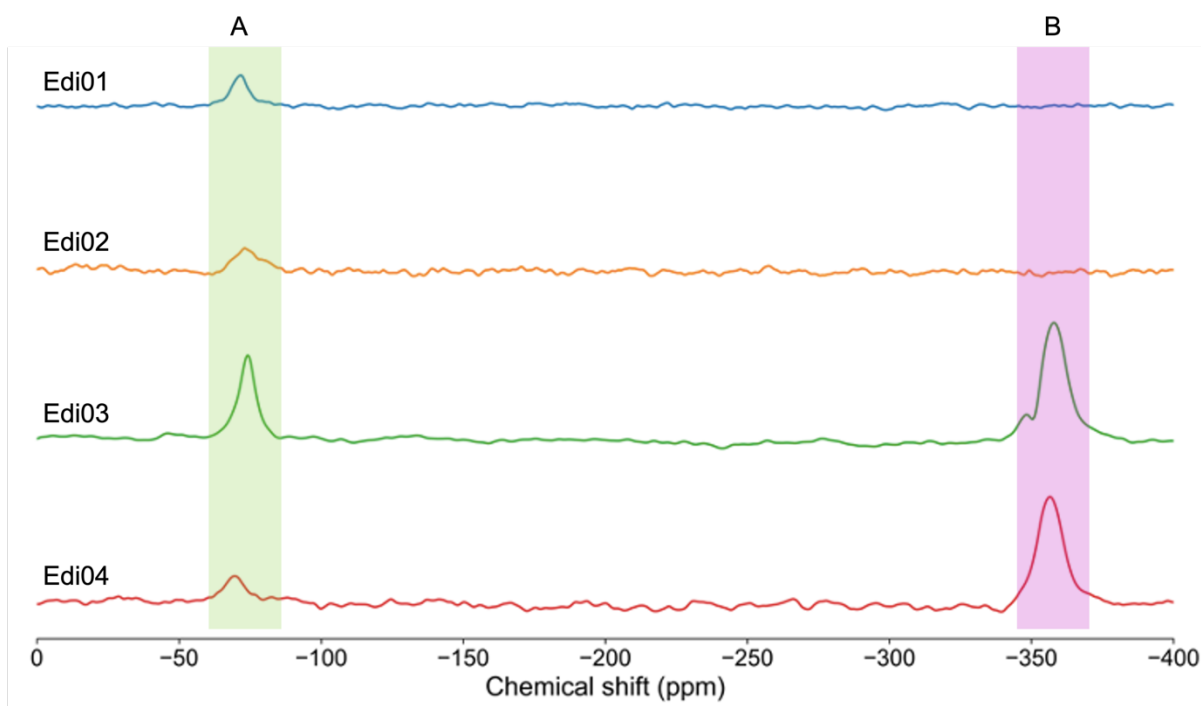


Figure 3.6: ¹⁵N MAS NMR spectra, acquired using a spin echo, for all samples collected for this study.

Spectra are referenced to nitromethane at 0 ppm. Two distinct peak features are evident, one in all samples (in the -60 to -80 ppm region) and one in samples Edi03 and Edi04 alone (in the -340 to -380 ppm region), highlighted by a light green and light violet band respectively.

Due to the difficulty in distinguishing between the two peaks in the -340 to -380 ppm region of the spectrum for sample Edi03, a further spectrum was collected by using cross polarization. The resulting CP MAS spectrum, presented in Figure 3.7, consists of 3 different peaks, centered at -349 ± 0.4 , -356 ± 2.1 and -371 ± 2.5 ppm respectively, labelled as B1, B2 and B3. The first two are noticeably sharper than the latter, and B2 is centered around the same chemical shift as the single peak in region B from sample Edi04.

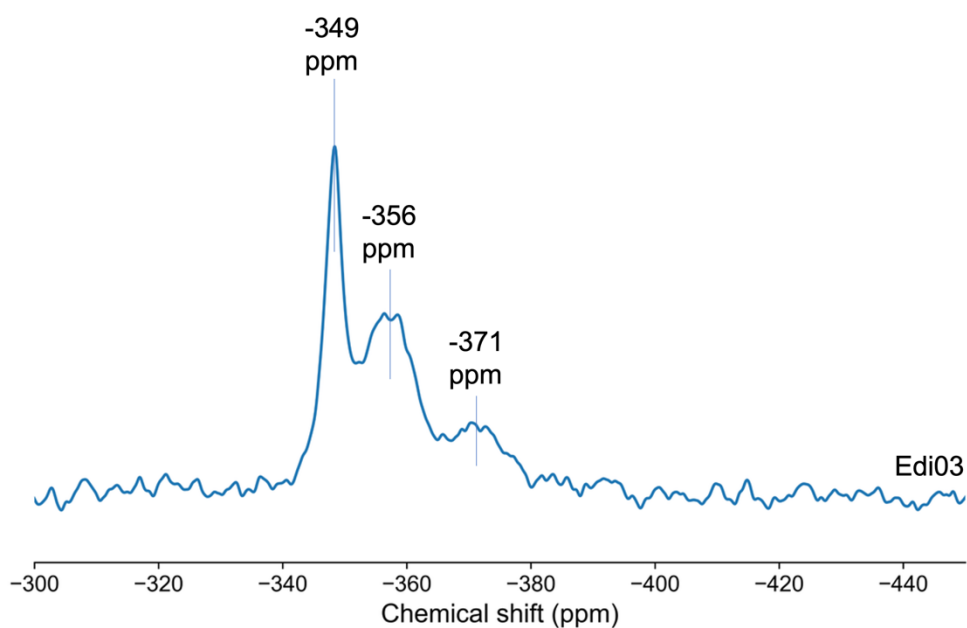


Figure 3.7. ^{15}N CP MAS NMR spectrum for sample Edi03. The spectrum is referenced to nitromethane at 0 ppm. Three partially overlapping peaks are distinguishable in the -340 to -380 ppm region of the spectrum, centred at -349 ± 0.4 , -356 ± 2.1 and -371 ± 2.5 ppm respectively.

Fitting of all spectra was performed using the Python open-source library Imfit. This was done to determine the relative abundance of the species present in samples Edi03 and Edi04. The results are presented in Figures 3.8 and 3.9 and the relative abundance of all species are reported in Table 3.6.

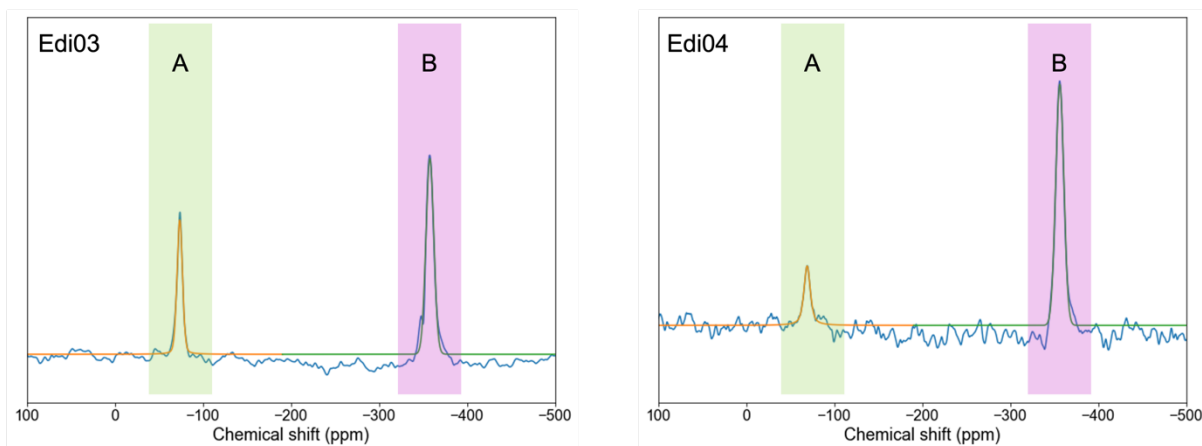


Figure 3.8: Results of fitting of the ^{15}N MAS NMR spectra for samples Edi03 and Edi04, performed with the Imfit Python library. Each peak was approximated with a PseudoVoigt function (i.e., convolution of a Gaussian and a Lorentzian function).

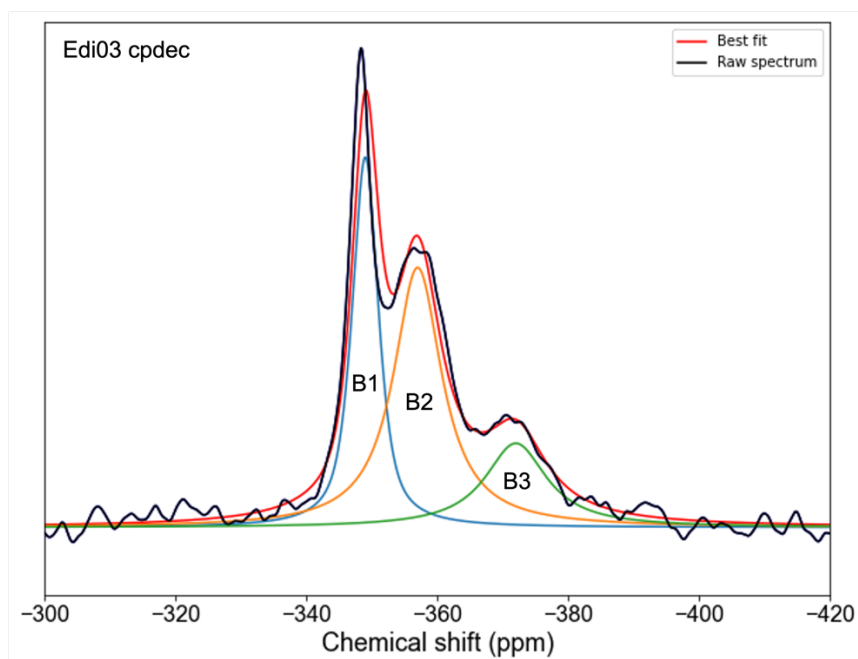


Figure 3.9: Fitting of the ^{15}N CP MAS NMR spectrum for sample Edi03, performed with the Imfit Python library. All peaks were approximated with a PseudoVoigt function (i.e., convolution of a Gaussian and a Lorentzian function). The best fit is provided (in red) as a visual aid to evaluate the precision of the fitting.

	Edi01	Edi02	Edi03	Edi04
Species A	100%	100%	32%	23%
Species B1	--	--	22%	--
Species B2	--	--	35%	77%
Species B3	--	--	11%	--

Table 3.6: Summary of the relative abundance of the ^{15}N species present in samples in this study, determined via fitting of the ^{15}N MAS NMR spectra with a convolution of multiple PseudoVoigt peaks.

As a final remark, it must be noted that MAS NMR spectroscopy is a bulk technique. Unlike all other samples, Edi03 consists of a melt phase and a quench fluid phase, thus it is impossible to determine how the various species are distributed between the two. Furthermore, due to the grinding process necessary for the analysis, it is also not possible to quantify exactly how much, if any, of the fluid phase was preserved.

3.4 – DISCUSSION

3.4.1 – Attainment of equilibrium.

The BSE images collected by EPMA (see Figure 3.1) were used to assess the equilibration of the synthesized glasses. Samples Edi01, Edi02 and Edi04 consisted of a clear homogeneous single-phase glass and were thus interpreted

as having reached full equilibrium. Sample Edi03 instead was deemed as not equilibrated, due to the presence of many μm -sized gaseous bubbles evenly distributed throughout the sample. Given its relative similarity to the other samples from a compositional standpoint, it is not unlikely that it also reached full equilibration before quenching. It is worth noting that for sample Edi04, the closest to Edi03 in composition, the volatile abundance (i.e., $\text{Cl} + \text{H}_2\text{O} + \text{N}$) is 8.23 wt%, while in Edi03 this is markedly higher at 12.1 wt%. This difference might be the reason why, when subjected to the sudden T drop induced by the quenching process, volatiles in Edi03 rapidly unmixed in a separated fluid phase before the glass transition was completed, in a process effectively analogous to natural magma degassing phenomena.

3.4.2 – Peak assignment.

3.4.2.1 – ^{15}N MAS NMR spectra interpretation.

The ^{15}N MAS NMR spectra collected from samples in this study contain peaks in two regions (see Figure 3.6): [1] a peak (labelled species A) in the -60 to -80 ppm region of the spectrum was detected in all samples, and [2] multiple peaks (labelled as species B1, B2 and B3) in the -340 to -380 ppm region of the spectrum were detected in samples Edi03 and Edi04 (see Table 3.7, for relative abundances).

DFT calculations (see Table 3.6 and Figure 3.4) allowed the identification of species A as molecular nitrogen (N_2) and species B1, B2 and B3 as different

forms of ammoniacal nitrogen (N—H). In more detail, the relative order in which the peaks related to these species appeared in the CP MAS spectrum collected from sample Edi03 (see Figure 3.6) suggests they are NH_4^+ , NH_3 and NH_2^- respectively (i.e., in order of decreasing shift). The difference in chemical shift between the experimental spectrum and the DFT calculations' outcome (i.e., 356 ppm) is due to the use of a different reference (i.e., nitromethane) in the experimental spectrum.

^{15}N MAS NMR of N speciation in silicate melts investigations in the current literature are rare. For this reason, while the chemical shift observed in glasses similar to those in this study for N_2 molecules has been reported before (Roskosz et al., 2006), no published material is available at the time of writing describes the chemical shift associated with ammoniacal nitrogen species in silicate melts, to the best of the author's knowledge.

The relative speciation of N in the glasses of this study is reported in Table 3.7. The concentration was calculated by multiplying N abundance as measured via SHRIMP and EPMA (see Figure 3.3 and Table 3.4) with the relative abundance of each individual species (reported in Table 3.6).

Sample	N ₂	NH ₄ ⁺	NH ₃	NH ₂ ⁻
Edi01	--	--	1400 µg/g	--
Edi02	--	--	700 µg/g	--
Edi03	1800 µg/g	600 µg/g	2000 µg/g	900 µg/g
Edi04	--	--	2200 µg/g	2900 µg/g

Table 3.7: Concentration of N species measured in samples of this study as determined via ¹⁵N MAS NMR and EPMA/SHRIMP.

It must again be stressed that, while the N speciation in sample Edi03 was easily resolved despite its relative complexity and the challenge of NMR spectroscopy of low- γ nuclei, MAS NMR spectroscopy being a bulk technique makes it impossible to determine the host phase(s) (i.e., melt and quench fluid) of each species.

3.4.2.2 – Raman spectra interpretation.

Peaks for the N—N bond vibration of ¹⁵N₂ in the Raman spectrum have been predicted using Equation 3.1 (adapted from McCreery, 2002) to occur at 2331 and 2255 cm⁻¹. Experimental observations in various silicate glassy systems (e.g., Dalou et al., 2019; Mysen, 2018; Roskosz et al., 2006; Ernst, 2001; and refs. therein) confirmed these predictions to be accurate. Hence, the low intensity, but distinguishable, peaks (see Figure 3.5) detected in samples Edi01 to Edi04 in these spectral regions were assigned to ¹⁴N₂ and ¹⁵N₂.

$$\omega_{15N \text{ species}} = \sqrt{\frac{M_{14N \text{ species}}}{M_{15N \text{ species}}}} * \omega_{14N \text{ species}}$$

Equation 3.1: Formula used to calculate the vibrational wavenumbers of ¹⁵N-based species from those of ¹⁴N-based species owing to the isotope effect (adapted from McCreery, 2002). M = mass of species, ω = raman shift of peak.

According to the retail source of the ¹⁵N-enriched reagents used during sample synthesis, 98% of all N should be ¹⁵N, and therefore only trace concentrations of ¹⁴N are expected. The peak in the ¹⁴N₂ region was thus likely due to N₂ molecules in the air (which consist of 78% N₂ at natural isotopic abundance (ca. 99.6% ¹⁴N), as the analyses were performed with the laser travelling in air before impacting the samples.

Sample	N ₂ abundance
Edi01	~900 μg/g
Edi02	~300 μg/g
Edi03	~1000 μg/g
Edi04	~400 μg/g

Table 3.8: Concentration of N₂ in samples from this study, obtained by multiplying N abundance (see Table 3.4 and Figure 3.3) with ¹⁵N₂ relative abundance in each sample. As only 2% of the N present in the starting materials was ¹⁴N, its abundance was not added to the data in this table, due to error on them being above 2%.

Peaks in the ¹⁵N₂ regions of samples Edi01 and Edi04 were detected. Only background signal was instead detected in sample Edi02, as the only visible peak

is in the $^{14}\text{N}_2$ region, therefore it is likely generated by $^{14}\text{N}_2$ molecules in air, as the N in the glass phase is supposed to be ca. 98% ^{15}N . Sample Edi03 was a dubious case, as a low intensity peak can be observed just to the left of the $^{15}\text{N}_2$ region, however it is impossible to assign this peak to $^{15}\text{N}_2$. This is because 3 other features exist at similar Raman shifts (see Figure 3.10). Due to the nature of this sample (see section 3.4.1), it was decided not to investigate this matter further.

The signal-to-noise ratio of the $^{15}\text{N}_2$ peak in sample Edi01 is noticeably higher than in sample Edi04, and this roughly correlates with the $^{15}\text{N}_2$ content of the two samples (i.e., ~ 900 vs ~ 437 $\mu\text{g/g}$ respectively, see Table 3.8).

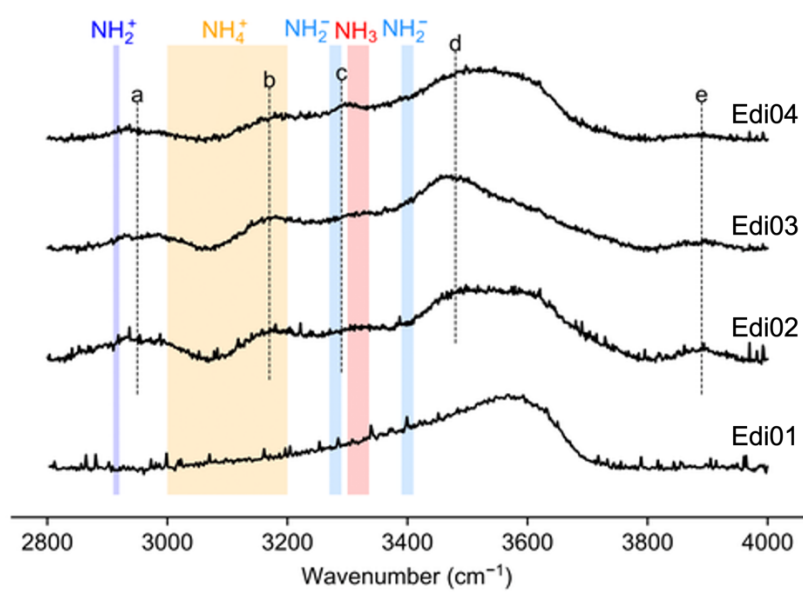


Figure 3.10: Expansion of the 2800 to 4000 cm^{-1} region of the Raman spectra collected from samples of this study. Spectral regions of interest for various N—H species are reported as coloured areas, while the dashed lines highlight the potential peak features observed in one or more spectra (identified as letters from 'a' to 'e'). Figure by Dr. Eleanor Mare.

The main feature observed in the spectra in Figure 3.10 is the broad peak of varying shape in the c.a. 3400 to 3700 cm^{-1} region. This feature is commonly associated with O—H bond stretching in OH^- groups (Mysen, 2018; Walrafen et al., 1999), and due the hydrous nature of the glasses of this study it was decided to assign this feature to the same phenomenon.

As evidenced by the dashed lines in Figure 3.10, a total of 5 potential N—H related peaks are identifiable in the 2800 to 4000 cm^{-1} spectral region. The faintness of these features makes peak assignment a challenging process.

Due to the relatively small difference in mass between ^{14}N and ^{15}N , the Raman shift difference between ^{14}N and ^{15}N -bearing N—H species is expected to be negligible. Experimental observations reported in literature support this assumption: as an example, the difference between $^{14}\text{NH}_3$ and $^{15}\text{NH}_3$ was quantified at around 6 cm^{-1} (i.e., 3320 and 3326 cm^{-1} respectively, Mysen et al., 2008; Kadik et al., 2016), and such a small difference in Raman shift was not measurable with the instrumentation utilised for this study.

Peaks in Raman spectra were identified as follows:

1. **Peak 'a'**: this peak was detected in all spectra apart from Edi01. Its Raman shift of ca. 2940 cm^{-1} is close to the band connected with the vibration of the N—H bond in amide (NH_2^+) groups (i.e., 2900 to 2915 cm^{-1} ; Mysen et al., 2008; Socrates, 2001), however it falls outside of this range. Additionally, the peak is most pronounced, albeit still of low intensity, in sample Edi02, where there is no evidence of ammoniacal nitrogen from NMR spectroscopy (see Table 3.10), hence it was deemed unlikely to be due to N—H groups.

2. **Peak 'b'**: this peak was detected in all spectra apart from Edi01. Its Raman shift of c.a. 3160 cm^{-1} falls well within the region where NH_4^+ related vibrations occur (Mysen et al., 2008; Socrates, 2001; Schmidt & Watenphul, 2010). However, as is the case with peak 'a' its amplitude is highest in sample Edi02, where NMR spectroscopy detected no ammoniacal nitrogen (see Table 3.10), thus this peak is unlikely to be related to N species.
3. **Peak 'c'**: this peak was detected only in sample Edi04. Its Raman shift of 3290 cm^{-1} has been in the past assigned to N—H bonds in amide (NH_2^-) groups ($3280\text{--}3290\text{ cm}^{-1}$; Kadik et al., 2015; Mosenfelder et al., 2019). While NMR analysis determined that most N (i.e., ~77%) in sample Edi04 is ammoniacal N, the only amides in glasses from this study were detected in sample Edi03, therefore this peak is likely not related to ammoniacal nitrogen.
4. **Peak 'd' and 'e'**: no evidence of these potential peaks being connected to ammoniacal nitrogen was found in published literature at the time of writing.

In conclusion, it was determined that none of the peaks detected in the $2800\text{ to }4000\text{ cm}^{-1}$ region of the Raman spectrum could be connected to nitrogen-based chemical species.

3.4.3 – Advantages and disadvantages of spectroscopic techniques used.

3.4.3.1 – The case for ^{15}N MAS NMR spectroscopy.

The use of MAS NMR spectroscopy to determine ^{15}N speciation has some important advantages over more traditional spectroscopic techniques. These include:

- I. All species are detected in a single analysis, whereas Raman spectroscopy struggles to detect ammoniac species at low N concentrations, hence often requiring integration by IR spectroscopy. This however introduces further complications with regards to relative quantification of each species, as two different standardisation procedures must be performed, one for each machine used, with two different external standards (i.e., one N_2 -rich and one NH_x -rich).
- II. MAS NMR is an isotope specific technique, therefore interference between different isotopes is not an issue. On the other hand, the Raman spectrum contains information from all Raman-active elements targeted by the analysis, which raises the risk of interference (e.g., see subsection 3.4.2.2). The consequences of this are exemplified by the peak assignment process operated in section 3.4.2: while Raman spectrum interpretation is heavily reliant on published literature, MAS NMR results can reliably be interpreted via DFT calculations, hence making the process less reliant on external datasets.

- III. Even for an element with a relatively low NMR sensitivity such as ^{15}N (Keeler, 2002), the detection limits are markedly higher for Raman spectroscopy, as evidenced by the difference in signal-to-noise ratio achievable in NMR and Raman spectra from Figures 3.6, 3.7 and 3.10. This difference in instrument sensitivity also makes similar species (e.g., NH_3 , NH_4^+ and NH_2^-) easier to discern.

Overall, the lower detection limits and better spectral resolution of MAS NMR over Raman spectroscopy, as shown by spectra from this study, can be a critical factor between detecting multiple clear signals or just low intensity peaks barely emerging from background noise.

3.4.3.2 – The case for Raman spectroscopy.

The main advantages of using Raman spectroscopy over MAS NMR spectroscopy in the study of N speciation include:

- I. Raman spectroscopy is comparatively simpler, faster, and cheaper to operate than MAS NMR instrumentation. The former can be operated after basic training and can deliver results in seconds or minutes, while the latter requires a highly trained individual, often a laboratory manager, and can take multiple days of analysis. This adds to the enormous cost difference between the two types of facilities (i.e., the cost of a whole Raman apparatus is often lower than the price of some components of an MAS NMR spectrometer), making extensive NMR analysis only worth performing in the context of a full research project,

while Raman and IR analysis can also be performed as routine investigations.

- II. Raman spectroscopy can detect signals from both ^{14}N and ^{15}N based species, while MAS NMR can only detect signals from ^{15}N —based species at N concentrations coherent with N abundance in geological environments (see section 1.3.2). This makes it very challenging (and sometimes impossible) to study any natural samples where nitrogen is present in trace quantities with natural $^{15}\text{N}/^{14}\text{N}$ ratios. As an example, the sample with the lowest N abundance in this study contained about $600\ \mu\text{g/g}$ of ^{15}N , and only a broad, low intensity peak could be detected via NMR spectroscopy (see Figure 3.6). At natural isotopic abundance (i.e., 99.6% ^{14}N), this would require an overall N concentration of c.a. $6 \times 10^5\ \text{mg/g N}$ (i.e., 6 wt%), which is well above even the highest N solubilities (i.e., 0.8-0.9 wt% of N; Dalou et al., 2019) reported in literature for mafic melts at the pressure used in this study (e.g., 2 GPa).
- III. Raman spectroscopy is an in-situ technique (i.e., it is not performed on a bulk volume of sample), therefore it can be performed on the same polished sample that is required for N abundance quantification (e.g., via EPMA or mass spectrometry), although analysis must be performed before the eventual metal coating (see section 2.2.3). In addition, its in-situ nature means it can be used in multiphase systems and identify the species contained in each phase. In contrast, NMR is a bulk technique, therefore it is impossible to accurately study such

systems: as an example, multiple N—H species were detected from sample Edi03 (see subsection 3.4.2.1), which however consisted of both a melt and a fluid phase. Due to the sample being powdered for NMR analysis, it was not possible to understand how the species were distributed between the two phases.

- IV. The expected Raman shift for a molecular bond can easily be predicted, often via simple formulas (e.g., see Equation 3.1). On the other hand, NMR chemical shift can be reasonably accurately predicted via DFT calculations, which must be performed on dedicated hardware due to the necessary computational performances.

In conclusion, the main advantages of Raman spectroscopy are related to its ease of use and to its lower cost, but its ability to perform in situ analysis and the lack of necessity of ¹⁵N-enrichment are also compelling arguments for its use over MAS NMR.

3.4.4 – Nitrogen speciation in silicate melts.

This study was not designed to investigate N solubility in silicate melts, as this would have implied N-saturating the samples, thus leading to a potential fluid phase speciation, which as shown by sample Edi03 greatly hinders the viability of NMR. For this reason, all samples contain N well below the solubility limits for mafic composition (i.e., upwards of 1 wt%, Dalou et al., 2017; Dalou et al., 2019; Li et al., 2015), therefore no information on N solubility can be inferred from the results of this study.

As already mentioned in section 3.1.3, investigating N speciation as a function of fO_2 was also deemed beyond the scope of this study. Recently published research (Dalou et al., 2019; Grewal et al., 2020) however has showed a clear connection between the variations in N speciation and fO_2 , to the point that the former parameter can now be used to infer the latter, rather than having to measure both independently.

The most suitable sample from this study for indirect fO_2 measurement is Edi04, due to its dual N speciation (see Table 3.8). Specifically, 77% of N is speciated as NH_3 , while the rest is speciated as N_2 . The presence of molecular nitrogen sets a lower limit for fO_2 of around IW–2 (Grewal et al., 2020), however the N_2 abundance itself is thought to be independent from fO_2 (Dalou et al., 2019), hence it should not be used as an fO_2 indicator. On the other hand, the presence of ammoniacal nitrogen in the NH_3 form, paired with the absence of atomic N, points towards an oxygen fugacity comprised between IW–1.5 and IW (Grewal et al., 2020).

The presence of ammoniacal nitrogen solely as ammonia in sample Edi04 agrees with the hypothesis by Mysen et al. (2009), which postulates that any other N–H species (e.g., ammonium, amide) is inherently unstable in silicate melts. While NH_4^+ and NH_2^- were both detected in sample Edi03, the bi-phasic nature of this sample makes it impossible to determine in which phase each species is hosted via a bulk technique such as MAS NMR. Furthermore, the fluid phase in sample Edi03 consists of many ca. μm -sized bubbles homogeneously distributed within the melt phase. It was thus impossible to analyse the fluid phase in isolation even via in-situ spectroscopic analysis (e.g., Raman spectroscopy).

Therefore, the presence of ammoniacal species that are not NH_3 in sample Edi03 does not inherently contradict the suggestion that ammonia is the only N—H species stable in silicate melts (Mysen et al., 2008).

Samples Edi01 and Edi02 both contain, according to MAS NMR results, only molecular nitrogen, thus placing those in broadly oxidizing conditions, certainly above the IW buffer (Grewal et al., 2020). Similar conditions were achieved in NS ($\text{Na}_2\text{O} + \text{SiO}_2$) glasses by Roskosz et al. (2006), however samples from that study also contained a minor but significant fraction of what was interpreted as N—O groups, which were instead absent in both Edi01 and Edi02 (see Table 3.8, and Figure 3.6), thus placing those at a relatively lower oxygen fugacity. The lack of a dual speciation in Edi01 and Edi02 makes any further attempt at indirect $f\text{O}_2$ quantification unfeasible.

3.5 – CONCLUSIONS

This study was carried out as a showcase of the potential of NMR spectroscopy in investigating N speciation in silicate melts. The analytical results discussed in section 3.4.3 show the indisputable potential of this technique in resolving complex N—H bonding environments. Nevertheless, Raman and IR spectroscopy have recently been shown (Dalou et al., 2019; Grewal et al., 2020) to be able to produce results of similar quality without the need for ^{15}N enrichment, albeit at the cost of a lower instrument sensitivity. Indeed, the results obtained by the latter techniques allowed for a reliable indirect determination of $f\text{O}_2$ conditions for the samples of this study. Furthermore, the advantages of not requiring

isotopic enrichment go beyond monetary cost, as this also enables the analysis of natural materials. Even if such samples hypothetically contained enough ^{15}N to be studied via ^{15}N MAS NMR, the results would still be hampered by any Fe present in the system, due to its highly paramagnetic nature. On this note, it must be remembered that Fe is the 4th most abundant element on planet Earth (Allègre, 1995), and that it is a key component of the IW (Fe—FeO) $f\text{O}_2$ buffer, one of the most common tools used in experimental petrology for $f\text{O}_2$ control during sample synthesis.

Despite its disadvantages, NMR spectroscopy in this study showed unparalleled precision during the study of a fluid phase, as it enabled for both the detection and relative quantification of different ammoniacal species, some of which are likely hosted solely by the fluid phase (Mysen, 2018; Dalou et al., 2017; Mysen et al., 2008). Unfortunately, there are no currently existing apparatuses that would allow to introduce fluids at geologically relevant conditions (i.e., T and P in the orders of magnitude of 100s K and MPa respectively) in an NMR machine. Fluids of this nature are typically C-O-H-N systems (Mikhail et al., 2017; Dalou et al., 2017; Li & Keppler, 2014; Mikhail & Sverjensky, 2014), which are all elements that could be studied via NMR spectroscopy, hence investing in the development of a technique able to study such phases might have applications in the study of multiple components of the fluid phase.

In conclusion, MAS NMR shows great potential for the study of N speciation in silicate melts, particularly in the study of low-concentration ammoniacal species and their relative abundance. This is despite the limitations caused by the need to use isotopically enriched materials and the inability to

study highly paramagnetic samples. Furthermore, the development of an experimental setting able to investigate hydrothermal fluids via NMR spectroscopy would have invaluable benefits for the study of systems so critically important for the geochemical understanding of the deep Earth.

~4 — EVIDENCE FOR F—Mg LOCAL BONDING ENVIRONMENT IN LOW PRESSURE CMAS SILICATE MELTS: IMPLICATIONS FOR THE VOLATILE BUDGET OF CHONDRITES~

4.1 – INTRODUCTION

The formation of terrestrial planets in the Solar System is thought to have consisted of a multi-staged accretion of planetesimals of increasing size through collisions promoted by gravity (Fischer & Ciesla, 2014). Meteorites and smaller-sized protoplanets are likely to have experienced constant partial melting and rapid recrystallization processes in the early turbulent Solar System (Mezger et al., 2021). In addition, at least three partial melting events on a planetary scale occurred during Earth's accretion (Nakajima & Stevenson, 2015). While the former events likely occurred at low pressures (i.e., <1 GPa), the latter took place when the Earth was already of a sufficient size to result in larger pressure range. The differences between F^- , OH^- and the other halogens (see subchapter 1.4) likely resulted in an increasing divergence in their behaviour during these melting

processes (Hanley & Koga, 2018). This variability of geochemical behaviour is likely to be reflected in the chemical speciation (i.e., local bonding environment) of these elements in melts.

The present chapter focuses on F speciation in low P melts, more similar to asteroidal P-T environments and the formation of basaltic melts on all telluric bodies, while high P melts, closer to later stage Planet-scale partial melting events, are investigated in chapter 5.

4.1.1 – The relationship between F and Mg during chondritic evolution.

The abundance of F and Cl in principal chondrite groups is shown in Figure 4.1. If the geochemistry of F relative to Cl in chondritic meteorites is considered, then notable variability for the F/Cl ratio across the different groups of chondritic meteorites are observed.

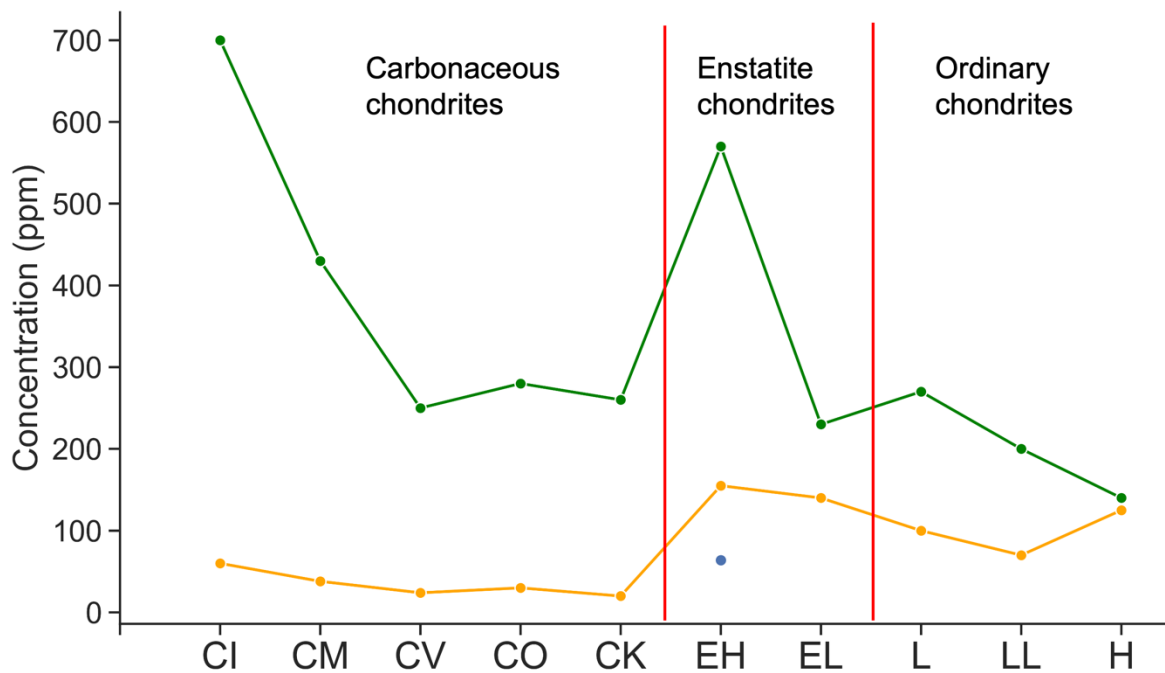


Figure 4.1: F and Cl (orange and green, respectively) abundance (ppm) in chondrite groups, on the x-axis (data from Lodders & Fegley, 1998). Points are connected by lines as a visual guide, the blue point represents F abundance when not considering data from Reed (1964) and Greenland & Lovering (1965) for EH chondrites, as recommended by Dreibus et al. (1979). Abbreviations for chondrite groups on x axis are as defined in Lodders & Fegley (1998), for the specific meaning of each acronym see Table 1.5.

A controversy in the published literature, due to Dreibus et al. (1979) disputing the validity of the method used to quantify F concentrations in EH and EL chondrite measured by Reed (1964) and Greenland and Lovering (1965), results in a debate over the F content in E-type chondrites. More recent literature (Lodders & Fegley, 1998; Brearly & Jones, 2018) considers all measurements valid, hence this thesis will consider the data represented by the orange line in Figure 4.1 as the accepted ones.

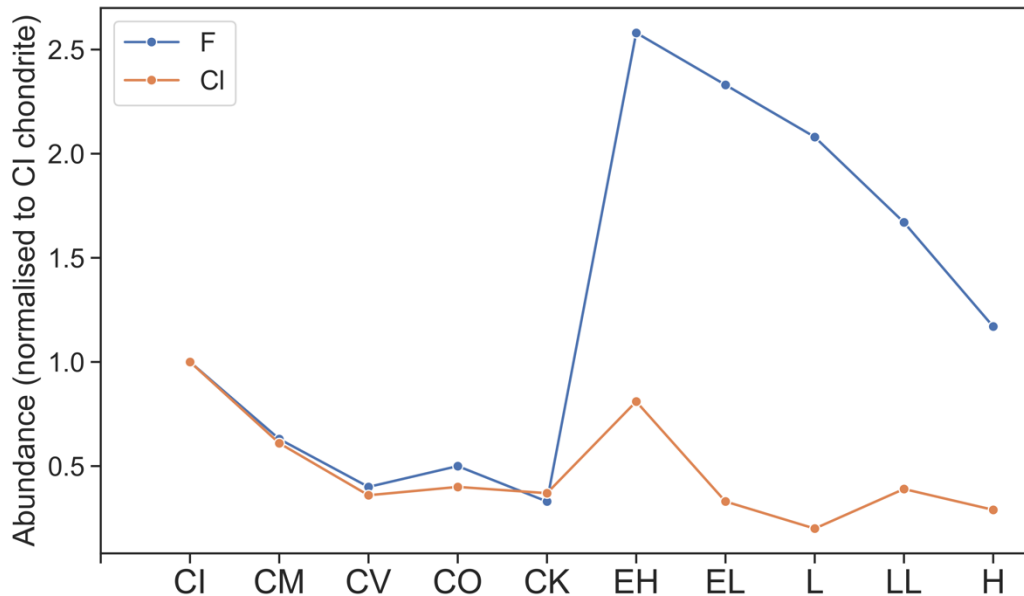


Figure 4.2: F and Cl abundance in chondrite groups normalised to CI chondrite (data from Lodders & Fegley, 1998). Abbreviations for chondrite groups on x axis are as defined in Lodders & Fegley (1998), for the specific meaning of each acronym see Table 1.5.

The behaviour of F and Cl is almost identical in carbonaceous chondrites (CI to CK). This is not true, however, for Enstatite and Ordinary chondrites: in such groups, F is around 5 times more enriched relative to Cl chondrite when compared to chlorine (see Figure 4.2). Indeed, the enrichment of F in more differentiated chondrite classes stands out among the more volatile elements (e.g., N, B), which tend to be more enriched in the carbonaceous chondrites instead (Lodders & Fegley, 1998; Wasson & Kallemeyn, 1986). This points towards a unique incorporation mechanism for F with respect to H, C, N, and B.

Enstatite type chondrites, particularly of the EH subtype, are arguably some of the most F- and Cl-rich chondrites (Rubin & Choi, 2009). Such meteorites also show Si and O stable isotope values similar to Earth, and this evidence is

commonly used to posit Earth's accretion comprised mostly of Enstatite chondrite-like material (Savage & Moynier, 2013). The main F-bearing phases in these meteorites are fluorophlogopite ($K(Mg,Fe)_3AlSi_3O_{10}F_2$), the F-saturated end member of the phlogopite solid solution, and richterite ($K(Na,Ca)Mg_5Si_8O_{22}(F,OH)_2$). In both minerals, F forms a complete solid solution with OH (Rubin & Choi, 2009). Notably, Cl in E-type chondrites is in contrast mostly stored in chondrule glass (Grossman et al., 1985; El Goresy et al., 1988), thus leading to a much less efficient Cl retention mechanism, as it is accumulated in the melt phase (Rubin & Choi, 2009). A similar, albeit less pronounced, discrepancy in light halogen enrichment is also observed in ordinary chondrites (Brearly & Jones, 2018; Lodders & Fegley, 1998).

Richterite and fluorophlogopite are structurally distinct, where the former is an amphibole (Della Ventura et al., 1993) and the latter a mica (Gianfagna et al., 2007). However, both host F^- and OH^- coordinated with Mg, thus suggesting a potential connection between these anions and Mg.

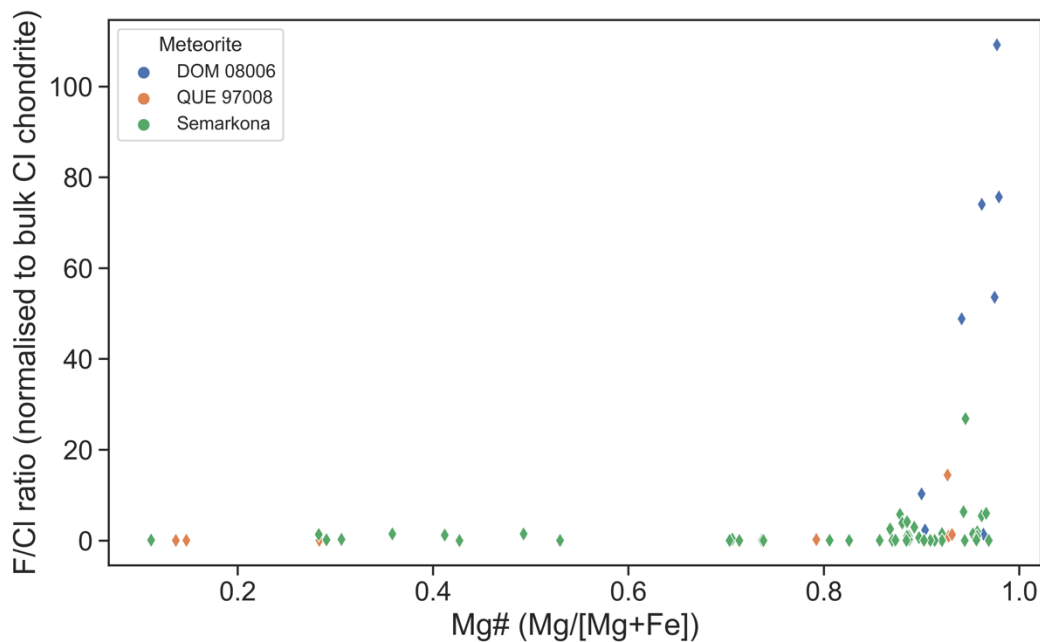


Figure 4.3: F/Cl ratio (normalised to bulk CI chondrite) vs Mg# in two ordinary (Semarkona and QUE 97008) and a carbonaceous (DOM 08006) chondrites (data from Shimizu et al., 2021).

Recently published data for F and Cl abundance in ordinary and carbonaceous chondrites that high Mg# (i.e., Mg/(Mg+Fe) ratio) is associated with F/Cl ratios >1 (see Figure 4.3). Indeed, a high Mg# seems to be a necessary, albeit not completely sufficient, condition for a chondrite to be F enriched relative to Cl, irrespective of the chondrite group. Even more interestingly, measurements by Shimizu et al. (2021) were performed on chondrule glass, thus suggesting the connection between F and Mg might not be limited to mineral phases. It follows that these two elements might be directly coordinating in the melt phase, and this would imply a direct influence of Mg—F local bonding environments on F retention during chondritic evolution.

F speciation in silicate melts has been thoroughly studied, however these investigations were mostly limited to felsic melts with relatively high (i.e., above

1000 $\mu\text{g/g}$) F concentrations (see section 1.4.4). Systems more akin to chondritic environments (i.e., at low pressure and with more mafic composition) are less well understood (Webster et al., 2018). It is currently assumed that F in such contexts tends to form either F—Mg or Al—F—Mg species (Kiczenski et al., 2004). However, these species were observed in melts with a nominal F concentration of $> 1 \text{ wt}\%$, and therefore might not be representative of F speciation in chondrites, where its abundance rarely surpasses 100 $\mu\text{g/g}$ (Lodders & Fegley, 1998; Brearly & Jones, 2018).

4.1.2 – Scope of this study.

This study was designed to investigate the local bonding environment of F in silicate melts of mafic to intermediate model compositions at 1 bar (atmospheric pressure), with F concentrations comparable to chondrites (i.e., between ca. 10 and 200 $\mu\text{g/g}$). These constraints were selected in order to remove any potential effect of higher concentrations (i.e., $\geq 1 \text{ wt}\%$, near saturation levels; Webster et al., 2018; Dolejš & Zajacz, 2018) on F speciation. More specifically, the main composition in this study was CMAS7G (O'Neill & Eggins, 2002), as it is well representative of intermediate silicate melts and has a relatively low melting point of 1129 °C at 1 atm. Alongside this, CMSe (Kushiro, 1972) and MAS1 (O'Neill & Eggins, 2002) were used to investigate the importance of Ca and Al in the system via their omission.

4.2 – METHODS SUMMARY

Six low pressure silicate glasses were synthesized for this study via a muffle furnace (see subsection 2.1.1.2). Composition of samples EdiF_2h, EdiF_4h, EdiF_7.5h and EdiF_18h was CMAS7G (see Table 2.1), with the only difference between them being experimental run time (see Table 2.2). Samples EdiF_MAS1 and EdiF_CMSe were MAS1 and CMSe respectively (see Table 2.1).

The composition of the major elements was analysed by EPMA (see subsection 2.2.3.2). F abundance was initially planned to be quantified by EPMA; however, it was found to be below the limit of detection (134 ug/g). Therefore, ^{19}F MAS NMR was used to measure F concentration (see subsection 2.2.1.3).

MAS NMR was also used to study F speciation (see subsection 2.2.1.2). This was done via collecting NMR spectra from all samples and from two reference materials (i.e., a synthetic fluorophlogopite, $\text{K}(\text{Mg},\text{Fe})_3\text{AlSi}_3\text{O}_{10}\text{F}_2$, and a natural richterite, $\text{K}(\text{NaCa})\text{Mg}_5\text{Si}_8\text{O}_{22}(\text{F},\text{OH})_2$) which are known to contain Mg—F and Al—F bonds. These materials were selected because of the well-known characteristic chemical shifts associated with the Mg/Al—F species present in these minerals, for their relatively low Fe content, and as they are considered to be the main carriers of F in enstatite chondrites (Rubin & Choi, 2008). In addition, synthetic ACS reagent grade $\gamma\text{-Al}_2\text{O}_3$ was employed as a F-free blank sample, which was used to collect an F-free reference background spectrum.

All results and their discussion and interpretation are presented in subchapter 4.3.

4.3 – RESULTS AND DISCUSSION

4.3.1 – Chemical composition.

4.3.1.1 – Glass appearance and major element composition.

All experimental samples appeared to be a clear glass in back-scattered electron imaging, with no apparent heterogeneity. The composition of samples investigated in this study (as determined via EPMA) are summarized in Table 4.1. Samples EdiF_2h, EdiF_4h, EdiF_7.5h and EdiF_18h were all prepared from the same CMAS7G starting mixture (see Table 2.1) and show limited compositional variation (< 0.5 wt%), with the exception of sample EdiF_4h which contains around 1 wt% more SiO₂ than the other CMAS7G samples (see Table 4.1). Variations of this magnitude were deemed compatible with different weighing of the same starting mixture and acceptable for the scope of this study. Samples EdiF_MAS1 and EdiF_CMSe contain minor abundances of CaO and Al₂O₃ respectively, likely due to minor impurities in the starting materials (see subsection 4.3.1.1). F analyses invariably yielded concentrations below the detection limit of the instrument (i.e., 134 µg/g), which is consistent with the results of slow-speed spectrometer scans across the F-K_α peak region using a 100 nA beam current, which did not show any discernable F peak.

Sample	CaO (wt%)	MgO (wt%)	Al ₂ O ₃ (wt%)	SiO ₂ (wt%)	Total (wt%)
EdiF_2h	26.12 ± 0.23	2.49 ± 0.25	12.23 ± 0.51	59.08 ± 0.56	99.91
EdiF_4h	25.66 ± 0.41	2.40 ± 0.12	11.89 ± 0.52	60.01 ± 0.36	99.93
EdiF_7.5h	25.74 ± 0.50	2.48 ± 0.19	12.33 ± 0.37	59.53 ± 0.74	100.09
EdiF_18h	25.47 ± 0.34	2.42 ± 0.07	12.68 ± 0.04	59.21 ± 0.30	99.76
EdiF_MAS1	0.16 ± 0.03	22.31 ± 0.31	16.57 ± 0.23	60.73 ± 0.30	99.77
EdiF_CMSe	19.78 ± 0.30	23.65 ± 0.15	0.27 ± 0.01	56.53 ± 0.20	100.23

Table 4.1: Composition of glasses from this study as measured by EPMA; Fluorine was always below detection limit (ca. 134 µg/g).

4.3.1.2 – F concentration quantification.

As evident from Figure 4.4, all of the ¹⁹F MAS NMR spectra collected from glasses in this study consist of a single broad and low intensity peak centred at approximately –175(±5) ppm, with the exception of EdiF_MAS1 (see Figure 4.5), for which the spectrum likely consisted solely of background noise.

The chemical shift of the signal is consistent with that observed for the richterite reference; however, its width (and poor intensity) prevents the extraction of a more precise chemical shift. For further investigation of F speciation, see subsection 4.3.2.2.

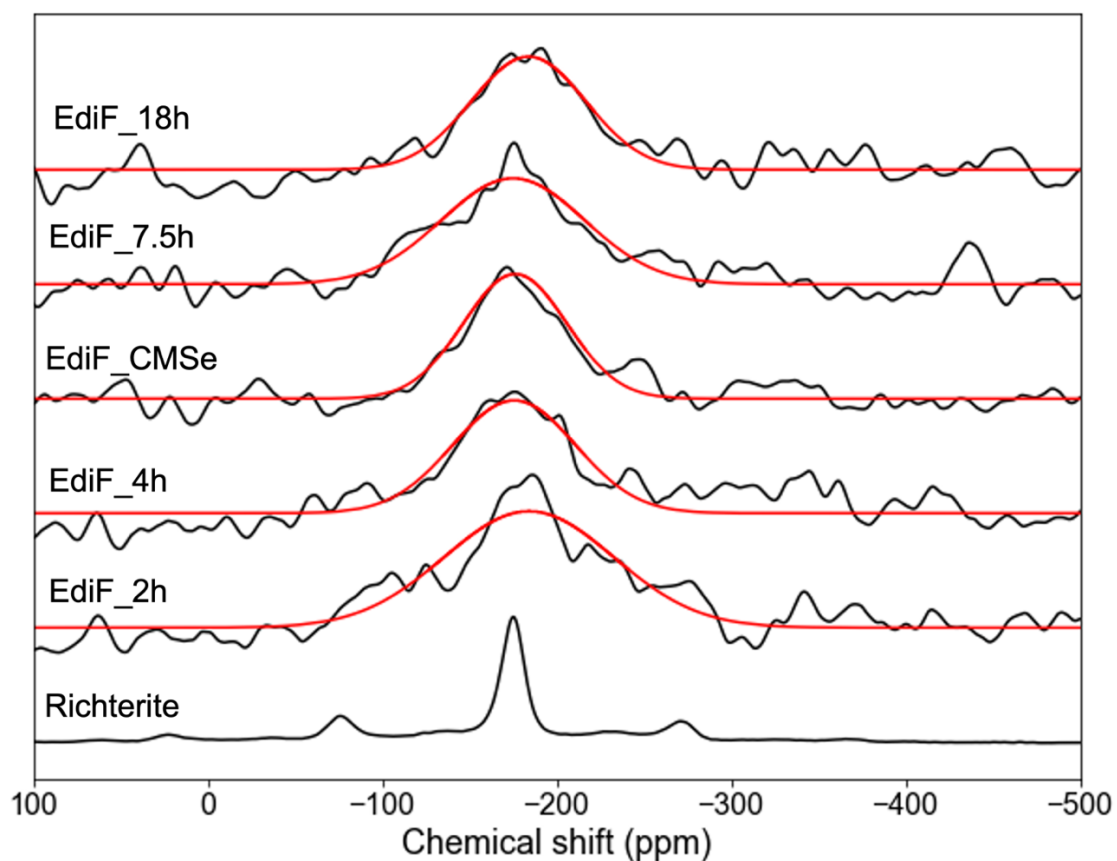


Figure 4.4: ^{19}F MAS NMR spectra collected from glasses of this study, along with analytical fits (red lines) and spectrum collected from the richterite (scaled by a factor of 10^{-3} for graphical purposes) used as a reference standard. Spectra are shown normalised to maximum intensity for ease of comparison. For the precise area under each peak, see Table 4.2. All samples were spun at 30 kHz under a field B_0 of 14.1 T.

Despite the low intensity of the NMR signal collected during each data acquisition, it was still possible to approximate each spectrum with a single gaussian peak. F quantification was thus successful in all samples except for EdiF_MAS1. Results are reported in Table 4.2. The F concentration was determined to be between ca. 7 and 20 $\mu\text{g/g}$ in all glasses except for EdiF_MAS1.

Sample	Sample mass / g	Total peak area (pixels)	F / $\mu\text{g/g}$
EdiF_2h	0.0182	3.73×10^{10}	18.6 ± 1.0
EdiF_4h	0.0168	3.83×10^{10}	19.1 ± 0.4
EdiF_7.5h	0.0158	2.45×10^{10}	12.2 ± 0.7
EdiF_18h	0.0179	1.47×10^{10}	7.4 ± 0.3
EdiF_MAS1	0.0180	//	//
EdiF_CMSe	0.0194	1.44×10^{10}	7.2 ± 0.4
Richterite	0.0198	4.61×10^{11}	230.00

Table 4.2: F concentration in glasses of this study as measured using ^{19}F MAS NMR spectroscopy, and in the richterite standard. No signal was observed in the spectrum collected from sample EdiF_MAS1.

For EdiF_MAS1, quantification was not possible due to lack of signal in the ^{19}F MAS NMR spectrum (see Figure 4.5). Two features are present at -116 and -158 ppm, however as these shifts are not coherent with more detailed analysis of the ^{19}F NMR spectra of the other glasses (see subsection 4.3.2.2), and because of their extremely low intensity, they were considered solely as background signal. The detection limit for the procedure used is presently unknown, however based on the F concentration in EdiF_CMSe (i.e., the glass with the lowest F content) of $7.2 \mu\text{g/g}$, it can be inferred that EdiF_MAS1 has a maximum F concentration of less than ca. $7 \mu\text{g/g}$.

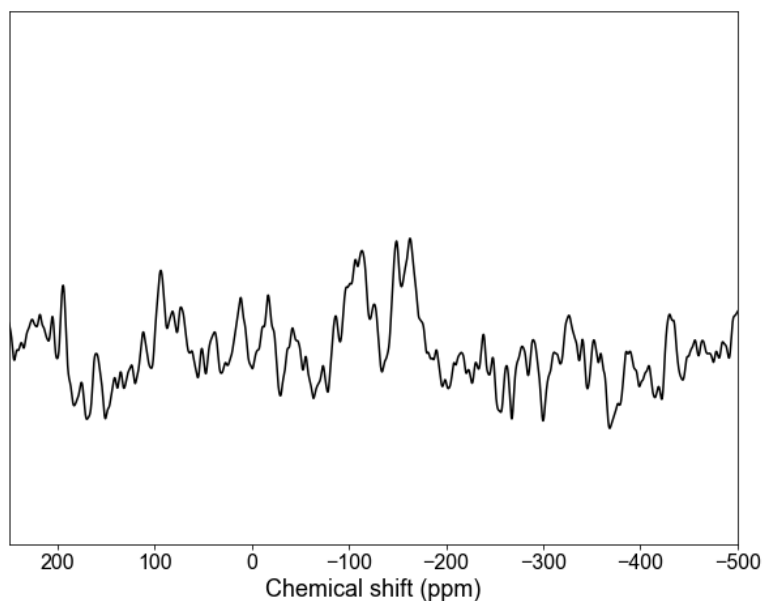


Figure 4.5: ^{19}F MAS NMR spectrum of EdiF_MAS1, consisting of only background noise. The sample was spun at 30 kHz under a field B_0 of 14.1 T.

4.3.2 – Fluorine speciation via ^{19}F MAS NMR spectroscopy.

The ^{19}F MAS NMR spectrum collected from sample EdiF_2h is presented in Figure 4.6, while spectra from all other glasses and from reference materials are in Figure 4.7. A broad gaussian peak centred at approximately -175 ± 3 ppm is feature common to all of the glass spectra. In addition, the spectrum of EdiF_2h contains a further peak, centred at ca. -132 ± 1.7 ppm.

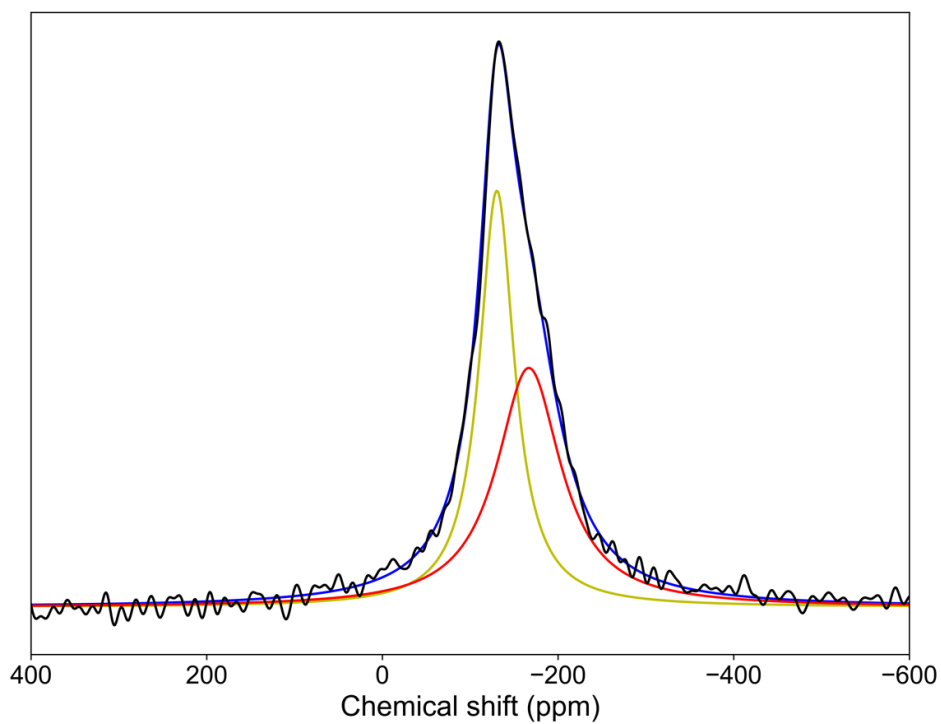


Figure 4.6: ^{19}F MAS NMR spectrum of EdiF_2h, along with peak fitting (blue line) and deconvolution (red and yellow). The sample was spun at 30 kHz under a field B_0 of 14.1 T, corresponding to a Larmor frequency of 564.7 MHz.

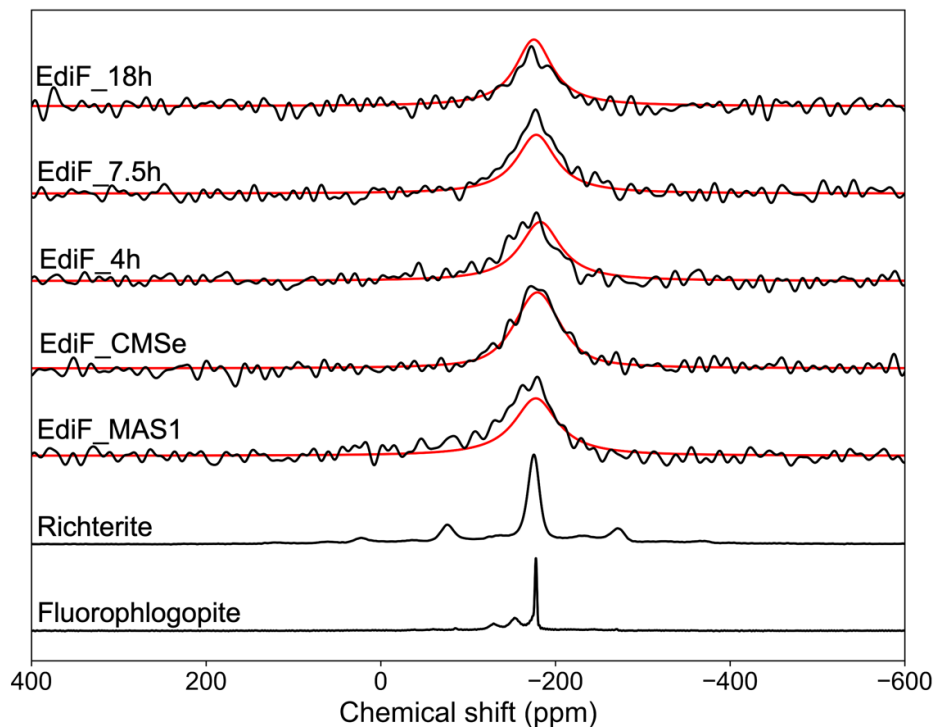


Figure 4.7: ^{19}F MAS NMR spectra of glasses in Table 4.3 (for EdiF_2h, see Figure 4.5), along with analytical fits (red lines). All spectra are reasonably consistent with a single broad peak centred at $-175(\pm 3)$ ppm. Spectra collected from standard materials are also shown. The spectrum collected from sample EdiF_MAS1 was scaled up by a factor of 1.8 for graphic consistency. Spectra from richterite and fluorophlogopite reference materials were scaled down instead, for the same reason. All samples were spun at 30 kHz under a field B_0 of 14.1 T.

The ^{19}F MAS NMR spectra of richterite and fluorophlogopite reference materials are also presented in Figure 4.7. The spectrum from the natural richterite consists of a main peak centred at -175 ± 0.7 ppm, along with spinning sidebands. The spectrum of synthetic fluorophlogopite consists of three peaks, a major signal centred at -177 ± 0.2 ppm, and two low intensity signals at -155 ± 1.9 and -130 ± 1.1 ppm, respectively. Low intensity spinning sidebands are also observed.

Chemical shifts of the centre band signals in the ^{19}F MAS NMR spectra of the reference materials and silicate glasses are summarised in Table 4.3.

Sample	Chemical shift (ppm)
EdiF_2h	$-132\pm 1.7, -175\pm 3$
EdiF_4h	-175 ± 3
EdiF_7.5h	-175 ± 3
EdiF_18h	-175 ± 3
EdiF_MAS1	-175 ± 3
EdiF_CMSe	-175 ± 3
Richterite	-175 ± 3
Fluorophlogopite	$-177\pm 0.2, -155\pm 1.9, -130\pm 1.1$

Table 4.3: ^{19}F chemical shifts of signals present in the spectra shown in Figure 4.7.

4.3.2.1 – Peak assignment in reference materials.

The three main peaks in the fluorophlogopite ^{19}F MAS NMR spectrum result from the three local bonding environments, all corresponding to non-planar arrangements where either Mg and/or Al from the octahedral layer of the mica are coordinated to a F atom located above it (Laboriau et al., 1995): [1] the peak at -177 ± 0.2 ppm corresponds to a Mg(3)—F complex, with 3 Mg atoms coordinated to one F atom (Fechtelkord et al., 2003; Huve et al., 1992); [2] the peak at -155 ± 1.9 ppm corresponds to a Mg(2)Al—F complex, with 2 Mg and 1 Al atoms coordinated with 1 F (Fechtelkord et al., 2003; Huve et al., 1992); and

[3] the peak at -130 ± 1.1 ppm corresponds to a Al(2)—F group, with 2 Al atoms coordinated with 1 F (Huve et al., 1992).

As evident from the spectra in Figure 4.7, the vast majority of the F contained in the synthetic fluorophlogopite analysed for this study is consistent with Mg(3)—F local bonding environments, with only a minor fraction neighbouring Al atoms. This agrees with the well-known tendency of F to prefer Mg over other cations (i.e., Fe and Al) as a coordinated neighbour in the framework of micas (Laboriau, 1995; Sanz & Stone, 1983).

The richterite spectrum exhibits a single peak centred at -175 ± 0.7 ppm (see Figure 4.7), which corresponds to a Mg(3)—F complex (Raudsepp et al., 1987) similar to that in fluorophlogopite (Robert et al., 1989). Therefore, all F can be considered as coordinated to Mg in the richterite analysed for this study.

4.3.2.2 – F speciation in silicate glasses.

Two peaks were observed in the ^{19}F MAS NMR spectra of the silicate glasses in this study (see Table 4.3): [1] one centred at -175 ± 3 ppm, which is present in all spectra, and [2] another centred at -132 ± 1.7 ppm, present solely in sample EdiF_2h.

The chemical shift of peak [1] agrees with that observed for a Mg(3)—F geometry (see Figure 4.8), as observed in both reference samples. It therefore follows that this peak corresponds to Mg(3)—F environments within the silicate melts, in accordance with observations from Kiczenski et al. (2004). The broadness of this feature, when compared to the sharpness of the peaks at the same chemical shift from crystalline reference materials, is evident of the Mg(3)—

F groups being dissolved in the melt structure and not incorporated in a crystalline structure (Ashbrook et al., 2014). As these species are present in all glasses regardless of the composition and experimental synthesis time, it is also likely that this form of F is stably incorporated in the melt structure, and thus that it is unlikely to be lost due to degassing processes.

The chemical shift of peak [2], -132 ± 1.7 ppm, consistent with either Al(2)—F groups (as observed in the fluorophlogopite; see subsection 4.3.2.1; Huve et al., 1992), or possibly Ca—F(2) groups in a CaF₂—like geometry (Miller, 1996; Li et al., 2014). While the likelihood of F being bonded to Al cannot be fully discounted, this peak is more likely related to Ca—F groups. This is because sample EdiF_2h arguably did not reach full equilibration (see section 4.3.3), and Ca—F complexes are due to the yet incomplete dissolution of the CaF₂ present in the starting mixture (Kiczenski & Stebbins, 2002). Conversely, if this peak was due to Al(2)—F groups, this would imply that during melting F disconnects from Ca to partially bind with Al (sample EdiF_2h), only for this bond to be broken shortly after and for all F to then bind to Mg (sample EdiF_4h and onwards). While this is by no means impossible, there is no direct evidence supporting this hypothesis, and therefore it was concluded that peak [2] represents Ca—F(2) groups (Miller, 1996).

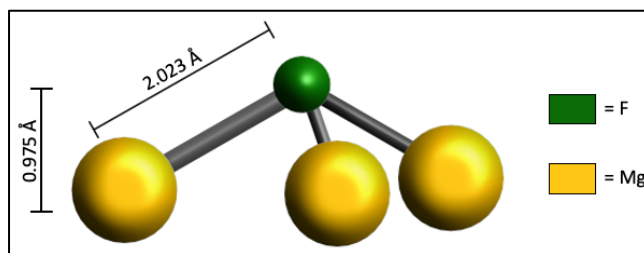


Figure 4.8: Local geometry of the Mg(3)—F species dissolved in the melts of this study. Modelled after the richterite described by Robert et al. (1989).

In summary, trace concentration of F in CMAS silicate melts at atmospheric pressure are stably incorporated into the melt structure as Mg(3)—F species, and even dramatic compositional changes (i.e., the almost total removal of either Al or Ca) have seemingly little impact on its speciation.

4.3.3 – Attainment of equilibrium.

The ^{19}F MAS NMR spectrum of sample EdiF_2h contains two signals, one corresponding to F bonded to Ca in a CaF_2 -like structure, suggesting the likely incomplete dissolution of the CaF_2 in the silicate melt. This dual speciation occurs only in EdiF_2h, which was held at high temperature for only 2 h, while all other samples held at high temperature for longer (see Table 2.2) show a constant F speciation, with only Mg—F species present. This indicates an equilibrium F distribution in the melt structure involves a transfer from Ca—F to Mg—F bonding only, as postulated by Kiczenski et al. (2004). Based on the discussion so far, all samples except for EdiF_2h are thus considered as fully equilibrated.

It is worth noting that the majority of the F was lost either during or before the melting process: the CMAS7G starting mixture contained around 4220 $\mu\text{g/g}$

of F, while MAS1 and CMSe mixtures contained ca. 4000 and 3900 $\mu\text{g/g}$ of F, respectively (see Table 2.1). All the glasses produced in this study, however, contain less than 20 $\mu\text{g/g}$ of F (see Table 4.2). Notably, the F concentration is remarkably consistent over all samples with the exception of EdiF_MAS1, suggesting that the Mg—F groups, remaining after the disappearance of Ca—F species during the melt equilibration process, are stably incorporated in the melt structure.

For EdiF_MAS1, the main difference between the synthesized glasses lies in the starting mixture, which contained MgF_2 as an F-enrichment agent, as opposed to the CaF_2 present for all other samples. EdiF_MAS1 was equilibrated at 1450 °C, in comparison to the 1250°C used for the CMAS7G samples, due to the higher melting point of the MAS1 composition. It is possible that the higher temperature contributed to a higher degree of F depletion from the melt.

4.3.4 – Implication for F storage during chondritic evolution.

F in the CMAS, MAS and CMS melts of this study, where it is stored as a Mg(3)—F species, is effectively behaving as a non-bridging oxygen (NBO), as previously postulated by Kiczenski et al. (2004), meaning that it only binds to network modifying cations (e.g., Ca, Mg) in the melt structure. This is facilitated by F^- having a relatively similar ionic radius to O^{2-} (133 and 152 pm respectively), when compared with the other halogens (e.g., Cl^- has an ionic radius of 175 pm). At

the concentrations used in this study (i.e., at the order of magnitude of F abundance in chondrites and BSE; Harlov & Aranovich, 2018), F formed no network forming species (e.g., Si—F and Al—F). All studies that report such species are based on samples with F concentrations above ca. 1000 $\mu\text{g/g}$ (Kiczenski & Stebbins, 2002; Stebbins & Zeng, 2000; Kiczenski et al., 2004; Baasner et al., 2014).

During the chondrite cooling processes, it is plausible that the Mg(3)—F species present in the melt structure were easily incorporated as is into the mineral components. This hypothesis is supported by the fact that in the chondrites with the highest F concentrations (i.e., E-types), the main F-hosting phases are richterite and fluorophlogopite (Rubin & Choi, 2008). Both these minerals store F in non-planar Mg(3)—F geometries (Hazen & Burnham, 1973) akin to the ones observed in the structure of glasses of this study. Indeed, a preference for Mg—F over Al—F, and especially Fe—F, in the framework of high-temperature phyllosilicates has been extensively documented (Mason, 1992; Huve et al., 1992). It must, however, be noted that a direct connection between these two phenomena has yet to be observed.

Cl, when compared to F, likely has too large an ionic radius to be stored via the same mechanism, thus being retained by the melt (e.g., in chondrule glass; Grossman et al., 1985; El Goresy et al., 1985). As shown in Figure 4.3, a high Mg# is sometimes linked with a high F/Cl ratio (Shimizu et al., 2021), evidencing how, while other yet unclear processes are likely at play, the local connection between Mg and F in the melt structure is relevant in the preferential

retention of F over Cl and the other halogens in chondritic meteorites (Hanley & Koga, 2018).

4.4 – CONCLUSIONS

The higher compatibility of F in comparison to the other halogens has historically been attributed to its similarities with O (Harlov & Aranovich, 2018). The present study concerned the speciation of fluorine in high temperature synthesis of CMAS, MAS and CMS model systems at a pressure of 1 atm. ^{19}F MAS NMR spectra from equilibrated samples showed that at low abundance (i.e., 10s of $\mu\text{g/g}$), akin that in the BSE and in Cl chondrites, F binds uniquely with Mg, resulting in the formation of Mg(3)—F environments similar to those observed in Mg-rich phyllosilicates (e.g., fluorophlogopite; Hazen & Burnham, 1973; Robert et al., 1993; Gianfagna et al., 2007) and amphiboles (e.g. richterite; Robert et al., 1989). Therefore, F^- under these conditions is found solely in non-bridging sites in the melt.

Enstatite type chondrites are arguably the most F-enriched chondrites (Lodders & Fegley, 1998). The main F reservoirs in these meteorites are fluorophlogopite and richterite (Rubin & Choi, 2008). Based on the results of this study, it can be hypothesized that Mg(3)—F complexes formed in the melt phase are the favoured mode of F incorporation in such minerals, thus promoting its retention by E-type chondrites over other meteorites. It is also worth noting that high Mg# (Mg/Mg+Fe) values are linked to marked increase in the F/Cl ratio of chondrules in both carbonaceous and ordinary chondrites (Shimizu et al., 2021).

This points to a potential Fe—F and Al—F avoidance in the melt structure, which has been thoroughly studied (Mason, 1992; Huve et al., 1992, and refs. therein) in high-temperature phyllosilicates (e.g., biotite, phlogopite), in which F is stored in sites similar to the Mg(3)—F species detected in the melts of this study. This is another relevant difference between F and Cl, with the latter showing no such avoidance of Fe or Al.

Based on the results of this study, the formation of Mg(3)—F species in low pressure silicate melts is the likely reason behind the higher compatibility of F than the other halogens. The formation and stability of these bonding environments is likely driven by the comparatively smaller ionic radius of F and its higher electronegativity (Rubin & Choi, 2008). However, to fully confirm this hypothesis, measurements of coexisting F and Cl speciation in a silicate melt is of paramount importance. Furthermore, while Mg(3)—F complexes are likely to be carried over from the melt to crystallising phases, direct experimental evidence is still lacking in this regard.

~5 — INVESTIGATING THE EFFECTS OF PRESSURE ON F SPECIATION IN CMAS SILICATE MELTS USING ¹⁹F MAS NMR SPECTROSCOPY~

5.1 – INTRODUCTION

Fluorine is the most enriched volatile element in the BSE at 25 $\mu\text{g/g}$ (McDonough & Sun, 1995), which is close to its abundance in CI chondrites of 60 $\mu\text{g/g}$ (Lodders & Fegley, 1998). As mentioned previously in section 1.1.2, fluorine is one order of magnitude more enriched in the Bulk Silicate Earth relative to both chlorine and the hydroxide ion, two anions which both possess an identical charge of -1 and similar electronegativity and ionic radius, especially in the case of OH^- (see Table 5.1).

Ion	Ionic radius / pm	Electronegativity
F^-	133	3.98
OH^-	133	3.55*
Cl^-	175	3.16

Table 5.1: Ionic radii and electronegativities of F, Cl and OH in their monovalent ionic form.

Electronegativity is given in Pauling units. * = group electronegativity, as defined by Gupta (2016).

Both F and Cl are classified as moderately volatile elements (Wood et al., 2019), while the heavier halogens (i.e., Br and I), due to their heavier weights and larger ionic radii are regarded as highly volatile elements (Lodders, 2003). This is reflected in their geochemical compatibility, with the latter being markedly more incompatible than the former (Harlov & Aranovich, 2018). The most similar anion to F⁻ is instead OH⁻, however F has been shown to be more compatible than OH in igneous minerals (Potts et al., 2021; Dalou et al., 2012; Mosenfelder & Rossman, 2013), and differences in their incorporation mechanisms and in their chemical speciation in the melts from which said minerals crystallise could be the key to explain their different level of enrichment in the BSE (see Figure 1.1).

5.1.1 – Fluorine in the BSE.

In the BSE, fluorine is hosted by phases with a stoichiometric F contents (e.g., phlogopite, humite group minerals) and by nominally anhydrous minerals (NAMs, e.g., olivine, pyroxenes), usually forming a solid solution with OH⁻ (Clay, 2021; Potts, 2021). The vast majority of the Earth's mantle comprises NAMs, thus the incorporation of F in NAMs is important. The sites at which F is located in the framework of NAMs are of various types (Beyer et al., 2012). The main substitution mechanisms for F in common BSE phases are:

1. Humites: Humite group minerals ($n((\text{Mg}, \text{Fe}^{\text{II}})_2\text{SiO}_4).(\text{Mg}, \text{Fe}^{\text{II}})(\text{F}, \text{OH})_2$, $1 < n < 4$) consist of a number (n) of olivine-like layers alternating with brucite/sellaite layers (commonly just referred to as “brucite layers” for simplicity), with $n = 1$ corresponding to norbergite, $n = 2$ to chondrodite, $n = 3$ to humite and $n = 4$ to clinohumite. When n is larger than 4, the brucite

layers are typically defined as “humite-type planar defects” in olivine crystals. Humite group minerals and humite-type planar defects in olivine crystals can contain potentially very large amounts of H₂O, depending on the occupancy of the F/OH site and on the value of n. A F/(F+OH) fraction of 0.25 in this site has a positive impact on the stability of the via the formation of H-bonds between neighbouring F and OH ions (Friedrich et al., 2002; Griffin et al., 2010). Consequently, the field of stability for F-rich humite-group minerals extends below the upper mantle and well into the transition zone (Grützner et al., 2017; Stalder & Ulmer, 2001). However, while F-rich clinohumite and chondrodite have been found in naturally occurring minerals in mantle xenoliths (Aoki et al., 1976), the occurrence of humite-type planar defects is yet to be directly observed in nature (Joachim et al., 2015).

2. Olivine: The $[\text{MgO}_2]^{2-} \leftrightarrow [\otimes\text{F}_2]^{2-}$ (\otimes = vacancy) substitution in forsterite (Bernini et al., 2013) mirrors the incorporation mechanism of OH⁻ via the formation of an Mg vacancy in the octahedral site observed in the same phase (Smyth et al., 2006). The OH solubility that can be achieved via this substitution is between 54 and 375 μg/g at upper mantle conditions (Mosenfelder et al., 2006), with similar values measured for F (Bernini et al., 2013). However, in a partial analogy to mechanism [1], OH/F sites clustered around Mg vacancies appear to be more favourable than isolated defects, particularly in the case of mixed OH⁻ and F⁻ occupancy of the neighbouring sites (Crepisson et al., 2014), due once again to H-bond formation between the two ions, caused by the orientation of the H⁺

ion (positively charged) of the OH group towards the negatively charged neighbouring F⁻ ion.

3. Clinopyroxene: ${}^{\text{IV}}\text{Al}^{3+} + \text{F}^{-} \leftrightarrow {}^{\text{IV}}\text{Si}^{4+} + \text{O}^{2-}$ and $\text{Na}^{+} + \text{F}^{-} \leftrightarrow \text{Ca}^{2+} + \text{O}^{2-}$ exchanges are thought to be the main mechanisms responsible for F storage in clinopyroxenes (Mosenfelder & Rossman, 2013). The former seems to be of particular relevance in diopside (Beyer et al., 2012), while other clinopyroxenes (e.g., omphacite) show a less strong correlation between F and Al content (Dalou et al., 2012), whereas the latter mechanism is more prominent in augite (Mosenfelder & Rossman, 2013).
4. Orthopyroxenes: The ${}^{\text{VI}}\text{Al}^{3+} + \text{F}^{-} \leftrightarrow 2 \text{Mg}^{2+} + \text{O}^{2-}$ substitution is the only currently documented mechanism for F incorporation in orthopyroxenes (Bernini et al., 2013), which themselves generally contain less F than clinopyroxenes (Mosenfelder & Rossman, 2013b; Hauri et al., 2006).
5. Garnets: F is primarily incorporated via the so-called hydrogarnet substitution (Bernini et al., 2013; and refs. therein), which consists of the $\otimes(\text{OH}/\text{F})_4^{4-} \leftrightarrow [\text{SiO}_4]^{4-}$ (\otimes = vacancy) equilibrium exchange. This causes the formation of a vacancy in place of the Si atom at the centre of the tetrahedra, thus triggering a notable increase in molar volume due to the lack of a positively charged Si ion (Lager et al., 1987). At pressures of ≤ 1 GPa the solubility is of a similar order of magnitude as the wt% (Manning & Bird, 1991). However, the presence of a Si vacancy implies his mechanism will exhibit a high sensitivity to pressure increases, which by compressing the framework cause the negative ions to progressively be

pushed closer to each other, thus leading to the noticeably lower F solubilities observed at pressures above 2.5 GPa (Bernini et al., 2013).

The mechanisms in [1] for F incorporation have F locally binding to Mg in the crystal lattice, and mechanism [2] has Mg and F both involved in the same substitution, though they are not bonded with each other. Meanwhile, mechanisms [3] and [4] have F bonded with Al. Mg—F and Al—F based complexes are also found in phases that contain stoichiometric F, such as phlogopites and amphiboles (Klemme & Stalder, 2018), while in other phases, such as apatite, F is coordinated to Ca (Frezzotti & Ferrando, 2018). Despite Mg, Al and Ca being all major constituents of the BSE, the most abundant cation ion here is Si (Allègre et al., 1995), yet Si—F bonding environments are strangely underrepresented in the upper mantle minerals, with the partial exception of mechanism [5], which does not feature Si—F complexes but sees the two elements being part of the same substitution (Bernini et al., 2013). Hence, the abundance of major elements alone is not sufficient to explain the speciation of F in upper mantle phases, suggesting that these bonding environments might be partially inherited from the melt phase from which minerals crystallize (Bernini et al., 2013; Beyer et al., 2012).

5.1.2 – Fluorine in silicate melts.

The solubility of F in silicate melts can be as high as 18 wt% in exotic $\text{NaF}_2\text{—SiO}_2$ model systems (Mysen & Virgo, 1985). However, in more geologically relevant systems (i.e., with more than two components) the solubility of F is much lower (Webster et al., 2018).

For F speciation, most studies have so far focused on granitic melts at crustal pressures (Dolejš and Zajacz, 2018). F tends to bind to Al and Na over Si in NAS ($\text{Na}_2\text{O—Al}_2\text{O}_3\text{—SiO}_2$) systems (Liu & Nekvasil, 2002), and more specifically Na—F and Na—F—Al species have been reported in nepheline, jadeite, and albite systems (Schaller et al., 1992; Mysen et al., 2004). When alkali earth elements are added to the system, and the composition becomes more akin to intermediate and mafic melts, and Ca—F (Luth, 1988) and Mg—F (Kiczenski et al., 2004) species become prevalent, but Na—F—Al groups are also relevant because the systems contain alkali metals with high activities (Baasner et al., 2014).

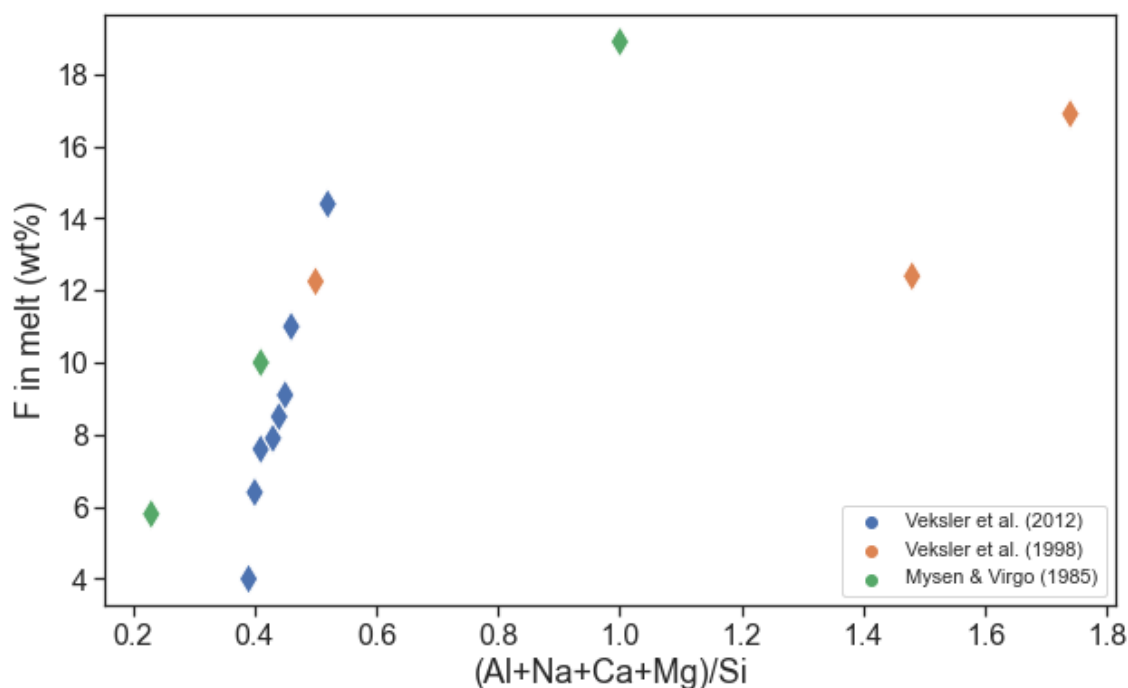


Figure 5.1: Plot showing the correlation between the (Al+Na+Ca+Mg)/Si ratio and F abundance in different melt compositions: Mysen & Virgo (1985) is NS ($\text{Na}_2\text{O}+\text{SiO}_2$), Veksler et al. (1998) is KCMAS ($\text{K}_2\text{O}+\text{CaO}+\text{MgO}+\text{Al}_2\text{O}_3+\text{SiO}_2$) and Veksler et al. (2012) is KNAS ($\text{K}_2\text{O}+\text{Na}_2\text{O}+\text{Al}_2\text{O}_3+\text{SiO}_2$).

F abundance in the melt phase strongly correlates with melt composition (expressed as the ratio of (Al+Na+Ca+Mg)/Si in Figure 5.1; Webster et al., 2018; and refs. Therein). This shows that Si is not a favourable bonding partner for F in the melt structure, despite it often being the most abundant element in the system.

It must be pointed out that studies carried out at pressures above ca. 3 GPa in this field are exceptionally rare: one exception is work by Brey et al. (2009), which reports Ca- and Mg-based F species at pressures up to 6 GPa. Karpukhina et al. (2007) reported on the increased stability of Al—F species when Al is V- and VI-fold coordinated (i.e., network modifying) over IV-fold (i.e., network forming) Al, yet studies at pressures where the former state is vastly prevalent over the latter (i.e., above 5 GPa) are lacking (Webster et al., 2018).

5.1.3 – Scope of this study.

This study was designed to investigate changes, or lack thereof, in F speciation as a function of pressure (from 1 to 20 GPa) in silicate melts under isothermal conditions in a model anhydrous silicate system (CMAS7G). These conditions were chosen as representative of the planetary-scale partial melting events that occurred during the later accretionary stages of the Earth (Nakajima & Stevenson, 2015), during which the F was transferred to the thus formed silicate melts and then re-incorporated into mineral phases more efficiently than the other volatiles, due to its higher compatibility.

Data about F speciation at high pressure are currently scarce (see section 5.1.2), and it was thus decided to investigate if and how changes in the average coordination number (see Figure 5.2) of the elements with which F binds within the melts structure had an impact on its speciation.

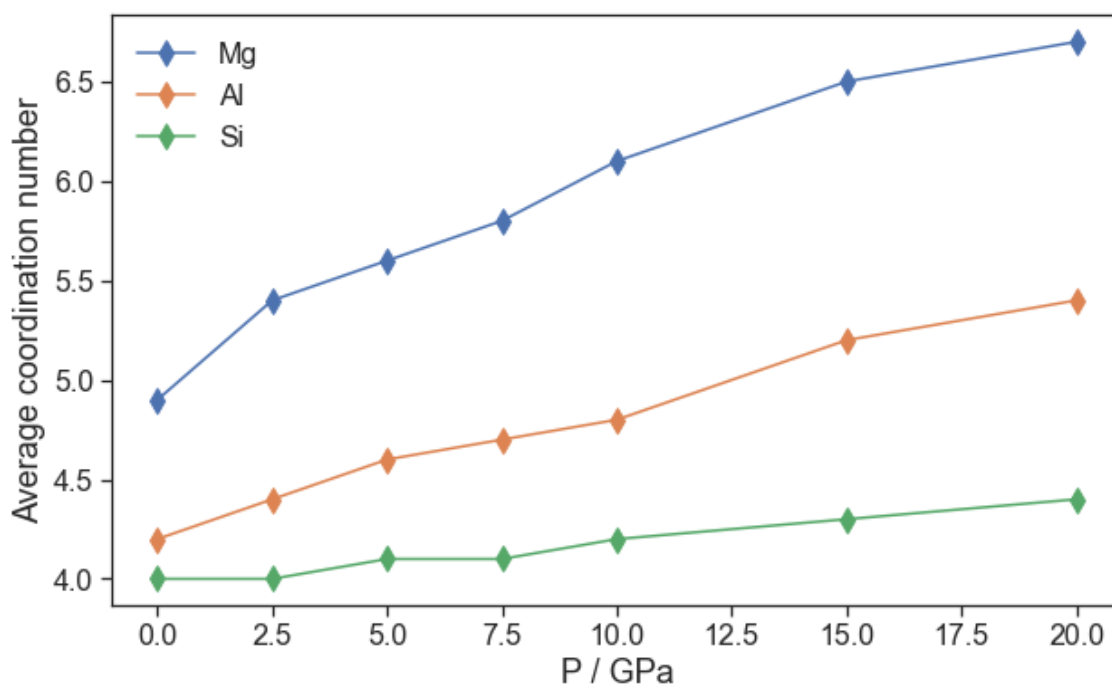


Figure 5.2: Plot showing changes in average coordination state of Mg, Al and Si in a Mid Ocean Ridge Basalt (MORB) melt as a function of pressure (P), at a temperature (T) of 2273 K. Data from DFT calculations by Solomatova & Caracas (2019).

5.2 – METHODS SUMMARY

Six high pressure silicate melts were synthesized for this study. Composition was CMAS7G (see Table 2.3) for all samples. Samples EdiF_01 and EdiF_02 were synthesized via a piston cylinder press, at a pressure of 2 and 1 GPa respectively, following the procedure in subsections 2.1.2.2 and 2.1.2.3, while samples BayF_01, BayF_02, BayF_03 and BayF_04 were synthesized via first preparing a CMAS7G glass at 1 atm (see subsection 2.1.1.2 for the procedure used) and then annealing the glass via a multi anvil press (see subsection 2.1.2.5) at the desired pressure (see Table 2.6).

As shown in Figure 5.3, the highest P at which a CMAS7G liquid has been produced is 8 GPa (Mare, 2017). The melting point at higher pressures must, therefore, be extrapolated from known P-T conditions of total melting (see Figure 5.3). The issue with this approach is that the further the extrapolation from known melting conditions, the greater the uncertainty is (Stebbins et al., 1995). Even if the melting temperature of CMAS7G increases linearly with pressure from the conditions shown in Figure 5.3, it would reach upwards of ca. 3000 °C at 20 GPa, which was the highest pressure in this study. Such a temperature would be an issue for the experimental set up, as the melting point of Pt, routinely used for the sample-bearing capsules, is 2268 (± 97) °C at 20 GPa (Kavner & Jeanloz, 1998), therefore a different material and set up would have been required, at the cost of consistency between the different experiments. Furthermore, the quenched glasses would not be representative of these temperatures, as the temperature recorded by a glass during its formation is the glass transition temperature (Webb & Dingwell, 1990). For the reasons described thus far, it was decided that instead of using a melt-quench procedure analogous to that utilised for piston cylinder experiments, it was decided to instead perform the annealing of glasses pre-synthesized at 1 atm of pressure.

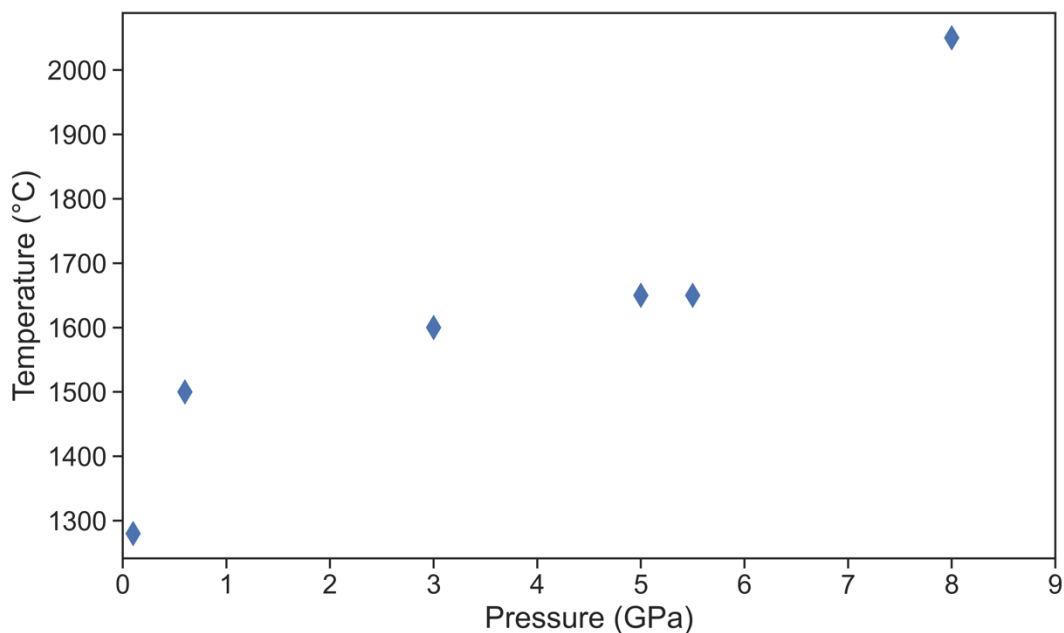


Figure 5.3: P-T conditions at which total melting of the CMAS7G composition occurs (Mare, 2017; O'Neill & Eggins, 2002).

Major elements composition and glass appearance was investigated only for sample BayF_01 via EPMA (see subsection 2.2.3.3). Sample BayF_04 and the starting glass for multi anvil synthesis were studied via Raman spectroscopy (see subsection 2.2.2.2) to evaluate the differences in average coordination state of the major elements of the glass structure, and to identify any potential crystalline phase in sample BayF_04. ^{19}F MAS NMR was used to measure F concentration and speciation (see subsections 2.2.1.2 and 2.2.1.3) in all samples.

Results of all analyses are presented in subchapter 5.3, and their discussion and interpretation are in subchapter 5.4.

5.3 – RESULTS

5.3.1 – Chemical and phase composition.

5.3.1.1 – Glass appearance and major element composition.

Owing to the relatively small amount of glass produced using the high-pressure apparatuses (i.e., tens of mg at most), even the removal of a few mg for EPMA analyses would have had a notable impact of the amount of sample available for NMR experiments. Therefore, it was decided to analyse only one of the four samples produced using the multi anvil press, as all were prepared from the annealing of the same starting glass. For the samples produced using the piston cylinder press, relevant sample loss during the capsule opening process resulted in the need to preserve the full amount of sample available for NMR experiments, and hence both glasses were ground and no EPMA investigation was performed. This was not deemed an issue, as the only critical concentration to measure was that of fluorine, which was carried out using NMR spectroscopy. In summary, therefore, only sample BayF_01 was analysed using EPMA. The sample appeared as a clear homogeneous glass in back scattered electrons imaging (see Figure 2.15). The major element composition is reported in Table 5.2.

	CaO (wt%)	MgO (wt%)	Al₂O₃ (wt%)	SiO₂ (wt%)	F (wt%)	Total
BayF_01	27.30	2.45	11.15	59.10	b.d.l.	100.00

Table 5.2: Chemical composition of BayF_01 as measured using EPMA. Abundances are normalised to 100 wt%. b.d.l. = below detection limit (200 µg/g).

5.3.1.2 – F concentration quantification using ¹⁹F MAS NMR.

Figure 5.4 shows that the spectra collected from the glasses all contain a broad signal, although all have different shapes. As the total F concentration is determined only from the integrated intensity of the total signal the investigation of the individual components which, when convoluted, resulted in the final feature, was not of interest in the context of this set of analyses. For a detailed study of the nature of the features of each spectrum (i.e., F speciation), see section 5.3.2.

All spectra were fitted using two Gaussian peaks, except those for BayF_01, BayF_02 and BayF_04, for which a single Gaussian peak was sufficient. The integrated intensity was then calculated, and the F concentration derived as described in subsection 2.2.1.3. The resulting F concentrations are summarised in Table 5.3.

Sample	Sample weight / g	Total peak area / pixels	F ($\mu\text{g/g}$)
Starting glass	0.0165	1.24×10^{11}	62 ± 1
EdiF_02	0.0053	1.38×10^{11}	69 ± 11
EdiF_01	0.0175	6.78×10^{10}	36 ± 2
BayF_03	0.0025	4.27×10^{10}	30 ± 12
BayF_04	0.0018	1.29×10^{11}	64 ± 13
BayF_02	0.0014	7.53×10^{10}	38 ± 15
BayF_01	0.0070	1.16×10^{11}	58 ± 5
Richterite	0.0198	4.61×10^{11}	230

Table 5.3: F concentration in glasses of this study as measured using ^{19}F MAS NMR, and in the richterite reference standard. The error on the F concentration is given at the 2σ interval. F concentration in richterite is from Pearson et al. (2003).

The F concentration was determined to be between 30 and 70 $\mu\text{g/g}$ in all samples, including the starting glass for multi anvil experiments. It is evident that the annealing process caused no measurable loss of F from the system. The concentration in BayF_01 was measured at 58 $\mu\text{g/g}$, which is consistent with this being well below the 200 $\mu\text{g/g}$ detection limit of the EPMA used for F quantification. Notably, the F concentration in samples EdiF_01 and EdiF_02, both produced using the piston cylinder press, is on the same order of magnitude, despite the different synthetic procedure.

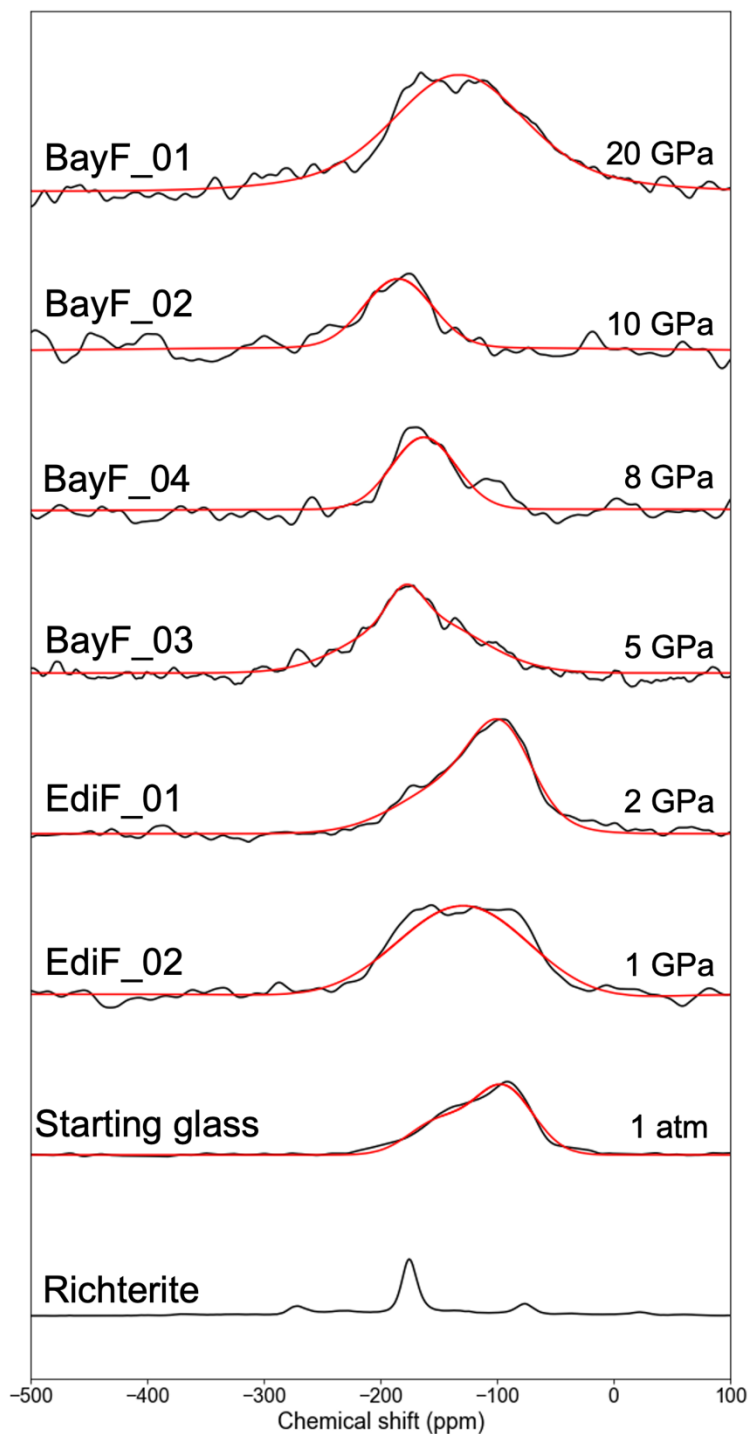


Figure 5.4: ^{19}F MAS NMR spectra collected from glasses of this study, fitted for F quantification (fitted peak is in red), and spectrum collected from the richterite (scaled by a factor of 2×10^{-3} for graphical purposes) used as a reference standard. Spectra are not scaled relative to each other, i.e., the area under each feature in this figure is not representative of F concentration. For the precise area under each peak, see Table 5.3. All samples were spun at 30 kHz under a field B_0 of 14.1 T.

5.3.1.3 – Phase characterization using Raman spectroscopy.

The Raman spectra collected from BayF_04 and the starting glass for multi anvil annealing experiments are shown in Figure 5.5. Owing to its synthetic nature, the starting glass was known to lack any long-range order. Both Raman spectra consist of two very broad features, in the 820 to 1200 cm^{-1} and 230 to 800 cm^{-1} regions. The first is consistent between both spectra, whereas the second goes from a symmetric Gaussian shape for the starting glass to an asymmetric feature with a maximum at ca. 620 cm^{-1} , which could be described as the sum of two Gaussian peaks.

The absence of any sharp peak was deemed sufficient to exclude the presence of major crystalline phases in BayF_04, therefore no further investigation was carried out.

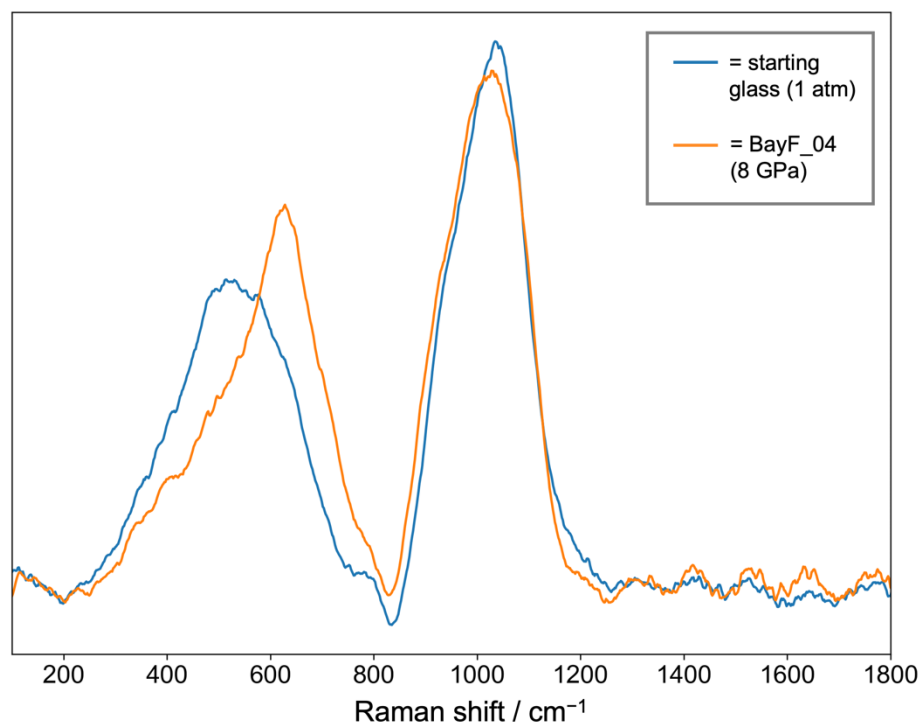


Figure 5.5: Raman spectra collected from sample BayF_04 and the starting glass for multi anvil experiments in the 100 to 1800 cm^{-1} region.

5.3.2 – Identifying Fluorine speciation using ^{19}F MAS

NMR.

The ^{19}F MAS NMR spectra collected from all samples are presented in Figure 5.6 except for spectrum of BayF_04, which is displayed in Figure 5.7 for added detail. The difference between the spectra of these figures and the ones in Figure 5.4 is attributed to the difference in pulse length and analytical run time. Errors on chemical shift were given by the fitting algorithm. Whenever the peaks from different spectra are treated as the same species, the reported error margin is always the highest one between the errors on each individual peak.

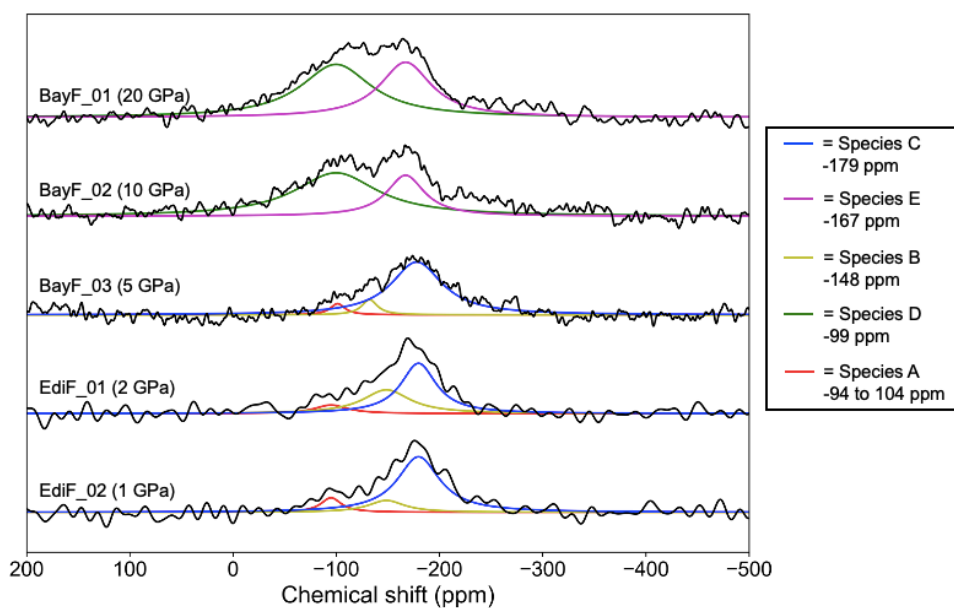


Figure 5.6: ^{19}F MAS NMR spectrum collected from samples of this study (see Figure 5.7 for BayF_04). The species identified via peak deconvolution, named A to E, are outlined in the legend to the right. All samples were spun at 30 kHz under a field B_0 of 14.1 T.

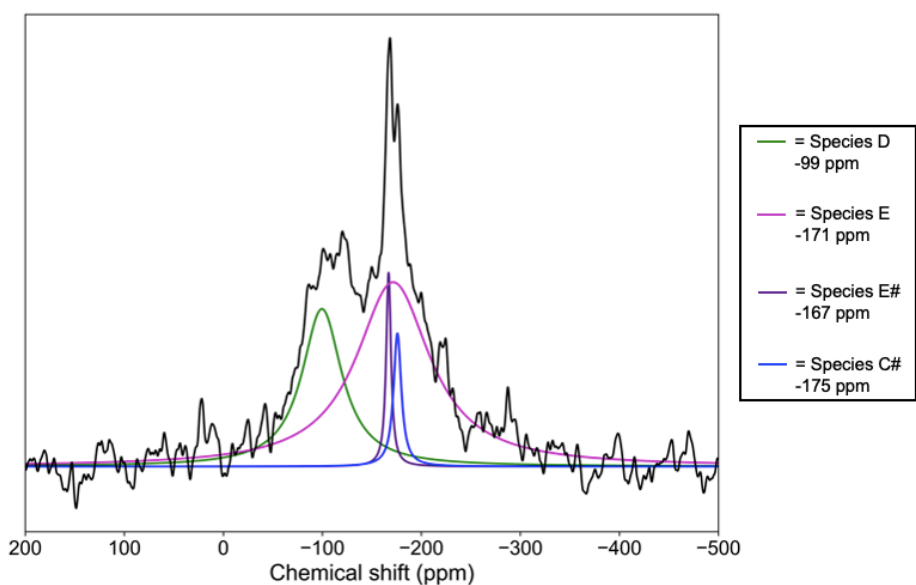


Figure 5.7: ^{19}F MAS NMR spectrum collected from sample BayF_04. The species identified via peak deconvolution, named D, E, C# and E#, are outlined in the legend to the right. All samples were spun at 30 kHz under a field B_0 of 14.1 T.

5.3.2.1 – F speciation up to 5 GPa.

Fitting the ^{19}F MAS NMR spectra of EdiF_02, EdiF_01 and BayF_03 revealed contributions from three distinct Gaussian line shapes (see Figure 5.6), each linked to a unique bonding environment. These environments were termed species A (-94 ± 4 to -104 ± 10 ppm), species B (-148 ± 12 ppm) and species C (-179 ± 7 ppm). For a detailed explanation of why peaks at different chemical shifts were considered as a single species, see subsection 5.4.1.1.

Deconvolution with two Gaussian line shapes was attempted, however these fits resulted in notably higher standard deviation from the experimental data (i.e., standard deviation is 59 vs 52 on average respectively). Furthermore, it was impossible to fit a peak at a chemical shift of ca. -175 ppm without including a third line shape. As a peak at the same chemical shift was the only one detected in all glasses synthesized at 1 atm (see Figures 4.6, and 4.7), a speciation which did not include this peak was deemed less likely.

5.3.2.2 – F speciation from 8 to 20 GPa.

Fitting the ^{19}F MAS NMR spectra of BayF_02 and BayF_01 identified two distinct peaks (see Figure 5.6), indicative of two distinct bonding environments, termed Species D (-99 ± 12 ppm) and Species E (-167 ± 7 ppm). A fit including three peaks, was attempted but the fitting algorithm always gave the third peak an intensity of zero. The reason why Species D was considered a different species relative to Species A, despite the overlap in chemical shift, is Species A is always a minor species in all glasses that contain it, while the opposite is true for Species D, which is relevant component of all spectra from glasses at or above 8 GPa.

The deconvolution of the spectrum from BayF_04 showed it to consist mostly of the same species, however two notably sharper features were also identified at -167 ± 0.3 and -175 ± 0.6 ppm, termed Species E# and C# respectively, and represent ca. 10% of the whole speciation. The peaks related to these species are absent from the spectrum collected from the same sample for F quantification (see Figure 5.4). While this could be due to the different pulse length and analytical run time, a conclusive explanation is currently lacking.

5.4 – DISCUSSION

5.4.1 – Peak assignment and F speciation in high pressure CMAS7G silicate melts.

5.4.1.1 – Peak assignment in ^{19}F MAS NMR spectra.

Table 5.4 summarises the contributions of the different signals to the ^{19}F MAS NMR spectra of the glasses studied here.

Sample	A	B	C	C#	D	E	E#
	-94 / -104	-147.5	-179	-175	-99	-167	-167
	ppm	ppm	ppm	ppm	ppm	ppm	ppm
EdiF_02	9.80	14.01	76.20	//	//	//	//
EdiF_01	9.38	33.83	56.79	//	//	//	//
BayF_03	3.76	20.46	75.78	//	//	//	//
BayF_04	//	//	//	4.83	29.34	61.35	4.49
BayF_02	//	//	//	//	69.12	30.88	//
BayF_01	//	//	//	//	56.55	43.45	//

Table 5.4: F species found in glasses of this study and their relative abundance, as determined via deconvolution of the peak features via the DMfit software (Massiot et al., 2002). // = species not present.

Errors are here omitted for improved readability, for specific error margins see section 5.3.2.

Based on existing data in the literature and the composition of the glasses in this study, peaks were assigned as follows:

1. Species A consists of low intensity broad peaks with a chemical shift comprised between -94 ± 4 and -104 ± 10 ppm. This species was determined to be $\text{Ca}(n)\text{—F}$ complexes, with $3 < n < 4$ (Li et al., 2014), as Ca bonded to F is the only possible environment in a CMAS system that can results in ^{19}F chemical shifts above ca. -110 ppm. These species can be described as non-planar complexes in which one F atom is coordinated with either 3 or 4 Ca atoms in a CaF_2 -like geometry and are akin to the ones observed in sample EdiF_2h, as described in Chapter 4 (see Figure 4.6). While in each single group n must either be integer, the average value

- of n will be a between 3 and 4. Specifically, a lower n corresponds to a higher chemical shift (Kiczenski et al., 2004). The low intensity of this signal suggests that the presence of species A may be a consequence of incomplete decomposition of CaF_2 from the starting mixture, similar to the phenomenon described in section 4.4.2.
2. Species B (-147 ± 12 ppm) could correspond to either [a] an $\text{Al—F—Ca}(N)$ bonding environment, with $1 < N < 2$ (Baasner et al., 2014), or [b] SiF_6^{2-} complexes dissolved in the melt structure (Miller, 1996). In detail, complexes of type [a] are groups where F acts as a bridge between a network forming (i.e., Al) and one or two network-modifying Ca cations (Kiczenski & Stebbins, 2002), and groups of type [b] contain octahedral SiF_6^{2-} dissolved within and not directly part of the melt structure (Liu & Tossel, 2003).
 3. Species C (-179 ± 7 ppm) likely consists of the same $\text{Mg}(3)\text{—F}$ complexes (Kiczenski et al., 2004) observed in CMAS7G glasses synthesized at 1 atm, discussed in chapter 4. These groups are non-planar complexes (see Figure 4.8) in a geometry akin to phyllosilicate structures (Huve et al., 1992).
 4. The chemical shift of Species D (-99 ± 12 ppm) is only consistent with a $\text{Ca}(n)\text{—F}$ complexes, with $3 < n < 4$ (Li et al., 2014), analogously to Species B. Unlike Species B, which consists solely of broad, low-intensity peaks, Species D is always a major component of F speciation, and above 10 GPa is the dominant bonding environment. Therefore, unlike in samples at or below 5 GPa, it is likely that the presence of $\text{Ca}(n)\text{—F}$ groups

is not a consequence of incomplete equilibration, but that such environments are instead stable at comparatively higher pressures. For this reason, despite the alignment in chemical shift, Species A and D were classified as distinct.

5. Species E (-167 ± 7 ppm) could correspond to three possible bonding environments, [a] a $\text{Mg}(x)\text{—F}$ bonding environment with $2 < x < 3$, [b] an Al—F cryolite-like bonding environment, with one F atom bridging between two AlF_6^{2-} groups (Baasner et al., 2014), or [c] two tetrahedrally coordinated Al atoms, each linked to three O atoms and one F atom shared between the two Al atoms (Zeng & Stebbins, 2000). The key difference between the Al—F groups in [b] and [c] is that Al is respectively VI-fold and IV-fold coordinated. $\text{Mg}(x)\text{—F}$ environments as in [a] can be described as non-planar complexes akin to Species C, but with a lower average number of Mg ions coordinated to F, as $\text{Mg}(3)\text{—F}$ and $\text{Mg}(2)\text{—F}$ complexes in phyllosilicate frameworks are identified by peaks at -175 and -152 ppm respectively (Miller, 1996). This would imply, however, that x would be closer to 3 than to 2 in this specific system. It follows that these groups are more akin to trioctahedral Mg-rich phyllosilicates than to their dioctahedral counterpart.
6. Species C# and E# (-175 ± 0.6 and -167 ± 0.3 ppm), found solely in BayF_04, have a chemical shift either remarkably close or coincident with Species C and E respectively, therefore were considered as a diagnostic of the same bonding environment. The noticeably sharper peaks however suggest that these species might not be incorporated in the melt structure,

but in crystalline phases instead (Miller, 1996). While Raman analysis of BayF_04 excluded the presence of any major crystalline phase, the minor occurrence of nanocrystalline domains, which would be extremely challenging to detect in a glassy matrix using Raman spectroscopy, cannot be excluded.

5.4.1.2 – Attainment of equilibrium.

To assess the equilibrium in the melt phase, the same rationale described in section 4.4.2 was applied, i.e., the full dissolution of unstable Ca—F species was taken to indicate that the melt had reached full equilibration, as proposed in Kiczenski & Stebbins (2002) for related CS compositions. Therefore, EdiF_02, EdiF_01 and BayF_03 (i.e., annealed at or below 5 GPa) can be considered as close to equilibrium but not fully equilibrated, due to the presence of minor (i.e., < 10% of observed F) but detectable Ca—F species, analogously to what inferred for glasses synthesized at 1 atm (see section 4.4.2), where the presence of such species can be utilised to identify incomplete equilibration. However, Ca—F species are much more abundant in BayF_04, BayF_02 and BayF_01 (i.e., annealed at or above 8 GPa) and, considering the relevant differences in synthesis pressure between these glasses and both the others investigated here and those analysed by Kiczenski & Stebbins (2002) and Kiczenski et al. (2004), the presence of such species cannot be considered a reliable indicator of equilibrium without further investigation. Thus, the full equilibration of samples annealed above 8 GPa cannot be definitely assessed.

5.4.1.3 – Peak assignment in Raman spectra.

A Raman spectrum was collected from BayF_04 and compared to that collected from the CMAS7G glass used as the starting material for the multi-anvil annealing experiments. Both spectra consisted of two broad features (see Figure 5.5), in the 820 to 1200 cm^{-1} and 230 to 800 cm^{-1} regions respectively. The two bands are related to the vibration of T—O and T—O—T bonds respectively (T = tetrahedrally coordinated network forming cation, i.e., Si or Al in CMAS systems; Neuville et al., 2008). The band associated with the lower Raman shift exhibits a notable change in shape with the increase in pressure, going from a Gaussian shape at 1 atm to the asymmetric sum of two Gaussian functions at 8 GPa (see Figure 5.8). This change has been correlated to either [1] a variation in the Mg content of the glass (Neuville et al., 2008), or to [2] a change of the average coordination state of Si or Al (Mysen & Virgo, 1985). As BayF_04 was prepared by annealing the glass synthesized at 1 atm, major changes in chemical composition are implausible, and as relevant changes in the coordination state of Si and especially of Al have been previously identified in CMAS7G systems between 5 and 10 GPa (Mare, 2017), it follows that the change in shape of the band between 200 and 700 cm^{-1} is diagnostic of an overall different coordination state of the network forming cations at 8 GPa compared to 1 atm.

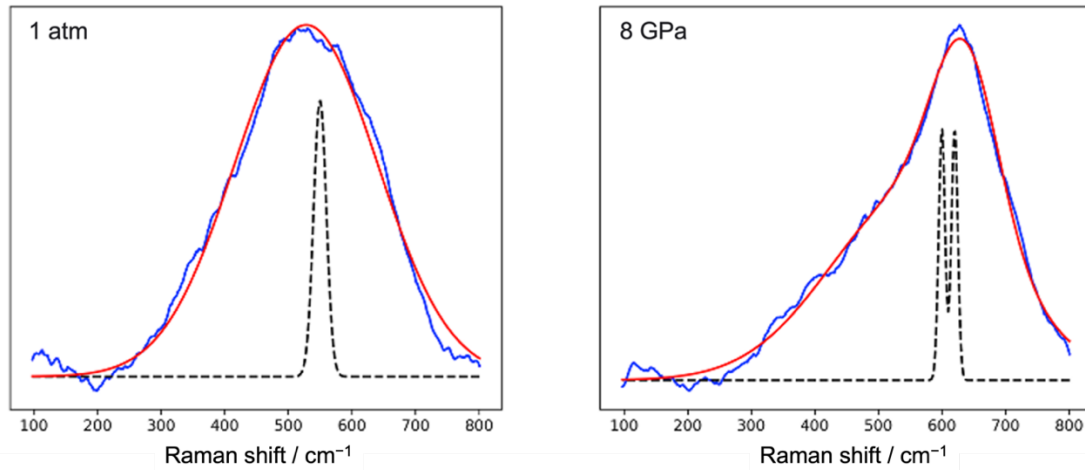


Figure 5.8: Fitting of the 100-800 cm^{-1} region Raman spectra collected from glasses synthesized at 1 atm and 8 GPa. The raw spectrum is in blue, the functions (one and two Gaussian peaks for the 1 atm and 8 GPa glass respectively) used as starting points are in dashed black, and the best fit is in red.

It must be noted, however, that the Raman analysis described thus far provides no information about F speciation in the system, owing to the very low F content of the sample (ca. 65 $\mu\text{g/g}$).

5.4.2 – The behaviour and speciation of Fluorine in high pressure silicate melts.

5.4.2.1 – Fluorine loss in high T conditions.

The F concentration of all experimental glasses is in the order of tens of $\mu\text{g/g}$ (Table 5.3), which is consistent with the F concentration of the BSE (McDonough & Sun, 1995). Hence, these data are representative – in terms of F concentration – to Earth's silicate interior. Nevertheless, F was added to starting mixtures in the order of 1000s of $\mu\text{g/g}$, thus the reason(s) behind the significant loss of F is a

point of interest. This is an especially curious phenomenon because of the different synthesis procedures adopted at Edinburgh and Bayreuth. For example, the piston cylinder samples (Edinburgh) were melted, quenched, and annealed under pressure whereas the multi anvil press samples (Bayreuth) were first synthesized at 1 atm in a muffle furnace (in a procedure analogous to the glasses in chapter 4) then annealed at high pressure after quenching. This implies that the majority of F loss occurred before the melting process (during preparation of the starting materials).

It is possible that F loss occurred during the decarbonation of the starting mixture. In absence of CaF_2 , the reaction that would have occurred is $\text{CaCO}_3 \rightleftharpoons \text{CaO} + \text{CO}_2$, with CO_2 being gradually lost to the surrounding environment as a gas, this reaction will cease when at full calcination of the Ca-carbonate. However, in presence of CaF_2 the $\text{CaCO}_3 + 2\text{HF} \rightleftharpoons \text{CaF}_2 + \text{CO}_2 + \text{H}_2\text{O}$ acid base reaction also takes place, with H_2O likely present as environmental moisture in the starting mixture. The calcination of the CaCO_3 occurs following the first reaction and triggers the decomposition of CaF_2 by the second reaction. While at present there is no definitive confirmation for this hypothesis, it is included here in hope of further investigations, which might limit F loss during high P-T experiments.

5.4.2.2 – The effect of increasing pressure on F speciation.

While the synthesis and experimental procedure adopted in this chapter resulted in significant F loss from the system, the silicate glasses still contained detectable and quantifiable concentrations of F, which enabled an examination of the effect of increasing pressure on F speciation in silicate (CMAS7G) glass.

Figures 5.6 and 5.7 show that the F speciation in silicate (CMAS7G) glass changes with increasing pressure. Once the possible F-based species presented in subsection 5.4.1.1 are compared with the pressure at which they are found, three possible scenarios emerge:

1. Species B and E correspond to $\text{Al—F—Ca}(n)$ and Al—F—Al respectively, thus between 5 and 10 GPa all Mg—F network-modifying species and $\text{Al—F—Ca}(n)$ species are destabilised, in favour of the formation of either AlF_6^{3-} complexes bridged by F atoms or $\text{Al}^{\text{IV}}\text{—F—Al}^{\text{IV}}$ groups. In both cases, F shifts from a completely network modifying role (i.e., $\text{F—Ca}(n)$, $\text{Al—F—Ca}(n)$ and $\text{Mg}(3)\text{—F}$ species) to a partially network forming one. While the vast majority (ca. 90%) of Al at 10 GPa should speciate as Al^{V} and Al^{VI} (Mare, 2017), the relatively small fraction of Al^{IV} still present is sufficient to bind the very low concentrations of F dissolved in the melt in $\text{Al}^{\text{IV}}\text{—F—Al}^{\text{IV}}$ groups.
2. Species B and E correspond to $\text{Al—F—Ca}(n)$ ($1 < n < 2$) and $\text{Mg}(x)\text{—F}$ ($2 < x < 3$) respectively. This implies that in the transition between 5 and 10 GPa the F bridging between Al and Ca atoms moves to bind solely with Mg (in $\text{Mg}(x)\text{—F}$ species) and Ca (in $\text{Ca}(n)\text{—F}$ species, $3 < n < 4$). It follows that in this scenario the drop in Al^{IV} concentration in the melt structure

causes the destabilisation of all Al-based F species. The increase in pressure also would have an impact on the geometry of Mg—F groups, as those would shift from solely Mg(3)—F to Mg(x)—F, hinting at a possible change in Mg coordination playing a role as well. It is known that between 0 and 14 GPa the Mg coordination state changes from predominantly IV-fold coordinated to mostly V-fold and VI-fold (Guillot & Sator, 2007; Solomatova & Caracas, 2019). It must, however, be pointed out that in Mg(3)—F and Mg(x)—F complexes the coordination of Mg is, respectively, fully VI-fold and between V-fold and VI-fold. Nevertheless, analogous to what was described for Al in scenario 1, the very low F concentrations in the system imply that the even at relatively low pressures (i.e., 1 to 5 GPa), where only around 10% of Mg is VI-fold coordinated, there would be enough Mg^{VI} to bond with F.

3. Species B and E correspond to F bridging between SiF₆²⁻ complexes (indicated as Si—F—Si from now on) and Mg(x)—F (2 < x < 3) complexes respectively. This scenario is largely analogous to scenario 2, with the important difference that part of F at 5 GPa and below is speciated into network forming species (i.e., Si—F—Si), which are lost at 10 GPa and above. The change in geometry of the Mg—F complexes mirrors that described for scenario 2. It is worth noting that in this scenario, the behaviour of F with increasing pressure goes from partially network forming to completely network modifying, in contrast with scenario 1, where the opposite happens.

The scenarios described thus far are summarised in Table 5.5.

	Scenario 1	Scenario 2	Scenario 3
< 5 GPa (EdiF_02, EdiF_01, BayF_03)	Ca(N)—F Al—F—Ca(n) Mg(3)—F	Ca(N)—F Al—F—Ca(n) Mg(3)—F	Ca(N)—F Si—F—Si Mg(3)—F
> 10 GPa (BayF_02, BayF_01)	Ca(n)—F Al—F—Al	Ca(n)—F Mg(x)—F	Ca(n)—F Mg(x)—F

Table 5.5: summary of the scenarios for changes in F speciation in CMAS7G silicate melts as a function of increasing pressure. $1 < n < 2$, $3 < N < 4$ and $2 < x < 3$.

The change in F speciation as a function of pressure is evident when comparing all of the samples annealed < 8 GPa with sample BayF_04, which was annealed at 8 GPa. The ^{19}F NMR spectra shows a four-fold speciation (see Figure 5.7), with ca. 90% of F in similar species to BayF_02 and BayF_01. This implies that at 8 GPa the Ca(n)—F complex is a stable species, and subsequently that the Ca(n)—F complex is stabilized between 5 and 8 GPa. The most notable features are the two sharp peaks at -175 ± 0.6 and -167 ± 0.3 ppm, termed C# and E# due to the coincidence of these chemical shifts with the ones associated to Species C and E. This was interpreted as 8 GPa being the pressure at which the lower pressure arrangement of Species C, no longer present in the glass, is destabilised in favour of the higher pressure arrangement of Species E, which is instead present. Furthermore, the similarity between the chemical shifts of Species C# and C was interpreted as a sign of these two bonding environments

being geometrically close at a molecular level, and likewise for Species E and E#. This implies that scenarios 2 and 3, in which Mg(3)—F transitions to a Mg(x)—F environment with increasing pressure, are the most plausible. This interpretation is by no means definitive however, as it relies on indirect interpretation and requires direct observations (to affirm or disprove).

The reason for the sharpness of the peaks of Species C# and E# when compared to all other peaks from NMR spectra of this study remains unclear. Sharp peaks are commonly associated with crystalline phases (e.g., see the difference in shape between peaks caused by Mg(3)—F complexes in a melt and crystalline phases in Figure 4.7). Nevertheless, after investigations performed via Raman spectroscopy (see subsection 5.4.1.3), no evidence for the presence of major crystalline phases was found. However, the minor occurrence of nanocrystalline domains, compatible with the trace F concentrations in BayF_04 is likely, as sharp peaks in an NMR spectrum are diagnostic of highly ordered structural states, and order on the nanoscale is difficult to detect via Raman spectroscopy when the ordered domains are present at low concentration (McCreery, 2000).

While it is still not certain what triggers the change in F speciation in sample BayF_04, the triggering factor is likely to be the changing Ca, Mg and/or Al average coordination number between the pressures of 5 and 10 GPa, as hypothesised by ab initio calculations (Guillot & Sator, 2007; Solomatova & Caracas, 2019). Moreover, the average Al coordination state has been directly measured to change from ca. 4.7 at 5 GPa to ca. 5.4 at 10 GPa, with few IV-fold coordinated Al left at 10 GPa in melts of similar or identical compositions to the

ones of this study (Mare, 2017). Raman analysis on BayF_04 and on the non-annealed starting material indeed show a marked difference in T—O—T bonds (T = Si, Al) between 1 atm and 8 GPa, likely due to the increasing average coordination state of Al.

5.4.2.3 – The impact of F speciation on the structure of the melt.

Fluorine is widely agreed to have an overall depolymerizing effect when dissolved within silicate melts (Dolejš & Zajacz, 2018 and ref. therein). While the low F concentrations in the melts studied here study likely prevent it from having a notable impact on the physical properties of the melt phase, this known behaviour of F can be used to determine the likeliest between the scenarios for F speciation summarised in Table 5.5. The effect that F-based species have on melt rheology is detailed in Table 5.6.

	Scenario 1	Scenario 2	Scenario 3
< 5 GPa	Network modifying	Network modifying	Network forming and modifying
> 10 GPa	Network forming and modifying	Network modifying	Network modifying

Table 5.6: impact of F species on the melt structure for each of the possible combinations of F speciation in the glasses studied here.

If scenario [1] is excluded due to the similarities observed between Species C and E observed in the NMR spectrum of BayF_04, as discussed above, this leaves scenarios [2] and [3] as plausible. In scenario [3], between ca. 15 and 34% of F occurs as Si—F—Si groups (Miller, 1996) below 5 GPa, therefore at comparatively lower pressures F would speciate partially into network forming species, hence negatively affecting its depolymerizing properties. This runs contrary with the current knowledge of the impact of fluorine on melt rheology and is, thus, regarded as less likely. This leaves with scenario [2], in which all F-based species present are network modifying.

As a final remark, it must be noted how Mg—F species are always the most prevalent component of F speciation at any pressure, with the sole exception of BayF_02 (annealed at 10 GPa of pressure). This is in agreement with the main F incorporation mechanisms in the upper mantle featuring different types of Mg—F complexes as well (see section 5.1.2), and therefore hinting at how the speciation of F in the melt phase is potentially inherited by the minerals that crystallise from the same melt.

5.5 – CONCLUSIONS

This study was carried out to investigate the speciation of F in CMAS7G silicate melts as a function of increasing pressure. The data show that F speciation in CMAS7G silicate melts is not constant as a function of pressure (up to 20 GPa). The same chemical composition was used for all samples to isolate pressure as the sole variable. In addition, the synthesis and experimental procedure adopted in this chapter also resulted in silicate glasses with similar concentrations of F among the samples, which are – conveniently – in the same order of magnitude as natural mafic silicate melts (i.e., tens to hundreds of $\mu\text{g/g}$; Webster et al., 2018), providing consistency with nature.

Based on the observations presented in this chapter, it is concluded that F in CMAS7G systems forms stable Al—F—Ca(*n*) species, with $1 < n < 2$, and Mg(3)—F complexes with minor but detectable quantities ($< 10\%$ of observed F) of Ca(*N*)—F groups with $3 < N < 4$ at pressures below 5 GPa. Between 5 and 8 GPa the Al—F bonds are replaced by Ca(*N*)—F species, with $3 < N < 4$. Then, once the pressure reaches ca. 8 GPa, F is found to be bound with a comparatively smaller number of Mg cations in Mg(*x*)—F species, with $2 < x < 3$. While this speciation is by no means a definitive interpretation of the measurements described in this chapter, it is regarded as the most likely, however this does not completely rule out the other scenarios identified in Table 5.5.

A wide array of follow-up investigations would be required first to confirm or disprove the interpretation presented here, and then to expand it towards a broader range of compositional systems. Adding F to the starting materials as

MgF₂ rather than CaF₂ would allow to determine if the Ca—F species identified above 8 GPa are effectively stable or if they are the result of incomplete equilibration. Investigating how F speciation changes in analogous systems when F coexists with other anions (e.g., Cl, OH) would be of particular importance, as it would show which specific differences in speciation, if any, drive the differences in geochemical behaviour of these anions in the deep Earth. Further investigations would also be critical in order to confirm if the omnipresent non-planar Mg(3)—F groups found in all samples of this study are transferred from the melt phase to the minerals during crystallisation, as this would clarify the evolution of degassing and volatile storage during magmatic processes.

~6 — FLUORINE AND HYDROXIDE

ORDERING IN HUMITE GROUP

MINERALS: A ^{19}F MAS NMR STUDY~

6.1 – INTRODUCTION

The Humite group is a class of four minerals with formula $n(\text{M}_2\text{SiO}_4)\text{M}_{1-x}\text{Ti}_x(\text{OH},\text{F})(\text{O})_{2x}$, where M is a divalent cation (typically Mg or Fe, but Mn, Ca, and Zn are also possible), and n is an integer between 1 and 4 (Jones et al., 1969). These minerals can be described, from a mineralogical point of view, as 1 to 4 olivine layers $((\text{Mg},\text{Fe})_2\text{SiO}_4)$ alternating with isolated Ti-bearing brucite/sellaite layers $((\text{Mg},\text{Fe})_{1-x}\text{Ti}_x(\text{OH},\text{F})_2)$, usually just referred to as “brucite layers” for simplicity. The value of n determines the nature of the specific mineral: with n = 1, 2, 3 and 4 corresponding to norbergite, chondrodite, humite and clinohumite, respectively (Jones et al., 1969). For the case of $n \gg 4$, the resulting structure is considered a planar defect in an olivine structure, and thus is commonly termed a “humite-like defect” or “humite-type lamella” (Herman et al., 2007; Kitamura et al., 1987). Together with high P-T micas (e.g., phlogopite, phengite), amphiboles of various types and dense hydrous magnesium silicates (DHMS), humite group minerals and defects in olivine are essential pieces of the puzzle in the complex system that leads to the retention of water and fluorine by subducting slabs of

oceanic crust, thus directly contributing to Earth's tectonic volatile element cycle (Liu et al., 2019; Barnes et al., 2018).

6.1.1 – Humite group minerals and their stability.

The most common humite-type mineral in nature is clinohumite ($4(\text{Mg}_2\text{SiO}_4)\text{Mg}(\text{OH},\text{F})_2$, considering only the Fe-free forsterite/brucite end member for simplicity), which is a product of the breakdown of serpentine ($\text{Mg}_3\text{Si}_2\text{O}_5(\text{OH})_4$) in subducting slabs of hydrothermally altered oceanic crust (Yamamoto & Akimoto, 1977).

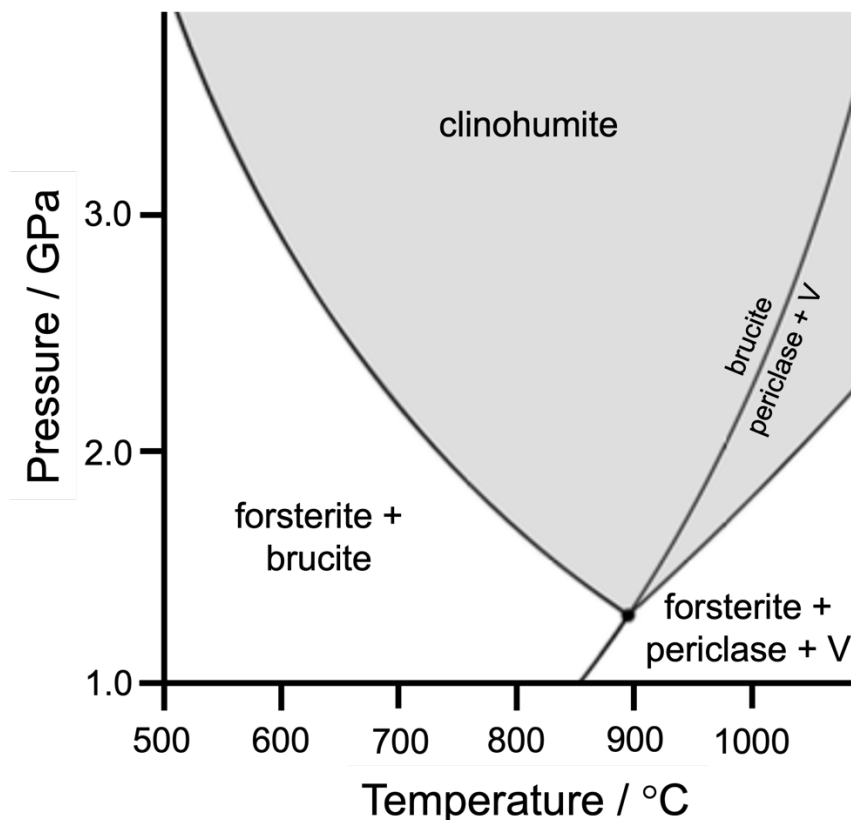


Figure 6.1: Field of stability of OH-rich clinohumite (in light grey) in high P-T conditions. The dehydration reaction of brucite ($\text{Mg}(\text{OH})_2 \Rightarrow \text{MgO} + \text{water vapour}$) is extended within it, however it does not impact the stability of clinohumite itself. V = water vapour. Data from Hughes & Pawley (2019).

OH-rich clinohumite is metastable at surface conditions. The lowest P-T stability conditions are ca. 1.4 GPa and 900 °C (see Figure 6.1), corresponding to a binary eutectic point (Hughes & Pawley, 2019). Its field of stability extends to pressures as high as 12 GPa; however, its high T stability is rather limited, with a maximum breakdown temperature of around 1160 °C (Grützner et al., 2017).

Two main factors can extend the field of stability of clinohumite: [1] the Ti fraction in the M4 site of the brucite layer (see Figure 6.2), an increase of which can extend its stability until near surface conditions (Aoki et al., 1976), and [2] the F fraction in the F/OH site ($F/(F+OH)$), termed as “F/OH fraction” from here onwards) which, when increased significantly, extends the field of stability towards T as high as 1800 °C and P as high as 20 GPa (Hughes & Pawley, 2019; Grützner et al., 2017). The stabilizing effect of Ti and F incorporation occurs in all humite group minerals and for humite-type lamellae intergrowing with olivine crystals (Shen et al., 2014).

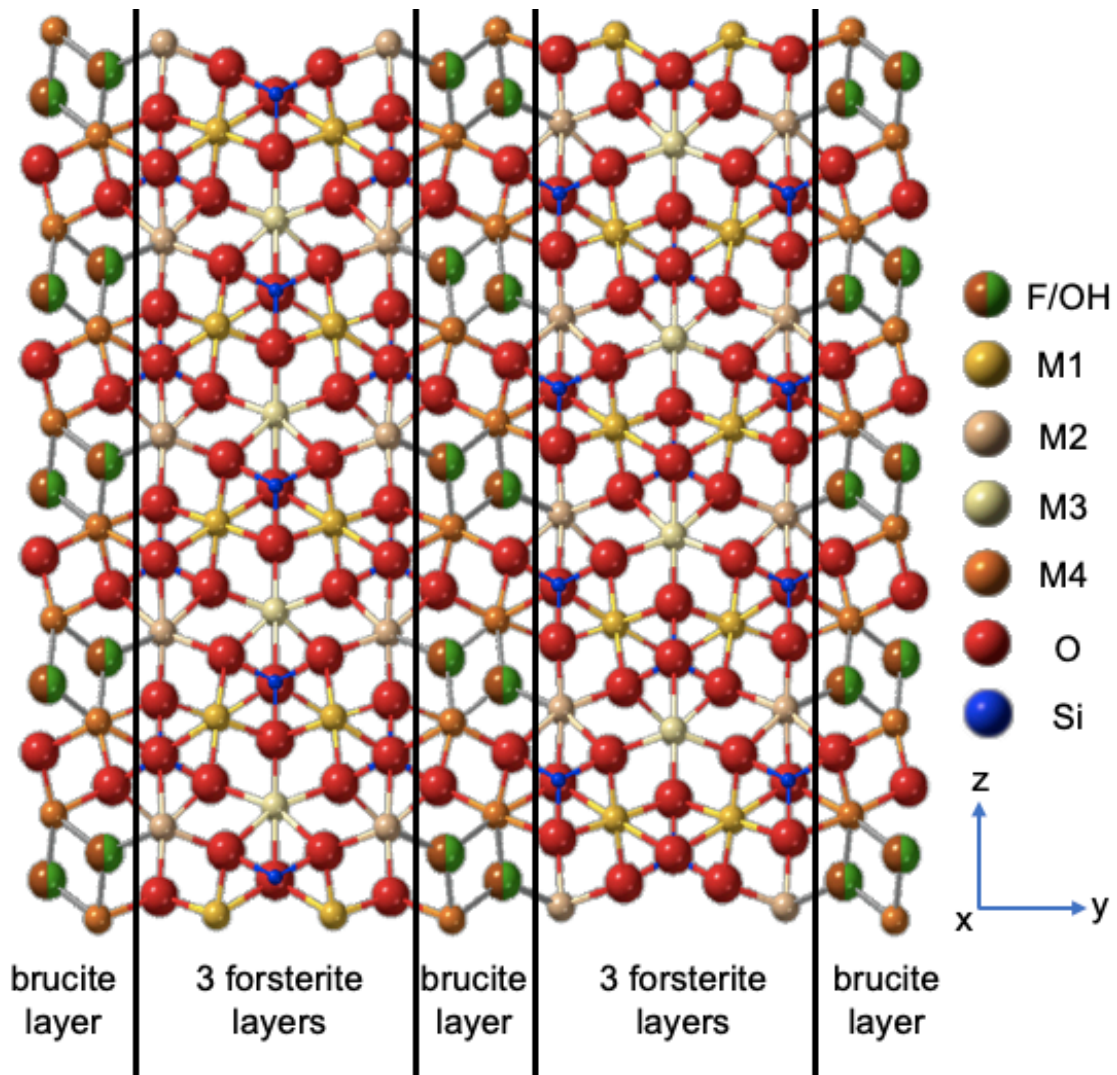


Figure 6.2: Crystalline structure of a humite *sensu stricto* (adapted from Ribbe & Gibbs, 1971). Sites M1 to M4 (numbered to distinguish M sites in the forsterite layers, M1 to M3, from the M4 site in the brucite layers) contain bivalent cations, with site M4 also potentially hosting Ti^{4+} . The site marked as F/OH contains either F^- or OH^- .

Both the $Ti^{4+} \leftrightarrow Mg^{2+} + 2H^+$ and the $F^- \leftrightarrow OH^-$ substitutions occur within the brucite layers and have a direct influence over both the stability of the mineral and its OH^- content, with the hydrogen atoms being stored in two possible but distinct sites adjacent to the O atoms. These sites remain vacant when F is incorporated in the F/OH site instead. These reactions are therefore of critical

importance for the water transport efficiency of humite group minerals in subduction zone settings (Grützner et al., 2017; Ohtani, 2015).

6.1.1.1 – The Ti \leftrightarrow Mg substitution.

Ti⁴⁺ and Mg²⁺ are two cations that have a relatively similar ionic radius of 74 and 86 pm respectively, but a difference in charge of +2. The Ti⁴⁺ \leftrightarrow Mg²⁺ + 2H⁺ occurs when a Ti⁴⁺ ion enters the M4 site in place of a Mg²⁺ ion, resulting in two hydrogen vacancies. The result of this is an overall reduction of H1···H1 interactions in the framework (Berry & James, 2002), which acts then as a stabilising factor (Griffin et al., 2010b). It must be pointed out that although Ti-rich humite group minerals are potentially stable at near surface conditions, this does not necessarily result in their effective formation in such environments. This is because in subducting slabs these minerals form following the breakdown of serpentine (Yamamoto & Akimoto, 1977), which does not occur until P-T conditions of 1.6 GPa and 680 °C at minimum (Padrón-Navarta et al., 2011).

Although the introduction of Ti into the humite group minerals results in an overall lower OH abundance, as it is accompanied by the loss of 2 H⁺, natural Ti-rich clinohumite with water contents as high as 1.53 wt% have been found (Weiss, 1997). This somewhat counterintuitively high water enrichment is even more pronounced, at upwards of 5.2 wt% of H₂O (Shen et al., 2014), in Ti-rich chondrodite (2(Mg₂SiO₄)Mg(OH,F)₂), although this effect is partially amplified by chondrodite containing twice the amount of brucite layers per formula unit. A clinohumite with the same H₂O content would thus have half (2.6 wt%) the water

abundance, which is still a markedly higher amount than that from the data of Weiss (1997).

One possible explanation for such H₂O concentrations is that the stabilising effect of Ti enrichment makes F occupancy in the F/OH sites in the brucite layer relatively less important for the stability of the mineral, and therefore this site can be populated almost exclusively by hydroxide anions without this causing the mineral to be less stable at the same P-T conditions.

6.1.1.2 – The F ↔ OH exchange and solid solution.

The solid solution between F⁻ and OH⁻ is almost ubiquitous in mineral phases which contain an OH⁻ site, owing to the identical charge of -1 and virtually identical ionic radius of 133 pm (Shannon, 1976; Jenkins & Thakur, 1979). Humite group minerals are thus not only important for water transport in subduction zones, but also play a critical role in the geological cycling of fluorine (Klemme & Stalder, 2018).

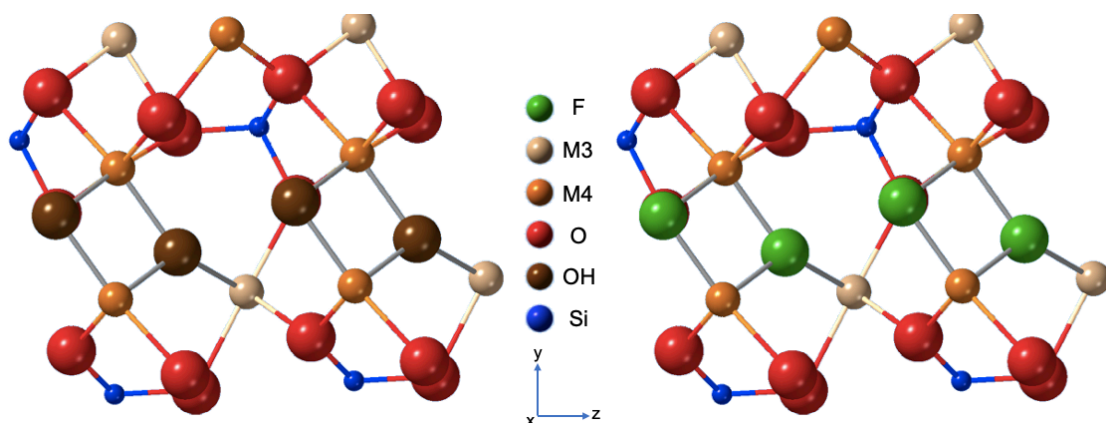


Figure 6.3: Detail of the brucite layer in a generic humite group mineral for the cases of OH-saturation and F-saturation (on the left and right, respectively). The hydroxide ion is represented by a single sphere for simplicity.

As shown in Figure 6.3, the F/OH sites in the brucite layers are adjacent in pairs, and each pair is coordinated by two Mg atoms in the M4 sites. When both adjacent sites contain a hydroxide anion, the two H1 sites are too close to be occupied simultaneously and the second H occupies the H2 position. However, as shown previously using NMR spectroscopy even at room temperature a dynamic exchange occurs (see Figure 6.4), with each OH bond reorienting on the microsecond scale, thus resulting in a constant alternation between H1/H2 and H2/H1 configuration (Griffin et al., 2010b). The presence of a F atom in one of the two sites results in the formation of a stable O—H···F hydrogen bond geometry, thus inhibiting the dynamic process, with the H atom being locked in position (Friedrich et al., 2002). This results in the greatly extended field of stability of F-rich humite group minerals compared to their OH-rich counterparts (Grützner et al., 2017).

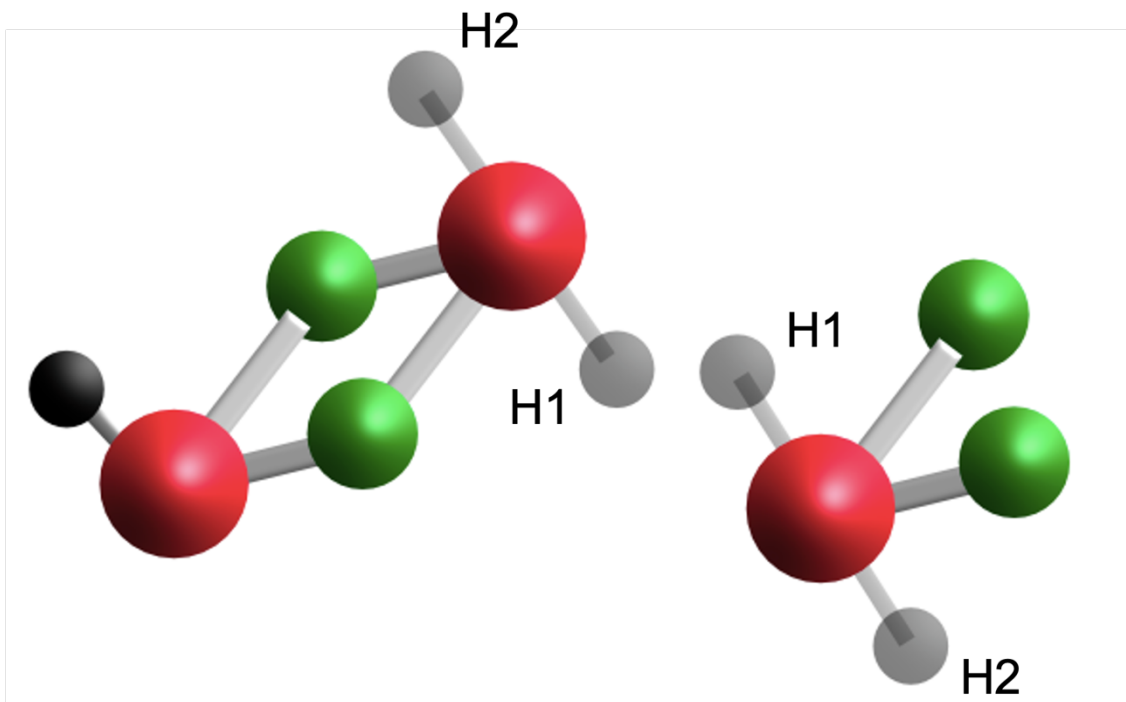


Figure 6.4: Simplified representation of the dynamics that occur when two OH^- occupy neighbouring sites in the brucite layer of humite group minerals. The two H1 sites are never occupied simultaneously. Mg atoms are in green, H atoms in black and O in red.

F incorporation in humite group minerals, while having a positive effect on their stability, also naturally hampers their water transport capacity, due to the F fraction hosted in the F/OH site resulting in a smaller proportion of the sites being available for OH storage. Nevertheless, the relationship between the F occupancy of the site and the extended stability field has yet to be quantified (Hughes & Pawley, 2019). For example, it is currently unclear if these two parameters are linearly connected, and thus the higher the F content the wider the stability field observed, or if the relationship is instead more complex.

6.1.2 – F and OH arrangement in humite group

minerals frameworks.

The OH groups in hydroxylated humites are arranged in two distinct chains of HO—HO hydrogen bonded pairs. However, to understand the longer-range arrangement or ordering of F and OH in F-substituted minerals would require a knowledge of the proportion of pairs occupied solely by F atoms (F—F pairs), solely by OH groups (OH—OH pairs) or those occupied by one F atom and one OH group (F—OH and OH—F pairs). Although a single crystallographic F site has been identified by diffraction for F-substituted minerals, ^{19}F MAS NMR spectra show four distinct F resonances, as shown in Figure 6.5a for a clinohumite synthesised with an F/OH fraction of 0.54 (Griffin et al., 2010), suggesting that the ^{19}F chemical shift is sensitive to the nature of the two neighbouring atoms in the chain (one within the nominal hydrogen bond and one in the next hydrogen bond along the chain). As shown in Figure 6.5b, the four resonances were assigned by Griffin et al. (2010) to four distinct F bonding environments using a combination of DFT calculations (on a 50% F/OH model system) and experimental ^{19}F NMR analyses.

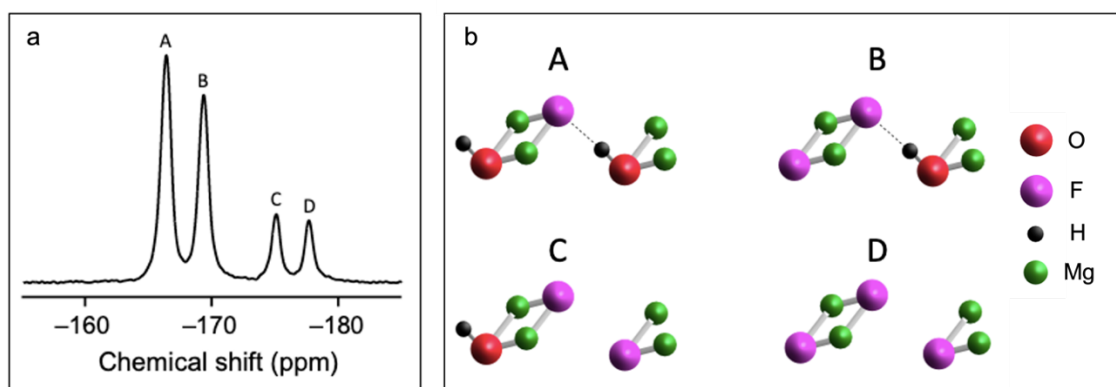


Figure 6.5: (a) ^{19}F MAS NMR spectrum of a synthetic clinohumite with an F/OH fraction of 0.54, collected from a sample rotated at 30 kHz at a field B_0 of 14.1 T, corresponding to a Larmor frequency of 564.7 MHz (adapted from Griffin et al., 2010). (b) Possible local arrangements of F^- and OH^- ions in the brucite layers of humite groups minerals, termed from A to D.

The four possible local configurations of F and OH within the brucite layer are here referred to as A, B, C and D (see Figure 6.5b). Of these, A and B feature a H-bond between two neighbouring F^- and OH^- ions, while C and D instead see two adjacent F atoms in the pair, and thus no H-bond is present. Two further configurations are possible, each containing two OH groups in the hydrogen bonded pair, and with either F or OH on the neighbouring site. The latter of these contains no F and so is not relevant for ^{19}F NMR, while the former would result in the neighbouring atom being in A or C configuration depending on what it itself is bonded to. It is worth noting that, in F/OH sites neighbouring Ti, F is likely found with lower abundance compared to O, as there is no H-vacancy that can form to counteract the charge imbalance introduced by Ti.

6.1.2.1 – The stabilizing effect of hydrogen bonds.

In order to gain insight into any preferential F/OH ordering upon F substitution, DFT+D calculations were carried out. These calculations were performed in 2011 by Prof. Sharon Ashbrook, as a follow up to the study in Griffin et al. (2010) and Griffin et al. (2010b), and their outcome formed the bases on which this study was built upon. For these reasons, they are presented as introductory material and not as results of this study.

Two F atoms were substituted into a fully hydroxylated $2 \times 1 \times 1$ supercell of clinohumite (with 50% of H placed on H1 and 50% on H2 to give fully ordered H-bonded pairs). Mixing enthalpies, calculated relative to the two end members (fully hydroxylated and fully fluorinated clinohumite), are given in Table 6.1. When one F is substituted into each of two adjacent OH—OH pair, leading to the formation of two OH—F hydrogen bonds, favourable mixing enthalpies are obtained (e.g., -0.4 eV). In contrast, when the two are substituted into the same OH—OH pair, leading to an F—F pair, there is a very small increase in the mixing enthalpy, suggesting this is not (enthalpically) favourable relative to phase separation. Interestingly, there is a small difference in the enthalpy depending on the exact ordering of the two OH—F hydrogen bonds, with F—HO F—HO being 0.06 eV more stable than the F—HO OH—F counterpart. Although a small change (and notably much smaller than the preference for H-bond formation), this would suggest there is a slight energetic preference for some ordering of the H-bonds along the chain. Analogous calculations were performed for a $2 \times 1 \times 1$ supercell of chondrodite, once again with very similar results, suggesting there is little interaction between the two chains of hydrogen bonds found in the minerals,

and that the longer-range structure can be neglected when considering how to efficiently and simply model ordering.

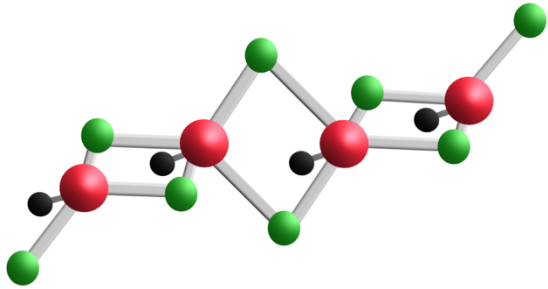
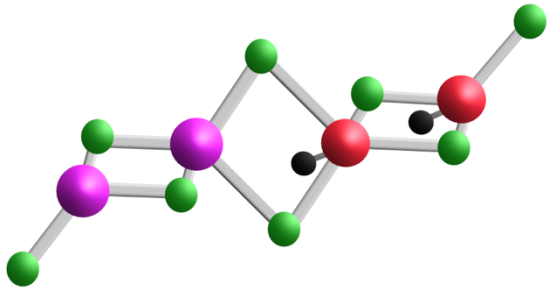
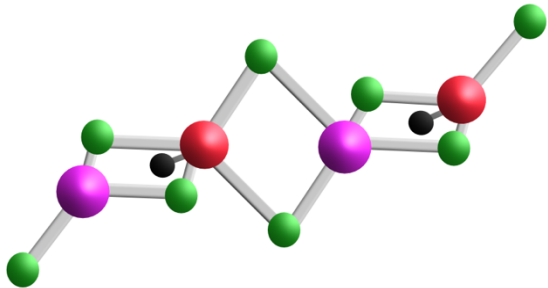
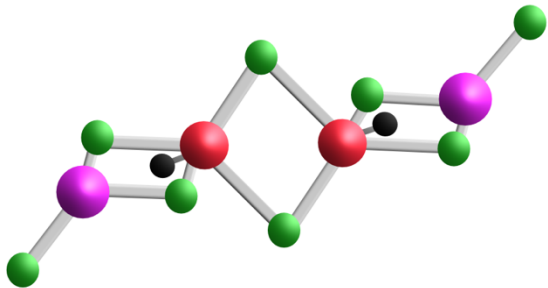
<u>Arrangement</u>	<u>Mixing energy / eV</u>
 OH-OH OH-OH	0.000
 F-F OH-OH	+0.005
 F-OH F-OH	-0.410
 F-OH OH-F	-0.360

Table 6.1: Relative mixing enthalpies (calculated using DFT and quoted relative to the relevant stoichiometric mix of the two end members) resulting from the substitution of two F in a $2 \times 1 \times 1$ supercell of fully hydroxylated clinohumite. Results obtained starting from a fully fluorinated framework (and substituting two OH) were very similar (not shown).

In summary, DFT calculations suggest that the formation of F—HO H-bonds (as opposed to an HO—HO H-bond and an F—F interaction) is significantly favoured for humites, and that there is a small preference for how ions in adjacent pairs are ordered along the chain (see Table 6.1). In other words, the F species termed A and B (see Figure 6.5b) should be the more preferred arrangements over C and D, as these contain the F—HO H-bonds as opposed to F—F and OH—OH interactions. This prediction is partially supported in the spectrum of Figure 6.5a, collected from a clinohumite with a F/OH fraction of 0.54, where the composition is such that there is no requirement to form environments C and D in significant amounts. Nevertheless, a minor, but still relevant fraction, of F is found in C and D environments (i.e., 21.70% of all F is speciated as C or D). The 0.04 difference between the F/OH fraction of the sample (0.54) and the ideal F/OH fraction at which only species A and B should exist (0.50) is not large enough to result in such a speciation. In other words, when around 50% of the F/OH sites are occupied by F and the other 50% by OH, it might be expected that solely F—OH pairs should form, as this would minimise the mixing energy of the framework, resulting in an NMR spectrum that contains signals attributable solely to species A and B (depending on the ordering of H-bonds along the chain), with a potentially small fraction of F speciated as C or D (~4%) due to the F/OH fraction being slightly above 0.5. Therefore, it follows that while H-bond formation clearly has a strong impact on the F and OH ordering in the humite minerals, other yet unknown phenomena must also have an influence. In addition, while the conclusions drawn in Griffin et al. (2010) are based on both analytical and computational results, the study relied on the analysis of solely two samples: [1]

the synthetic clinohumite discussed above, and [2] a natural Ti-rich clinohumite, investigated to understand if the F/OH ordering observed in the synthetic samples was also seen in natural samples, or if instead it was the result of the synthetic process. Consequently, as robust as these results are, further research is needed to understand whether the same conclusions apply to different humite group minerals other than clinohumite, as well as if they remain valid when the F/OH fraction is significantly different from 0.5.

6.1.3 – Scope of this study.

This study was designed to build on the results presented by Griffin et al. (2010, 2010b). More specifically, the aims of the study were: [1] to understand the extent of the preference for the formation of H-bond bearing over non-H-bond bearing F species (i.e., A and B over C and D, see Figure 6.5b) during the crystallization and equilibration of humite group minerals; [2] to investigate whether the small preference for F-OH pairs to be neighboured by another F-OH pair suggested by simple DFT calculations in model systems (see Table 6.1) has any impact on the F speciation in real samples, and if so to determine the relative importance of this relative to the preference for H-bond formation; [3] to experimentally determine whether differences exist in the preferences in [1] and [2] with mineral composition and between different humite group minerals, and if so to understand such differences, or if, as suggested by DFT calculations (Griffin et al., 2010), each brucite layer does not experience any potential interaction with the neighbouring brucite layers owing to the intergrown forsterite layers, thus rendering each an effectively isolated system.

To achieve the aims of the study, a set of synthetic humite group minerals (see Table 6.2) was analysed to determine the F speciation using ^{19}F MAS NMR spectroscopy. In parallel with the experimental data, a computational model able to simulate F and OH distribution within the brucite layers of each mineral was developed using the Python coding language. In the program, F speciation was influenced only by the F/OH fraction and the preferences described in points [1] and [2] of the previous paragraph. Therefore, the successful reproduction by the algorithm of experimentally measured F speciation would strongly suggest that the preferences for H-bond formation and F-OH pair ordering are the main driving forces of F speciation in humite group minerals. The quantification of these preferences would then lead to a more precise understanding of the optimal F/OH fraction for framework stability in high P-T conditions, with implications for the effective F and OH content of subducted humite group minerals and humite lamellae in subduction zones and therefore on the deep global cycling of water and fluorine.

6.2 – METHODS SUMMARY

A total of 5 humite minerals were chosen for this study, one of which was the synthetic clinohumite investigated previously in Griffin et al. (2010), termed C3095. The other minerals were a clinohumite (C4346), a chondrodite (C4602), a mixture of clinohumite and forsterite (D1658), and a mixture of chondrodite and norbergite (CH001). All samples except C3095 were synthesized via piston cylinder press following the procedure in subsection 2.1.2.3. The synthetic

procedure for sample C3095 was analogous, and it is detailed in Griffin et al. (2010).

The phase association of samples C3095, D1658, C4346 and C4602 was identified and quantified by Prof. Andrew Berry in 2009 via Rietveld refinement of data collected via powder X-Ray Diffraction (pXRD). Due to these analyses being performed in 2009, the details of the analytical procedure utilised were lost. The phase distribution of sample CH001 was determined via Raman spectroscopy for this study (see subsection 2.2.2.3).

F/OH fraction in sample C3095 was measured by Griffin et al. (2010), while in all other sample it was determined via quantification of F abundance via ^{19}F MAS NMR following the procedure in subsection 2.2.1.4. F speciation was analysed via the same technique, and the analytical procedure is detailed in the same subsection. The nature of the samples used for this study is summarized in Table 6.2.

Sample name	Phase composition	F/OH fraction
D1658	94% chum, 6% forst	0.19
C4346	100% chum	0.27
C3095	100% chum	0.54
C4602	100% chon	0.58
CH001	88% chon, 12% norb	0.77

Table 6.2: Phase composition (from X-ray diffraction or Raman spectroscopy) and F/OH fraction (from ^{19}F NMR spectroscopy) of the humite group minerals analysed for this study. Chum = clinohumite, chon = chondrodite, norb = norbergite and forst = forsterite. F/OH fraction = $F/(F+OH)$.

Computational modelling was performed via the python programming language to determine if preferences identified via DFT calculations (see subsection 6.1.2.1) for model systems were relevant for real systems as well. This was done via a custom-built algorithm. Its development and functioning are detailed in the following section (6.2.1).

6.2.1 – Numerical modelling.

The algorithm was constructed using a set of assumptions:

1. The forsterite layers prevent any interaction between different brucite layers, regardless of their number. Therefore, the specific nature of the humite group mineral does not influence the ordering of F⁻ and OH⁻ ions in the brucite layers. A possible exception to this assumption could be norbergite, as the single forsterite layer between each brucite layer might not be enough to prevent inter-layer interactions. Nevertheless, this was deemed able to be neglected, as only a minor fraction of one single sample (i.e., 12% of CH001) was norbergite, thus this effect is unlikely to exert any major influence over F speciation in the sample set.
2. The chemical shift of each F/OH site is determined solely by the nature of the two neighbouring anion sites, as in Figure 6.5b, and longer-range differences between sites do not need to be considered.
3. All M4 sites in the structure are considered as occupied by Mg atoms, and thus have no influence on F and OH ordering.

Assumptions [1] and [2] are based on the results of the DFT calculations described above, while assumption [3] is rooted in the synthetic nature of the

studied samples, which guarantees strict control over their chemical composition. These assumptions were motivated by the need to exclude any possible influence over F and OH ordering outside of the preference for the formation of F—OH pairs and for each of those pairs to be followed by another F—OH pair. Based on these assumptions, it was possible to reduce the brucite layers to a one-dimensional array, with each cell populated by either a 1 or a 2, which represented F (1) and OH (2) respectively, or a 0, representing an empty/vacant site in the array.

The model operates by generating an empty one-dimensional array (termed “chain” from now onwards) of an arbitrarily chosen number of cells (termed as “sites” from here onwards), represented by zeroes to distinguish them from sites populated by F and OH. The algorithm then populates sites in a random order with either F or OH, with the probability of each depending on: [1] the F/OH fraction, from 0 to 1, of the mineral (e.g., if F/OH = 0.6, then the probability of F and OH being chosen for incorporation starts as 60% and 40% respectively), and [2] the nature of the atomic species in the neighbouring site (either the site preceding or following in the chain, arbitrarily decided by the operator), if any is present. More specifically, the algorithm chooses an anion to introduce in the chain, initially influenced solely by the F/OH fraction given as input (e.g., if F/OH fraction is 0.25, there is a 25% chance that the chosen anion is F⁻).

Assuming an F is obtained, the algorithm then chooses whether this can be inserted into the chain, based on the atom present in the neighbouring site (i.e., that with which a hydrogen bond could potentially be formed). If this site is empty the atom is always inserted. If this site is OH (i.e., the two sites are different,

and an F-HO hydrogen bond could be formed) the atom is always inserted. If, however, this site is occupied by F (i.e., the two atoms are similar and an F-HO hydrogen bond will not be formed), the atom is inserted based on a preference (termed Pref_{FOH} from here onwards, varying between 0 and 100). If $\text{Pref}_{\text{FOH}} = 0$ the atom is always inserted (resulting in no preference for F-HO hydrogen bond formation). If $\text{Pref}_{\text{FOH}} = 100$ the atom is always rejected (resulting in insertion only if F-HO hydrogen bonds can be formed).

Where the conditions for the incorporation of the chosen anion are met (see flowchart in Figure 6.6), the empty site (0) is replaced by either a F or OH (i.e., represented as 1 or 2). This procedure continues until the chain is either full or until a predetermined number of empty sites has been filled (i.e., a number of vacancies can be specified), depending on the operator's choice. The latter approach significantly reduces the computational time and allows a number of vacancies in the chain to be simulated, in order to produce a result closer to real-world materials. The process described thus far (summarised in the flow chart of Figure 6.6) results in a chain populated by F and OH ions, with a potential (but small) number of vacancies. (In this work the number of vacancies was not varied but fixed at 1.6% - see later).

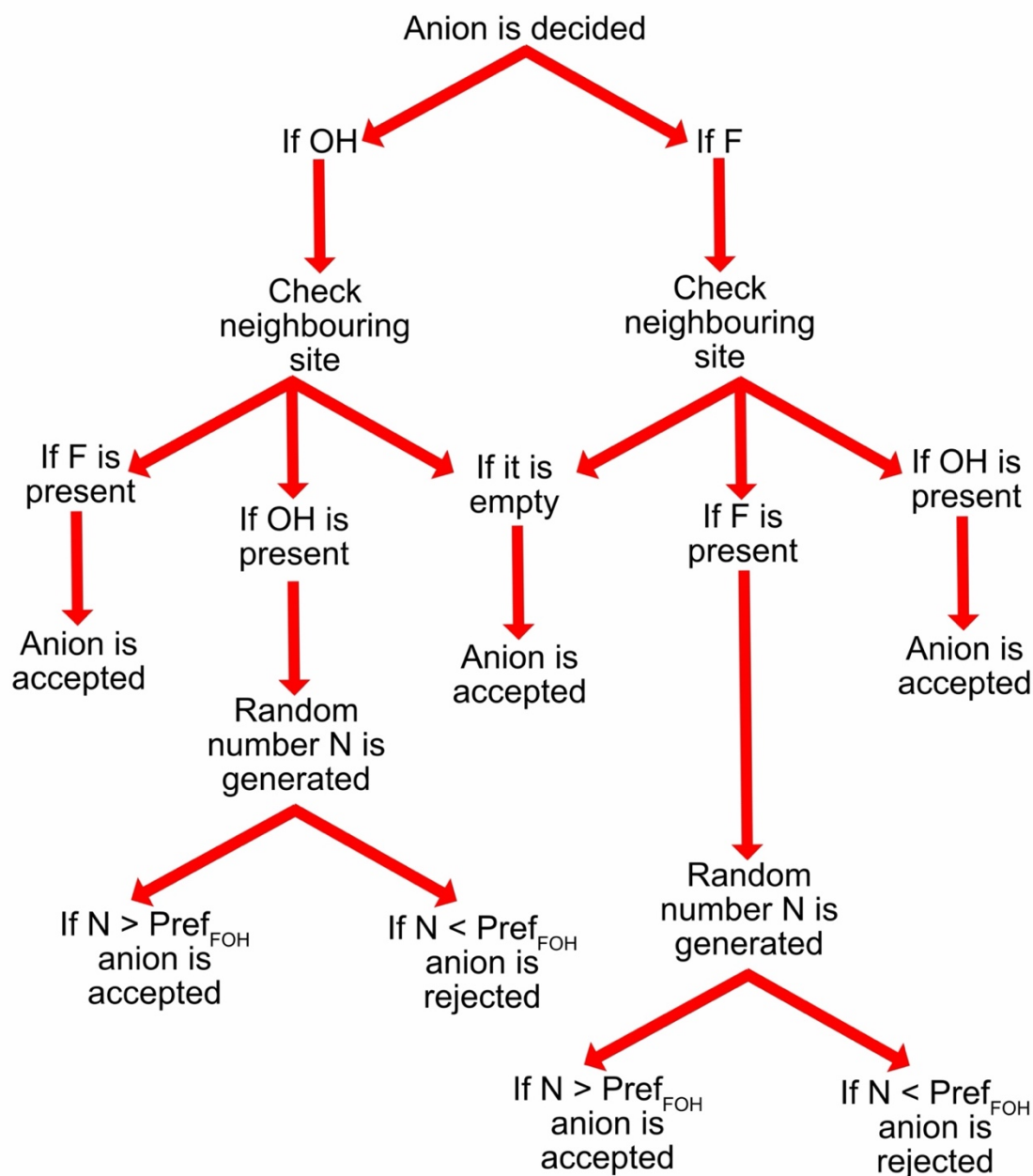


Figure 6.6: Flowchart summarizing the rationale behind the first stage of the modelling (i.e., the filling of the chain by F and OH ions). Pref_{FOH} = preference for F—OH pairs to form in neighbouring sites (i.e., the one in which a F—HO hydrogen bond could be formed) of the chain (integer between 1 and 100), N = random integer comprised between 1 and 100.

In a subsequent step, the algorithm then simulates the preference of F—OH pairs to be followed by another F—OH pair over an OH—F pair (termed

P_{ORDER} from here onwards, and with a value between 0 and 100). This is achieved by checking every pair of H-bonded sites in the chain, and in cases where an OH—F pair is found to follow a F—OH pair, the order of the ions in the second pair is swapped with a probability equal to P_{ORDER} (e.g., if a F—OH pair is followed by an OH—F pair with $P_{\text{ORDER}} = 25\%$, then there is a 25% probability that the order of the ions in the second pair is swapped). This procedure (see Figure 6.7) does not impact either the F/OH fraction nor the abundance of F—OH pairs in the chain, only their ordering. It should be noted that for this model no swapping is carried out if the adjacent pair is OH—OH or F—F (even though this could have an effect on the exact numbers of each type of F). A preference for additional ordering in this way could be considered in the future.

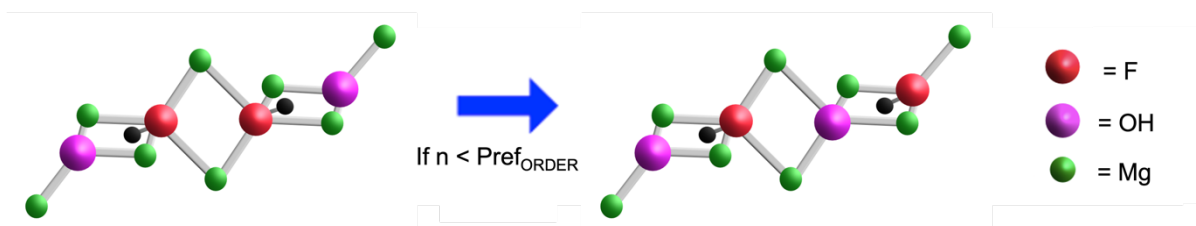


Figure 6.7: Schematic of the ordering performed in the chain following the preference for F—OH pairs to be followed by another F—OH pair rather than an OH—F pair. P_{ORDER} is an integer between 1 and 100 and n is a random integer between 1 and 100.

Once the ordering of the chain is concluded, a counting algorithm determines how many F—OH, OH—OH and F—F pairs are present on the two sites that form the “hydrogen bond”, as well as the relative abundance of F species A, B, C and D. The whole process (i.e., from the generation of the new chain) is then iterated for a predetermined number of times, with each iteration representing a single brucite layer. The preferences are kept constant between

different iterations, while the F/OH fraction is varied based on the expression in Equation 6.1. This was carried out to simulate the local variation in the F/OH fractions that could be expected as a result of the compositional heterogeneity arising during the crystal growth and retained due to the absence of interaction between different brucite layers and between individual crystallites.

$$F/OH_{changed} = F/OH_{initial} * (\pm y), X \% \text{ of times.}$$

Equation 6.1: Formula used to vary the F/OH fraction between different iterations of the model.

$F/OH_{changed}$ = F/OH fraction of the specific iteration, $F/OH_{initial}$ = starting F/OH fraction (given as input), y is a random number between 0.16 and 0.56, the sign of the variation is randomly decided each iteration. The lower limit for y (0.16) was chosen to ensure that each F/OH variation is large enough to be relevant, and the upper limit (0.56) to avoid an excessive number of iterations being discarded due to F/OH being outside of the 0 to 1 interval. These limits can be changed by the user if desired. F/OH is varied X% of times, with X being an arbitrary integer between 1 and 100 chosen by the user. If the change results in a F/OH fraction below 0 or above 1, the calculation is iterated until a positive result is achieved.

The results of all iterations are then averaged, and the final result is given both as a data table and as a bar graph (see Figure 6.8). The full set of variables utilised by the model is reported in Table 6.3.

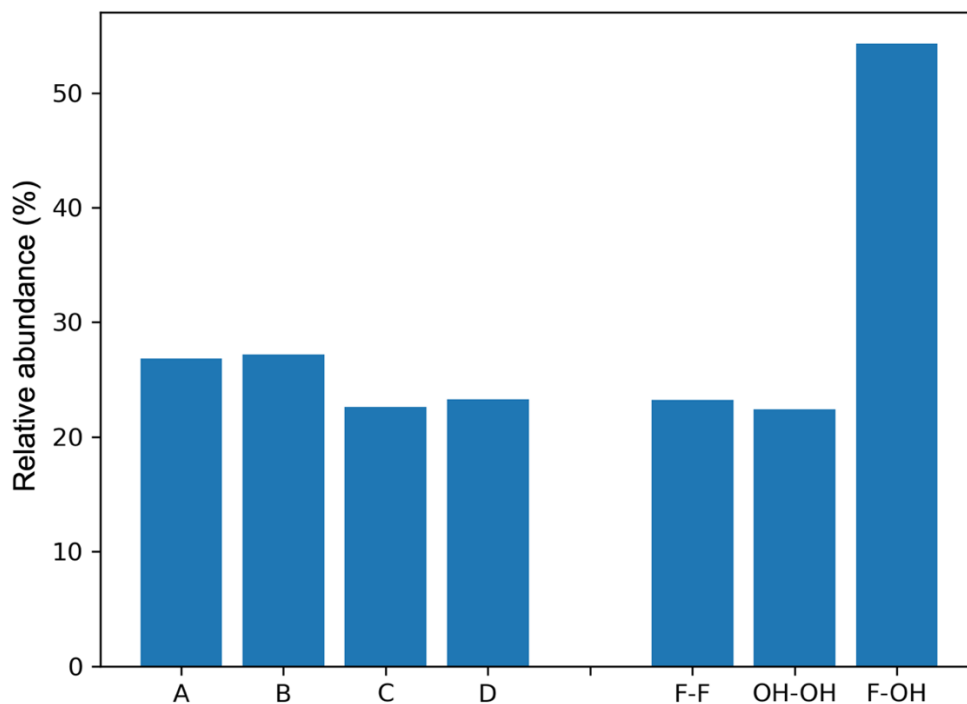


Figure 6.8: Example of the graphical output of the modelling algorithm. A, B, C and D are the possible F local bonding environments defined in Figure 6.5, while F—F, OH—OH and F—OH are the possible pairs of ions occupying the two sites in the pairs of atoms that would be hydrogen bonded in fully hydroxylated humites. Note that $A + B + C + D$ has to equal 100% (i.e., all of the F content) and also that $F—F + OH—OH + F—OH$ has to equal 100% (i.e., all of the linkages).

Variable	Definition	Possible values
Length _{CHAIN}	Length of the array used to simulate the F/OH sites in each brucite layer.	Arbitrary positive integer. Always fixed at 12500 in this work.
Pref _{FOH}	Preference for the formation of F—OH pairs over F—F and OH—OH pairs.	Integer from 0 to 100.
Pref _{ORDER}	Preference for F—OH pairs to have neighbouring F—OH pairs rather OH—F pairs.	Integer from 0 to 100.
F/OH _{initial}	F/OH fraction given as the initial input.	Integer from 0 to 100.
F/OH _{changed}	F/OH fraction varied between different iterations of the algorithm, as decided via equation 6.1.	Integer from 0 to 100.
y	Entity of the variation of the F/OH fraction via equation 6.1.	Floating point number from 0.16 to 0.56.
N _{vacancies}	Number of empty sites accepted in each chain.	Arbitrary positive integer. Always fixed at 200 in this work (i.e., 1.6%).
N _{ITERATIONS}	Number of times the model is iterated.	Arbitrary positive integer. Always fixed at 250 in this work.

Table 6.3: Summary of the variables used by the algorithm as input.

6.3 – RESULTS

6.3.1 – Phase identification via Raman spectroscopy.

The only sample that required phase identification in the context of this thesis was sample CH001, as all other samples has already been analysed previously. To do this, a total of 9 Raman spectra were collected on two chips of sample CH001 (see Figure 6.9 and 6.10).

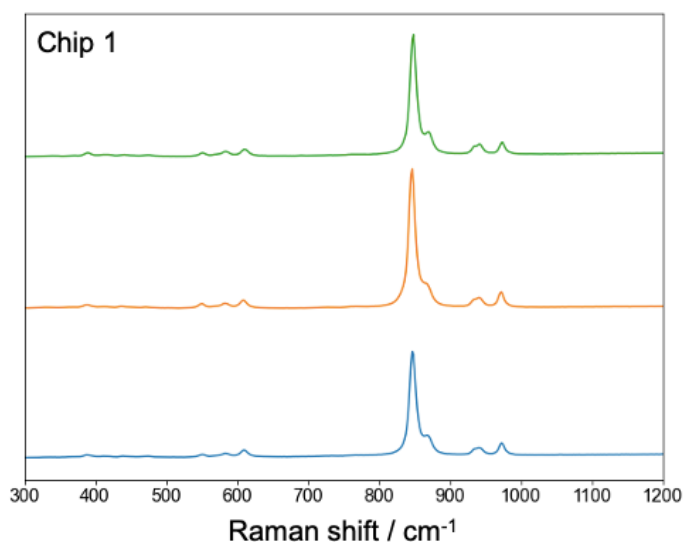


Figure 6.9: Raman spectra collected from the first chip from sample CH001. Only the region of interest (i.e., between Raman shifts of 300 and 1200 cm⁻¹) is reported.

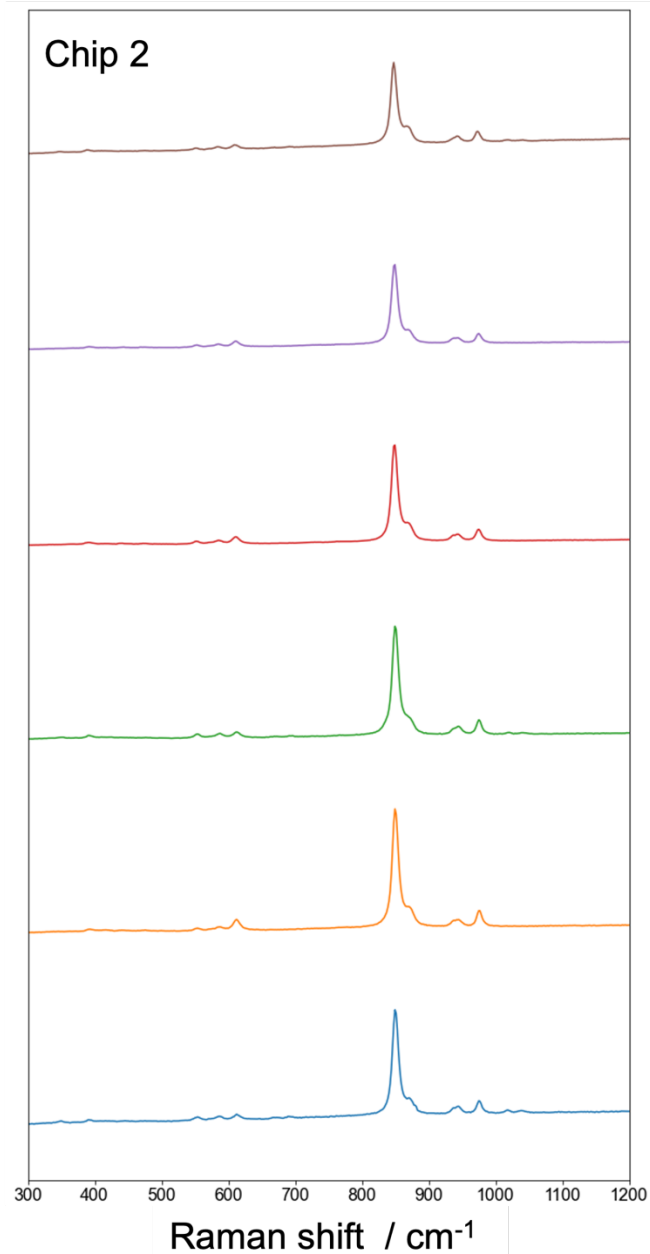


Figure 6.10: Raman spectra collected from the second chip from sample CH001. Only the region of interest (i.e., between Raman shifts of 300 and 1200 cm⁻¹) is reported.

All spectra overlap, indicating that both chips consisted of the same phase distribution. The absence of any features in the 700-800 cm⁻¹ region of the spectra was considered indicative of the absence of humite and clinohumite in the sample (Frost et al., 2007). The spectra were averaged and the peak feature

in the 800-900 cm^{-1} region was fitted via a custom algorithm built using the Imfit Python library (see Figure 6.11a). The sample was determined to consist predominantly of chondrodite, however a minor, but still relevant, norbergite component is also present (see Figure 6.11b). The areas under the two chondrodite-related peaks were summed together and, when compared to the single norbergite-related peak, it was determined that sample CH001 consisted of a mixture of 88% chondrodite and 12% norbergite.

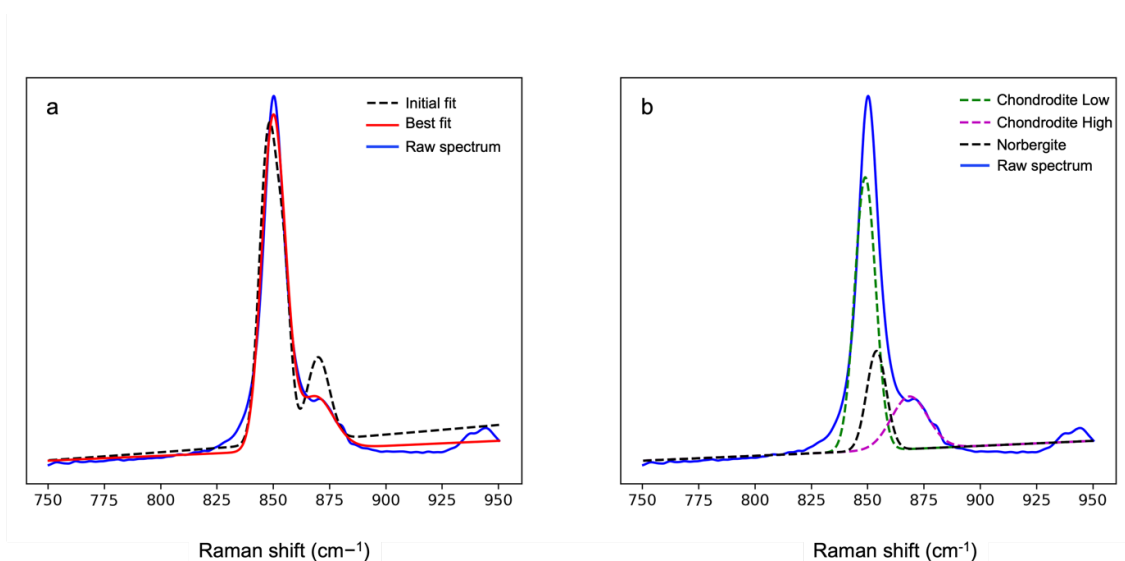


Figure 6.11: (a) Fitting of the averaged Raman spectrum collected from the two chips from sample CH001. (b) Deconvoluted components of the fitted spectrum. The two components relative to the chondrodite are termed “Chondrodite Low” and “Chondrodite High”.

6.3.2 – ^{19}F MAS NMR spectroscopy.

6.3.2.1 – Quantification of the F/OH fraction.

^{19}F MAS NMR spectra collected in this study are presented in Figure 6.12. The F/OH fraction in sample C3095 (see Figure 6.5a) was known from Griffin et al.

(2010). A natural Mg-rich clinohumite, termed as NCH from here onwards, ($\text{Mg}_{8.85}\text{Fe}_{0.01}\text{Ti}_{0.2}(\text{Si}_{3.94}\text{O}_{16})\text{O}_{0.4}\text{F}_{0.97}(\text{OH})_{0.63}$), with a F/OH fraction of 0.48, also analysed by Griffin et al. (2010), was used as a standard for the analysis of the unknown samples. Due to the relevant Ti content of this sample, which the model described in section 6.2.1 was not designed to take into account, no further investigation was carried out on it. All spectra consisted of four relatively broad Gaussian-like peaks centred at -164 ± 0.1 , -168 ± 0.1 , -174 ± 0.1 and -177 ± 0.1 ppm, which correspond to species A, B, C and D respectively (Griffin et al., 2010). The spectrum collected from sample NCH also contained a fifth peak at a chemical shift at -163 ± 0.2 ppm, due to the presence of F neighboured by Ti atoms (Griffin et al., 2010). The resulting compositions from the quantification procedure are reported in Table 6.4.

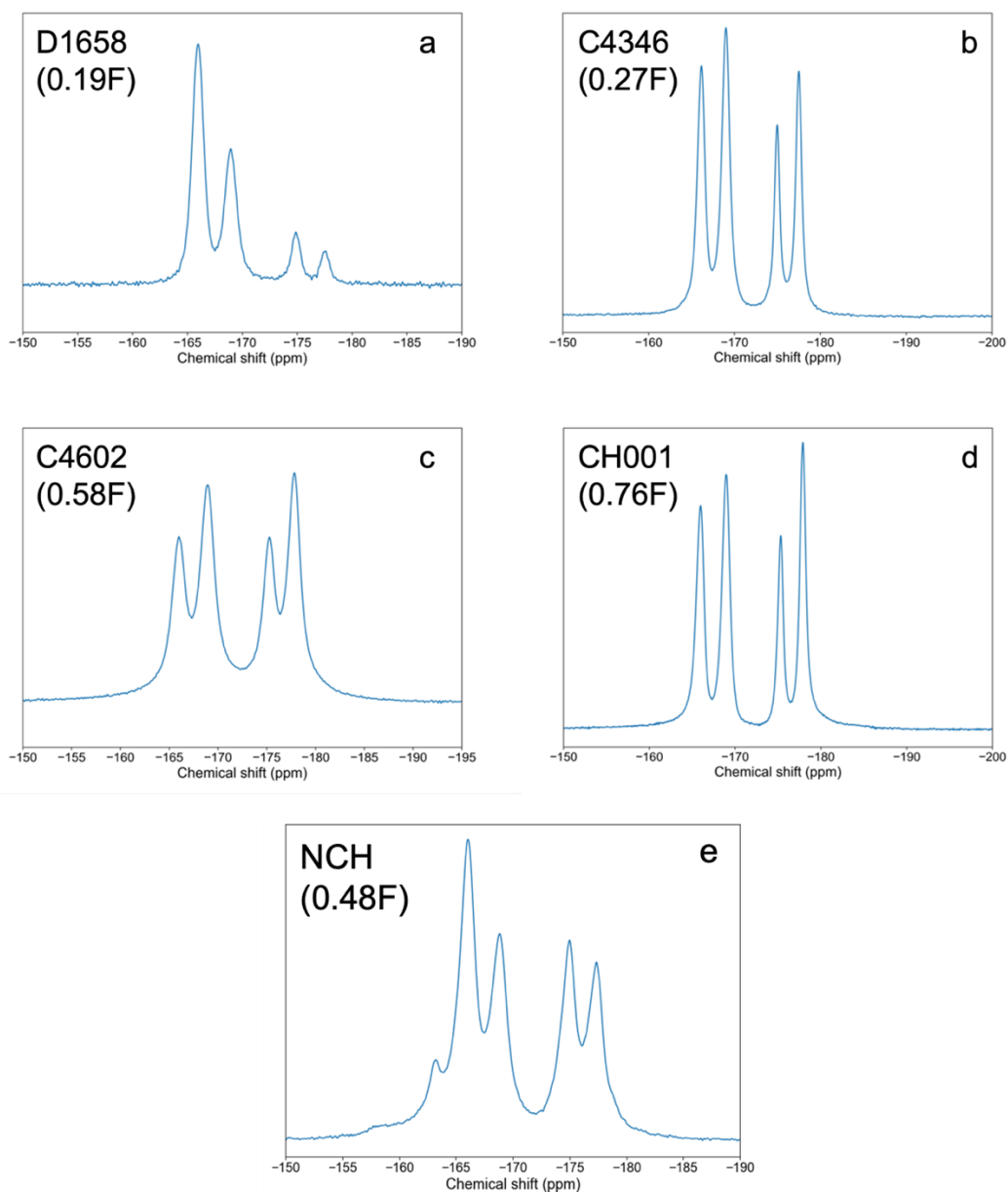


Figure 6.12: ^{19}F MAS NMR spectra collected from samples analysed in this study, rotated at 30 kHz at a magnetic field B_0 of 14.1 T, corresponding to a Larmor frequency of 564.7 MHz. F/OH fraction of each sample is reported in brackets.

Sample	Sample mass / mg	Phase composition	Scaling factor	Scaled signal	F/OH fraction
D1658	2.0	94% chum, 6% forst	1.063	21689.59	0.19
C4346	2.6	100% chum	1.000	28995.345	0.27
NCH	5.3	100% chum	1.000	51547.28	0.48
C4602	10.4	100% chon	1.828	113859.35	0.58
CH001	14.9	88% chon, 12% norb	1.982	163892.43	0.77

Table 6.4: F concentration in the samples of this study as measured using ^{19}F MAS NMR. F concentration in C3095, measured via EPMA, is from Griffin et al. (2010). Chum = clinohumite, chon = chondrodite, norb = norbergite and forst = forsterite.

6.3.2.2 – F speciation analysis.

The relative abundance of the different F local environments, as determined by fitting of the peaks in the ^{19}F MAS NMR spectra (see Figure 6.12), of the samples investigated for this study is reported in Table 6.5. The sum of the species involved in OH—F H-bonds (A and B) and those that are not (C and D) is also given.

Sample	A	B	C	D	A+B	C+D	F/OH fraction
D1658	54.8	30.3	9.2	5.6	85.1	14.9	0.19
C4346	27.7	34.1	15.5	22.8	61.7	38.3	0.27
C3095	42.6	35.7	11.5	10.2	78.3	21.7	0.54
C4602	21.4	31.3	18.6	28.7	52.7	47.3	0.58
CH001	26.8	29.7	15.6	27.9	56.5	43.6	0.77

Table 6.5: Relative abundance (given in % unit) of F species in samples of this study, as determined via fitting of ^{19}F MAS NMR spectra in Figure 6.5b.

As evident from both Table 6.5 and Figure 6.12, F involved in H-bonds are dominant over those that are not for all compositions, suggesting a significant preference for the presence of these interactions in the brucite layers. This is particularly true for samples D1658 and C3095, while sample C4346, despite having a F/OH fraction closer to D1658, exhibits a F speciation more akin to samples with a much higher F content (i.e., above 0.6), particularly C4602. It is also evident that, while the relative abundance of non-H-bonded F increases up to almost 50%, this increase is mostly driven by an increase in D, which ca. quintuples when going from 0.19 to 0.58 in F/OH, rather than in C, which only doubles in the same F/OH interval. The most predominant species at $\text{F/OH} < 0.54$ is species A, while above this threshold species B becomes more prevalent, reflecting the higher level of F in the sample. The trends are summarised in Figure 6.13.

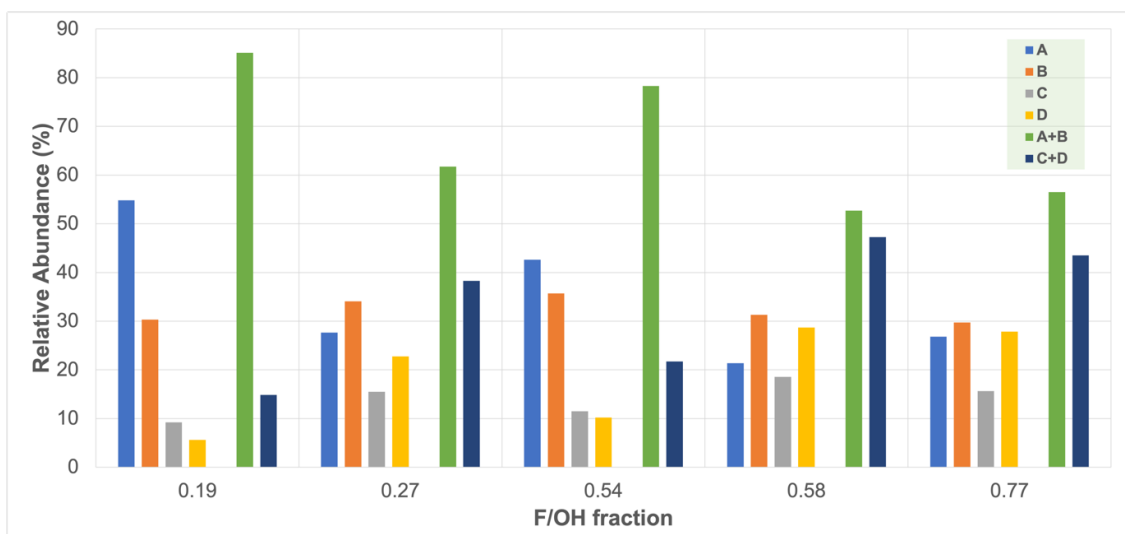


Figure 6.13: Plot showing the distribution of F species in samples of this study as a function of F/OH fraction.

6.3.3 – Numerical modelling.

6.3.3.1 – Model testing and optimization.

Due to the custom-built nature of the algorithm implemented for modelling in this study, testing and optimization were carried out to ensure that calculations were functioning as intended under specific conditions. The algorithm was initially run with a F/OH fraction of 0.5 and no preference for either H-bond formation or ordering of the F—OH pairs (i.e., with Pref_{FOH} and $\text{Pref}_{\text{ORDER}}$ both being set to 0), which, as expected, generated a completely random distribution of F and OH in the chain of sites, with equal abundance of species A, B, C and D, and the number of F—OH pairs being double the level of OH—OH and F—F pairs (as F—OH and OH—F pairs are combined). Subsequently, the algorithm was run again with no preference being imposed on F and OH ordering but with a F/OH fraction of 0.25, which resulted in OH—OH pairs and species A becoming prevalent within the

pairs and species distribution, respectively, as shown in Figure 6.14. The same modelling performed with a F/OH fraction of 0.75 instead resulted in an increase in the amount of F—F pairs and in species D, mirroring the abundance of OH—OH pairs and species A at F/OH = 0.25. Species B and C, which both contain the same number of F and OH (although different H-bonding interactions), were always present in equal concentrations. The results described thus far (shown in Figure 6.14) proved that the model, in the absence of any preference for F and OH ordering, was effectively distributing anions randomly within the chain, with the only influence on the abundance of different F species and different pairs being the F/OH fraction.

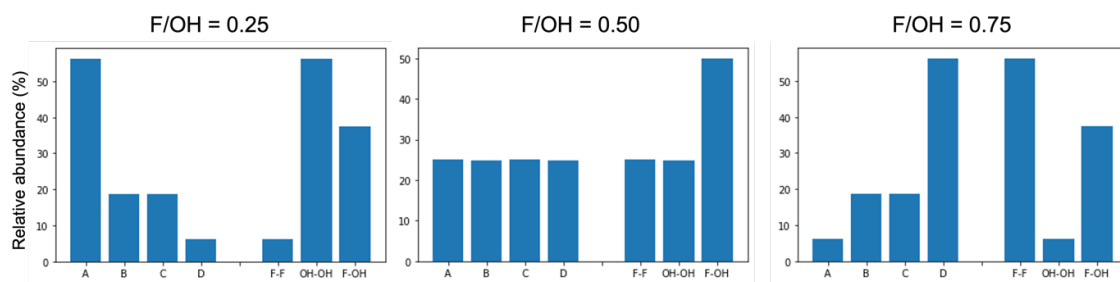


Figure 6.14: Distribution of species and pairs in the site chain as modelled with no preference for F and OH ordering, as a function of F/OH fraction. $N_{\text{sites}} = 12500$, $N_{\text{vacancies}} = 200$, $N_{\text{ITERATIONS}} = 250$.

Following this initial testing, the effect of including a preference for H-bond formation was investigated, with a fixed F/OH fraction of 0.50, by progressively increasing Pref_{FOH} from 0 to 90 in steps of 10 (see Figure 6.15, only steps with $\text{Pref}_{\text{FOH}} > 50$ are reported as a lower preference resulted in only minor impacts on the F speciation). This results in a progressive rise in F—OH bearing species (i.e., A and B), hence showing that this variable is behaving as intended.

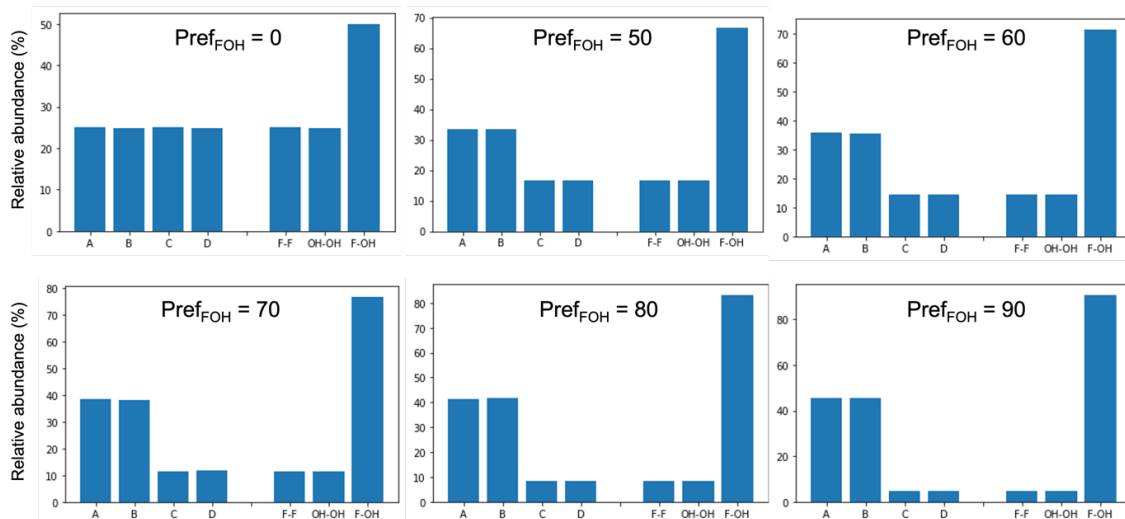


Figure 6.15: Plots showing the distribution of species and pairs in the chain as modelled with preference for H-bond formation (Pref_{FOH}) varying from 50 to 90, with a fixed F/OH fraction of 0.5. $N_{\text{sites}} = 12500$, $N_{\text{vacancies}} = 200$, $N_{\text{ITERATIONS}} = 250$.

Finally, the effect of the $\text{Pref}_{\text{ORDER}}$ variable was tested by progressively increasing its value from 10 to 20 (Pref_{FOH} and F/OH were fixed at 80 and 0.5 respectively). This resulted in a relative increase in species A over species B (see Figure 6.16).

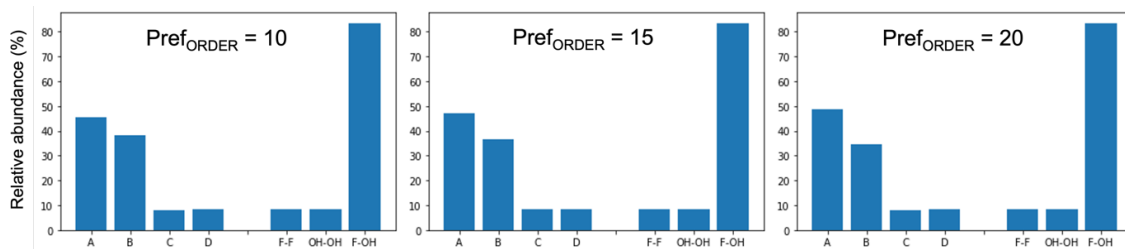


Figure 6.16: Plot showing the distribution of species and pairs in the chain as modelled with preference for F—OH pair ordering ($\text{Pref}_{\text{ORDER}}$) varying from 10 to 20, with a fixed F/OH fraction of 0.5 and $\text{Pref}_{\text{FOH}} = 80$. $N_{\text{sites}} = 12500$, $N_{\text{vacancies}} = 200$, $N_{\text{ITERATIONS}} = 250$.

The results of the testing performed thus far were deemed acceptable evidence for the model working as intended.

6.3.3.2 – F speciation prediction results.

After the testing phase, the model was applied to chains with F/OH fractions determined for the experimental samples from NMR spectroscopy, with the aim of producing a F speciation as qualitatively close as possible to that measured experimentally (see Table 6.5). The most similar speciation relative to experimentally measured results closest match was reached with $\text{Pref}_{\text{FOH}} = 83$ and $\text{Pref}_{\text{ORDER}} = 17$ (see Table 6.6). It was decided to use these values as it provided, on average, the best fit for relative abundance of F species in all samples, as varying the value of the preferences from one sample to the other would introduce the risk of overfitting the data. It is possible that the preference for the formation of F-OH hydrogen bonds does vary with composition of course, but the preliminary DFT results shown above (carried out for OH rich and F rich structures) show no evidence for this enthalpically at least.

Sample	A	B	C	D	A+B	C+D	F/OH fraction
D1658	82.18	15.63	1.68	0.50	97.81	2.18	0.19
C4346	61.38	30.94	4.31	3.37	92.32	7.68	0.27
C3095	40.81	35.52	10.75	12.92	76.33	23.67	0.54
C4602	32.84	33.76	13.91	19.48	66.60	33.39	0.58
CH001	8.28	21.15	16.21	54.36	29.43	70.57	0.77

Table 6.6: Relative abundance of F species in samples of this study as predicted by the algorithm developed for this study. $N_{\text{sites}} = 12500$, $N_{\text{vacancies}} = 200$, $N_{\text{ITERATIONS}} = 250$. $\text{Pref}_{\text{FOH}} = 83$, $\text{Pref}_{\text{ORDER}} = 17$.

When compared to the F speciation determined using ^{19}F NMR spectroscopy, the results of the modelling have mixed agreement (see Figure 6.17). More specifically, when the F/OH fraction is between 0.5 and 0.6 (i.e., in samples C3095 and C4306) the results predicted by the algorithm are in good agreement with those measured experimentally. The results are less accurate for D1658 (which has a lower F/OH fraction of 0.19), with the algorithm overestimating the relative abundance of species A. Similarly, the abundance of species D is overestimated over the other species for CH001, where F/OH is 0.77. Despite this, the results from the latter two samples, while not as accurate as in the case of the former, still are in good qualitative agreement with the experimental results. For C4346, however, the speciation predicted by the model is completely different from that determined from the experimental NMR spectroscopy.

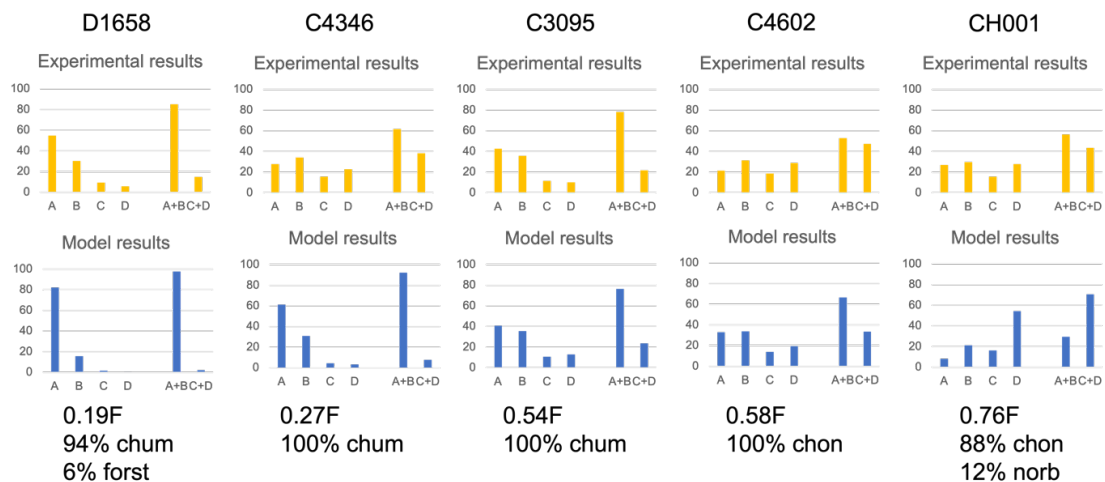


Figure 6.17: Plots showing the relative abundance of F species as predicted by the algorithm compared to the F speciation determined from ^{19}F NMR spectroscopy. Chum = clinohumite, chon = chondrodite, norb = norbergite and forst = forsterite. $N_{\text{sites}} = 12500$, $N_{\text{vacancies}} = 200$, $N_{\text{ITERATIONS}} = 250$.

6.4 – DISCUSSION

6.4.1 – F and OH ordering in humite type minerals.

6.4.1.1 – Modelled vs. experimentally determined F speciation.

The relative abundance of species A, B, C and D predicted by the algorithm is of mixed agreement with the experimental NMR results, however the qualitative trend of an increase in species C and D with increasing F/OH fraction is reasonably well reproduced (see Figure 6.18), with significant discrepancies observed only in sample C4346. In addition, a systematic increase in the abundance of F—OH pairs is seen with increasing F/OH, which coincides with an almost mirrored decrease in the level of OH—OH pairs, with F—F pairs increasing only with a very high F/OH fraction (see Figure 6.19).

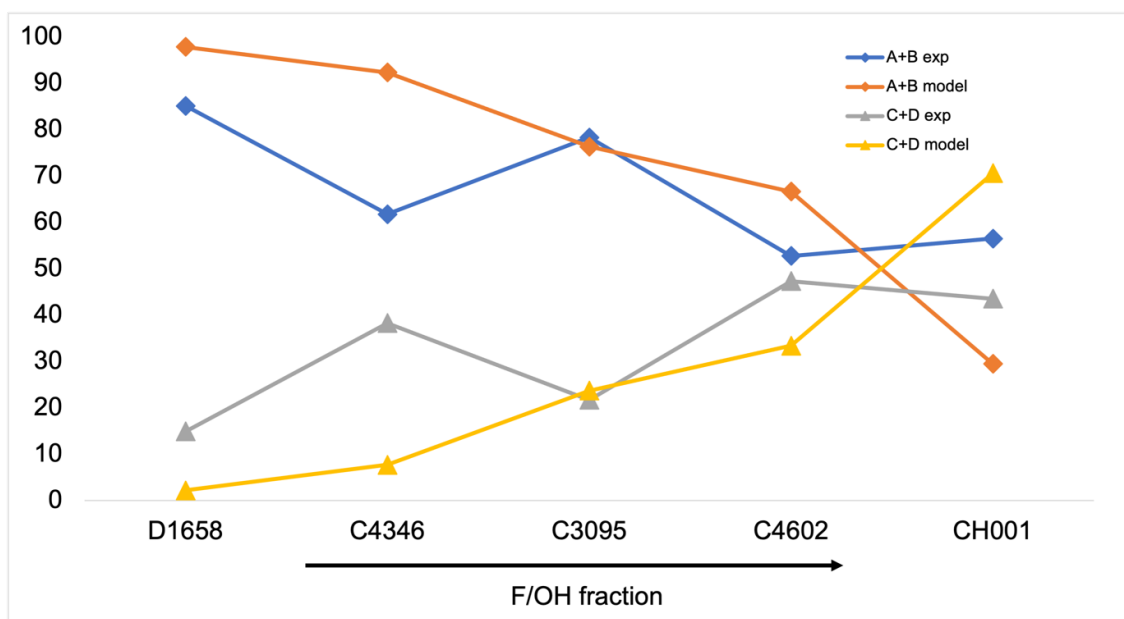


Figure 6.18: Plot showing relative abundance of the sum of F in H-bond (A+B) and not in H-bonds (C+D) as determined via NMR analyses (exp) and as predicted via modelling (model), from Table 6.6. Points are connected via a line only as a guide for the eye. Error on each value is given by the size of the symbols representing each point.

The results predicted from the algorithm for the distribution of the different F and OH pairs in the minerals (see Table 6.7 and Figure 6.19), seem to broadly agree with results from ^{19}F NMR spectroscopy, as F—OH pairs seem to be the preferential arrangement (i.e., A and B are always the prevalent species). This is because, even with either very low or very high F/OH fractions (i.e., sample D1658 and CH001, with F/OH of 0.19 and 0.77 respectively), they still make up a significant fraction of all pairs (i.e., above 30% and 40% of the total respectively). In contrast, the abundance of F—F and OH—OH pairs is much more variable, as predicted by the model. Interestingly, for F/OH ratios of 0.5-0.6 F—F pairs are notably higher in concentration (i.e., around 10%) than OH—OH pairs (almost absent). The latter pair should thus be regarded as actively disfavoured by the

framework, in contrast with F—F pairs, which are instead perhaps neither favoured nor disfavoured (see Figure 6.19), as the presence of H⁺ ions in H1/H2 sites has been shown to lead to motion (Griffin et al., 2010). However, it should be noted how while these speculations are solid in the case of F/OH fraction being comprised between 0.5 and 0.6, outside of this range the predictions from the model starts to vary from the experimentally determined F speciation, and thus their validity must be investigated more thoroughly.

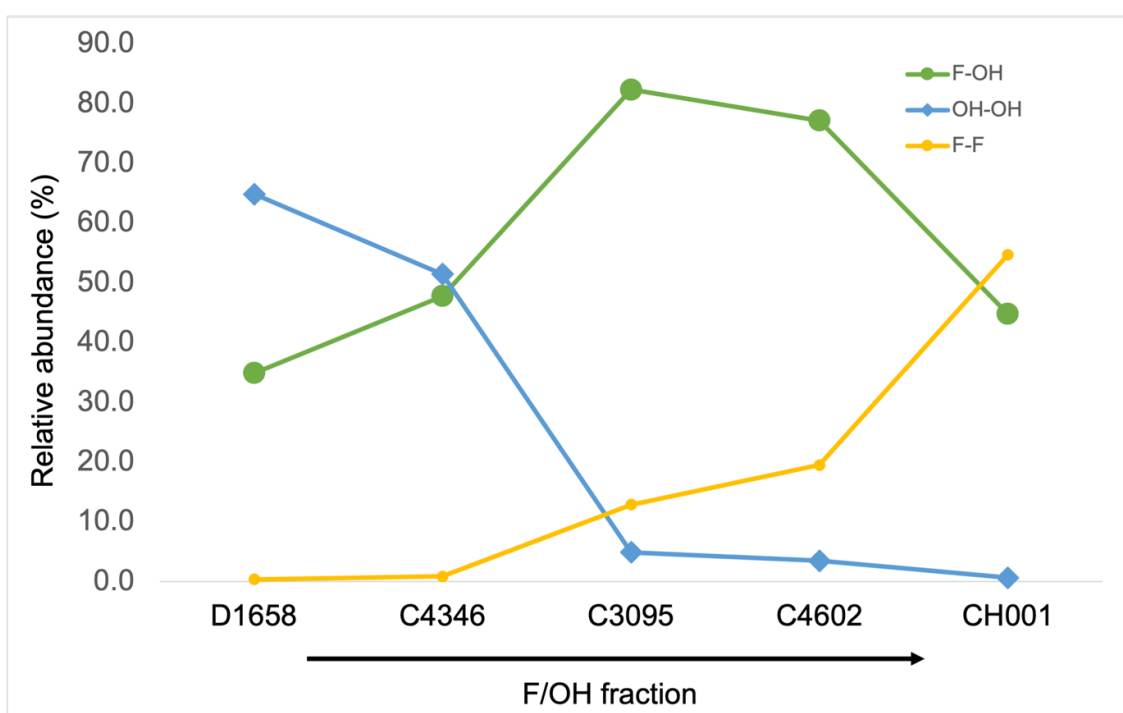


Figure 6.19: Plot showing relative abundance of F—OH, OH—OH and F—F pairs at the F/OH fractions of samples of this study, as predicted by the algorithm. The shape of the function connecting points at different F/OH fractions is based on a 2nd order polynomial fitting of the dataset. Points are connected via a line only as a guide for the eye. Error on each value is given by the size of the symbols representing each point.

Sample	F—OH	OH—OH	F—F
D1658	34.84	64.81	0.35
C4346	47.73	51.42	0.85
C3095	82.31	4.84	12.84
C4602	77.12	3.42	19.46
CH001	44.74	0.60	54.66

Table 6.7: Relative abundance of F—OH, OH—OH and F—F pairs in samples of this study, as predicted by the algorithm.

The preference for F—OH pairs to be followed by a further F—OH pair was also confirmed via the implementation of the Pref_{ORDER} parameter and the improved agreement with the experimental results (as evidenced in Figure 6.17, model predictions better approximate the experimental results when this preference is implemented), and this also agrees with the mixing energies calculated using DFT (see Table 6.1). Notably, this parameter is independent from the abundance of F—OH pairs, as it does not influence the F/OH fraction, only the ordering of these pairs, and thus its predictions can be considered as reliable regardless of the considered F/OH fraction.

Finally, it must be pointed out that the most accurate predictions by the algorithm are achieved for C3095 and C4602, a clinohumite and a chondrodite respectively, while the least accurate correspond to C4346, another clinohumite, and the mixed samples D1658 and CH001, consisting of mostly clinohumite and chondrodite respectively, see predictions of similar accuracy. This shows that the

phase composition of the investigated samples likely has no significant impact on F speciation, yet again in agreement with DFT calculations predictions.

In conclusion, modelling performed in the context of this study shows how the preference for F—OH pairs over F—F and especially OH—OH pairs in humite minerals, alongside the preference for F—OH pairs to be followed by another F—OH pair in the anionic chains, is likely to be the driving force behind F speciation in humite group minerals when F and OH are at similar concentrations. These preferences still influence F speciation when one of the two anions is significantly prevalent over the other, yet they are not sufficient on their own to reproduce the F speciation observed experimentally, at least in the initial work carried out here. This leads to the conclusion that other phenomena, not modelled by the current algorithm, must also be relevant. One such phenomenon could be heterogeneity in the distribution of F and OH in the chain of sites: at the present state, the algorithm is not able to control the F/OH fraction in local sections of each chain, only to randomly vary it between different iterations of the modelling procedure. Although this is similar in principle, there is no guarantee that the final result would be the same in both cases. It should also be noted that the uncertainty in the level (and sometimes presence) of impurities will affect the agreement between modelling and experiment. Measurement of F/OH composition using e.g., electron microscopy could also be useful, although it would be necessary to ensure this was phase specific.

6.4.1.2 – Implications for humite group minerals stability.

While not being primarily designed with this scope in mind, this study provides indirect insights into how high the F occupancy in the F/OH site must be to maximise H-bond formation with adjacent OH groups, thus stabilising the framework (Lager et al., 2001) while at the same time though reducing the mineral's efficacy as a water carrier (Ohtani, 2015).

Clinohumite, the most common humite group mineral in subducted slabs (Yamamoto & Akimoto, 1977), is not present in the surficial phases of the subduction process, but instead forms following the breakdown of various hydrous phases such as micas and serpentine (Barnes et al., 2018). It must be noted that stable OH-rich clinohumite can coexist with these phases only in warm slabs, while the addition of Ti and F to its framework make it possible for it to occur in cold slabs and in the attached mantle respectively (Grützner et al., 2017).

As of the writing of this thesis, no quantitative estimate exists for the contribution of clinohumite (and humite group minerals in general) to the overall water carrying capacity of a subducted slab. This is not just because of the high number of variables influencing the stability of these phases and the OH content (e.g., F/OH fraction, Ti content, availability of water at the time of formation, type of humite, etc.), but also because of the interconnection between some of these variables: for example, a high Ti content reduces the overall number of sites that can host OH⁻ anions, but can allow the mineral to form at lower P-T conditions (Herman et al., 2007), when less water has been lost to the mantle wedge (Debret & Sverjensky, 2017). According to the results of this study, the F/OH fraction which corresponds to the most pervasive H-bond formation within the framework

is between 0.5 and 0.6 (see Figure 6.19). Assuming that this factor is the main driving force behind the augmented field of stability of clinohumite in high P-T conditions (Grützner et al., 2017), it can be calculated that only ca. 3 wt% of OH is incorporated by the most stable crystals, as opposed to the ca. 5.8 wt% of a fully hydroxylated clinohumite.

Clinohumite in ultramafic rocks is often found as an accessory phase, however quantitative measurements of its abundance in natural samples are exceedingly rare, due presumably to its breakdown at near-surficial conditions. The more accepted estimates put its average abundance in subducted slab phase associations at ca. 1-2 vol% (Barnes et al., 2018; Trommsdorf & Evans, 1980). In this regard, the chloritoid-rich harzburgites from the Cerro del Almiraz massif in Spain (López Sánchez-Vizcaíno et al., 2005) constitute a relevant case study, as these rocks feature notable F-rich clinohumite (i.e., F occupancy of 0.4-0.6 in the F/OH site) which was likely equilibrated outside the typical stability field of OH-rich clinohumite (López Sánchez-Vizcaíno et al., 2009). This feature is in agreement with the estimates inferred from the outcome of this study, corroborating thus the validity of the positive impact of H-bond formation on clinohumite's stability in subduction zones and beyond (Barnes et al., 2018).

6.5 – CONCLUSIONS

This study was designed to investigate the role played by the preference for H-bond formation within the brucite layers of humite group minerals over the lower degree of disorder present in their frameworks when relevant F abundances are incorporated (Griffin et al., 2010b), and, furthermore, to investigate whether this effect is connected to the extended high P-T field of stability characteristic of F-rich clinohumite (Grützner et al., 2017). This phenomenon, alongside the incorporation of Ti in the M4 site (Shen et al., 2014; Griffin et al., 2010), has the potential to greatly influence the efficiency of clinohumite as a water carrier up until transition zone levels of depth. In further detail, this study was devised with the primary goal to evaluate the importance of the preference for H-bond formation between neighbouring F and OH anions and to understand if this phenomenon is relevant for water transport towards the deep Earth.

Based on the outcome of the modelling and analysis performed for this study, it can be concluded that the preference for the formation of H-bond-bearing species over non-H-bond-bearing species in humite group minerals' frameworks is the driving force behind F speciation, when the F occupancy in the F/OH site is between 0.5 and 0.6 (see Figure 6.17), regardless of the specific mineral considered. This preference remains a relevant variable in a wider interval of F/OH fractions (i.e., between the around 0.2 and 0.8 studied here), however in this wider region the preference alone is not a sufficient variable to accurately predict F speciation, thus hinting at other yet unknown phenomena being active (see Figure 6.17). On this note, a preference for F—OH pairs to be neighboured

by another F—OH pair in the framework (see Table 6.1), predicted initially via DFT calculations, was found to be a minor but still relevant factor in controlling the relative abundance of the two H-bond-bearing species (i.e., A and B).

The accuracy of the predicted F speciation from the modelling of this study is at its worst in a clinohumite with F/OH fraction of 0.27, which notably is not the sample with the lowest F/OH fraction investigated in this study. This could be due in misidentification of the phase association of the sample, thus further analyses are necessary to verify that C4346 is effectively a clinohumite. If this was confirmed, however, it would imply that the preference for F—OH pair formation is not the only variable controlling F and OH ordering. Nevertheless, the nature of any other phenomena, as well as of the variable(s) controlling it, is presently unknown. The modelling algorithm however does not consider any variable outside of the two preferences investigated in this study, hence substantial upgrades to the code would be necessary for other factors to be able to influence F speciation in the modelled structure.

Findings of this study show how clinohumite with F/OH fraction between 0.5 and 0.6 is likely stable in the widest possible range of pressure and temperature, in agreement both with experimental results (Grützner et al., 2017) and data from natural samples (López Sánchez-Vizcaíno et al., 2005; Padrón-Navarta et al., 2011). This can potentially result in the halving of the water carrying capabilities of clinohumite in subduction zone settings. To test this prediction, the synthesis and analysis of samples in a wider set of P-T conditions, compared to the relatively narrow region used for the ones of this study, is paramount. In addition to this, quantitative estimates of the relevance of

clinohumite in OH storage in the subducted slab are currently lacking. While outside of the scope of this study *sensu stricto*, building on the available knowledge regarding this phase quantitative abundance in subducted slabs could provide novel and useful insights into how water is transported to, and stored in, the deep Earth.

~7 — CONCLUSIONS AND FURTHER

RESEARCH~

7.1 – CONCLUSIONS

The broad aim of this thesis was to undertake an investigation of the chemical speciation of negatively charged ions in silicate melts and minerals. This topic is often overlooked in geochemistry in favour of the study of cations, despite anions having often a strong influence over the physical and chemical properties of silicates (e.g., fluorine), and being essential building blocks of life on Earth (e.g., nitrogen).

Work on the investigation of nitrogen in CMAS silicate melts as a function of fO_2 confirmed that redox geochemistry controls nitrogen speciation (e.g., Grewal et al., 2020, and ref. therein), even when all other variables (i.e., temperature, pressure, and major elements composition) remain constant (see Table 3.1). This implies that, if the redox conditions of a planet's interior during its evolution are sufficiently reducing (i.e., below IW), outgassing of N to its atmosphere could be hindered due to the sequestration of ammoniacal nitrogen by mineral phases, with massively negative impacts on its habitability. Furthermore, it has been shown that solid-state NMR spectroscopy has the potential to produce highly detailed information on nitrogen speciation (see Figure

3.6) in silicate melts (Roskosz et al., 2006). Although the work in this thesis used ^{15}N -enriched and Fe-free materials, there is scope to expand this towards real phases with recent advances in probe technology and high magnetic fields, although some limitations still remain (i.e., NMR being a bulk technique, as opposed to the in situ nature of Raman spectroscopy).

The work in this thesis primarily concerned the study of fluorine. In the CMAS, MAS and CMS silicate melts of this study, F was found to be present as $\text{Mg}(3)\text{—F}$ species in all glass compositions. This finding suggests that the F speciation is insensitive to even strong variations in the chemical nature of the system (see Figures 4.6 and 4.7), when F is present at BSE-like concentrations (i.e., 10s of $\mu\text{g/g}$). Therefore, the chemical composition of the system can be safely neglected when studying F speciation in silicate melts of this sort, as long as enough Mg to bind with F is present. The preferential coordination of F with Mg likely results in its stable storage in phases such as fluorophlogopite and richterite during the cooling of enstatite chondrites. This translates to F being mostly retained by the asteroidal material that coalesced into the larger bodies which eventually evolved into planet Earth, as opposed to other volatiles which were instead less efficiently retained and that are thus far more depleted relative to CI chondrite compared to F.

Fluorine speciation was also shown to be sensitive to increasing pressure, and that this is likely linked to changes in the average coordination number of the major chemical components of the melt (see Figures 5.8 and 5.9), with all other conditions (i.e., temperature, pressure, and melt composition) being constant. More specifically, F was shown to bind predominantly with Mg and Al at pressures

below 5 GPa, and solely with Mg and Ca between 8 and 20 GPa. F is binding with the same elements in all the major upper mantle minerals (see subchapter 5.1), hinting at F speciation in igneous mineral phases being at least partially inherited from the melt. This in turn suggests that during the planetary-scale partial melting events that occurred during Earth's accretion (Nakajima & Stevenson, 2015) F moved from the minerals in which it was stored at lower pressures (i.e., micas and amphiboles) to major phases of the upper mantle (e.g., olivine, pyroxenes) owing to its speciation in the melt phase.

Notably, studies on fluorine speciation were carried out with F present at concentrations typical of the BSE, rather than in highly F-enriched systems, thus making the observations and conclusions more applicable to natural phases. This is possible as long as excessive amounts of paramagnetic elements are avoided, as showed by the natural minerals (richterite, Ti-clinohumite) analysed as reference materials (see Figure 4.7 and Figure 6.12), owing to the high sensitivity of ^{19}F NMR spectroscopy.

For humite group minerals, this work has shown why it is important to investigate the geochemical behaviour of anions in silicate phases. In this specific case, the interaction of fluorine with neighbouring hydroxide ions is able to expand the field of stability of such minerals to higher pressure and temperature conditions (Friedrich et al., 2002; Griffin et al., 2010; Grützner et al., 2017). In addition, while F has a positive effect on the stability field of humite group minerals, its incorporation into the F/OH site also negatively impact the number of sites in which OH could be stored instead, thus limiting their water-carrying capabilities in subducting slabs. This shows how F availability within a planet's

interior has strong impacts over the cycling of water as well, and therefore how without its efficient storage mechanisms during planetary formation and evolution this cycle would likely look much different.

In conclusion, this thesis shows, perhaps more than anything else, the great potential that solid-state NMR spectroscopy has when applied to the geosciences. Although more conventional approaches, such as ^{29}Si MAS NMR, have been widely applied to minerals over many years, it is clear that hardware advances are opening up the study of less common, more challenging, and lower abundance nuclei in both model systems and natural minerals to provide new insights into the systems studied and problems addressed by Earth scientists.

7.2 – STUDYING DEEP EARTH SILICATE MELTS

AND AQUEOUS FLUIDS VIA NMR

SPECTROSCOPY

As summarised in section 3.4.3, there are pros and cons to the use of ^{15}N MAS NMR in lieu of Raman and IR spectroscopy. While the latter techniques are the only choice for *in situ* analysis of multi-phase systems (due to solid-state NMR being a bulk technique), the former is much more efficient in discriminating between different N species, thanks to its element specific nature enabling even the relative quantification of coexisting ammoniac species (see Figure 3.9), a much

harder feat for Raman and IR spectroscopy due to high levels of fluorescence of glassy phases, especially at the relatively low N concentrations of the samples of this study (see Figure 3.5). Despite this, solid-state NMR is not a flawless technique: its main disadvantages are the low sensitivity of ^{14}N , the by far most abundant nitrogen isotope, and the significant peak broadening that can be caused by high concentrations of paramagnetic elements (e.g., Fe). While the first problem is easily solved by studying ^{15}N instead (as done for this thesis), the second is somewhat trickier, as one of the major constituents of the BSE is Fe, which is paramagnetic (see Table 1.1). Nevertheless, the use of higher magnetic field NMR spectroscopy can partially mitigate this issue (e.g., 850 MHz or above, as opposed to the 400 MHz used for the samples of this thesis). In addition, the very fast spin relaxation induced by the paramagnetic nature of Fe could be utilised as an advantage, as it would allow for a much shorter recycle delay compared to the one used in this work, thus allowing a higher number of scans to be acquired for each experiment, which in turn translates to more signal being acquired in the same analytical run time. Notably, however, this would not reduce the paramagnetic shift, only the signal to noise ratio, so problems might still arise.

In summary, it can be concluded that the choice of the analytical technique for the study of N speciation in silicates ultimately depends on the type of information being sought: if the material being studied is a natural (i.e., not ^{15}N enriched) multi-phase system, and a margin of error on relative quantification of the N species can be tolerated, then Raman and IR spectroscopy are probably the best choice. On the other hand, if a higher precision is required, especially in

relative quantification of the N species present, and if the abundance of ^{15}N is high enough, then solid-state NMR is by far the superior choice.

A novel field of study that has seen some recent developments (Chamas et al., 2019) is the study of light element speciation (e.g., C) in fluid phases of geological interest using solid-state NMR spectroscopy. This has been made possible owing to the development of novel MAS rotor apparatuses that allow for the stable storage and analysis of high P and T fluid phases up to 225 °C and 25 MPa (Chamas et al., 2019, and refs. therein). While such conditions are still relatively surficial from a geological perspective, considerable progress is possible in the future, and results from this work demonstrate that ^{15}N CP MAS NMR experiments can discriminate between different N—H bonding environments in geological aqueous fluid phases with unparalleled precision and accuracy (see Figure 3.8). The investigation of N-rich fluids allows the limitations that emerge when studying silicate melts to be by-passed, as Fe is rarely a major element in geological fluids by the virtue of their composition being primarily in the C-O-H-N system (e.g., Mikhail et al., 2017). In addition, as N is a major component of these systems, even without isotopic enrichment ^{15}N would be present at least at the level of 100s of $\mu\text{g/g}$, which results from this thesis have shown to be sufficient for accurate speciation analyses (see subsection 3.3.2.3).

In summary, this thesis has shown how the investigation of silicate melts using NMR spectroscopy has the potential to study N speciation alongside the already commonly studied C and H speciations, thus providing a more comprehensive overview of the chemical species present in silicate melts with an accuracy that Raman and IR spectroscopy cannot rival. Therefore, applying the

data collection procedures developed for ^{15}N in silicate melts to geological fluids would be the next logical step in this field of research. Notably, the study of supercritical aqueous and carbon-rich fluids is not a purely academic endeavour but has direct application in the development of carbon capture and storage techniques in geological reservoirs (Kelemen et al., 2019). Nitrogen is both a major component of such fluids (Li & Keppler, 2014) and a key component of nitrous oxides, which are well known greenhouse gases that made up ca. 7% of US greenhouse gas emissions in the decades between 1990 and 2010 (EPA, 2022). Therefore, the development of carbon capture techniques applied not only to the safe storage of C-based gases, but also to N-based gases, would be also beneficial outside of the academic world. This, however, would require a thorough understanding of N speciation at varying high P and T conditions, particularly in porous systems such as depleted hydrocarbon reservoirs. This is because these techniques are the most well researched and established (Kelemen et al., 2019), and hence are currently considered as the safest option for the capture of greenhouse gases in the near future (Jenkins et al., 2015). Coincidentally, NMR spectroscopy has already been shown to be a highly effective technique for the relative and absolute quantification of the different components of fluids stored in porous systems (Mohebbi et al., 2019).

7.3 – FLUORINE STORAGE DURING MELT

CRYSTALLIZATION

As shown in both Chapter 4 and 5, F preferentially binds with Mg at pressures below 5 GPa in CMAS systems. However, while the speciation observed in the melts investigated in this thesis was directly measured, its incorporation into mineral phases during crystallization is still an unknown process. To investigate this, hydrous phases such as the phlogopite and richterite studied in Chapter 4 would need to be crystallized from a melt with a known F speciation, and then any variation (or lack thereof) in speciation due to the crystallization process could easily be detected by solid-state NMR, owing the high sensitivity to any variation in the F local bonding environment (see section 5.3.2).

A possible alternative to the use of synthetic samples would be to analyse natural materials. More specifically, this would consist of the study of F speciation in F-bearing Mg-rich phenocrysts equilibrated with a low-pressure silicate melt using MAS NMR spectroscopy, by separating the crystals from the matrix and also analysing the phenocryst-free matrix. Potential candidates for such a study could be the phlogopite and olivine from the nephelinitic lavas erupted from quaternary volcanoes of the Balangida rift in North Tanzania (Baudouin & Parat, 2020). The phlogopites in particular are of great interest, as they have a relatively high Mg# (i.e., $Mg/[Mg+Fe]$ between 0.7 and 0.95), contain up to 0.8 wt% of F, and are immersed in a comparatively very F poor matrix, consisting mostly of pyroxenes and olivine with at most a few tens of $\mu\text{g/g}$ of F (Baudouin & Parat,

2020). This would pose challenges for the study of F speciation in the ground matrix, and the phlogopites, while relatively Mg-rich, still contain upwards of ca. 10 wt% of Fe, which would likely result in notable paramagnetic broadening of any peak in the NMR spectrum. Nevertheless, both issues are not insurmountable: F speciation was detected and even quantified in samples of this study which also contained F in the tens of $\mu\text{g/g}$ of concentration, and the paramagnetic broadening due to the high Fe content would at least partially be counterbalanced by the very high F abundance in the phlogopites and likely by more rapid relaxation, which would increase sensitivity per unit time. For these reasons, the study of such lavas, alongside other potential equivalent materials, may shed light on the processes that drive F and volatile storage in general during the cooling of silicate melts.

7.4 – QUANTIFICATION OF FLUORINE LOSS

DURING HIGH TEMPERATURE SAMPLE

SYNTHESIS

The loss of fluorine that occurred during the synthesis of the samples that were the object of the study of chapter 5 (see subsection 5.4.2.1), while resulting in a F concentration similar to that in the BSE, was unplanned and unexpected. A likely reason was identified in the decomposition of CaF_2 that may have occurred

during the decarbonation of the starting materials that preceded the melting procedure, as this was the only high T process that was common to both of the starting mixtures prepared. In order to demonstrate this directly, however, an alternative preparation procedure for the starting mixture that does not involve the high T decarbonation phase would be necessary. More specifically, a simple yet effective approach might be to add CaO directly to the starting mix, rather than using CaCO₃. While this would likely result in the addition of water to the mixture, due to the former being highly hygroscopic, this would not be an issue, as the aim of the study would solely be to identify the cause for the F loss, and the melt being hydrous would not interfere with F quantification, which would be performed via the element-specific MAS NMR by the quantification procedure described in subsection 2.2.1.3. In addition to this, heating the sample at temperatures slightly above 100 °C immediately before sealing the Pt capsule shut via welding would ensure the loss of at least the non-structurally bonded water, thus reducing its content while avoiding the F loss due to the high T heating required for the decarbonation of CaCO₃ to occur.

7.5 – THE DESTABILIZATION OF Al—F SPECIES

WITH INCREASING PRESSURE

As concluded in subsection 5.4.2.2, F speciation in a CMAS7G melt structure undergoes major changes with increasing pressure. To describe these changes in speciation, three possible scenarios were proposed (see Table 5.8), and

ultimately scenario 2 was deemed the most likely. In this case, the changes seen in the ^{19}F NMR spectrum as P increases from 5 to 8 GPa were interpreted as [1] the destabilization of $\text{Al—F—Ca}(n)$ species, [2] the stabilization of $\text{Ca}(N)\text{—F}$ species and [3] $\text{Mg}(3)\text{—F}$ complexes transforming into $\text{Mg}(x)\text{—F}$ complexes ($1 < n < 2$, $3 < N < 4$, $2 < x < 3$). While the reactions in point [1] and [3] are of relatively unambiguous assignment (see section 5.4.2), the existence of Al—F bonds is assumed as a result of indirect interpretation of the results, rather than direct observation (see subsections 5.4.2.2, and 5.4.2.3).

The natural extension of the studies carried out thus far regarding F speciation in high-pressure CMAS silicate melts would be to directly detect the existence of Al—F bonds (or lack thereof) in the melt structure. To do this, one approach would be Al/F heteronuclear correlation spectroscopy (Frydman & Harwood, 1995), where pulses are applied to both nuclei in the same experiment, leading to a two-dimensional spectrum with peak positions showing the chemical shifts of any interacting Al-F pairs. In order to do this, however, samples with a higher F concentration than the ones synthesized for this thesis might be necessary, as the fraction of F involved in Al—F species in samples which contained them is comprised between ca. 14% and 34%. Considering that F concentration in these glasses is between ca. 29 and 69 $\mu\text{g/g}$, this would mean a F abundance in Al—F species of 10-20 $\mu\text{g/g}$, which is close to the detection limit even for a nucleus as NMR sensitive as ^{19}F (see Table 4.4). While this situation could be improved by performing NMR experiments at a higher field (e.g., 850 MHz, or 1 GHz) and for longer run times than the ones used in the context of this thesis, the research described in subchapter 7.4 should be performed beforehand,

in order to guarantee that the significant F loss which occurred in samples of this thesis is not involuntarily repeated.

7.6 – THE DRIVING FORCE BEHIND F SPECIATION IN HUMITE GROUP MINERALS

Based on the outcome of the study carried out on F and OH ordering in the brucite layers of humite group minerals, two possible avenues for further research could be developed. The first would involve the synthesis of other humite group minerals, at different P and T conditions, with the hope of better constraining the effect of these parameters over F speciation and F/OH ordering, thus providing potential direct evidence of the impact of H-bond formation in humite group minerals during their subduction. In practice, this would be performed using the synthesis and characterization of a humite group mineral with the procedures described in section 2.1.2. After thorough analyses, the humites would be annealed at increasing pressures, at temperatures below the melting point, for a sufficient time to allow the structure to re-equilibrate, before being quenched and re-analysed. The process would ideally be analogous to that performed on silicate glasses in chapter 5. As the sample used would be effectively the same, the only influence on F speciation would be the P-T conditions, thus their impact could be accurately assessed.

The second possible study that could be considered would be based on the algorithm used for modelling of the F/OH sites in the minerals framework and

would be focused on using this to build a deep learning algorithm that can associate a set of parameters to resulting crystalline frameworks, in an approach analogous to that described in Le Losq et al. (2021) for the modelling and prediction of physical properties (e.g., viscosity) of a silicate melt structure. In more detail, the algorithm developed for this thesis could be used to generate a high number (e.g., 10000) of chains of sites, each built using a randomly generated set of parameters (see Table 6.3), and the F speciation would be measured as described in subsection 2.2.1.4. The speciations for each chain would be then fed, along with the parameters used to generate it, to a deep learning algorithm (e.g., the TensorFlow algorithm, managed via the Keras python library; Abadi et al., 2016). The algorithm would look for patterns in the speciations and parameters associated with each, and once the training and test phases are completed could be fed a F speciation from experimentally analysed samples and would return the entity of the preference for H-bond formation in the unknown sample. While this algorithm *sensu stricto* would have a very narrow field of application, simple changes to the structure of the array which represents the crystalline structures could be performed, thus extending its validity to other deep Earth hydrous phases. In conclusion, this would be a remarkably unique situation to try and implement deep learning approaches to the geosciences, a field which is still extremely novel, and thus this study would be an important steppingstone in developing the methodologies that could be applied within it.

~8 — REFERENCES~

Abadi, M., Barham, P., Chen, J., Chen, Z., Davis, A., Dean, J., Devin, M., Ghemawat, S., Irving, G., Isard, M., Kudlur, M., Levenberg, J., Monga, R., Moore, S., Murray, D.G., Steiner, B., Tucker, P., Vasudevan, V., Warden, P., Wicke, M., Yu, Y., & Zheng, X. (2016). TensorFlow: A System for Large-Scale Machine Learning. Proceedings of the 12th USENIX Symposium on Operating Systems Design and Implementation (OSDI '16). ISBN: 978-1-931971-33-1

Alexander, C.M.O'D., Howard, K.T., Bowden, R., Fogel, M.L. (2013). The classification of CM and CR chondrites using bulk H, C and N abundances and isotopic compositions. *Geochimica et Cosmochimica Acta* 123, 244–260. <https://doi.org/10.1016/j.gca.2013.05.019>

Allègre, C. J., Poirier, J.-P., Humler, E., & Hofmann, A. W. (1995). The chemical composition of the Earth. *Earth and Planetary Science Letters*, 134, 515—526. [https://doi.org/10.1016/0012-821X\(95\)00123-T](https://doi.org/10.1016/0012-821X(95)00123-T)

Aoki, K., Fujino, K., & Akaogi (1976). Titanochondrodite and Titanoclinohumite Derived from the Upper Mantle in the Buell Park Kimberlite, Arizona, USA. *Contributions to Mineralogy and Petrology*, 56, 243—253.

Armbruster, T. (1985). Ar, N₂, and CO₂ in the structural cavities of cordierite, an optical and X-ray single-crystal study. *Physics and Chemistry of Minerals* 12(4), 233–245. Doi: 10.1007/bf00311293

Armstrong, L.S., Hirschmann, M.M., Stanley, B.D., Falksen, E.G., & Jacobsen, S.D. (2015). Speciation and solubility of reduced C–O–H–N volatiles in mafic melt: Implications for volcanism, atmospheric evolution, and deep volatile cycles in the terrestrial planets. *Geochimica et Cosmochimica Acta* 171, 283—302. <http://dx.doi.org/10.1016/j.gca.2015.07.007>

Arzamastsev, A.A., & Glaznev, V.N. (2008). Plume-lithosphere interaction in the presence of an ancient sublithospheric mantle keel: An example from the Kola alkaline province. *Doklady Earth Sciences* 419, 384—387. <https://doi.org/10.1134/S1028334X08030069>

Ashbrook, S.E., Dawson, D.M., & Griffin, J.M. (2014). Solid-State Nuclear Magnetic Resonance Spectroscopy, In *Local Structural Characterization, 2014*, edited by O'Hare D. & Walton R.I., published by *John Wiley & Sons*. <https://doi.org/10.1002/9781118681909.ch1>

Baasner, A., Schmidt, B.C., Dupree, R., & Webb, S.L. (2014). Fluorine speciation as a function of composition in peralkaline and peraluminous Na₂O-CaO-Al₂O₃-SiO₂ glasses: A multinuclear NMR study. *Geochimica et Cosmochimica Acta*, 132, 151—169. <https://doi.org/10.1016/j.gca.2014.01.041>

Barber, D.J. (1981). Matrix phyllosilicates and associated minerals in C2M carbonaceous chondrites. *Geochimica et Cosmochimica Acta* 95, 3945–3970. [https://doi.org/10.1016/0016-7037\(81\)90120-4](https://doi.org/10.1016/0016-7037(81)90120-4)

Bastin, G.F., & Heijligers, H.J.M. (1991). Quantitative Electron Probe Microanalysis of Ultra-Light Elements (Boron-Oxygen), in *Electron Probe Quantitation, 1991*, edited by Heinrich, K.F.J., & Newbury, D.E., published by Springer.

Barnes, J.D., Manning, C.E., Scambelluri, M., & Selverstone, J. (2018). The Behaviour of Halogens During Subduction-Zone Processes, in *The Role of Halogens in Terrestrial and Extraterrestrial Geochemical Processes, 2018*, edited by Harlov D.E. & Aranovich L., published by Springer Geochemistry

Baudouin, C., & Parat, F. (2020). Phlogopite-Olivine Nephelinites Erupted During Early Stage Rifting, North Tanzanian Divergence. *Frontiers in Earth Science* 8, 277. Doi: 10.3389/feart.2020.00277

Bebout, G.E., Fogel, M.L., and Cartigny, P., (2013). Nitrogen: Highly Volatile yet Surprisingly Compatible. *Elements*, 9, 333–338. Doi: 10.2113/gselements.9.5.333

Bebout, G.E., Lazzeri, K.E., and Geiger, C.A., (2016). Pathways for nitrogen cycling in Earth's crust and upper mantle: A review and new results for microporous beryl and cordierite. *American Mineralogist*, 101, 7–24. <http://dx.doi.org/10.2138/am-2016-5363>

Bernini, D., Wiedenbeck, M., Dolejš, D., & Keppler, H. (2013). Partitioning of halogens between mantle minerals and aqueous fluids: Implications for the fluid flow regime in subduction zones. *Contributions to Mineralogy and Petrology*, 165(1), 117–128. <https://doi.org/10.1007/s00410-012-0799-4>

Berry, A.J., & James, M. (2002). Refinement of hydrogen positions in natural chondrodite by powder neutron diffraction: implications for the stability of humite minerals. *Mineralogical Magazine*, 66, 441–449. Doi: 10.1180/0026461026630040

Beyer, C., Klemme, S., Wiedenbeck, M., Stracke, A., & Vollmer, C. (2012). Fluorine in nominally fluorine-free mantle minerals: Experimental partitioning of F between olivine, orthopyroxene and silicate melts with implications for magmatic processes. *Earth and Planetary Science Letters*, 337–338, 1–9. <https://doi.org/10.1016/j.epsl.2012.05.003>

Birner, S.K., Cottrell, E., Warren, J.M., Kelley, K.A., & Davis, F.A. (2018). Peridotites and basalts reveal broad congruence between two independent records of mantle fO₂ despite local redox heterogeneity. *Earth and Planetary Science Letters* 494, 172–189. <https://doi.org/10.1016/j.epsl.2018.04.035>

- Bloch, F. Nuclear Induction. *Physical Review* 70, 460—474.
- Boyd, F.R., & England, J.L. (1960). Apparatus for Phase-Equilibrium Measurements at Pressures up to 50 Kilobars and Temperatures up to 1750°C. *Journal of Geophysical Research* 65. Doi: 10.1029/JZ065i002p00741
- Brearily, A.J., & Jones, R.H. (2018). Halogens in Chondritic meteorites, in *The Role of Halogens in Terrestrial and Extraterrestrial Geochemical Processes*, 2018, edited by Harlov D.E. & Aranovich L., published by *Springer Geochemistry*
- Brey, G.P., Bulatov, V.K. & Girnis, A.V. (2009). Influence of water and fluorine on melting of carbonated peridotite at 6 and 10 GPa. *Lithos*, 1125, 249—259. Doi: 10.1016/j.lithos.2009.04.037
- Budisa, N., Kubyshkin, V., & Schulze-Makuch, D. (2014). Fluorine-Rich Planetary Environments as Possible Habitats for Life. *Life* 4, 374—385. Doi: 10.3390/life4030374
- Burke, E.A.J. (2001). Raman microspectrometry of fluid inclusions. *Lithos*, 55, 138—158. [https://doi.org/10.1016/S0024-4937\(00\)00043-8](https://doi.org/10.1016/S0024-4937(00)00043-8)
- Busigny, V., Lebeau, O., Ader, M., Krapeš, B., Bekker, A., (2013). Nitrogen cycle in the late archean ferruginous ocean. *Chemical Geology* 362, 115—130. <http://dx.doi.org/10.1016/j.chemgeo.2013.06.023>
- Busigny, V., & Bebout, G. E., (2013). Nitrogen in the Silicate Earth: Speciation and Isotopic Behavior during Mineral – Fluid Interactions. *Elements*, 9, 353—358. <https://doi.org/10.2113/gselements.9.5.353>
- Carpenter, J.E. (1987). Extension of Lew structure concepts to open-shell and excited-state molecular species. Ph.D. Thesis, University of Wisconsin, Madison, WI, USA.
- Cartigny, P., Harris, J.W., and Javoy, M., (2001). Diamond genesis, mantle fractionations and mantle nitrogen content: a study of $\delta^{13}\text{C}$ —N concentrations in diamonds. *Earth and Planetary Science Letters* 185, 85—98. [https://doi.org/10.1016/S0012-821X\(00\)00357-5](https://doi.org/10.1016/S0012-821X(00)00357-5)
- Chamas, A., Qi, L., Mehta, H.S., Sears, J.A., Scott, S.L., Walter, E.D., & Hoyt, D.W. (2019). High temperature/pressure MAS-NMR for the study of dynamic processes in mixed phase systems. *Magnetic Resonance Imaging*, 56, 37—44. <https://doi.org/10.1016/j.mri.2018.09.026>
- Chargaff, E. (1950). Chemical Specificity of Nucleic Acids and Mechanism of their Enzymatic Degradation. *Experientia*, VI(6), 201—240.

Clay, P. (2021). Halogen Abundances and Isotopes, in Encyclopedia of Geology (Second Edition), 2021, edited by Alderton, D., and Elias, S.A., published by *Elsevier Academic Press*.

Cloutis, E. A., Izawa, M. R. M., & Beck, P. (2018). Reflectance spectroscopy of chondrites. Primitive Meteorites and Asteroids: Physical, Chemical, and Spectroscopic Observations Paving the Way to Exploration. Published by *Elsevier Inc*. <https://doi.org/10.1016/B978-0-12-813325-5.00004-5>

Crépisson, C., Blanchard, M., Bureau, H., Sanloup, C., Withers, A. C., Khodja, H., & Balan, E. (2014). Clumped fluoride-hydroxyl defects in forsterite: Implications for the upper-mantle. *Earth and Planetary Science Letters*, 390, 287–295. <https://doi.org/10.1016/j.epsl.2014.01.020>

Dalou, C., Koga, K.T., Shimizu, N., Boulon, J., & Devidal, J. (2012). Experimental determination of F and Cl partitioning between lherzolite and basaltic melt. *Contributions to Mineralogy and Petrology* 163, 591–609. Doi: 10.1007/s00410-011-0688-2

Dalou, C., Hirschmann, M. M., von der Handt, A., Mosenfelder, J., & Armstrong, L. S. (2017). Nitrogen and carbon fractionation during core–mantle differentiation at shallow depth. *Earth and Planetary Science Letters* 458, 141–151. Doi: 10.1016/j.epsl.2016.10.026

Dalou, C., Hirschmann, M.M., Jacobsen, S.D., & Le Losq, C. (2019). Raman spectroscopy study of C-O-H-N speciation in reduced basaltic glasses: Implications for reduced planetary mantles. *Geochimica et Cosmochimica Acta* 265, 32–47. <https://doi.org/10.1016/j.gca.2019.08.029>

Dalsgaard, T. Thamdrup, B. and Canfield, D.E. (2005). Anaerobic ammonium oxidation (anammox) in the marine environment. *Research in Microbiology*, 156, 457–464. <https://doi.org/10.1016/j.resmic.2005.01.011>

Debret, B., & Sverjensky, D.A. (2017). Highly oxidising fluids generated during serpentinite breakdown in subduction zones. *Nature – Scientific Reports*, 7:10351. <https://doi.org/10.1038/s41598-017-09626-y>

Della Ventura, G., Robert, J.-L., Bény, J.-M., Raudsepp, M., Hawthorne, F.C. (1993). The OH-F substitution in Ti-rich potassium richterite: Rietveld structure refinement and FTIR and micro-Raman spectroscopic studies of synthetic amphiboles in the system K₂O-Na₂O-CaO-MgO-SiO₂-TiO₂-H₂O-HF. *American Mineralogist* 78, 980–987.

Dingwell, D.B., & Mysen, B.O. (1985). Effects of water and fluorine on the viscosity of albite melt at high pressure: a preliminary investigation. *Earth and Planetary Science Letters* 74, 266–274. [https://doi.org/10.1016/0012-821X\(85\)90026-3](https://doi.org/10.1016/0012-821X(85)90026-3)

Dolejš, D., & Baker, D. R. (2004). Thermodynamic modeling of melts in the system Na₂O-NaAlO₂-SiO₂-F₂O₋₁: Stability of fluorine-bearing minerals in felsic igneous suites. Contributions to Mineralogy and Petrology 146, 762—778. <https://doi.org/10.1007/s00410-003-0533-3>

Dolejš, D., & Baker, D. R. (2005). Thermodynamic modeling of melts in the system Na₂O-NaAlO₂-SiO₂-F₂O₋₁. Geochimica et Cosmochimica Acta 69, 5537—5556. doi:10.1016/j.gca.2005.07.006

Dolejš, D., & Zajacz, Z. (2018). Halogens in Silicic Magmas and Their Hydrothermal Systems, in The Role of Halogens in Terrestrial and Extraterrestrial Geochemical Processes, 2018, edited by Harlov D.E. & Aranovich L., published by Springer Geochemistry

Dreibus, G., Spettel, B. & Wänke, H. (1979). Halogens in meteorites and their primordial abundances. Physics and Chemistry of the Earth, 11, 33—38. [https://doi.org/10.1016/0079-1946\(79\)90005-3](https://doi.org/10.1016/0079-1946(79)90005-3)

Dyl, K.A., Boyce, J.W., Guan, Y., Bland, P. A., & Eiler, J. M. (2014). Characterizing Early Solar System Fluids on the Allende (CV3) Parent Body: Nanosims Study of Phosphate Volatile Contents. Meteoritics and Planetary Science 49 (S1). <http://dx.doi.org/10.1111/maps.12359>

El Goresy, A., Yabuki, H., Ehlers, K., Woolum, D., & Pernicka, E. Qingzhen and Yamato-691: A tentative alphabet for the EH Chondrites. Proceedings of the NIPR Symposium on Antarctic Meteorites 1, 65—101.

Ehrenfreund, P., Glavin, D.P., Botta, O., Cooper, G., & Bada, J.L. (2001). Extraterrestrial amino acids in Orgueil and Ivuna: Tracing the parent body of CI type carbonaceous chondrites. Proceedings of the National Academy of Sciences 98(5), 2138—2141. <https://doi.org/10.1073/pnas.051502898>

EPA. (2022). Draft Inventory of U.S. Greenhouse Gas Emissions and Sinks: 1990-2020. U.S. Environmental Protection Agency, EPA 430-P-22-001. <https://www.epa.gov/ghgemissions/draft-inventory-us-greenhouse-gas-emissions-and-sinks-1990-2020>.

Falkowski, P.G., Barber, R.T., Smetacek, V. (1998). Biogeochemical controls and feedbacks on ocean primary production. Science, 281, 200—206. Doi: 10.1126/science.281.5374.200

Fechtelkord, M., Behrens, H., Holtz, F., Fyfe, C.A., Groat, L.A., & Raudsepp, M. (2003). Influence of F content on the composition of Al-rich synthetic phlogopite: Part I. New information on structure and phase-formation from ²⁹Si, ¹H, and ¹⁹F MAS NMR spectroscopies. American Mineralogist 88, 47—53. <https://doi.org/10.2138/am-2003-0106>

Fischer, T. P., Hilton, D. R., Zimmer, M. M., Shaw, A. M., Sharp, Z. D. and Walker, J. A. (2002). Subduction and recycling of nitrogen along the central American margin. *Science*, 297, 1154–1157. Doi: 10.1126/science.1073995

Fischer, R.A., & Ciesla, F.J. (2014). Dynamics of the terrestrial planets from a large number of N-body simulations. *Earth and Planetary Science Letters* 392, 28–38. <http://dx.doi.org/10.1016/j.epsl.2014.02.011>

Frezzotti, M.L., & Ferrando, S. (2018). The Role of Halogens in the Lithospheric Mantle, *The Role of Halogens in Terrestrial and Extraterrestrial Geochemical Processes*, 2018, edited by Harlov D.E. & Aranovich L., published by *Springer Geochemistry*

Friedrich, A., Lager, G.A., Ulmer, P., Kunz, M., and Marshall, W.G. (2002). High-pressure single-crystal X-ray and powder neutron of F,OH/OD-chondrodite: Compressibility, structure and hydrogen bonding. *American Mineralogist*, 87, 931–939. <https://doi.org/10.2138/am-2002-0716>

Frost, D.J., Liebske, C., Langenhorst, F., McCammon, C.A., Trønnes, R.G., Rubie, D.C., (2004). Experimental evidence for the existence of iron-rich metal in the earth's lower mantle. *Nature* 428, 409–412. Doi: 10.1038/nature02413

Frost, R.L., Palmer, S.J., Bouzaid, J.M., & Reddy, J. (2007). A Raman spectroscopic study of humite minerals. *Journal of Raman Spectroscopy*, 38, 68–77. Doi: 10.1002/jrs.1601

Frydman, L., & Harwood, J.S. (1995). Isotopic Spectra of Half-Integer Quadrupolar Spins from Bidimensional Magic-Angle Spinning NMR. *Journal of the American Chemical Society*, 117(19), 5367–5368. <https://doi.org/10.1021/ja00124a023>

Gaffey, M.J., & Gilbert, S.L. (1998). Asteroid 6 Hebe: The probable parent body of the H-type ordinary chondrites and the IIE iron meteorites. *Meteoritics and Planetary Science* 33, 1281–1295. <https://doi.org/10.1111/j.1945-5100.1998.tb01312.x>

Gao, S., Luo, T., Zhang, B., Zhang, H., Han, Y., Zhao, Z., & Hu, Y. (1998). Chemical composition of the continental crust as revealed by studies in East China. *Geochimica et Cosmochimica Acta* 62. 1959–1998. [https://doi.org/10.1016/S0016-7037\(98\)00121-5](https://doi.org/10.1016/S0016-7037(98)00121-5)

Gaudio, S.J., Leshner, C.E., Maekawa, H., & Sen, Sabyasachi, S. (2015). Linking high-pressure structure and density of albite liquid near the glass transition. *Geochimica et Cosmochimica Acta*, 157, 28–38. <http://dx.doi.org/10.1016/j.gca.2015.02.017>

Gaussian 09, Revision D.01, Frisch, M.J., Trucks, G.W., Schlegel, H.B., Scuseria, G.E., Robb, M.A., Cheeseman, J.R., Scalmani, G., Barone, V., Mennucci, B., Petersson, G.A., Nakatsuji, H., Caricato, M., Li, X., Hratchian, H.P., Izmaylov, A.F., Bloino, J., Zheng, G., Sonnenberg, J.L., Hada, M., Ehara, M., Toyota, K., Fukuda, R., Hasegawa, J., Ishida, M., Nakajima, T., Honda, Y., Kitao, O., Nakai, H., Vreven, J.A., Montgomery, J.A.Jr., Peralta, J.E., Ogliaro, F., Bearpark, M., Heyd, J.J., Brothers, E., Kudin, K.N., Staroverov, V.N., Keith, T., Kobayashi, R., Normand, J., Raghavachari, K., Rendell, A., Burant, J.C., Iyengar, S.S., Tomasi, J., Cossi, M., Rega, N., Millam, J.M., Klene, M., Knox, J.E., Cross, J.B., Bakken, V., Adamo, C., Jaramillo, J., Gomperts, R., Stratmann, R.E., Yazyev, O., Austin, A.J., Cammi, R., Pomelli, C., Ochterski, J.W., Martin, R.L., Morokuma, K., Zakrzewski, V.G., Voth, G.A., Salvador, P., Dannenberg, J.J., Dapprich, S., Daniels, A.D., Farkas, O., Foresman, J.B., Ortiz, J.V., Cioslowski, J., & Fox, D.J. (2016). Gaussian Inc., Wallingford CT, 2013.

Gianfagna, A., Scordari, F., Mazziotti-Tagliani, S., Ventruti, G., & Ottolini, L. (2007). Fluorophlogopite from Biancavilla (Mt. Etna, Sicily, Italy): Crystal structure and crystal chemistry of a new F-dominant analog of phlogopite. *American Mineralogist* 92, 1601—1609. Doi: 10.2138/am.2007.2502

Goldblatt, C., Claire, M. W., Lenton, T. M., Matthews, A. J., Watson, A. J., & Zahnle, K. J. (2009). Nitrogen-enhanced greenhouse warming on early Earth. *Nature Geoscience*, 2, 891–896. <https://doi.org/10.1038/NGEO692>

Goldschmidt, V.M. (1937). The Principles of Distribution of Chemical Elements in Minerals and Rocks. *The Seventh Hugo Müller Lecture*, delivered before *The chemical society* on March 17th, 1937. Transcript published in *Journal of the Chemical Society*.

Goldstein, J.I., Newbury, D.E., Michael, J.R., Ritchie, N.W.M., Scott, J.H.J., & Joy, D.C. (2018). Scanning Electron Microscopy and X-Ray Microanalysis. Published by *Springer Press*.

Greenland, L., & Lovering, J.F. (1965). Minor and trace element abundances in chondritic meteorites. *Geochimica et Cosmochimica Acta* 29, 821–858.

Grewal, D.S., Dasgupta, R., Holmes, A.K., Costin, G., Li, Y., & Tsuno, K. (2019). The fate of nitrogen during core-mantle separation on Earth. *Geochimica et Cosmochimica Acta* 251, 87—115. <https://doi.org/10.1016/j.gca.2019.02.009>

Grewal, D.S., Dasgupta, R., & Farnell, A. (2020). The speciation of carbon, nitrogen, and water in magma oceans and its effect on volatile partitioning between major reservoirs of the Solar System rocky bodies. *Geochimica et Cosmochimica Acta* 280, 281—301. <https://doi.org/10.1016/j.gca.2020.04.023>

Grewal, D.S., Dasgupta, R., Hough, T., & Farnell, A. (2021). Rates of protoplanetary accretion and differentiation set nitrogen budget of rocky planets. *Nature Geosciences* 14, 369—376. <https://doi.org/10.1038/s41561-021-00733-0>

Griffin, J.M., Yates, J.R., Berry, A.J., Wimperis, S., & Ashbrook, S.E. (2010). High-Resolution ¹⁹F MAS NMR Spectroscopy: Structural Disorder and Unusual J Couplings in a Fluorinated Hydroxy-Silicate. *Journal of the American Chemical Society* 132, 15651—15660. Doi: 10.1021/ja105347q

Griffin, J. M., Miller, A. J., Berry, A. J., Wimperis, S., & Ashbrook, S. E. (2010b). Dynamics on the microsecond timescale in hydrous silicates studied by solid-state 2H NMR spectroscopy. *Physical Chemistry Chemical Physics*, 12, 2989—2998. <https://doi.org/10.1039/b924666e>

Grossman, J.N., Rubin, A.E., Rambald, E.R., Rajan, R.S., & Wasson, J.T. (1985). Chondrules in the Qingzhen type-3 enstatite chondrite: possible precursor components and comparison to ordinary chondrite chondrules. *Geochimica et Cosmochimica Acta* 49, 1781—1795. [https://doi.org/10.1016/0016-7037\(85\)90149-8](https://doi.org/10.1016/0016-7037(85)90149-8)

Grützner, T., Klemme, S., Rohrbach, A., Gervasoni, F., & Berndt, J. (2017). The role of F-clinohumite in volatile recycling processes in subduction zones. *Geology*, 45(5), 443—446. Doi: 10.1130/G38788.1

Guillot, B., & Sator, N. (2007). A computer simulation study of natural silicate melts. Part II: High pressure properties. *Geochimica et Cosmochimica Acta*, 71, 4538—4556.

Gupta, V.P. (2016). Characterization of Chemical Reactions, in *Principles and Applications of Quantum Chemistry 2016*, edited by Gupta V.P., published by *Elsevier Academic Press*.

Halama, R., Bebout, G.E., John, T. & Scambelluri, M., (2012). Nitrogen recycling in subducted mantle rocks and implications for the global nitrogen cycle. *International Journal of Earth Sciences*, 103, 2081—2099. <https://doi.org/10.1007/s00531-012-0782-3>

Halama, R., Bebout, G.E., Marschall, H.R., and John T., (2017). Fluid-induced breakdown of white mica controls nitrogen transfer during fluid–rock interaction in subduction zones. *International Geology Review*, 59:5—6, 702—720. <https://doi.org/10.1080/00206814.2016.1233834>

Hall, A., (1999). Ammonium in granites and its petrogenetic significance. *Earth-Science Reviews* 45, 145—165. Doi: 10.1016/S0012-8252(99)00006-9

Hanley, J.J., & Koga, K.T. (2018). Halogens in Terrestrial and Cosmic Geochemical Systems: Abundances, Geochemical Behaviors, and Analytical Methods, in *The Role of Halogens in Terrestrial and Extraterrestrial Geochemical*

Processes, 2018, edited by Harlov D.E. & Aranovich L., published by *Springer Geochemistry*

Harlov, D.E., & Aranovich, L. (2018). The Role of Halogens in Terrestrial and Extraterrestrial Geochemical Processes. *Springer Geochemistry*.

Hauri, E.H., Gaetani, G.A., Green, T.H. (2006). Partitioning of water during melting of the Earth's upper mantle at H₂O-undersaturated conditions. *Earth and Planetary Science Letters*, 248, 715—734. Doi: 10.1016/j.epsl.2006.06.014

Hazen, R.M., & Burnham, C.W. (1973). The Crystal Structures of One-Layer Phlogopite and Annite. *American Mineralogist* 58, 889—900.

Hermann, J., Fitz Gerald, J.D., Malaspina, N., Berry, A.J., & Scambelluri, M. (2007). OH-bearing planar defects in olivine produced by the breakdown of Ti-rich humite minerals from Dabie Shan (China). *Contributions to Mineralogy and Petrology*, 153(4), 417—428. Doi: 10.1007/s00410-006-0155-7

Hollas, J.M. (2002). Basic Atomic and Molecular Spectroscopy. Published by *The Royal Society of Chemistry Publishing*.

Honma, H., Itihara, Y., (1981). Distribution of ammonium in minerals of metamorphic and granitic rocks. *Geochimica et Cosmochimica Acta* 45, 983—988. [https://doi.org/10.1016/0016-7037\(81\)90122-8](https://doi.org/10.1016/0016-7037(81)90122-8)

Hughes, L., & Pawley, A. (2019). Fluorine partitioning between humite-group minerals and aqueous fluids: implications for volatile storage in the upper mantle. *Contributions to Mineralogy and Petrology*, 174(78). <https://doi.org/10.1007/s00410-019-1614-2>

Huve, L., Delmotte, L., Martin, P., Le Dred, R., Baron, J., & Sehr, D. (1992). ¹⁹F MAS—NMR study of structural fluorine in some natural and synthetic 2:1 layer silicates. *Clay and Clay Minerals* 40(2), 186—191.

Ireland, T.R., Clement, S., Compston, W., Foster, J.J., Holden, P., Jenkins, B., Lanc, P., Schram, N., & Williams, I.S. (2008). Development of SHRIMP. *Australian Journal of Earth Sciences* 55, 937—954. Doi: 10.1080/08120090802097427

Itihara, Y., Suwa, K., Hoshino, M., (1986). Organic matter in the Kavirondian sedimentary rocks of Archaean period in Kenya. *Geochemical Journal* 20, 201—207.

Jacobson, M.C., Charlson, R.J., Rodhe, H., Orians, G.H., (2000). Earth system science from biogeochemical cycles to global change. Published by Academic Press, San Diego (CA), USA.

Jagoutz, E., Palme, H., Baddenhausen, H., Blum, K., Cendales, M., Dreibus, G., Spettel, B., Lorenz, V., & Wänke, H. (1979). The abundances of major, minor and trace elements in the earth's mantle as derived from primitive ultramafic nodules. Lunar and Planetary Science Conference, 10th, Houston, Tex., March 19-23, 1979, Proceedings. Volume 2. New York, Pergamon Press, Inc., 1979, p. 2031-2050

Javoy M., 1997. The major volatile elements of the Earth: Their origin, behaviour and fate. Geophysical Research Letters 24, 177—180. <https://doi.org/10.1029/96GL03931>

Jenkins, H. D. B., & Thakur, K. P. (1979). Reappraisal of Thermochemical Radii for Complex Ions. Journal of Chemical Education, 56, 576—577.

Jenkins, C.R., Cook, P.J., Ennis-King, J., Undershultz, J., Boreham, C., Dance, T., De Caritat, P., Etheridge, D.M., Freifeld, B.M., Hortle, H., Kirste, D., Paterson, L., Pevzner, R., Schacht, U., Sharma, S., Stalker, L., & Urosevic, M. (2012). Safe storage and effective monitoring of CO₂ in depleted gas fields. Proceedings of the National Academy of Sciences, 109, 35—41. www.pnas.org/cgi/doi/10.1073/pnas.1107255108

Joachim, B., Pawley, A., Lyon, I. C., Marquardt, K., Henkel, T., Clay, P. L., Ruzié, L., Burgess, R., & Ballentine, C. J. (2015). Experimental partitioning of F and Cl between olivine, orthopyroxene and silicate melt at Earth's mantle conditions. Chemical Geology, 416, 65—78. <https://doi.org/10.1016/j.chemgeo.2015.08.012>

Joachim, B., Stechern, A., Ludwig, T., Konzett, J., Pawley, A., Ruzié-Hamilton, L., Clay, P. L., Burgess, R., & Ballentine, C. J. (2015). Effect of water on the fluorine and chloring partitioning behavior between olivine and silicate melt. Contributions to Mineralogy and Petrology 172(15). Doi: 10.1007/s00410-017-1329-1

Johnson, B., & Goldblatt, C. (2015). The Nitrogen Budget of Earth. Earth Science Reviews, 148, 150—173. <https://doi.org/10.1016/j.earscirev.2015.05.006>

Jones, N.W., Ribbe, P.H., & Gibbs, G.V. (1969). Crystal Chemistry of the Humite Minerals. American Mineralogist 54, 391—411.

Kadik, A.A., Koltashev, V.V., Kryukova, E.B., & Plotnichenko, V.G. (2011). Studying the forms of dissolution of hydrogen, carbon, nitrogen and oxygen volatiles in magmatic melts of the early Earth's mantle by the methods of IR and Raman spectroscopy. Vestnik Otdelenia nauk o Zemle RAN, 3, NZ6031. Doi: 10.2205/2011NZ000161

Karpukhina, N.G., Werner-Zwanziger, U., Zwanziger, J.W., & Kiprianov, A.A. (2007). Preferential Binding of Fluorine to Aluminium in High Peralkaline

Aluminosilicate Glasses. *Journal of Physical Chemistry*, 111, 10413–420. Doi: 10.1021/jp073687j

Kasting, J.F., Egger, D.H., & Raeburn, S.P. (1993). Mantle Redox Evolution and the Oxidation State of the Archean Atmosphere. *The Journal of Geology* 101, 245–257.

Kavner, A. & Jeanloz, R. (1997). High-pressure melting curve of platinum. *Journal of Applied Physics*, 83, 7553. <https://doi.org/10.1063/1.367520>

Kawai, N., & Endo, S. (1970). The generation of ultrahigh hydrostatic pressures by a split sphere apparatus. *Review of Scientific Instruments* 41. 1178–1181. Doi: 10.1063/1.1684753

Keeler, J. (2002). Understanding NMR Spectroscopy. Published by *Cambridge University Press*.

Keil., K. (1968). Mineralogical and chemical relationships among enstatite chondrites. *Journal of Geophysical Research* 73, 6945–6976

Kelemen, P., Benson, S.M., Pilorgé, H., Psarras, P., & Wilcox, J. (2019). An Overview of the Status of CO₂ Storage in Minerals and Geological Formations. *Frontiers in Climate*, 1. Doi: 10.3389/fclim.2019.00009

Kendrick, M.A., Arculus, R., Burnard, P. & Honda, M. (2013). Quantifying brine assimilation by submarine magmas: Examples from the Galápagos Spreading Centre and Lau Basin. *Geochimica et Cosmochimica Acta* 123, 150–165. <http://dx.doi.org/10.1016/j.gca.2013.09.012>

Kiczanski, T.J., & Stebbins, J.F. (2002). Fluorine sites in calcium and barium oxyfluorides: F-19 NMR on crystalline model compounds and glasses. *Journal of Non-Crystalline Solids* 306, 160–168. [https://doi.org/10.1016/S0022-3093\(02\)01157-2](https://doi.org/10.1016/S0022-3093(02)01157-2)

Kiczanski, T. J., Du, L. S., & Stebbins, J. F. (2004). F-19 NMR study of the ordering of high field strength cations at fluoride sites in silicate and aluminosilicate glasses. *Journal of Non-Crystalline Solids*, 337(2), 142–149. <https://doi.org/10.1016/j.jnoncrysol.2004.03.123>

Kitamura, M., Kondoh, S., Morimoto, N., Miller, G.H., Rossman, G.R., & Putnis, A. (1987). Planar OH-bearing defects in mantle olivine. *Nature*, 328, 143–144

Klemme, S. & Stalder, R. (2018). Halogens in the Earth's Mantle: What We Know and What We Don't, in *The Role of Halogens in Terrestrial and Extraterrestrial Geochemical Processes*, 2018, edited by Harlov D.E. & Aranovich L., published by *Springer Geochemistry*

Koga, K.T., & Rose-Koga, E.F. (2018). Fluorine in the Earth and the solar system, where does it come from and can it be found?. *Comptes Rendus Chimie* 21(8), 749—756. <https://doi.org/10.1016/j.crci.2018.02.002>

Krauskopf, K.B. (1979). Introduction to geochemistry (2nd edition). Published by *McGraw-Hill*

Kurth, S., Marquez, M.A.L., & Gross, E.K.U. (2005). Density Functional Theory, 395—402. Published by *Elsevier*. <https://doi.org/10.1016/B0-12-369401-9/00445-9>

Kushiro, I. (1972). Determination of liquidus relations in synthetic silicate systems with electron probe analysis: the system forsterite-diopside-silica at 1 atmosphere. *American Mineralogist* 57, 1260—1271.

Laboriau, A., Kim, Y.-W., Chipera, S., Bish, D.L., & Earl, W.L. (1995). A ¹⁹F Nuclear Magnetic Resonance study of natural clays. *Clay and Clay Minerals* 43(6), 697—704.

Lager, G.A., Armbruster, Th., & Faber, J. (1987). Neutron and X-ray diffraction study of hydrogarnet Ca₃Al₂(O₄H₄)₃. *American Mineralogist*, 72, 756—765.

Lager, G.A., Ulmer, P., Miletich, R., & Marshall, W.G. (2001). O-D…O bond geometry in OD-chondrodite. *American Mineralogist*, 86, 176—180. <https://doi.org/10.2138/am-2001-0119>

Lazzeri, K.E. (2012) Storage of Nitrogen in Silicate Minerals and Glasses. ProQuest Dissertations Publishing, 1511594.

Le Losq, C., Valentine, A., Mysen, B., & Neuville, D. (2021). Structure and properties of alkali aluminosilicate glasses and melts: insights from deep learning. *Geochimica et Cosmochimica Acta*, In press. Doi: 10.1016/j.gca.2021.08.023

Li, Y. (1991). Distribution patterns of the elements in the ocean: A synthesis. *Geochimica et Cosmochimica Acta* 55, 3223—3240. [https://doi.org/10.1016/0016-7037\(91\)90485-N](https://doi.org/10.1016/0016-7037(91)90485-N)

Li, Y., Wiedenbeck, M., Svyatoslav, S. & Keppler, H. (2013). Nitrogen solubility in upper mantle minerals. *Earth and Planetary Science Letters*, 377-378, 311—323. Doi: 10.1016/j.epsl.2013.07.013

Li, Y. and Keppler, H. (2014). Nitrogen speciation in mantle and crustal fluids. *Geochimica et Cosmochimica Acta* 129, 13— 32. <https://doi.org/10.1016/j.gca.2013.12.031>

Li, Y., Shu, Q., & Chou, K. (2014). Structural Study of Glassy CaO–SiO₂–CaF₂–TiO₂ Slags by Raman Spectroscopy and MAS-NMR. *ISIJ International* 54, 721–727. <http://dx.doi.org/10.2355/isijinternational.54.721>

Li, Y., Huang, R., Wiedenbeck, M., & Keppler, H. (2015). Nitrogen distribution between aqueous fluids and silicate melts. *Earth and Planetary Science Letters* 411, 218–228. <http://dx.doi.org/10.1016/j.epsl.2014.11.050>

Lilley, M.D., Butterfield, D.A., Olson, E.J., Lupton, J.E., Macko, S.A. and McDuff, R.E. (1993). Anomalous CH₄ and NH₄⁺ concentrations at an un-sedimented mid-ocean-ridge hydrothermal system. *Nature*, 364, 45–47. Doi: 10.1038/364045a0

Lin, Y., & Kimura, M. (1998). Petrographic and mineralogical study of new EH melt rocks and a new enstatite chondrite grouplet. *Meteoritics and Planetary Science* 33, 501–514. <https://doi.org/10.1111/j.1945-5100.1998.tb01654.x>

Litasov, K. D., Shatskiy, A., Ponomarev, D. S., & Gavryushkin, P. N. (2017). Equations of state of iron nitrides ε-Fe₃N_x and γ-Fe₄N_y to 30 GPa and 1200 K and implication for nitrogen in the Earth's core. *Journal of Geophysical Research: Solid Earth* 122, 3574–3584. <https://doi.org/10.1002/2017JB014059>

Liu, Y., & Nekvasil, H. (2002). Si-F bonding in aluminosilicate glasses: Inferences from ab initio NMR calculations. *American Mineralogist* 87, 339–346. <https://doi.org/10.2138/am-2002-2-317>

Liu, Y., & Tossell, J. (2003). Possible Al-F Bonding Environment in Fluorine-Bearing Sodium Aluminosilicate Glasses: From Calculation of ¹⁹F NMR Shifts. *Journal of Physical Chemistry* 107, 11280–11289. Doi: 10.1021/jp0350417

Liu, D., Pang, Y., Ye, Y., Jin, Z., Smyth, J.R., Yang, Y., Zhang, Z., & Wang, Z. (2019). In-situ high-temperature vibrational spectra for synthetic and natural clinohumite: Implications for dense hydrous magnesium silicates in subduction zones. *American Mineralogist*, 104, 53–63. <https://doi.org/10.2138/am-2019-6604>

Lodders, K., and Fegley, B. J. (1998). The Planetary Scientist's Companion. Edited by Oxford University Press, Oxford, UK, 1998.

Lodders, K. (2003). Solar System abundances and condensation temperatures of the elements. *The Astrophysical Journal*, 591, 1220–1247. <https://doi.org/10.1086/375492>

López Sánchez-Vizcaíno, V., Trommsdorff, V., Gómez-Pugnaire, M.T., Garrido, C.J., Müntener, O., & Connolly, J.A.D. (2005). Petrology of titanian clinohumite and olivine at the high-pressure breakdown of antigorite serpentinite

to chlorite harzburgite (Almirez Massif, S. Spain). *Contributions to Mineralogy and Petrology*, 149, 627—646. Doi: 10.1007/s00410-005-0678-3

López Sánchez-Vizcaíno, V., Gómez-Pugnaire, M.T., Garrido, C.J., Padrón-Navarta, J.L., & Mellini, M. (2009). Breakdown mechanisms of titanoclinohumite in antigorite serpentinite (Cerro del Almirez massif, S. Spain): A petrological and TEM study. *Lithos*, 107, 216—226. Doi: 10.1016/j.lithos.2008.10.008

Luth, R.W. (1988). Effect of F on phase equilibria and liquid structure in the system NaAlSiO₄-CaMgSi₂O₆-SiO₂. *American Mineralogist*, 73, 306—312.

Lv, Q., Xilian, J., Tian, C., Quan, Z., Ying, L., Youchun, W., Kuo, B., Xing, M. (2014). Crystal structures and electronic properties of solid fluorine under high pressure. *Chinese Physics B*, 26, 076103.

Klein, C. & Hurlbut, C. S. (1993). Manual of Mineralogy, 21st Edition. *John Wiley & Sons*.

MacKenzie, K.J.D., & Smith, M.E. (2002). Multinuclear Solid-State Nuclear Magnetic Resonance of Inorganic Materials. Published by *Elsevier*.

Mallik, A., Li, Y., & Wiedenbeck, M. (2018). Nitrogen evolution within the Earth's atmosphere—mantle system assessed by recycling in subduction zones. *Earth and Planetary Science Letters* 482, 556—566. <https://doi.org/10.1016/j.epsl.2017.11.045>

Manning, C.E., & Bird, D.K. (1991). Porosity evolution and fluid flow in the basalts of the Skaergaard magma-hydrothermal system, East Greenland. *American Journal of Science*, 291, 201—257.

Mare, E.R. (2017). Silicate melt under pressure: coordination changes and trace element partitioning (PhD thesis). Submitted to the Australian National University.

Marty, B. (2012). The origins and concentrations of water, carbon, nitrogen and noble gases on Earth. *Earth and Planetary Science Letters* 313—314, 56—66. Doi: 10.1016/j.epsl.2011.10.040

Marty, B., Zimmermann, L., Pujol, M., Burgess, R. and Philippot, P. (2013). Nitrogen isotopic composition and density of the Archean Atmosphere. *Science*, 342, 101—104. Doi: 10.1126/science.1240971

Mason, R.A. (1992). Models of order and Iron-Fluorine avoidance in biotite. *Canadian Mineralogist* 30, 343—354.

Massiot, D., Fayon, F., Capron, M., King, I., Le Calvé, S., Alonso, B., Durand, J.O., Bujoli, B., Gan, Z., & Hoatson, G. (2002). Modelling one and two-

dimensional solid-state NMR spectra. *Magnetic Resonance Chemistry*, 40, 70—76. <https://doi.org/10.1002/mrc.984>

McCreery, R.L. (2000). Raman Spectroscopy for Chemical Analysis. Published by *John Wiley & Sons*.

McDonough, W.F., & Sun, S.S. (1995). The composition of the Earth. *Chemical Geology*, 120, 223—253. [https://doi.org/10.1016/0009-2541\(94\)00140-4](https://doi.org/10.1016/0009-2541(94)00140-4)

McDonough, W. F. (2014). Compositional model for the Earth's core. In R. W. Carlson, *The Mantle and Core*, 559—577. Edited by Elsevier, Amsterdam, NE.

Meija, J. Coplen, T.B., Berglund, M. Brand, W.A., De Bièvre, P. Gröning, M. Holden, N.E. Irrgeher, J., Loss, R.D. Walczyk, T. and Prohaska, T. (2015). Atomic weights of the elements 2013 (IUPAC Technical Report). *Pure Applied Chemistry*, 88, 265-291. Doi: 10.1515/pac-2015-0305

Mezger, K., Maltese, A., & Vollstaedt, H. (2021). Accretion and differentiation of early planetary bodies as recorded in the composition of the silicate Earth. *Icarus* 365, 114497. <https://doi.org/10.1016/j.icarus.2021.114497>

Mi, J.X., & Pan, Y. (2018). Halogen-Rich Minerals: Crystal Chemistry and Geological Significances, in *The Role of Halogens in Terrestrial and Extraterrestrial Geochemical Processes*, 2018, edited by Harlov D.E. & Aranovich L., published by *Springer Geochemistry*

Mikhail, S. and Sverjensky, D.A. (2014). Nitrogen speciation in upper mantle fluids and the origin of Earth's nitrogen-rich atmosphere. *Nature Geoscience*, 7, 816—819, Doi: 10.1038/NGEO2271

Mikhail, S., and Howell, D., (2016). A petrological assessment of diamond as a recorder of the mantle nitrogen cycle. *American Mineralogist*, 101, 780—787. <http://dx.doi.org/10.2138/am-2016-5464>

Mikhail, S., Barry, P.H., & Sverjensky, D.A. (2017). The relationship between mantle pH and the deep nitrogen cycle. *Geochimica et Cosmochimica Acta* 209, 149—160. <http://dx.doi.org/10.1016/j.gca.2017.04.007>

Miller, J. M. (1996). Fluorine-19 magic-angle spinning NMR. *Progress in Nuclear Magnetic Resonance Spectroscopy*, 20, 225—281. [https://doi.org/10.1016/0079-6565\(95\)01024-6](https://doi.org/10.1016/0079-6565(95)01024-6)

Mills, I. Cvitas, T. Homann, K. Kallay, N. and Kuchitsu K. (1988). In Quantities, Units and Symbols in Physical Chemistry, edited by *Blackwell Scientific Publications*, Oxford, UK, 1988.

Mohebbi, B., Claussen, J., & Blümich, B. (2019). Fast and robust quantification of liquid inside thin fibrous porous materials with single-sided NMR. Magnetic Resonance Imaging, 56, 131—137. <https://doi.org/10.1016/j.mri.2018.09.022>

Momma, K., Ikeda, T., Nishikubo, K., Takahashi, N., Honma, C., Takada, M., Furukawa, Y., Nagase, T., & Kudoh, Y. (2011). New silica clathrate minerals that are isostructural with natural gas hydrates. *Nature Communications*, 2, 196. <https://doi.org/10.1038/ncomms1196>

Mosenfelder, J.L., Deligne, N.I., Asimow, P.D., & Rossman, G.R. (2006). Hydrogen incorporation in olivine from 2—12 GPa. *American Mineralogist*, 91, 285—294. Doi: 10.2138/am.2006.1943

Mosenfelder, J.L., & Rossman, G.R., (2013). Analysis of hydrogen and fluorine in pyroxenes. *American Mineralogist* 98, 1026—1054. <https://doi.org/10.2138/am.2013.4413>

Mosenfelder, J.L., & Rossman, G.R., (2013b). Analysis of hydrogen and fluorine in pyroxene: I. Orthopyroxene. *American Mineralogist* 98, 1026—1054. <https://doi.org/10.2138/am.2013.4413>

Mosenfelder, J. L., Von Der Handt, A., Furi, E., Dalou, C., Hervig, R. L., Rossman, G. R., and Hirschmann, M. M. (2019). Nitrogen incorporation in silicates and metals: results from SIMS, EPMA, FTIR, and laser-extraction mass spectrometry. *American Mineralogist* 104, 31—46. <https://doi.org/10.2138/am-2019-6533>

Mueller, C. (2019). In Chem U100 Chemistry of Living Things, LibreTexts, University of South California Upstate, 2021.

Müller-Reichert, T., & Pignino, G. (2019). Three Dimensional Electron Microscopy. Published by *Elsevier Press*.

Mundl-Petermeier, A. (2021). Core Mantle Interactions, in *Encyclopedia of Geology (Second Edition)*, 2021, edited by Alderton, D., and Elias, S.A., published by *Elsevier Academic Press*.

Mysen, B.O., Cody, G.D., & Smith, A. (2004). Solubility mechanisms of fluorine in peralkaline and meta-aluminous silicate glasses and in melts to magmatic temperatures. *Geochimica et Cosmochimica Acta* 68, 2745—2769. Doi: 10.1016/j.gca.2003.12.015

Mysen, B.O., Yamashita, S., & Chertkova, N. (2008). Solubility and solution mechanisms of NOH volatiles in silicate melts at high pressure and temperature—amine groups and hydrogen fugacity. *American Mineralogist*, 93, 1760—1770. Doi: 10.2138/am.2008.2879

Mysen, B. (2018). Mass transfer in the Earth's interior: fluid- melt interaction in aluminosilicate–C–O–H–N systems at high pressure and temperature under oxidizing conditions. *Progress in Earth and Planetary Science*, 5:6. Doi: 10.1186/s40645-017-0161-6.

Nag, P.K. (2011). Heat and Mass Transfer. Published by *The McGraw—Hill Company Limited*.

Nakajima, M., & Stevenson, D.J. (2015). Melting and mixing states of the Earth's mantle after the Moon-forming impact. *Earth and Planetary Science Letters* 427, 286—295. <http://dx.doi.org/10.1016/j.epsl.2015.06.023>

Neuville, D.R., Cormier, L., Montouillout, V., Florian, P., Millot, F., Rifflet, J.-C., & Massiot, D. (2008). Structure of Mg- and Mg/Ca aluminosilicate glasses: ²⁷Al NMR and Raman spectroscopy investigations. *American Mineralogist*, 93, 1721—1731. Doi: 10.2138/am.2008.2867

O'Hagan, D., Schaffrath, C., Cobb, S.L., Hamilton, J.T.G., & Murphy, C.D. (2002). Biosynthesis of an organofluorine molecule. *Nature*, 416, 279. <https://doi.org/10.1038/416279a>

O'Neill, H. S. C., & Eggins, S. M. (2002). The effect of melt composition on trace element partitioning: An experimental investigation of the activity coefficients of FeO, NiO, CoO, MoO₂ and MoO₃ in silicate melts. *Chemical Geology*, 186, 151—181. [https://doi.org/10.1016/S0009-2541\(01\)00414-4](https://doi.org/10.1016/S0009-2541(01)00414-4)

Ohtani, E. (2015). Hydrous minerals and the storage of water in the deep mantle. *Chemical Geology*, 418, 6—15. <http://dx.doi.org/10.1016/j.chemgeo.2015.05.005>

Padrón-Navarta, J.L., López Sánchez-Vizcaíno, V., Garrido, C.J., & Gómez-Pugnaire, M.T. (2011). Metamorphic Record of High-pressure Dehydration of Antigorite Serpentinite to Chlorite Harzburgite in a Subduction Setting (Cerro del Almirez, Nevado-Filábride Complex, Southern Spain). *Journal of Petrology*, 52(10), 2047—2078. <https://doi.org/10.1093/petrology/egr039>

Pearson, D.G., Canil, D., & Shirley, S.B. (2003). Mantle Samples Included in Volcanic Rocks: Xenoliths and Diamonds, in *Treatise on Geochemistry*, Volume 2. 2014, edited by Carlson, R.W., published by *Elsevier*

Plessen, B., Harlov, D.E., Henry, D., Guidotti, C.V., (2010). Ammonium loss and nitrogen isotopic fractionation in biotite as a function of metamorphic grade in metapelites from western Maine, USA. *Geochimica et Cosmochimica Acta* 74, 4759—4771. <https://doi.org/10.1016/j.gca.2010.05.021>

Potts, N., Bromiley, G.D., & Brooker, R.A. (2021). An experimental investigation of F, Cl and H₂O mineral-melt partitioning in a reduced, model lunar system.

Price, M. (1996). Introducing groundwater (2nd edn). Published by *Chapman and Hall*

Purcell, E.M., Torrey, H.C., & Pound, R.V. (1946). Resonance Absorption by Nuclear Magnetic Moments in a Solid. *Physical Review* 69, 37—38.

Quan, T., van de Schootbrugge, B., Field, M., Rosenthal, Y., Falkowski, P., (2008). Nitrogen isotope and trace metal analyses from the Mingolsheim core (Germany): Evidence for redox variations across the Triassic-Jurassic boundary. *Global Biogeochemical Cycles* 22, GB2014. <https://doi.org/10.1029/2007GB002981>

Rabi, I.I. (1938). A New Method of Measuring Nuclear Magnetic Moment. *Physics Reviews* 53, 318.

Raudsepp, M., Turnock, A.C., Hawthorne, F.C., Sherriff, B.L., & Hartman, J.S. (1987). Characterization of synthetic pargasitic amphiboles (NaCa₂Mg₄M³⁺Si₆Al₂O₂₂(OH,F)₂: M³⁺ = Al, Cr, Ga, Sc, In) by infrared spectroscopy, Rietveld structure refinement, and ²⁷Al, ²⁹Si, and ¹⁹F MAS NMR spectroscopy. *American Mineralogist* 72, 580—593.

Redfield, A.C., Ketchum, B.H. and Richards, F.A. (1963). The influence of organisms on the composition of sea-water. In *The Sea*, edited by MN Hill, New York, USA, 1963.

Reed, G.W. (1964). Fluorine in stone meteorites. *Geochimica et Cosmochimica Acta*, 28, 1729–1743. [https://doi.org/10.1016/0016-7037\(64\)90019-5](https://doi.org/10.1016/0016-7037(64)90019-5)

Regier, M., Hervig, R.L., Myers, M., Roggensack, K., & Wilson, C. (2016). Analyzing Nitrogen in Natural and Synthetic Silicate Glasses by Secondary Ion Mass Spectrometry. *Chemical Geology*, 447, 27—39. Doi: 10.1016/j.chemgeo.2016.10.019

Ribbe, P.H., & Gibbs, G.V. (1971). Crystal structure of the humite minerals: III Mg/Fe ordering in humite and its relation to other ferromagnesian silicates. *American Mineralogist*, 56, 1155—1173.

Rindt, C.C., & Gaastra-Nedea, S.V. (2015). Modeling thermochemical reactions in thermal energy storage systems. *Advances in Thermal Energy Storage Applications*, 375—415. Published by *Woodhead Publishing*.

Robert, J.-L., Della Ventura, G., & Thauvin, J.-L. (1989). The infrared OH-stretching region of synthetic richterites in the system Na₂O-K₂O-CaO-MgO-SiO₂-H₂O-HF. *European Journal of Mineralogy* 1, 203—211.

Robert, J.L., Beny, J.M., Della Ventura, G., & Hardy, M. (1993). Fluorine in micas: Crystal-chemical control of the OH—F distribution between trioctahedral and dioctahedral sites. *European Journal of Mineralogy*, 5, 7—18. Doi: 10.1127/ejm/5/1/0007.

Roskosz, M., Mysen, C., & Cody, G.D., (2006). Dual speciation of nitrogen in silicate melts at high pressure and temperature: An experimental study. *Geochimica et Cosmochimica Acta*, 70, 2902—2918. Doi: 10.1016/j.gca.2006.03.001

Roskosz, M., Bouhifd, M., Jephcoat, A., Marty, B., and Mysen, B., (2013). Nitrogen solubility in molten metal and silicate at high pressure and temperature. *Geochimica et Cosmochimica Acta* 121, 15—28. Doi: 10.1016/j.gca.2013.07.007

Rubin, A.E., & Choi, B.G. (2009). Origin of Halogens and Nitrogen in Enstatite Chondrites. *Earth, Moon and Planets*, 105, 41—53. <https://doi.org/10.1007/s11038-009-9316-9>

Rudenberg, H.G., & Rudenberg, P.G. (2010). Origin and Background of the Invention of the Electron Microscope: Commentary and Expanded Notes on Memoir of Reinhold Rüdberg. *Advances in Imaging and Electron Physics* 160, 207—286. [https://doi.org/10.1016/S1076-5670\(10\)60006-7](https://doi.org/10.1016/S1076-5670(10)60006-7)

Rudnick, R., and Gao, S. (2014). Composition of the Continental Crust. *Treatise on Geochemistry* 4, 1—69. Doi: 10.1016/B0-08-043751-6/03016-4

Saal, A.E., Hauri, E.H., Langmuir, C.H., & Perfit, M.R. (2002). Vapour undersaturation in primitive mid-ocean-ridge basalt and the volatile content of Earth's upper mantle. *Nature* 419, 451—455. Doi: 10.1038/nature01073

Salters, V.J.M., & Stracke, A. (2004). Composition of the depleted mantle. *Geochemistry Geophysics Geosystems*. Doi: 10.1029/2003GC000597

Sanz, J., & Stone, W.E.E. (1983). NMR applied to minerals: IV. Local order in the octahedral sheet of micas: Fe-F avoidance. *Clay Minerals* 18, 187—192.

Savage, P., & Moynier, F. (2013). Silicon isotopic variation in enstatite meteorites: Clues to their origin and Earth-forming material. *Earth and Planetary Sciences Letters* 361, 487—496. <http://dx.doi.org/10.1016/j.epsl.2012.11.016>

Schaller, T., Dingwell, D.B., Keppler, H., Knöller, W., Merwin, L., & Sebald, A. (1992). Fluorine in silicate glasses: A multinuclear nuclear magnetic resonance study. *Geochimica et Cosmochimica Acta*, 56, 701—707.

Schmidt, C., & Watenphul, A. (2010). Ammonium in aqueous fluids to 600 °C, 1.3 GPa: A spectroscopic study on the effects on fluid properties, silica solubility, and K-feldspar to muscovite reactions. *Geochimica et Cosmochimica Acta*, 74, 6852—6866. Doi:10.1016/J.GCA.2010.08.040

Shannon, R.D. (1976). Revised effective ionic radii and systematic studies of interatomic distances in halides and chalcogenides. *Acta Crystallographica*, A32, 751—767. <https://doi.org/10.1107/S0567739476001551>

Shen, T., Hermann, J., Zhang, L., Padrón-Navarta, J.A., and Chen, J. (2014). FTIR spectroscopy of Ti-chondrodite, Ti-clinohumite, and olivine in deeply subducted serpentinites and implications for the deep water cycle. *Contributions to Mineralogy and Petrology*, 168, 1037. <https://doi.org/10.1007/s00410-014-1037-z>

Shimomura, C., Takemura, K., Fujii, Y., Minomura, S., Mori, M., Noda, Y., & Yamada, Y. (1978). Structure analysis of high-pressure metallic state of iodine. *Physical Review B*, 18, 715.

Shimizu, K., Alexander, M. O'D. C., Hauri, E., Sarafian, A.R., Nittler, L.R., Wang, J., Jacobsen, S.D., & Mendybaev, R.A. (2021). Highly volatile element (H, C, F, Cl, S) abundances and H isotopic compositions in chondrules from carbonaceous and ordinary chondrites. *Geochimica et Cosmochimica Acta* 294. <https://doi.org/10.1016/j.gca.2021.03.005>

Smart, K.A., Tappe, S., Stern, R.A., Webb, S.J., & Ashwal, L.D. (2016). Early Archaean tectonics and mantle redox recorded in Witwatersrand diamonds. *Nature Geoscience* 9, 255—260. Doi: 10.1038/NGEO2628

Socrates, G. (2001). Infrared and Raman Characteristic Group Frequencies. Tables and Charts. *Journal of the American Chemical Society*, 124(8), 1830. <https://doi.org/10.1021/ja0153520>

Sokol, A.G., Sokol, E.V., Kupriyanov, I.N., & Sobolev N.V. (2018). Synthesis of NH₄-Substituted Muscovite at 6.3 GPa and 1000°C: Implications for Nitrogen Transport to the Earth's Mantle. *Doklady Earth Sciences*, 479, 404—407. Doi: 10.1134/S1028334X18030315

Solomatova, N.V., & Caracas, R. (2019). Pressure-Induced Coordination Changes in a Pyrolytic Silicate Melt From Ab Initio Molecular Dynamics Simulations. *Journal of Geophysical Research: Solid Earth* 124, 11232—11250. <https://doi.org/10.1029/2019JB018238>

Speelmanns, I. M., Schmidt, M. W., and Liebske, C. (2018). Nitrogen solubility in core materials. *Geophysical Research Letter* 45, 7434—7443. <https://doi.org/10.1029/2018GL079130>

Speelmanns, I. M., Schmidt, M. W., and Liebske, C. (2019). The almost lithophile character of nitrogen during core formation. *Earth and Planetary Science Letters* 510, 186—197. <https://doi.org/10.1016/j.epsl.2019.01.004>

Stalder, R., & Ulmer, P. (2001). Phase relations of a serpentine composition between 5 and 14 GPa: Significance of clinohumite and phase E as water carriers into the transition zone. *Contributions to Mineralogy and Petrology*, 140(6), 670–679. <https://doi.org/10.1007/s004100000208>

Stamboulis, A., Hill, R.G., & Law, R.V. (2004). Characterization of the structure of calcium alumino-silicate and calcium fluoro-alumino-silicate glasses by magic angle spinning nuclear magnetic resonance (MAS-NMR). *Journal of Non-Crystalline Solids* 333, 101–107. Doi: 10.1016/j.jnoncrysol.2003.09.049

Stebbins, J.F., & Zeng, Q. (2000). Cation ordering at fluoride sites in silicate glasses: a high-resolution ¹⁹F NMR study. *Journal of Non-Crystalline Solids* 262, 1–5. Doi: 10.1016/S0022-3093(99)00695-X

Stebbins, J.F., Kroeker, S., Lee, S.K., & Kiczenski, T.J. (2000). Quantification of five- and six-coordinated aluminum ions in aluminosilicate and fluoride-containing glasses by high-field, high-resolution ²⁷Al NMR. *Journal of Non-Crystalline Solids* 275, 1–6. Doi: 10.1016/S0022-3093(00)00270-2

Stolper, E. (1982). The speciation of water in silicate melts. *Geochimica et Cosmochimica Acta* 46, 2609–2620. [https://doi.org/10.1016/0016-7037\(82\)90381-7](https://doi.org/10.1016/0016-7037(82)90381-7)

Thamdrup, B. (2012). New pathways and processes in the global nitrogen cycle. *Annual Review of Ecology, Evolution, and Systematics*, 43, 407–428. <https://doi.org/10.1146/annurev-ecolsys-102710-145048>

Tolstikhin, I. N. & Marty, B. (1998). The evolution of terrestrial volatiles: a view from helium, neon, argon and nitrogen isotope modelling. *Chemical Geology*, 147(1–2), 27–52. [https://doi.org/10.1016/S0009-2541\(97\)00170-8](https://doi.org/10.1016/S0009-2541(97)00170-8)

Trail, D., Watson, E.B., & Tailby, N.D. (2011). The oxidation state of Hadean magmas and implications for early Earth's atmosphere. *Nature* 480, 79–84. Doi: 10.1038/nature10655

Trommsdorf, V., & Evans, B.W. (1980). Titanian hydroxyl-clinohumite – formation and breakdown in antigorite rocks (Malenco, Italy). *Contributions to Mineralogy and Petrology*, 72, 229–242.

Van Bolhuis, F., Koster, P.B., & Migchelsen, T. (1967). Refinement of the crystal structure of iodine at 110° K. *Acta Crystallographica*, 23, 90–91. <https://doi.org/10.1107/S0365110X6700218X>

Van Schmus, W.R., & Wood, J.A. (1967). A chemical-petrologic classification for the chondritic meteorites. *Geochimica et Cosmochimica Acta* 31, 747–754. [https://doi.org/10.1016/S0016-7037\(67\)80030-9](https://doi.org/10.1016/S0016-7037(67)80030-9)

Veksler, I.V., Dorfman, A.M., Dulski, P., Kamenetsky, V.S., Danyushevsky, L.V., Jeffries, T., & Dingwell, D.B. (2012). Partitioning of elements between silicate melt and immiscible fluoride, chloride, carbonate, phosphate and sulfate melts, with implications to the origin of natrocarbonatite. *Geochimica et Cosmochimica Acta*, 79, 20—40. Doi: 10.1016/j.gca.2011.11.035

Villeneuve, J., Libourel, G., Soulié, C. (2015). Relationships between type I and type II chondrules: Implications on chondrule formation processes. *Geochimica et Cosmochimica Acta* 160, 277—305. <http://dx.doi.org/10.1016/j.gca.2015.03.033>

Walker, D., Carpenter, M.A., & Hitch, C.M. (1990). Some simplifications to multi anvil devices for high pressure experiments. *American Mineralogist* 75. 1020—1028.

Walrafen, G.E., Yang, W.H., & Chu, Y.C. (1999). Raman Spectra from Saturated Vapor to the Supercritical Fluid. *Journal of Physical Chemistry*, 103(8), 1332—1338. <https://doi.org/10.1021/jp9831233>

Wasson, J.T., & Kallemeyn, G.W. (1988). Compositions of chondrites. *Philosophical Transactions of the Royal Society of London. Series A, Mathematical and Physical Sciences*, 325(1587), 535—544. <https://doi.org/10.1098/rsta.1988.0066>

Watenphul, A., Wunder, B., Wirth, R., & Heinrich, W. (2010). Ammonium-bearing clinopyroxene: A potential nitrogen reservoir in the Earth's mantle. *Chemical Geology* 270, 240—248. Doi: 10.1016/j.chemgeo.2009.12.003

Webb, S.L., & Dingwell, D.B., (1990). The Onset of Non-Newtonian Rheology of Silicate Melts. *Physics and Chemistry of Minerals* 17, 125—132. <https://doi.org/10.1007/BF00199663>

Webster, J.D., Tappen, C.M., & Mandeville, C.W. (2009). Partitioning behavior of chlorine and fluorine in the system apatite–melt–fluid. II: Felsic silicate systems at 200 MPa. *Geochimica et Cosmochimica Acta* 73, 559—581. Doi: 10.1016/j.gca.2008.10.034

Webster, J.D., Baker, D.R., & Aiuppa, A. (2018). Halogens in Mafic and Intermediate-Silica Content Magmas, in *The Role of Halogens in Terrestrial and Extraterrestrial Geochemical Processes*, 2018, edited by Harlov D.E. & Aranovich L., published by Springer Geochemistry

Weiss, M. (1997). Clinohumites: a field and experimental study (PhD thesis). Submitted to ETH Zurich.

Wing, M.R., & Bada, J.L. (1991). The origin of the polycyclic aromatic hydrocarbons in meteorites. *Origins of life and evolution of the biosphere* 21, 375—383. <https://doi.org/10.1007/BF01808308>

Wood, B. J., Walter, M. J., & Wade, J. (2006). Accretion of the Earth and Segregation of its core. *Nature*, 441(7095), 825–833.

Wood, B.J., Smythe, D.J., & Harrison, T. (2019). The condensation temperatures of the elements: A reappraisal. *American Mineralogist*, 104, 844–856. <https://doi.org/10.2138/am-2019-6852CCBY>

Worden, R.H. (2018). Halogen Elements in Sedimentary Systems and Their Evolution During Diagenesis, in *The Role of Halogens in Terrestrial and Extraterrestrial Geochemical Processes*, 2018, edited by Harlov D.E. & Aranovich L., published by *Springer Geochemistry*

Yamamoto, K., & Akimoto, S. (1977). The system MgO—SiO₂—H₂O at high pressures and temperatures – Stability field for hydroxyl-chondrodite, hydroxyl-clinohumite and 10 Å-Phase. *American Journal of Science*, 277, 288–312.

Yoshioka, T., Wiedenbeck, M., Shcheka, S., and Keppler, H., (2018). Nitrogen solubility in the deep mantle and the origin of Earth's primordial nitrogen budget. *Earth and Planetary Science Letters*, 488, 134–143. <https://doi.org/10.1016/j.epsl.2018.02.021>

Zeng, Q., & Stebbins, J.F. (2000). Fluoride sites in aluminosilicate glasses: High-resolution ¹⁹F NMR results. *American Mineralogist* 85, 863–867. <https://doi.org/10.2138/am-2000-5-630>

Zerkle, A.L. and Mikhail, S. (2017). The geobiological nitrogen cycle: From microbes to the mantle. *Geobiology*, 15, 343–352. <https://doi.org/10.1111/gbi.12228>

Zerkle, A.L. (2018). Biogeodynamics: Bridging the gap between surface and deep Earth processes. *Philosophical Transactions of the Royal Society A: Mathematical, Physical and Engineering Sciences*, 376(2132). <https://doi.org/10.1098/rsta.2017.0401>

Zhang, Y. and Zindler, A. (1993). Distribution and evolution of carbon and nitrogen in Earth. *Earth and Planetary Science Letters*, 117, 331–345. [https://doi.org/10.1016/0012-821X\(93\)90088-Q](https://doi.org/10.1016/0012-821X(93)90088-Q)

~9 — LIST OF FIGURES, TABLES AND EQUATIONS~

9.1 – LIST OF FIGURES

Figure 1.1.....	Page 5
Figure 1.2.....	Page 13
Figure 1.3.....	Page 32
Figure 1.4.....	Page 34
Figure 1.5.....	Page 44
Figure 2.1.....	Page 47
Figure 2.2.....	Page 52
Figure 2.3.....	Page 53
Figure 2.4.....	Page 54
Figure 2.5.....	Page 60
Figure 2.6.....	Page 60
Figure 2.7.....	Page 61
Figure 2.8.....	Page 67
Figure 2.9.....	Page 69
Figure 2.10.....	Page 69
Figure 2.11.....	Page 79
Figure 2.12.....	Page 80

Figure 2.13.....	Page 83
Figure 2.14.....	Page 84
Figure 2.15.....	Page 90
Figure 3.1.....	Page 107
Figure 3.2.....	Page 107
Figure 3.3.....	Page 111
Figure 3.4.....	Page 112
Figure 3.5.....	Page 114
Figure 3.6.....	Page 116
Figure 3.7.....	Page 117
Figure 3.8.....	Page 118
Figure 3.9.....	Page 118
Figure 3.10.....	Page 124
Figure 4.1.....	Page 137
Figure 4.2.....	Page 138
Figure 4.3.....	Page 140
Figure 4.4.....	Page 145
Figure 4.5.....	Page 147
Figure 4.6.....	Page 148
Figure 4.7.....	Page 149
Figure 4.8.....	Page 153
Figure 5.1.....	Page 164
Figure 5.2.....	Page 166
Figure 5.3.....	Page 168

Figure 5.4.....	Page 172
Figure 5.5.....	Page 174
Figure 5.6.....	Page 175
Figure 5.7.....	Page 175
Figure 5.8.....	Page 183
Figure 6.1.....	Page 194
Figure 6.2.....	Page 196
Figure 6.3.....	Page 198
Figure 6.4.....	Page 200
Figure 6.5.....	Page 202
Figure 6.6.....	Page 213
Figure 6.7.....	Page 214
Figure 6.8.....	Page 216
Figure 6.9.....	Page 218
Figure 6.10.....	Page 219
Figure 6.11.....	Page 220
Figure 6.12.....	Page 222
Figure 6.13.....	Page 225
Figure 6.14.....	Page 226
Figure 6.15.....	Page 227
Figure 6.16.....	Page 227
Figure 6.17.....	Page 229
Figure 6.18.....	Page 231
Figure 6.19.....	Page 232

9.1 – LIST OF TABLES

Table 1.1.....	Page 2
Table 1.2.....	Page 9
Table 1.3.....	Page 11
Table 1.4.....	Page 29
Table 1.5.....	Page 33
Table 1.6.....	Page 39
Table 2.1.....	Page 50
Table 2.2.....	Page 50
Table 2.3.....	Page 55
Table 2.4.....	Page 56
Table 2.5.....	Page 57
Table 2.6.....	Page 62
Table 3.1.....	Page 97
Table 3.2.....	Page 104
Table 3.3.....	Page 108
Table 3.4.....	Page 109
Table 3.5.....	Page 113
Table 3.6.....	Page 119
Table 3.7.....	Page 122
Table 3.8.....	Page 123
Table 3.9.....	Page 111

Table 3.10.....	Page 114
Table 4.1.....	Page 144
Table 4.2.....	Page 145
Table 4.3.....	Page 150
Table 5.1.....	Page 158
Table 5.2.....	Page 170
Table 5.3.....	Page 171
Table 5.4.....	Page 178
Table 5.5.....	Page 187
Table 5.6.....	Page 190
Table 6.1.....	Page 205
Table 6.2.....	Page 209
Table 6.3.....	Page 217
Table 6.4.....	Page 223
Table 6.5.....	Page 224
Table 6.6.....	Page 228
Table 6.7.....	Page 233

9.3 – LIST OF EQUATIONS

Equation 2.1.....	Page 73
Equation 2.2.....	Page 74
Equation 2.3.....	Page 74

Equation 2.4.....	Page 76
Equation 2.5.....	Page 76
Equation 3.1.....	Page 123
Equation 6.1.....	Page 215